THESIS
submitted to obtain the degree of
Doctor of Philosophy

Delivered by: **Université sorbonne paris Nord**

Gallilée doctoral school in collaboration with the department of Materials Science of the university of California Los Angeles

Speciality : **Materials science**

PhD student: **Etienne NGENZI**

Connecting atomistic and continuum description of grain boundary to investigate their migration in FCC polycrystalline materials.

PhD thesis defended on the November 9th 2022
before a jury composed of:

Referees:

Samuel FOREST, CdM, Mines ParisTech, CNRS
Vincent TAUPIN, LEM3, University of Lorraine, CNRS

Examination committee:

Brigitte BACROIX, CNRS, Sorbonne Paris Nord University
Jaime MARIAN, University of California Los Angeles
Oguz Umut Salman, CNRS, Sorbonne Paris Nord University
Anna Ask, DMAS, ONERA

Thesis adviser and co-adviser:

Yann CHARLES, LSPM, Sorbonne Paris Nord University, CNRS
Sylvain QUEYREAU, LSPM, Sorbonne Paris Nord University, CNRS

Abstract

Understanding microstructure evolution under thermo-mechanical loading is a critical industrial challenge, in link to materials design and optimisation, alleviation of structures, and prediction of the life in use of components. Microstructure evolution is also rooted in deep physical questions related to the interface atomic structures and its consequence upon their properties, or the mutual interactions between interfaces and other crystalline defects such as impurities and dislocations. The ultimate challenge in the field, is to formulate a model for microstructure evolution with real predictive capabilities. To this goal, the present PhD work associates atomistic simulations to mesoscopic phase field simulations focusing on Ni as a well known and model system for FCC metals.

First, great care has been paid to build and relax grain boundaries as inputs for Molecular Dynamics simulations. We then systematically investigated the migration of a single GB in a bi-crystal. To assess the generality of the migration results observed we considered a large panel of different GBs, including low and high misorientation angles around [001], and GB characters including tilt, twist and mixed GB. In contrast to most previous studies, we systematically explored the driving force (P)-temperature (T) parametric space, in order to clearly identify the type of migration that the GB follows from so-called thermally activated, athermal or antithermal behaviours. Most GBs experience a transition from an exponential to linear regime as function of P. These results, in agreement with existing literature when available, allowed us to formulate a unique mesoscopic migration law that reproduces MD results over the entire range of configurations, and can be passed onto larger scale simulations.

Next, we employed the phase field model of Admal et al.(Admal et al., 2018) which derives from the so-called KWC model. This model that describes GB as geometrically necessary dislocation distributions, and connects with classical crystal plasticity, is promising model, among a few other, for including the mutual interactions between GB migration and crystal dislocations in a polycrystal. After a sensitivity study, we showed that this model naturally captures key features of GB migration as observed in MD, such as the GB energy value, shear coupling coefficient and the existence of non-linear and linear regimes observed for the GB mobility. Finally, to connect quantitatively the two scales, we derived a closed form analytical solution for the 1D KWC formalism, building upon the work of Lobkovsky (Lobkovsky and Warren, 2001). This work paves the way for a realistic description of the microstructure evolution in a polycrystal, thanks to atomistically informed PF.

Résumé en français

Comprendre l'évolution de la microstructure sous chargement thermo-mécanique est un défi industriel critique, en lien avec la conception et l'optimisation des matériaux, l'allègement des structures, et la prédiction de la durée de vie en service des composants. L'évolution de la microstructure est également ancrée dans des questions physiques profondes liées aux structures atomiques des interfaces et à leurs conséquences sur leurs propriétés, ou aux interactions mutuelles entre les interfaces et d'autres défauts cristallins tels que les impuretés et les dislocations. Le défi principal dans ce domaine est de formuler un modèle d'évolution de la microstructure avec de réelles capacités de prédiction. Dans ce but, le présent travail de thèse associe des simulations atomistiques à des simulations de champs de phase mésoscopiques en se concentrant sur le Ni, un système bien connu et modèle pour les métaux CFC.

Tout d'abord, un grand soin a été apporté à la construction et à la relaxation des joints de grains (JdG) comme données d'entrée pour les simulations de dynamique moléculaire. Nous avons ensuite étudié systématiquement la migration d'un seul JdG dans un bi-cristal. Pour évaluer la généralité des résultats de migration observés, nous avons considéré un large panel de différents JdG, y compris des angles de désorientation faibles et élevés autour de [001], et des caractères de JdG, comprennant des joints de flexion, de torsion et des JdG mixtes. Contrairement à la plupart des études précédentes, nous avons systématiquement exploré l'espace paramétrique force motrice (P)-température (T), afin d'identifier clairement le type de migration que suit le JdG parmi les comportements dits thermiquement activés, athermiques ou antithermiques. La plupart des JdGs connaissent une transition d'un régime exponentiel à un régime linéaire en fonction de P. Ces résultats, en accord avec la littérature existante lorsqu'elle est disponible, nous ont permis de formuler une loi de migration mésoscopique unique qui reproduit les résultats DM (Dynamique moléculaire) sur toute la gamme de configurations, et qui peut être transmise à des simulations à plus grande échelle.

Ensuite, nous avons utilisé le modèle de champ de phase d'Admal et al.(Admal et al., 2018) qui dérive du modèle dit KWC. Ce modèle qui décrit les JdGs comme des distributions de dislocations géométriquement nécessaires, et se connecte à la plasticité cristalline classique, est un modèle prometteur, parmi quelques autres, pour inclure les interactions mutuelles entre la migration des JdGs et les dislocations cristallines dans un polycristal. Après une étude de sensibilité, nous avons montré que ce modèle capture naturellement les caractéristiques clés de la migration des JdGs telles qu'observées en DM, telles que la valeur de l'énergie des JdGs, le coefficient de couplage en cisaillement et l'existence de régimes non linéaires et linéaires observés pour la mobilité des JdGs. Enfin, pour relier quantitativement les deux échelles, nous avons dérivé une solution analytique pour le formalisme 1D KWC, en nous appuyant sur (Lobkovsky and Warren, 2001). Ce travail ouvre la voie à une description réaliste de l'évolution de la microstructure dans un polycristal, grâce à une PF paramétré de manière atomistique.

Aknowledgement

First of all, i would like to thank Dr Sylvain Queyreau for offering me a special yet great research subject, complex and challenging but yet original and ambitious. His supervision was different but complementary both on a personal and scientific level, and that's good. I really liked his way of supervising, it was not a bossy style on contrary it was always like a conversation between friends but yet fruitful all time. Of course, there were a few hiccups and we were able to overcome them and i think that's what friends do. In addition, i learned a lot from his very great scientific competence. I feel privileged to have been able to work with him. In addition, i would like to express my deep gratitude to my thesis director Yann Charles. Thank you for your support, availability, patience, your advice and the help you have given me.

I like to thank Dr Brigitte Bacroix, Dr Charlie Khalhoun and Dr Oguz Umut Salman for their support, encouragement and stimulating discussions. As well i like to thank all people In MECAMETA research group that i met during my stay, especially Mrs Ouafa RAHMANI , Mrs Wisline BEUCIA, Dr Benoit Fer, Miss Ayda MAJOUL, Dr Matthieu DEGEITER and all people involved in this group for their assistance and stimulating discussions. I like to express my gratitude to LABEX SEAM for the financial resources for my research and scientific exchange in an international surrounding.

Thanks to the department of materials science of the University of California Los Angeles (UCLA) for funding my stay at UCLA and more importantly for allowing me to use the Hoffman2 Cluster to run simulations at mesoscopic scale. For that i am very grateful to Prof. Jame Marian for making this possible and also for his support, encouragement and useful discussions. Many thanks to Dr Nikhil Chandra Admal from University of Illinois at Urbana-Champaign for the useful discussions.

Finally, many thanks to my family and friends for supporting me all the way, for enabling this work, for their encouragement and understanding.

Table of content

List of Figures

List of Tables

General introduction

Crystalline materials -such as metals- are found in polycrystalline form characterised by an agglomerate of differently oriented grains. Mechanical properties of crystalline materials are controlled by their crystalline nature, but mostly by the evolution of lattice defects such as internal surfaces -grain boundaries (GB)- separating two differently oriented grains. For industrial applications, mechanical properties and durability of these polycrystalline materials need to be optimised to meet the application requirements. One common way to improve materials properties is by applying one or a sequence of various thermo-mechanical treatments. The materials microstructure evolves greatly during these treatments and in a rather very complex manner. Microstructural changes typically involves many elementary mechanisms operating simultaneously such as grain boundary migration (normal motion) accompanied or not by grain boundary rotation and shear coupling (transversal motion). GB migration may be triggered by various driving forces and GB motion may be impeded by other GB motion, existing dislocations in microstructures or impurities... Figure 1 a) to c) provides an example of such microstructural evolution observed experimentally at LSPM. It consists of the in-situ evolution of the polycrystalline microstructure within a SEM of pure polycrystalline aluminium annealed at 400° for 2h30 and then deformed in traction at 3%. The EBSD maps show a complex -non-linear and anisotropic- rearrangement of grains through grain boundary migration in connection with the rotation of grains (associated with grain colour changes) but also in correlation to the dislocations within grains.

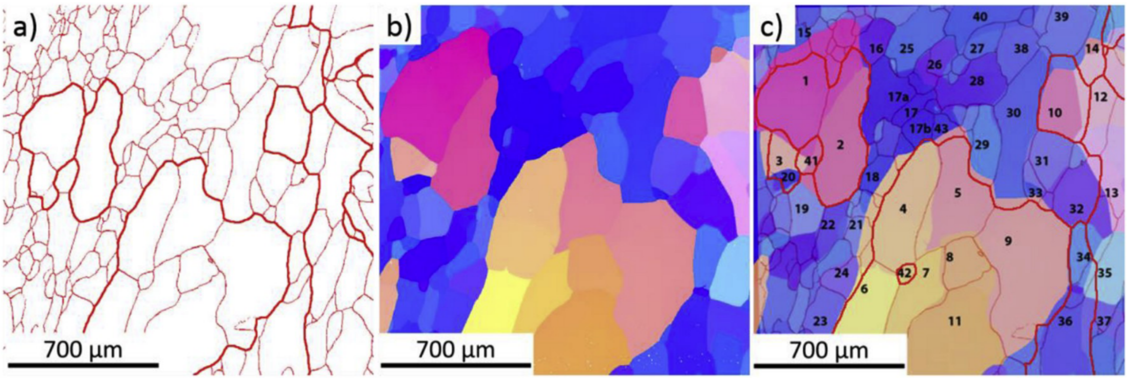

Figure 1: The EBSD polycrystal of pure aluminium subjected to thermo-mechanical treatment a) annealed for 2h30 at 400° with a strain rate of 3% b) annealed for 2h30 at 400° with a strain rate of 3% and re-heated at 400° for 2h30 c) superposition of a) and b). Note that the colour code indicate the RD orientation (according to the colour code triangle) with respect to the crystal frame (Beucia et al., 2019).

The mesoscopic picture shown above needs to be understood in terms of microscopic mechanisms that control microstructure evolution. The microscopic mechanisms strongly depend on the atomic structure of a grain boundary and the structure-property relationship is far from being understood despite an abundant literature on the subject (Sutton, 1996; Priester, 2012; Homer et al., 2014b; Homer, 2015; O'Brien and Foiles, 2016). However, a clear understanding of structure-property relationship can only be achieved through atomisitic simulations since conventional methods (experimental methods) cannot track the GB atomic structure during microstructure changes (Sutton, 1996). Besides, the knowledge of the atomic structure must be acquired for the large variety of GB that may exist in a microstructure, as we discuss next.

One major challenge at atomic level is how to define unambiguously a grain boundary. From a purely geometrical point, a grain boundary can be described using five macroscopic degrees of freedom (dof), related to rotations and GB plane. However, at the atomic level, another degree of complexity may be found as there exist numerous grain boundaries of the same macroscopic degrees of freedom but with different microscopic dof among the four additional dof (Sutton, 1996; Priester, 2012). In the literature, there exist studies that attempted to characterise a grain boundary atomic structure based on atomic arrangement. For instance, for a cubic crystallographic structure, few 3D structures -or structural units- suffice to describe arrangement of atoms within a grain boundary (Sutton, 1996; Han et al., 2017b; Banadaki and Patala, 2017). However, this structural unit model is purely geometrical and since structural units may be distorted, it is not clear that this model can describe physical properties of a grain boundary. A competing or alternative approach is to model grain boundary using dislocations in a continuous distribution or as an array of discrete segments (Bollman, 1972; Vattré and Demkowicz, 2013; Anderson et al., 2017).

In general, the atomic structure of grain boundaries controls their response to impacting factors (temperature, driving force, interaction with impurities etc..) that influence their motion and, overall, the -normal- migration of grain boundaries controls the rate of evolution of a microstructure. The velocity (v) of a moving grain boundary reads $v = \boldsymbol{MP}$, where $\boldsymbol{M}$ is mobility and $\boldsymbol{P}$ is driving force. Depending on a grain boundary, the extent of migration and the dependence on temperature and applied driving force can vary dramatically. For a pure material, different mechanical driving forces for grain boundary migration have been identified and they range from a) GB curvature (related as the second derivative of grain boundary energy), b) differences in elastic strain density between two abutting grains and c) differences in stored energy associated to dislocation microstructures on both sides of the interface (Priester, 2012; Zhang et al., 2004b). The mobility function ($\boldsymbol{M}$) defined above may exhibit a complex dependence on both temperature and motive force and GB type (Olmsted et al., 2009b,c; Priester, 2012; Mishin et al., 2010; Homer et al., 2015; Deng and Schuh, 2011b), and the origins of these differences are poorly known. v is typically considered independent of the nature of the driving force, but may not be uniquely defined (Deng and Schuh, 2011b; Ngenzi et al., 2021) or an intrinsic property to a given GB. Temperature largely affects mobility (Homer et al., 2013, 2014b; Mishin et al., 2010; Rajabzadeh et al., 2013; O'Brien and Foiles, 2016). Systematic molecular dynamics studies of grain boundary migration have reported that various temperature behaviours can be observed ranging from thermally activated, viscous to antithermal behaviours (Olmsted et al., 2009b,c; Homer et al., 2014b; O'Brien and Foiles, 2016; OMAR, 2019). Again atomistic data could help but analysing the GB structure during migration proved to be even more difficult than when immobile. Nonetheless, some elementary mechanisms at the origin of grain boundary motion have been identified and can depend on atomic structure of a grain boundary, temperature and magnitude of applied motive force (Deng and Schuh, 2011a,b; Rajabzadeh et al., 2013; Ngenzi et al., 2021). For example, grain boundary motion can operate through uncorrelated atomic shuffling events motion in which atoms initially in grain one move to match the crystallographic orientation of atoms in grain two. This mechanism may or may not be thermally activated depending on the grain boundary structure (Sutton, 1996). In addition, in some other grain boundaries, the atomic shuffling may be correlated and is associated with the nucleation and propagation of a pair of disconnections (defects that exhibit both a dislocation and a step like character) on the surface of a grain boundary (Rajabzadeh et al., 2013).

Although, atomisitic simulations have revealed the rich physics behind grain boundary migration, up to date, there is no predictive model for grain boundary migration. There are few successful attempts (Sutton, 1996; Rajabzadeh et al., 2013; Race et al., 2014) to develop such models. For instance, in (Sutton, 1996) for thermally activated grain boundaries that move by nucleation and propagation of step was devised for pure twist grain boundaries and in (Rajabzadeh et al., 2013) for predicting the Gibbs free energy for motion and it was developed for grain boundaries that move through nucleation and propagation of disconnections. However, all these models were developed for some specific grain boundaries, generalization may not be possible and may not be straightforward to implement. Having in a place a robust and generic mesoscale model that can work for several grain boundaries (regardless of the character of a grain boundary) to predict grain boundary evolution can permit to reduce both the time and cost associated with atomistic simulations.

In contrast to atomistic methods, continuum scale methods offer a way to investigate microstructure evolution at the larger length scale of a polycrystal (Warren et al., 2003). In this context of Phase field approaches (Warren et al., 2003) formulated based on a set of field variables that are assumed to be continuous across the interface regions (Elder et al., 2002; Warren et al., 2003; Elder and Grant, 2004; Ask et al., 2018)), Kobayashi Warren and Carter (Warren et al., 2003) (KWC) have derived a model that takes into account the energy, evolution and crystal rotation of diffuse grain boundaries. However, this model lacks connection with dislocation activity within grains. In the literature, there exist more recent models, for instance, in Ask et al. (Ask et al., 2018) and in Admal et al. (Admal et al., 2018) phase field models both derived by extending the KWC phase field model to incorporate the evolution of dislocation density (For example see figure 2 for results from Admal and Marian's phase field model). However, the main challenge at this scale is to capture grain boundary evolution with crystal plasticity simultaneously while still including the rich physics observed from atomisitic simulations. Indeed, to devise a model that preserves the physics observed in atomistic simulations would require bridging atomistic and continuum scale approaches. In the literature, there exist some attempts to connect both scales for different phenomena (Denoual et al., 2010; Reina et al., 2014; Bragard et al., 2002). Despite these progresses, today, there is no physically based model for predicting microstructure evolution at polycrystalline length scale in FCC materials. In this work, we attempt to fill this gap by associating **Molecular Dynamics (MD) simulations with a unified Admal and Marian's Phase Field (PF) framework (Admal et al., 2018) to predict crystal plasticity and microstructure evolution in FCC materials.**

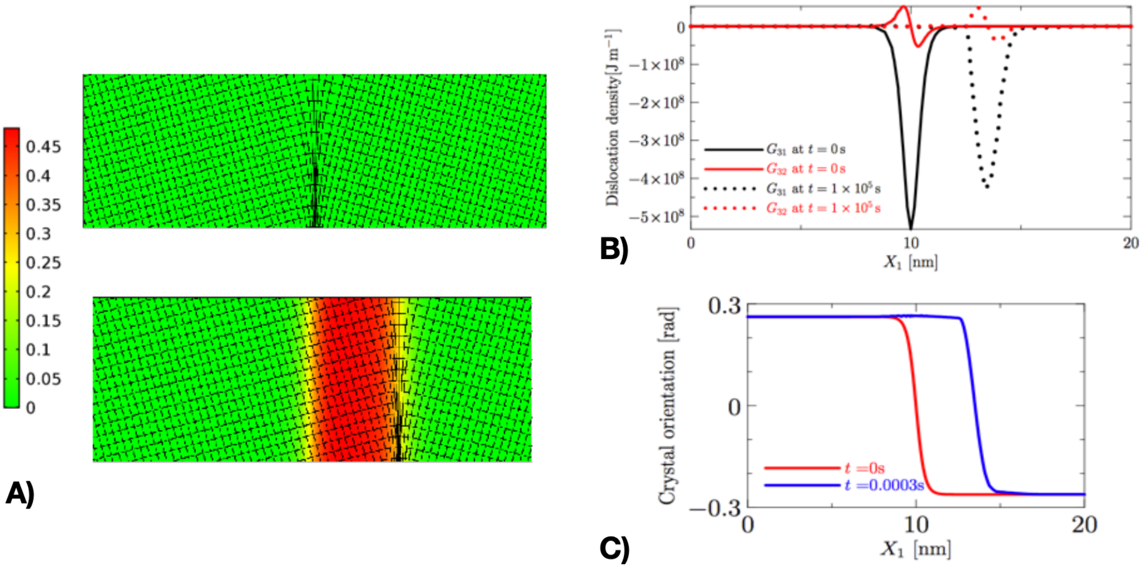

Figure 2: A) A continuous domain with a symmetric tilt grain boundary inserted in the center. When a sufficiently enough driving force is applied a grain boundary moves to the right. The colour level shows the extent of plastic deformation induced by grain boundary motion. B) shows the associated evolution of the dislocation density (components $\boldsymbol{G}_{31}$ and $\boldsymbol{G}_{32}$ C) shows the orientation of abutting grain at before and after migration (Admal et al., 2018).

This manuscript work is divided into two main parts.

- The first and principal part of this work is concerned with atomistic simulations of [001] symmetric Coincidence Site Lattice (CSL) grain boundaries in Nickel as representative of other FCC materials. For this, large scale MD simulation will be concerned with a comprehensive set of CSL grain boundaries including low ($\theta \leq 15°$) and high ($\theta \geq 15°$) misorientation angles of different characters (tilt, mixed, twist). Since atomic structure of a grain boundary controls many aspects of a grain boundary, great care has be paid to building, relaxation and characterisation of atomic structure of a GB, using in-house tools. Consequently, a well established semi-empirical Embedded Atom multi-body (EAM) inter-atomic potential (Foiles and Hoyt, 2006) developed for mechanical application will be used to describe atomic interaction. We will see, that the GB energy obtained here is in nice agreement with existing studies, when possible, which validates our methodology and tools.

- In the second step of this first part, we will do a systematic study of the parametric space of GB migration in terms of temperature and applied driving force. To move a grain boundary, we will apply a synthetic driving force of Janssens (Janssens et al., 2006). We will apply a driving force of magnitude sufficient enough to move a grain boundary and the temperature will be varied. This systematic study will allow to unveil clear migration behaviours and common mobility trends for *a priori* different grain boundaries. Contrary to previous similar investigations, we will see that the trends observed in study are clear. As for the mobility of dislocations in bcc metals, many GB exhibit first a thermally activated regime at low temperature, low driving force, that changes into a linear behaviour for large stresses, high temperatures (Tang et al., 1998; Rodney and Proville, 2009; Naamane et al., 2010; Gilbert et al., 2011; Queyreau et al., 2011). A systematic exploration of this space will allow to devise phenomenological mobility function that can be straightforwardly imported in the phase field model.

- In the second part of this work, we have conducted phase field simulations on STGB grain boundary investigated in the first part using the model of Admal & Marian (Admal et al., 2018). The central idea of this model, is to make use of the kinematic equivalency of GB in terms of dislocations distributions, whose field are solved through classical crystal plasticity. Then, we propose a sensitivity test of the model's parameters. We will see that the values obtained are close to the values (α, ϵ, s, e) suggested in (Warren et al., 2003). This will be followed by a comparison of grain boundary energy predicted by this model and atomisitic method. We will see that the prediction of this model compares favourably with atomistics. In the next step, we will do dynamic simulations to investigate ability of this phase field model to recover on it own some of the trends observed from atomistic simulations, such as GB energies, shear coupling factor and GB migration trends. Therefore, we will see that describing a grain boundary as dislocation arrays (or GND distribution) is very effective and promissive, at least for the STGB considered here. In the final step we will propose a method to parameterise this phase field model using atomistic information.

Part I

Atomic scale investigation of grain boundary structures and properties

Chapter 1

Defects in crystalline materials

1.1 Introduction

Most applications of FCC metals use these materials in their polycrystalline form. A wide array of mechanical properties of such materials are influenced not only by the distribution of grain sizes (Petch, 1953; Hall, 1951) and their orientations (Sutton, 1996) but also by the density and nature of lattice defects (Sutton, 1996; Priester, 2012; Gottstein et al., 1998; Hull and Bacon, 2001), such as vacancies, dislocations and grain boundaries.
Defects are very common in polycrystalline materials. They exist in different dimensions, therefore, dimensionality provides a more convenient scheme to classify them. The aim of this chapter is to give fundamental details of polycrystalline defects. The defects are classified based on their dimensionality, since lower dimension defects may act as building blocks of higher dimension defects or interact with each other. in this chapter, we will focus on single element systems for the sake of simplicity.

1.1.1 Point defects

Zero dimension defects are very common, thanks to their low formation energy. Punctual defects may form spontaneously thanks to thermal vibration or by a plastic deformation of a crystal. Two types of punctual defects are typically considered, in the form of vacancies and (self) interstitial atoms. In the GB context; vacancies may considerably alter the GB structure (see later) and impurities may impede GB motion (Zener effect).

1.1.2 Dislocation

Dislocations are one dimensional defects that accommodate distortion in a crystal. They are metastable defects associated to large amount of (mostly elastic) strain energy and are thus initially present in crystals. Dislocation is one of the important crystallographic defects and they control most of the plastic behaviour of crystalline materials (Hull and Bacon, 2001; Hirth and Lothe, 1992; Fang, 2018; Kelly and Knowles, 2020). Dislocations may also be used to describe the structure of grain boundaries (see later). Therefore, an elementary understanding of dislocation is required before introducing grain boundaries. For this, it is important to start by showing how it is created in a perfect crystal.

Kinematically speaking, a dislocation is introduced in a crystal by making a cut in a perfect crystal. Next, one side is shifted relative to the other by a translation vector $\overrightarrow{\mathbf{b}}$ which is not equal to the lattice vector (Bulatov and Cai, 2006). This translation vector is known as Burgers vector. Inside the crystal, at the edge of the cut surface, remains a line of atoms with a higher distortion which fades away by going further from this line. This line separates the sheared and unsheared regions. The region in immediate surrounding of this line, where linear elasticity does not apply, is known as dislocation core (Hull and Bacon, 2001).

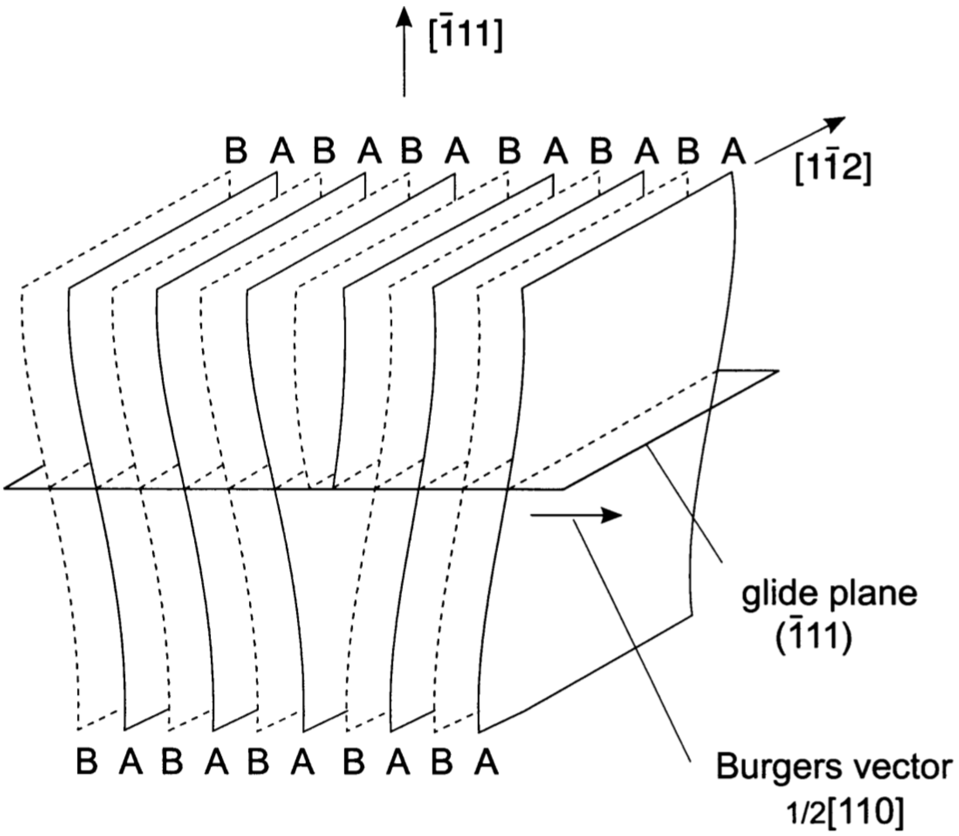

Figure 3: An edge dislocation in a face centred cubic crystal (Hull and Bacon, 2001).

Figure 3 shows an FCC crystal made of (110) planes which have a two fold stacking sequence ABAB.... The crystal contains a dislocation created by inserting two extra (110) half planes. Note that the (110) planes are perpendicular to the Burgers vector. The angle (θ) between the Burgers vector and the dislocation line can take any value. This angle defines the character of a resulting dislocation, which controls some of its properties. When $\theta = \frac{\pi}{2}$, a dislocation has a pure edge character (Taylor, 1934) (see figure 4(a)). For example, dislocation shown in figure 3. When θ=0, a dislocation has a pure screw character (see figure 4(b)). A general dislocation is called mixed dislocation. Figure 4(c) shows a mixed dislocation in which at point E, it is a pure edge as the dislocation line is perpendicular to $\overrightarrow{b}$. At point S, it is a pure screw because the dislocation line is parallel to $\overrightarrow{b}$ and the remainder of dislocation is regarded to have mixed characters. $\overrightarrow{b}$ can be resolved into the edge $\overrightarrow{b}_1 = \overrightarrow{b}\sin(\theta)$ and screw $\overrightarrow{b}_2 = \overrightarrow{b}\cos(\theta)$ contribution. Figure 4(d) illustrates geometrically the orientation of these two components relative to the dislocation line xy. Since a dislocation represents a line of misfit in crystal, it moves when enough driving force (called Peach-Koehler Force) is applied. The main type of motion is (conservative) gliding in which the atoms above and below glide plane are displaced with respect to each other by a translation vector $\overrightarrow{\mathbf{b}}$ (figure 5). Consequently, crystal deformation is a progressive displacement of dislocations through a crystal. The kinetics of dislocation motion may depend upon dislocations character (Gilman, 1994; Hull and Bacon, 2001; Rodney, 2004; Wang and Fang, 2000).

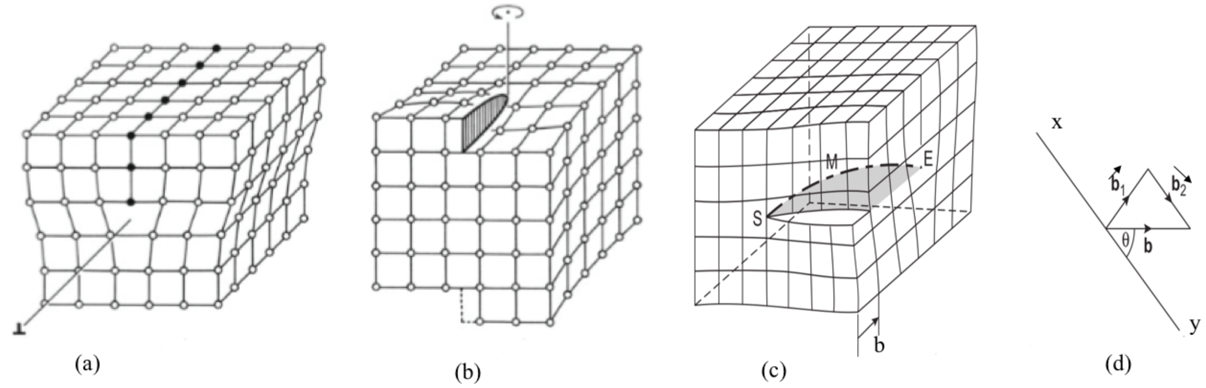

Figure 4: Illustration of classical dislocations (a) edge dislocation (b) screw dislocation (c) mixed dislocation (Hull and Bacon, 2001) and (d) resolving burger vector into its components (Hull and Bacon, 2001).

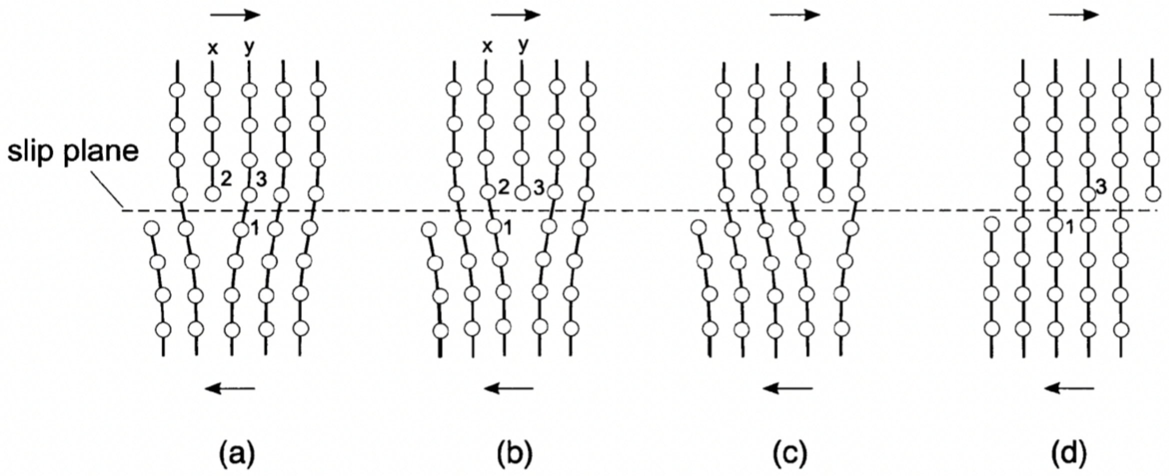

Figure 5: Movement of an edge dislocation by gliding. (a)-(b) A shift of atom 1 relative to atoms 2 and 3 moves extra half-plane from x to y (c)-(d) the process repeats as the dislocation continues to glide.Note that the arrows indicate the applied shear stress.

Dislocations glide usually on specific crystallographic planes, as a consequence of dislocations core structure. The mean rate plastic deformation $\dot{\gamma}$ due to dislocation motion during a time interval δt is given by equation 1.1 where ρ_m is density of mobile dislocations, v is average velocity of dislocations and b the Burgers displacement (Orowan, 1934; Johnston and Gilman, 1959).

$$\dot{\gamma} = \rho_m b v \tag{1.1}$$

In the FCC structure, dislocations may dissociate into partial (Shockley) dislocations separated by a stacking fault ribbon. These partials may be found in some GB structures. The Thompson's tetrahedron allows to decompose perfect dislocations into possible partial dislocations. This tetrahedron comes from the fact that the four different sets of $\{111\}$ planes lie parallel to the four faces of a regular tetrahedron. In addition, the edge of tetrahedron lie parallel to the $\langle 110 \rangle$ slip directions (Zhu et al., 2011) (see figure 6 for more details). In figure 6, A, B, C and D denote the corners of tetrahedron and α, β, γ, δ denote the mid points of the opposite faces. The edges (AB, BC, CD,...) of tetrahedron define in magnitude and direction the Burgers vectors of perfect dislocations. The lines from the corners to the center ($A\gamma$, $B\alpha$,...) define the Burgers vectors of Shockley partial dislocations.

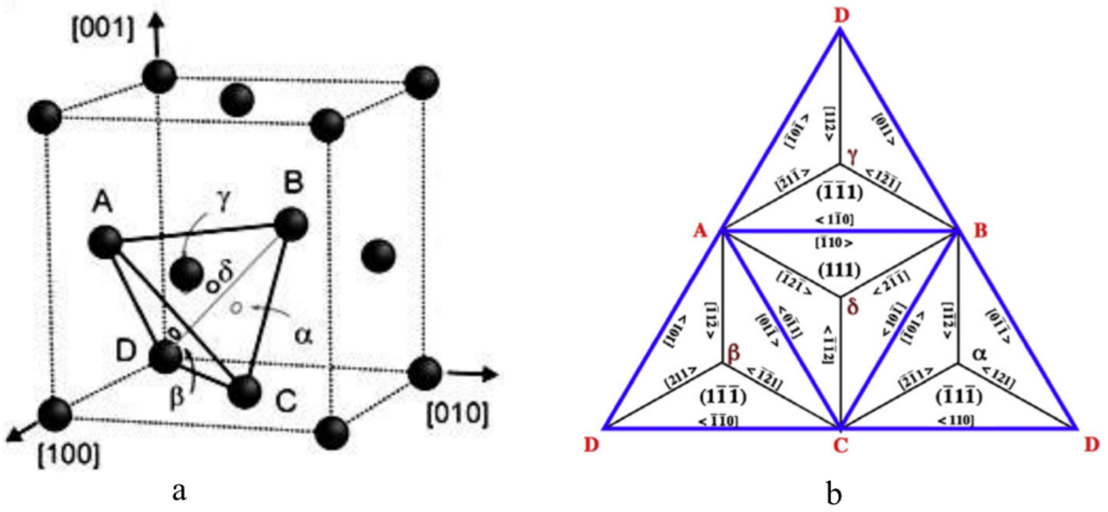

a b

Figure 6: Thompson's tetrahedron a) representation of Thompson's tetrahedron in FCC unit cell b) Two dimensional representation of Thompson's tetrahedron showing all possible slip planes and the Burgers vectors of possible dislocations.

1.2 Grain boundary

In the section, we will present the most relevant background regarding Grain Boundaries, 2D defects that are at the heart of the present work. In the past, intense experimental and numerical efforts have been directed towards a clear description of grain boundaries (Kronberg and Wilson, 1949; Read and Shockley, 1950; Weins, 1972; Sutton and Balluffi, 1987; Yip and Wolf, 1992; Aust et al., 1993; Sutton, 1996; Gleiter, 1996; Priester, 2012).

Hence, there exits several ways to describe a grain boundary (Priester, 2012). Description of grain boundaries allows to define, categorise and model grains boundaries. Among all other descriptions, the following sections focus first on geometrical descriptions of grain boundary, description of grain boundary as an array of dislocation and description of grain boundary as a periodic sequence of structural units .

1.2.1 Geometrical description of grain boundary

Geometrical description of grain boundary has been proposed several decades ago (Kronberg and Wilson, 1949) and it has become a cornerstone of research on grain boundary. From a purely geometrical argument and as lattices are discrete in nature, adjoining two rotated crystals will lead to sites of (exact or close to) atomic coincidence separated by non-coinciding regions (shown in pale green colour in figure 7b). An increase in the number of coincidence sites implies a good fit between adjacent grains. Describing a grain boundary as an array of coincidence sites makes a grain boundary structure easy to visualise even on a two dimensional diagram, called the dichromatic pattern.

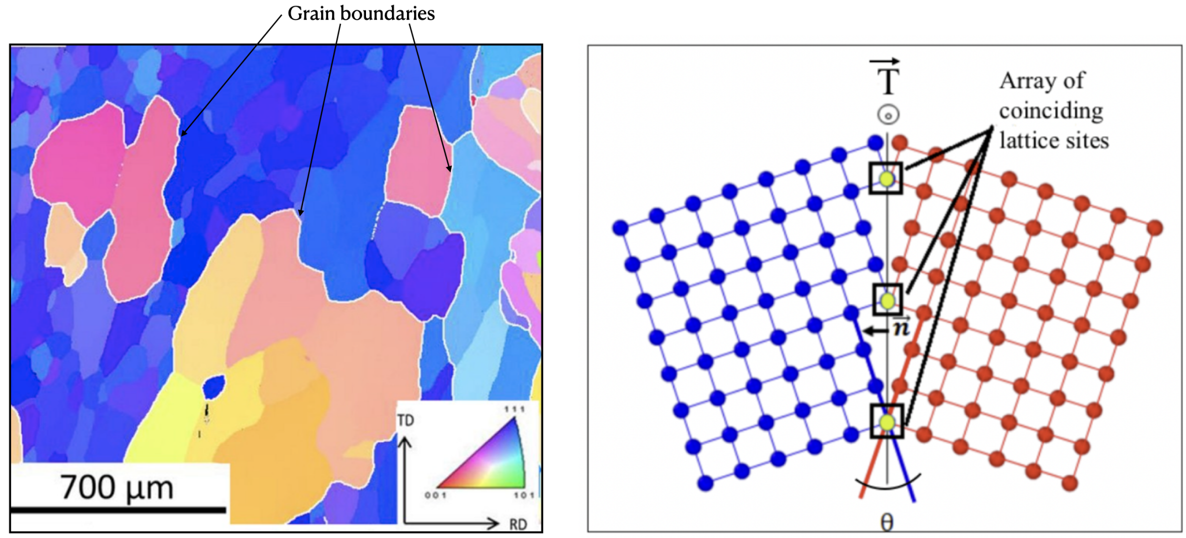

(a) **(b)**

Figure 7: (a) EBSD maps and discrete Inverse Pole Figure (IPF) of 4N pure aluminum nicrostructure containing several grain boundaries (Beucia et al., 2019) b) Macroscopic degrees of freedom of a grain boundary.

A grain boundary exhibits nine geometrical degrees of freedom (dof) (five macroscopic and four microscopic) (Randle, 1996; Sutton, 1996; Priester, 2012). Macroscopic degrees of freedom describe the overall orientation change between two grains at grain boundary (Sutton, 1996; Priester, 2012) as figure 7 b) shows. More precisely, the crystallographic orientation change between perfectly orientated lattice and new misorientated lattice is described by a misorientation axis ($\vec{T}$) which corresponds to two degrees of freedom and a misorientation angle (θ) between two adjacent and differently orientated grains, associated to one degree of freedom. The crystallographic orientation of the grain boundary surface, known as grain boundary plane ($\overrightarrow{n}$), itself corresponds to two degrees of freedom.

The remaining four microscopic parameters describe a localised translational and expansion dof between two grains at grain boundary. Geometrical descriptions of a grain boundary are widely used in structural research of grain boundary in an attempts to understand the structure-property relationship of GB. Figure 8 gathers some classifications of grain boundary that we will use in this study.

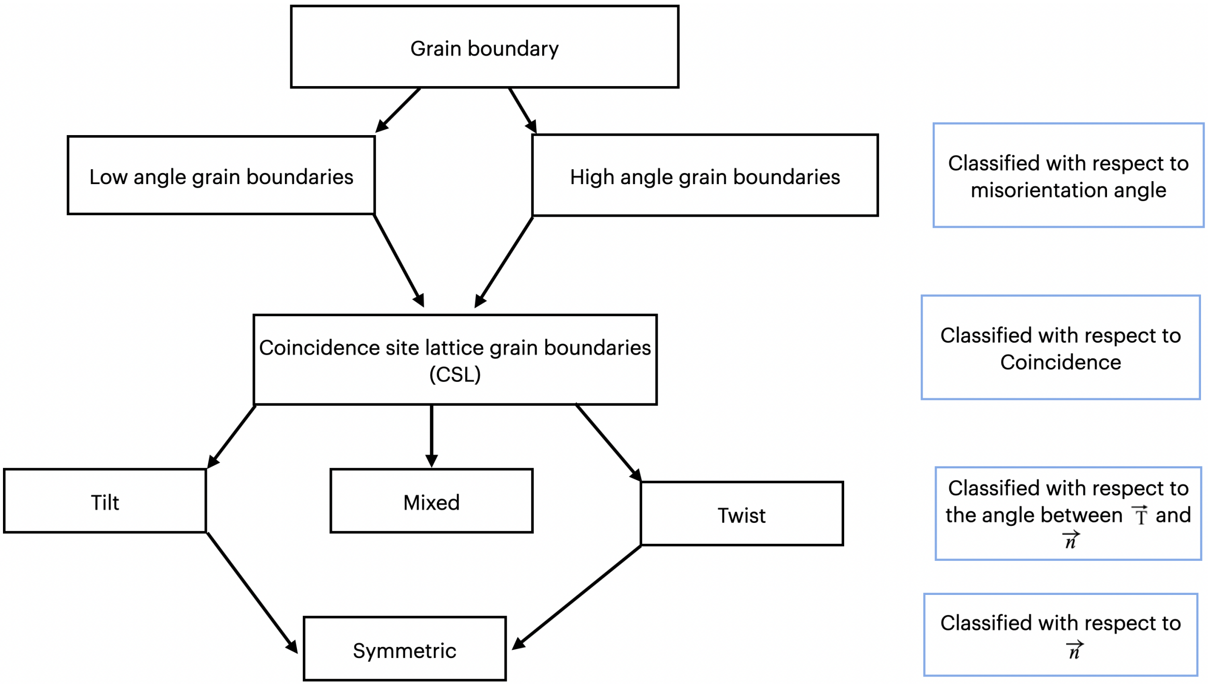

Figure 8: Classification of grain boundaries that are discussed in this work.

1.2.1.1 Coincidence Site Lattice (CSL) grain boundaries

Some grain boundaries correspond to an exact coincidence site lattice (Grimmer, 1976; Randle, 1996; Sutton, 1996; Priester, 2012) as demonstrated in figure 9. From the theoretical work of Ranganathan, equation 1.2 can be derived for CSL GB (Ranganathan, 1966; LORD, 2006; Talaei et al., 2019b), where grain 1 can be related to grain 2 by a rotation of θ about rotation axis $\overrightarrow{T}(a, b, c)$.

$$\tan\left(\frac{\theta}{2}\right) = \frac{Y\sigma}{X} \tag{1.2}$$

Where X and Y are prime numbers and $\sigma = \sqrt{a^2 + b^2 + c^2}$. The inverse of the number of coinciding sites is noted Σ. According to Ranganathan (Ranganathan, 1966),

$$\Sigma = \frac{1}{m}\left(X^2 + \sigma^2 Y^2\right), \tag{1.3}$$

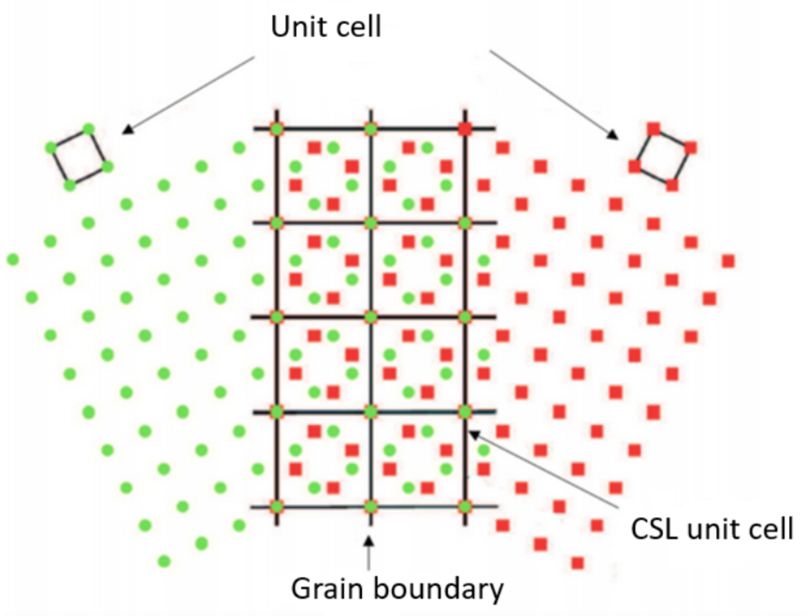

Figure 9: A $\Sigma 5$ CSL grain boundary of $\theta = 36.9$ degrees and rotation axis $[0, 0, 1]$ (OMAR, 2019).

where

$$m = \begin{cases} 1, & \text{if } X^2 + \sigma^2 Y^2 \text{ is odd} \\ 2, 4 & \text{depending on whether 2 or 4 is the even factor of } X^2 + \sigma^2 Y^2 \end{cases}$$

The definition of Σ can also be given in terms of volume of coincidence site lattice unit cell (V_{CSL}) and unit cell of an FCC crystal (V_{UC}) (Priester, 2012)

$$\Sigma = \frac{V_{CSL}}{V_{UC}} \tag{1.4}$$

For example, $\Sigma 5$ CSL grain boundary is produced by a rotation of $36.9°$ about [001]. $\Sigma 5$ means that one in 5 atoms is a coincidence as figure 9 shows.

1.2.1.2 Rotational symmetry in CSL grain boundaries

Since CSL grains boundaries have several rotational symmetries, both numerical and theoretical analysis limit themselves to fundamental zone (FZ) that captures all natural crystallographic symmetries of the underlying CSL structure. This is why we now present the fundamental zones of GB.

In Patala and Schuh (Patala and Schuh, 2013), it has been shown that the CSL boundary-plane spaces possess several point group symmetries. Later, the work of Homer et al.(Homer et al., 2015) has shown that these symmetries may help in understanding the CSL structure-property relationship and provide a relevant way to visualize GB character space (see later). For example, grain boundary symmetries are used for the graphical

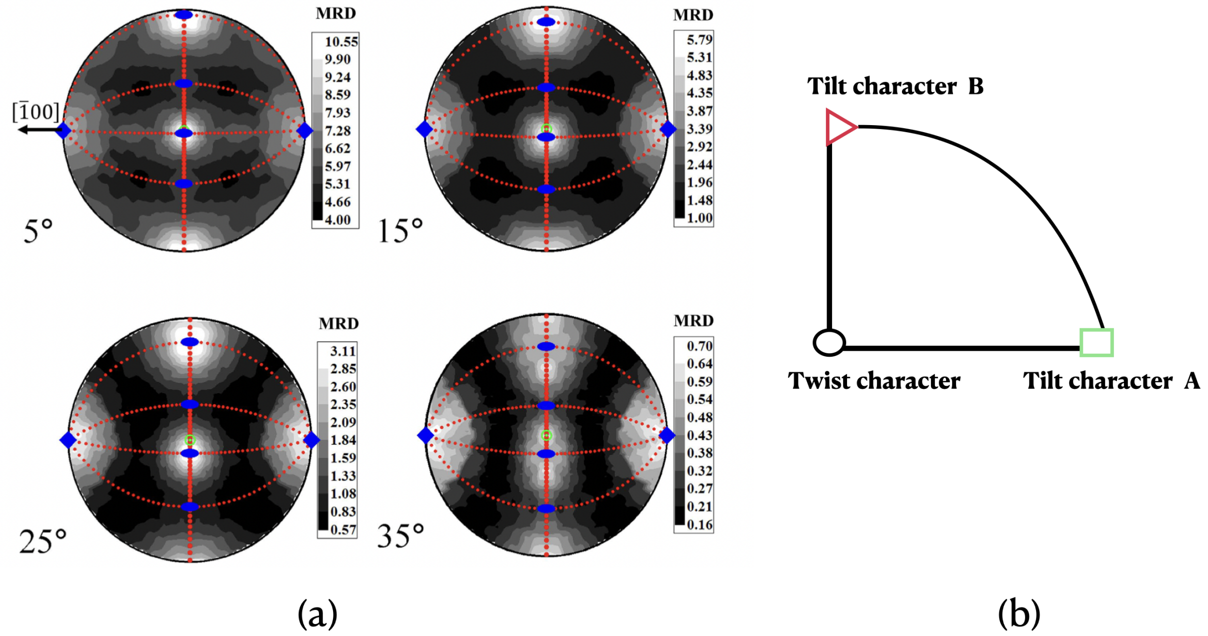

Figure 10: a) Grain boundary distribution overlaid with the bicrystal symmetries of the misorientation angles 5°, 15°, 25° and 35° with misorientation axis [001] (Rohrer et al., 2004) b) Identification of pure grain boundary character (pure twist, tilt character A and B) in a triangular fundamental zone.

representations of the possible grain boundary plane orientation.

For any grain boundary type (Σ), there is an infinite number of possible boundary planes of normal $\overrightarrow{n}_i$ oriented differently in space. Consequently, grain boundary analysis now limits to the analysis of the Fundamental Zone (FZ) for a given GB family. FZ is obtained from a stereographic projection of possible boundary plane for a given Σ with $\overrightarrow{n}_i$ along the z direction. Here we give an example in figure 10a) of grain boundaries of misorientation angle 5°, 15°, 25° and 35° with a corresponding misorientation axis [001]. They show the spatial distribution of all possible boundary planes. The dashed red lines which are mirror planes capture the symmetry of boundary plane distribution. Here we can easily notice the natural rotation of the symmetries by increasing the misorientation angle. Consequently, one can readily see that only one triangular region in any images is self sufficient to describe the entire boundary plane distribution. Triangular zone captures all natural crystallographic symmetries of the underlying CSL structure.

Figure 10 b) shows a triangular fundamental zone in which pure grain boundary characters can easily be identified. For more details on the subject see (Patala and Schuh, 2013; Homer et al., 2015).

1.2.1.3 Displacement shift complete (DSC) lattice

From figure 9, one can notice that there exist very small vectors which conserve the CSL if the location of the coincidence sites are allowed to change.

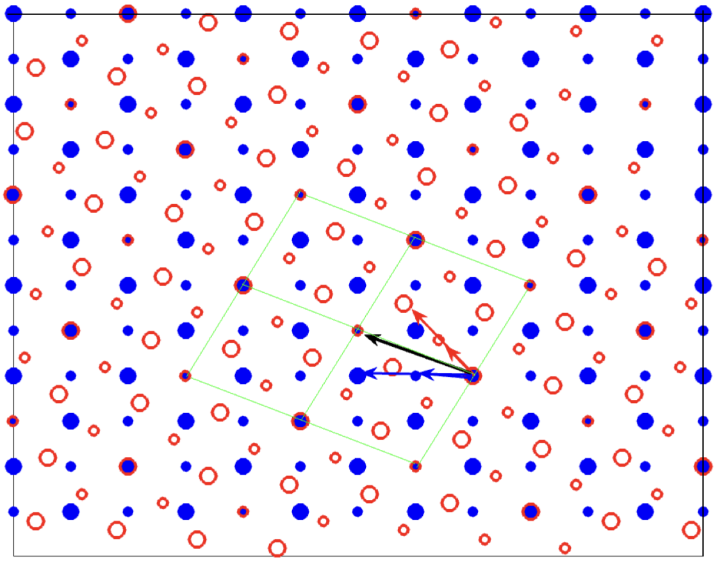

Figure 11: A DSC lattice in Σ5(36.9°) with a misorientation axis [001] in which the coincidence lattice sites are shown in blue colour encircled by red. The blue atoms belong to grain one and red to grain two. The smaller atoms belong to a lower layer whereas bigger atoms belong to a top layer of the stacking.

Examples of such vectors are shown in figure 11. These vectors are called Displacement shift complete (DSC) and are shown in black, red and blue in figure 11 in which green square box show a unit of this lattice. In other words, it means that, the coincidence site lattice will shift as a whole, if either grain one or grain two is translated by one of these vectors. Figure 11 shows the DSC lattice of Σ5 grain boundary in which blue atoms encircled by red colour are in perfect coincidence sites, the blue atoms belong to grain one and the red atoms to the grain two. Note that smaller and bigger circles correspond to lower and upper layer of the stacking respectively.

Obvisouly, a blue atom encircled by red can be translated to occupy the place of an other blue atom encircled by red without affecting the CSL lattice, the same goes for blue to blue, red to red, red to blue, blue atom encircled by red to blue, blue atom encircled by red to red and vice versa. All translation vectors of the CSL and crystal lattice are as well DSC vectors. Therefore, DSC vectors form a DSC lattice. DSC lattice is defined as the largest lattice containing two crystals. The definitions of CSL and DSC lattices are, of course, purely geometrical and based on a non relaxed atomic geometry. However, in reality, small adjustments of atomic positions at grain boundary and close to it are to be expected. Extension of coincidence concept to include in near-coincidence has thus been proposed to continue transitioning toward more realistic grain boundary picture.

1.2.1.4 Bollmann approach: O and O_2-lattices

If any factor causes a CSL grain boundary to deviate from its coincidence sites, a grain boundary reacts with a tendency to preserve its structure. This is achieved either by a crystal lattice translation or a DSC lattice translation. Consequently, translation linear defects are produced which maintain the structure of a grain boundary. These linear defects are called structural or intrinsic dislocations (Bollmann, 1972). Therefore, by taking advantage of these dislocations, any grain boundary structure can be described in terms of these dislocations.

O-lattice

Despite the success of CSL theory in explaining some of the spacial orientation relationship between two adjacent grains, it is not applicable to some grains boundaries because CSL model requires a very exact coincidence which is not achievable for some rotation angles. Bollmann extends the coincidence concept with the introduction of a more generalised coincidence model called O-lattice. The O-lattice describes a grain boundary geometry and provides a description of a GB in terms of structural dislocations (Bollmann, 1972; Priester, 2012).

The O-lattice is viewed as the collection of points in zone of good fit surrounded by zones of bad fit between two abutting grains. Unlike the CSL model, the coincidence points may have internal coordinates in the unit cell of both grains. Hence, the O-lattice is continuous for all grain boundary misorientations and each point O is regarded as the origin of the transformation that relates grain one to grain two. Considering a O-lattice point x, marked by vector $\overrightarrow{x}_o$ in a grain boundary plan, which remains invariant during transformation, the O-lattice is described by Bollmann's equation

$$\overrightarrow{B}_m = \left(I - R^{-1}\right) \overrightarrow{x}_O \tag{1.5}$$

in which **I**, **R** are identity and rotation matrix respectively and $\overrightarrow{B}_m$ is a translational vector also known as the Burgers vector of structural dislocations. Despite encouraging results obtained for different metals (Bollmann, 1972), this model does not explain angular deviation from the closest coincidence around a misorientation axis $\overrightarrow{T}(a, b, c)$ observed in high angle grain boundaries. Consequently, Bollmann introduced later an other lattice powerful enough to take into account this angular deviation.

O_2-lattice

Still following Bollmann's considerations (Bollmann, 1972), high angle grain boundaries may undergo an angular deviation ($\Delta\theta$) from the closest coincidence in particular situations. The O_2-lattice, mathematically, defines a set of all invariant points between two

DSC translation lattices of the bi-crystals rotated by $\Delta\theta$ around $\vec{T}$. This deviation is accommodated by secondary structural dislocations whose Burgers vectors belong to associated DSC lattice (Bollmann, 1972; Priester, 2012). Considering that the O_2-lattice is described in a similar way as O-lattice, the fundamental equation of O_2-lattice is similar to equation 1.5.

$$\vec{B}_{DSC} = \left(I - D^{-1}\right)\vec{x}_{O2} \tag{1.6}$$

Interestingly, the deviation matrix D is unique which makes O_2 - lattice unique for a given $\Delta\theta$.

1.2.2 Discrete and continuous approach to describe a grain boundary as an array of dislocations

There exist two approaches to describe a grain boundary as an array of dislocations. The first approach is the discrete approach and the second approach is the continuous approach which describes the grain boundary as a continuous distribution of dislocations using a dislocation tensor (Hull and Bacon, 2001; Priester, 2012). However, discrete dislocations-based models are necessary limited to low angle grain boundaries, for which individual dislocation may be distinguished (Li, 1972). For large misorientation angles, it is commonly considered that the dislocation cores would overlap to form a now extended 2D defect. In the following sections, we will focus on the fundamental aspects of both approaches.

1.2.2.1 The discrete approach of Read and Shockley

The first quantitative study of that model was conducted by Read and Shockley (Read and Shockley, 1950) for grain boundaries with small misorientation angles. In this model, a low angle grain boundary is described as a periodic sequence of dislocations (Read and Shockley, 1950). For example, figure 12 illustrates a periodic arrangement of edge dislocations in a low angle grain boundary. This model was the first to link the grain boundary misorientation angle θ and spacing d between two dislocations with a Burgers vector b.

$$d = \frac{b}{\theta} \tag{1.7}$$

The key result of the classical work of Read and Shockley is a formula for the dependence of grain boundary energy per unit area, γ_θ, on misorientation angle θ between neighboring grains. By considering that dislocations forming a grain boundary are linearly arranged and equidistant and using energy of a single dislocation and summing over the number of dislocations in a grain boundary (two sets of dislocations that come from the two neighboring grains), the energy of symmetric low angle grain boundary is given by

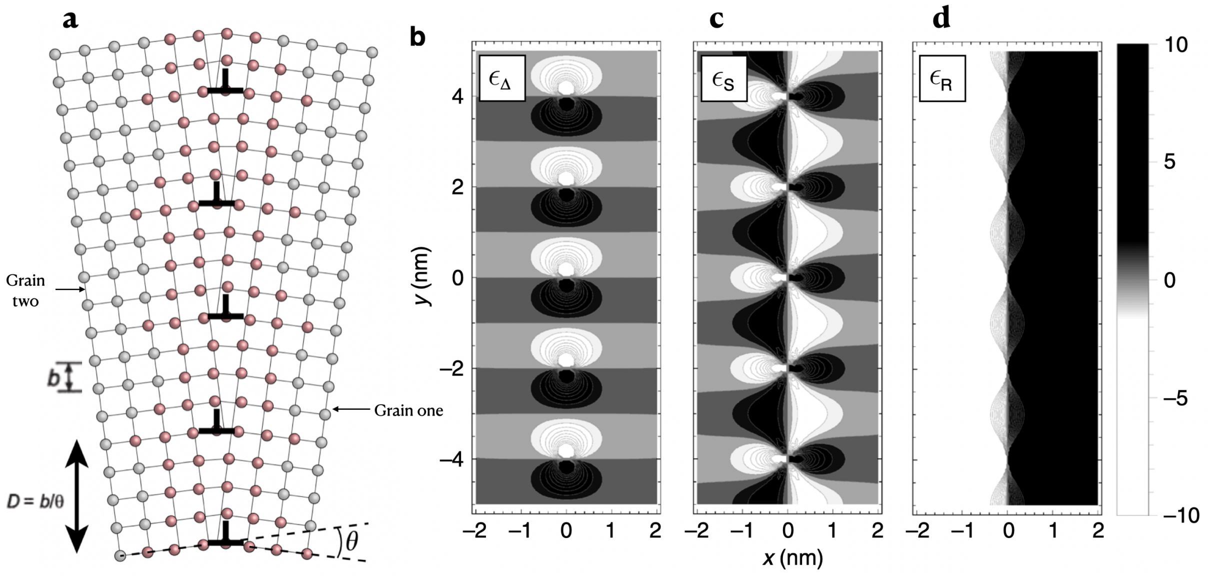

Figure 12: a) A periodic array of dislocations in a symmetric low angle tilt grain boundary. Examining the brown atoms reveals that they are displaced by a vector $\overrightarrow{b}$, the resulting strain maps are shown here b) hydrostatic strain $\varepsilon_\Delta = \frac{-b}{2\pi}\frac{(1-2\nu)}{(1-\nu)}\frac{y}{x^2+y^2}$ c) pure shear strain $\varepsilon_s = \frac{b}{4\pi(1-\nu)}\frac{x(x^2-y^2)}{(x^2+y^2)^2}$ and rotation $\varepsilon_R = \frac{b}{\pi}\frac{x}{(x^2+y^2)}$ with the scale bar showing the percent strain (10^{-2}) (Hanus et al., 2018)

equation 1.8.

$$\gamma_\theta = \gamma_0 \theta \,(A - \ln\theta) \tag{1.8}$$

Where $\gamma_0 = \frac{\mu}{4\pi}(1-\nu)$ and $A = \frac{b}{2\pi r_o}$ with μ the shear modulus, ν the Poisson coefficient and r_0 the dislocation core radius. This equation was validated by experimental and numerical data (Gjostein and Rhines, 1959; Wagner and Chalmers, 1960). It is worthy emphasising that the Read and Shockley model is applied only when the dislocations in the boundary are uniformly spaced as figure 12 a) shows. However, this is only possible in some particular cases where dislocation spacing is an integer multiple of the lattice parameter. Later, this energetic model (equation 1.8) was extended to high angle symmetric tilt grain boundaries ($\theta \geq 15°$) by Wolf (Wolf, 1989a). The range of validity of this energetic model comes from the assumption that θ is small enough, such that $sin\theta \approx 0$. Without such assumption the equation 1.8 becomes

$$\gamma_\theta = \gamma_0 \sin\theta \,[A - \ln(\sin\theta)] \tag{1.9}$$

1.2.2.2 The discrete approach of Bollmann

Another generalisation of the Read and Shockley to any grain boundary was proposed by Bollmann (Bollman, 1972). Based on the previously explained formulations on O and O_2 lattice,

$$\sum n_i b_{mi} = \left(I - R^{-1}\right)\overrightarrow{k} \tag{1.10}$$

With **I**, **R** are identity and rotation matrices that transform one grain into an other, $\overrightarrow{k}$ is a vector in grain boundary plane, n_i is the number of geometrically necessary dislocations and b_{mi} is their Burgers vectors (Bollman, 1972; Priester, 2012). The equation 1.10 relates projection of the transformation matrix to go from one grain into the other through a discrete Burgers vector. Bollmann extended the idea of coincidence of lattice points to coincidence of any point within the cells of two misoriented grains by considering Burgers vector $\mathbf{B} = \sum n_i b_{mi}$. The Bollmann approach considers the misfit zone to be made of primary and secondary dislocations. The primary dislocation are necessary dislocations. These dislocations have a Burgers vectors (b_m) of perfect dislocations, in addition, they form a network with the same periodicity. The spacing d of these dislocations is calculated following.

$$d = \frac{b_m}{2\sin\left(\frac{\Delta\theta}{2}\right)} \tag{1.11}$$

From equation 1.11, one can see that for a very low angle, $2\sin\left(\frac{\Delta\theta}{2}\right) \approx \theta$ which is identical to Read and Shockley model (equation 1.7). The secondary dislocations are also necessary dislocation with smaller Burgers vectors which are partials of the nearest coincidence site lattice. They are also known as the displacement shift complete dislocations. Their role is to ensure a good registry between two crystals at the boundary.

1.2.2.3 The continuous approach: Frank-Bilby

This approach, which results from the work of Frank and Bilby is widely used to determine the dislocation content of grain boundaries (Frank, 1950b,a). Frank (Frank, 1950a) described the density of dislocations which form a grain boundary between grain I and II. Later in 1955, Bilby (Bilby, 1955) came with a systematic way of dealing with the distribution of dislocations in surface delimiting two grains with a discontinuity of the distortion $[\beta]$ field between them.

$$\varepsilon_{ijk} n_1 \beta_{sj}^{I} - \varepsilon_{ijk} n_1 \beta_{sj}^{II} = \alpha_{ks} \tag{1.12}$$

With α_{ks}: dislocation density tensor, k: Burgers vectors, s: dislocation line, n : normal to grain boundary plane in direction from grain I to grain II and ε_{ijk} the permutation tensor. The reformulation of equation 1.12 in matrix form leads to what is known as Frank-Bilby equation 1.13.

$$\overrightarrow{B} = (X_I^{-1} - X_{II}^{-1}).\overrightarrow{X} \tag{1.13}$$

With X_I and X_{II} are transformations that generate the crystal I and II respectively and $\overrightarrow{X}$ is a vector in grain boundary plane. This equation is based on the Frank circuit construction (figure 13). In figure 13, a vector $X_I = X_{II}$ is drawn in crystal I. Next, it is surrounded by a closed circuit in which the origin of vector is considered both the origin

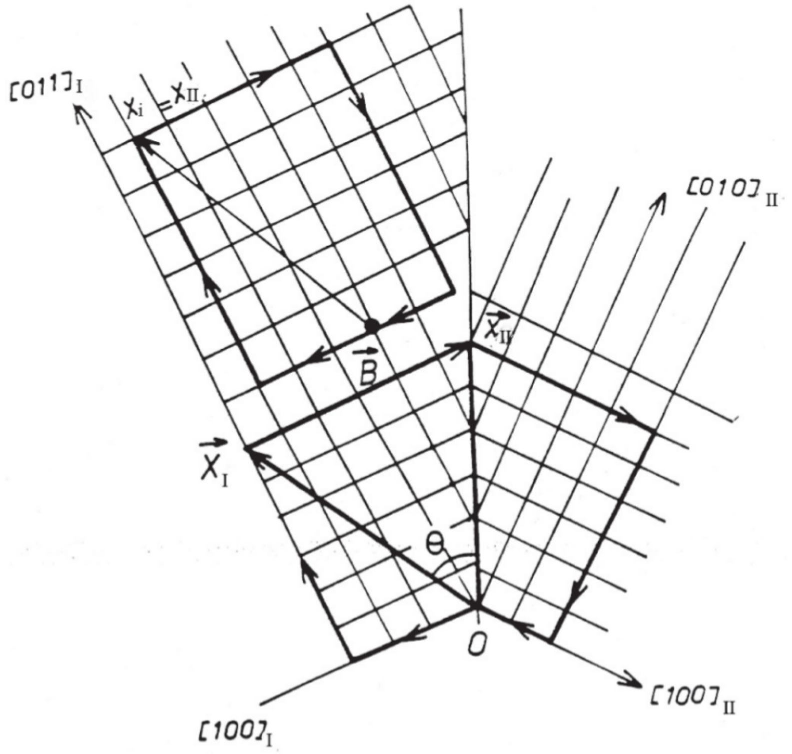

Figure 13: The Frank circuit used to define the closure failure (Priester, 2012).

and the end point. The same circuit is drawn around a grain boundary. It starts at the extremity of X_{II} passes through the point O and ends at the extremity of X_I. The latter circuit displays a closure failure $\overrightarrow{B}$ relative to the former circuit. The equation 1.13 relates the net Burgers Vectors $\overrightarrow{B}$ in grain boundary and the lattice deformation X_I and X_{II}. This deformation converts the reference crystal, from which the bicrystal is created, into real crystals I and II. To note that the reference crystal used could be one of I or II. The transformation of Crystal I into Crystal II is achieved by use of a rotation matrix **R**. For example, a reference vector X_I in crystal I is transformed into vector X_{II} following equation which reads:

$$\overrightarrow{X}_I = R^{-1}\overrightarrow{X}_{II} \tag{1.14}$$

The two crystal lattices are obtain by rotation of both crystal with equal but opposite angle $\frac{\theta}{2}$ on rotation axis Γ. In this case $\overrightarrow{B}$ is given by Frank's equation 1.15.

$$\overrightarrow{B} = 2\sin(\frac{\theta}{2})(\overrightarrow{X} \wedge \Gamma) \tag{1.15}$$

The Frank-Bilby equation can be used to determine the primary and secondary dislocations (Balluffi and Olson, 1985) described in earlier section. It is achieved by carrying out a Frank's circuit construction. However, from equation 1.13, there is no unique solution as **B** is only obtained from X_I or X_{II} and $\overrightarrow{X}$ and not the dislocation line which is unspecified. In addition, the choice of reference lattice is not unique as well.

1.2.3 Description of grain boundary as a periodic sequence of structural units

This model considers how atoms are arranged at grain boundary. Grain boundaries can be described as a sequence of a finite number of building blocks called structural units (Balluffi and Bristowe, 1984; Han et al., 2017a). Figure 14 gives an example of a sequence of structural units in **Σ11{332}** grain boundary in Nickel. It is an intermediate (mixture of singular and special related GB) grain boundary made of two structural units D of grain boundary **Σ3(111)** and E of grain boundary **Σ9(221)**. The structural units were confirmed both by numerical simulation and by High-Resolution Transmission Electron Microscopy (HRTEM) (Duparc et al., 2000). A structural unit is typically defined as a small group of atoms arranged in a characteristic configuration like polyhedron (Banadaki and Patala, 2017). This model was first proposed by Bishop and Chalmers (Bishop and Chalmers, 1968) and extended in 1983 by Vitek and Sutton to a variety of symmetric tilt grain boundaries (Sutton and Vitek, 1983a,b).

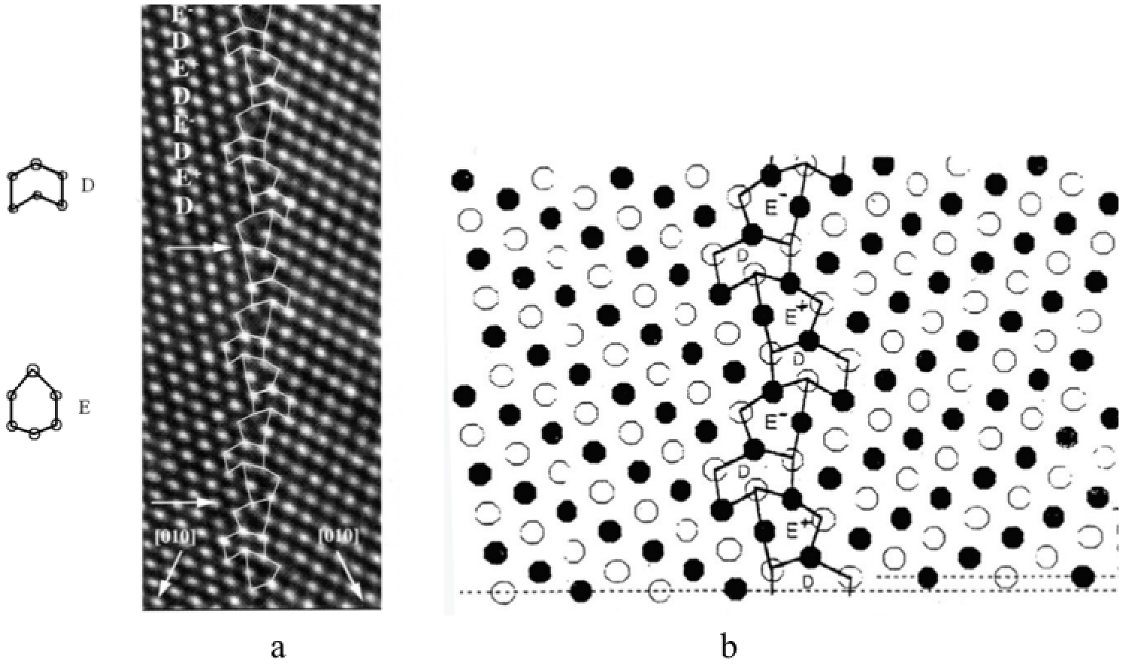

Figure 14: Structural unit arrangement in in pure Nickel grain boundary **Σ11{332}** a) from HRTEM b) from molecular dynamics simulations (Duparc et al., 2000).

The description of grain boundary structure relies upon a reference grain boundary. The reference grain boundaries also known as favoured grain boundaries are made of only one type of structural units that are indivisible. In general, there exists a limited number of such structural units (Ashby et al., 1978; Priester, 2012). There are seven structural units, shown in figure 15, that may constitute grain boundary structural unit.

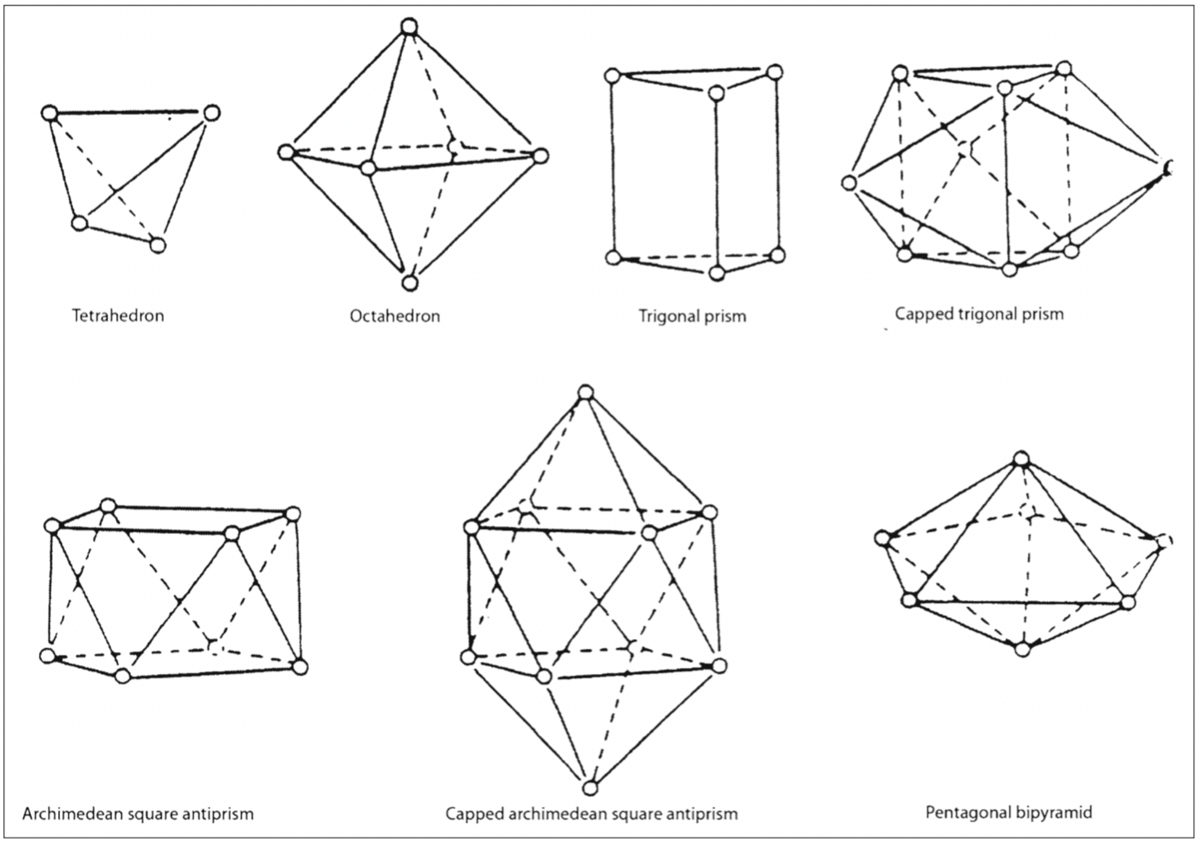

Figure 15: The seven energetically stable polyhedra that may constitute grain boundary structural units (Priester, 2012).

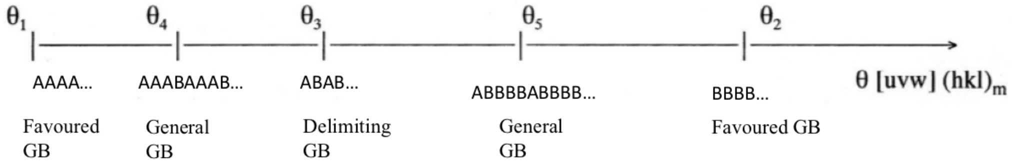

Figure 16: The diagram representing a grain boundary with a misorientation angle (θ) in terms of structure units (Priester, 2012).

In general, grain boundaries composed of regular arrays of a single type of structural unit possess often a relatively low energy (Priester, 2012). The intermediate grain boundaries which are between favoured grain boundaries are composed of a mixture of at least two structural units. In general, low index (delimiting) grain boundaries are made of a periodic sequence of two structural units and the rest are called general grain boundaries and they have higher energy compared to other GB. For example, figure 16 illustrates description of grain boundaries in terms of structural units A and B along a misorientation angle θ. It shows these three classes described above (favoured, delimiting and general grain boundary). Table 1.1 gives example of some grain boundaries described in terms of their misorientation angle θ, grain boundary plane, structural units along with their respective energies in Nickel materials. This model exhibits some limitations. first, it might be expected that the structure of any [100] STGB is a combination of A and B structural units as previously shown. However, there is a large misorientation deviation from structural units in delimiting or general grain boundaries which implies a distortion of some of the building structural units. To illustrate this point, figure 17b shows $\Sigma 5(36.87°)$ described as $|AB{\cdot}AB|$ in terms of alternating structural units A and B. The left figure 17a shows the favoured grain boundary made of A structural units and to its right, figure 17c is another favoured grain boundary of structural unit B. Comparing 17b from 17a and 17c the structure of individual A and B units from $|AB.AB|$ GB is, on average, compressed by 7.4% (Han et al., 2017b).

Table 1.1: Example of grain boundaries described in terms of structural units, of symmetrical and asymmetrical ⟨110⟩ tilt grain boundaries with their respective energies in nickel (Duparc et al., 2000; Priester, 2012)

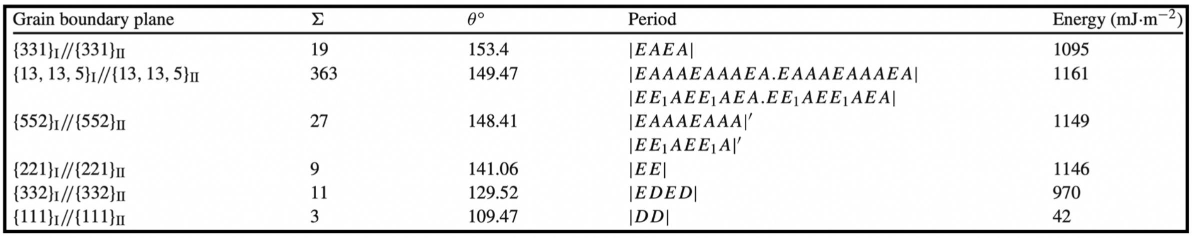

Grain boundary plane	Σ	θ°	Period	Energy (mJ·m^{-2})
$\{331\}_{\mathrm{I}}//\{331\}_{\mathrm{II}}$	19	153.4	$\|EAEA\|$	1095
$\{13, 13, 5\}_{\mathrm{I}}//\{13, 13, 5\}_{\mathrm{II}}$	363	149.47	$\|EAAAEAAAEA.EAAAEAAAEA\|$ $\|EE_1AEE_1AEA.EE_1AEE_1AEA\|$	1161
$\{552\}_{\mathrm{I}}//\{552\}_{\mathrm{II}}$	27	148.41	$\|EAAAEAAA\|'$ $\|EE_1AEE_1A\|'$	1149
$\{221\}_{\mathrm{I}}//\{221\}_{\mathrm{II}}$	9	141.06	$\|EE\|$	1146
$\{332\}_{\mathrm{I}}//\{332\}_{\mathrm{II}}$	11	129.52	$\|EDED\|$	970
$\{111\}_{\mathrm{I}}//\{111\}_{\mathrm{II}}$	3	109.47	$\|DD\|$	42

The structural unit model is unable to quantify the distortion in structural units and it fails to establish a straightforward relationship between energy and grain boundary struc-

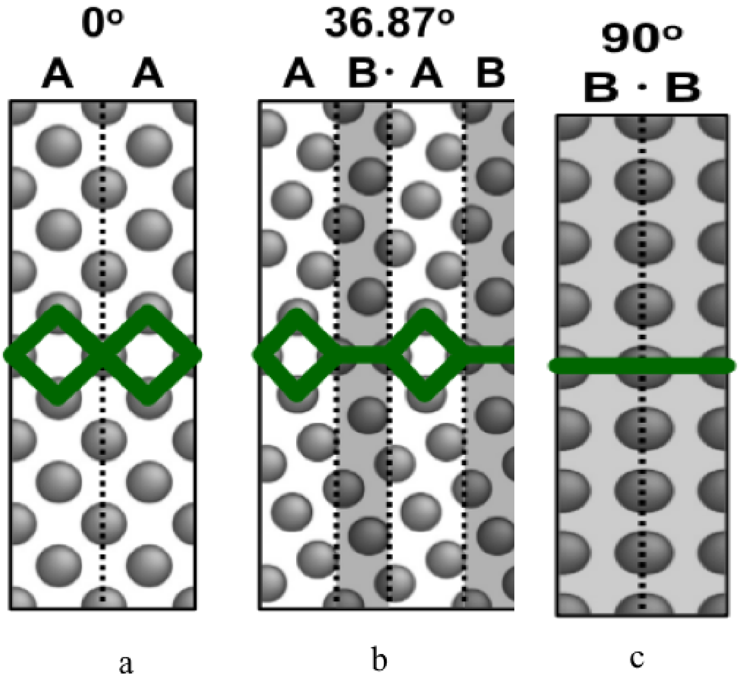

Figure 17: Distortion in structural unit of $|AB{\cdot}AB|$ of Σ5 36.87°[100] compared from favoured grain boundary AA and BB (Han et al., 2017a).

ture. Secondly, it does not predict the structural units of a grain boundary with a mixed character (tilt/twist). To consider structural unit distortion, a new model was recently proposed by Banadaki and Patala (Banadaki and Patala, 2017). This new model completes the previous structural unit model by providing a detailed atomic description of a grain boundary across its five macroscopic degrees of freedom. Consequently, it quantifies any distortion associated with three dimension polyhedral structural units and captures the structure of many variety of grain boundaries including mixed grain boundaries.

1.3 Thermodynamic and kinetic properties

1.3.1 Energy of grain boundaries

The existence of a grain boundary is associated with an increase in energy and volume of the system (Merkle et al., 1998; Shen et al., 2008; Shvindlerman et al., 2006; Uesugi and Higashi, 2011; Wolf, 1989b). It is very important to quantify this energy as it permits to discuss the relative stability of grain boundary structure. In addition, this interfacial energy (γ) acts also one of the driving forces for grain boundary migration.

The excess energy (γ) and excess volume (ϑ) of a system are generally determined using equations

$$\begin{aligned}\gamma &= \frac{E_{gb} - E_{pc}}{A_{(T,P)}} \\ \vartheta &= \frac{V_{gb} - V_{pc}}{A_{(T,P)}}\end{aligned} \tag{1.16}$$

Where E_{gb}, E_{pc} are the total energy of the relaxed bi-crystal containing a grain boundary and of a perfect crystal containing equal number of atoms respectively. In a similar way, V_{gb}, V_{pc} are total volume of bi-crystal with a grain boundary and the total energy of a perfect crystal respectively. A is the cross-section area of a grain boundary at a given temperature T and pressure P.

The calculation of energy and volume using equation 1.16 takes into account the size of simulation box, type of inter-atomic potential, the approach to finding the ground state of a grain boundary. However, in all calculations, the contribution of entropy is generally not taken into account. This is due to the fact that entropy is challenging to quantify. Grain boundary energy is often calculated at 0K. In literature, grain boundary energy and volume has been reported to be proportional regardless of the type of potential used in calculations and their value strongly depends on grain boundary plane (Bean and McKenna, 2016; Wolf, 1989b; Olmsted et al., 2009b).

From data points reported in literature, even if very rough trends may be seen, grain boundary energy varies from one misorientation angle to another, from one rotation axis to an other and from one FCC material to another as figure 18 shows. Atomistic results using equation 1.16 is in a good agreement with experimental data as figure 19 a) shows, however, there is a certain lack of results concerning mixed GB and more general misorientation. This demonstrates once again the need of a model that takes into account macroscopic degrees of freedom of a grain boundary to predict its energy. The Read and

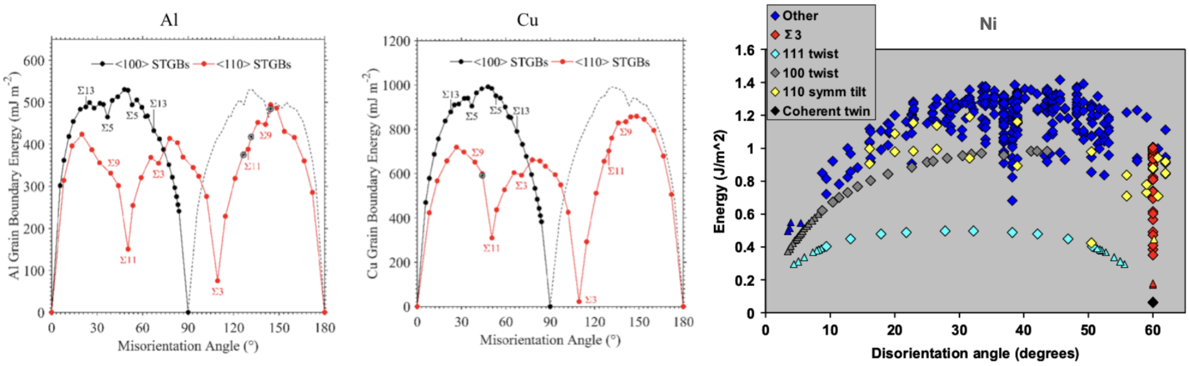

(a) (b) (c)

Figure 18: Grain boundary energy (γ_θ), from molecular dynamics, plotted function of misorientation angle (θ) for [100] and [110] symmetric tilt grain boundaries in (a) Aluminium (Tschopp et al., 2015), (b) Copper (Tschopp et al., 2015) and (c) symmetric of different character in Nickel (Olmsted et al., 2009b).

Shockley model is a model which takes into account the misorientation angle θ. Of course, it is only accurate for low angle symmetric tilt grain boundaries in which a grain boundary is described as periodic arrays of edge dislocations (Read and Shockley, 1950). The relationship between grain boundary energy γ_θ and misorientation angle θ reads,

$$\gamma_\theta = \begin{cases} \gamma_{max} \frac{\theta}{\theta_0}(1 - \log(\frac{\theta}{\theta_0})), & \text{if } \theta < \theta_0 \\ \gamma_{max} & \theta > \theta_0 \end{cases}$$

Where $\gamma_{max} = \frac{\mu b \theta_0}{4\pi(1-\nu)}$ and $\theta_0 = 15°$, μ is shear modulus, ν is the Poisson coefficient and r_0 the dislocation core radius. This model offers a simpler way of calculating energy if spacing d of dislocations in a grain boundary and core radius r_o of dislocation are known. The number of dislocations n present in a grain boundary is given by $n = \frac{1}{d} = \frac{\theta}{b}$ and the energy of a grain boundary reads

$$\gamma_\theta = nE_{sd} \tag{1.17}$$

Where $E_{sd} = \frac{\mu b^2}{4\pi(1-\nu)} \ln\left(\frac{d}{r_o}\right)$ is energy of a single dislocation. Figure 19 b) compares Molecular dynamics results from Sangid et al (Sangid et al., 2010) and from Read-Shockley model for low angle symmetric grain boundaries along [110] axis in pure Nickel. The model of Read and Shockley does not consider all macroscopic degrees of freedom of a grain boundary.

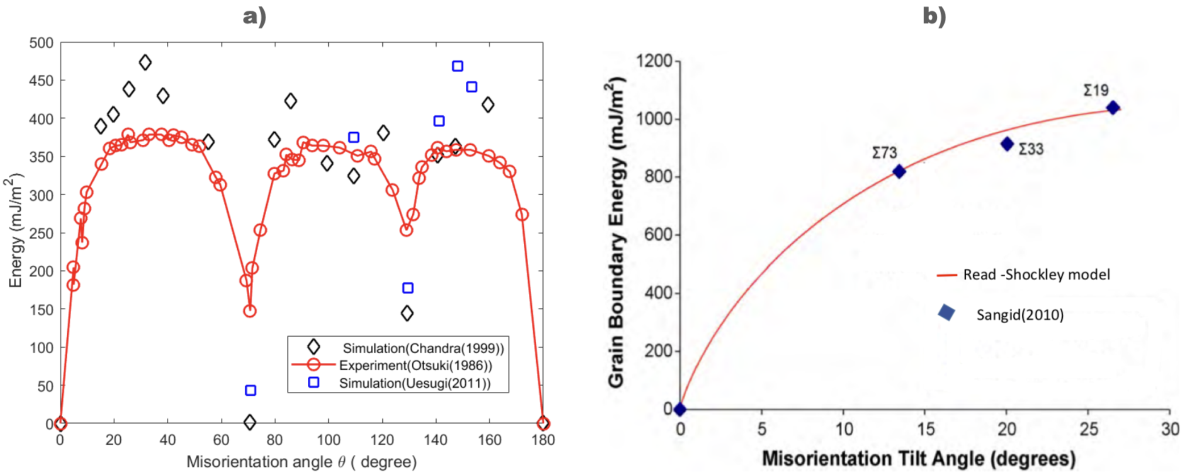

Figure 19: a) Comparison of calculated by molecular dynamics (Chandra and Dang, 1999; Uesugi and Higashi, 2011) and experimental (Otsuki and Mizuno, 1986) Energy of symmetric tilt grain boundaries with misorientation axis [110] in pure aluminium b) comparison of energies from Read-Shockley model and simulation of CSL symmetric tilt grain boundaries along[110] axis in pure Nickel (Sangid et al., 2010)

The most recent model of Bulatov et al.(Bulatov et al., 2014) associates all five macroscopic degrees of freedom with grain boundary energy. This model is the first attempt of this kind. It is based on interpolation which is done in two consecutive steps. The first step is to quantify and fit the grain boundary energy variation within a sampled low dimensional subsets of the five macroscopic space. The second step is to use the fitted lower dimensional subsets as scaffolding to build a five dimensional energy functions. Here, the scaffolding is selected based on energy criterion. Only subsets of a five space where energy is locally minimal with respect to the variation in direction orthogonal to the subsets are selected. The interpolated five dimensional energy function is simplified in a sense that it requires only two element specific parameters and all others are similar for all metals. Due to availability of atomistic data, this function has been successfully tested on four FCC metals (Ni, Al, Au and Cu) as figure 20 show. However, there is still much to understand regarding the evolution of grain boundary energy, up to date, there is no predictive model that takes into account all macroscopic and microscopic degree of freedom of a grain boundary.

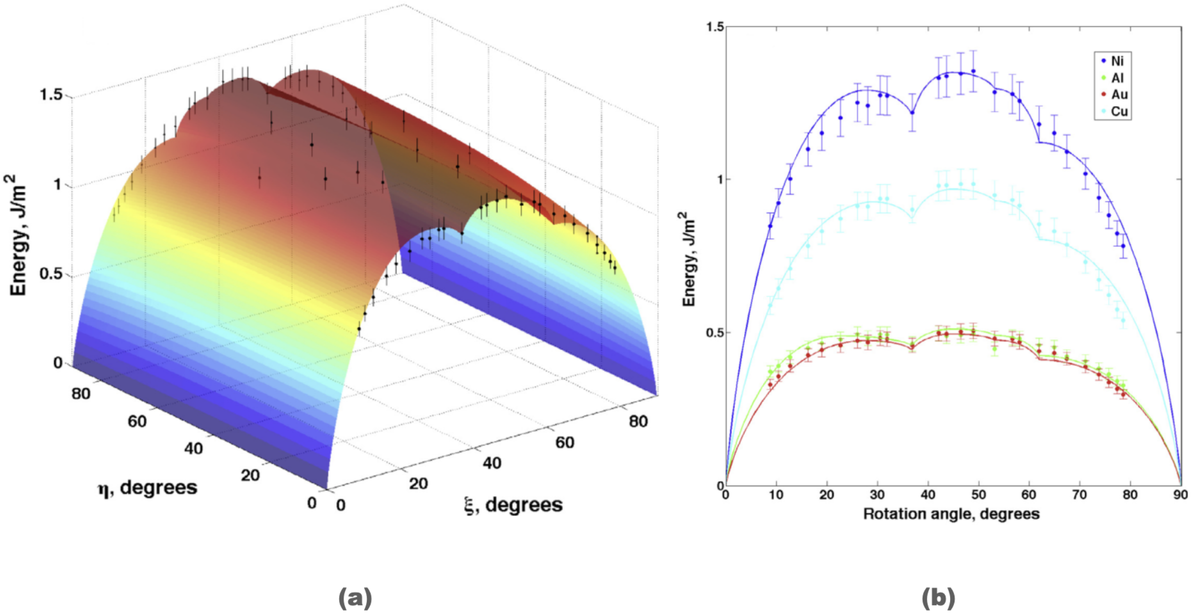

Figure 20: Fitted energy of symmetric (a) and asymmetric tilt grain boundaries against rotation angle ξ and asymmetric angle η for Nickel (b) tilt grain boundaries in Ni, Al, Au, Cu (Bulatov et al., 2014).

1.3.2 Grain boundary migration

Grain boundary motion is viewed in the following as the growth of grain I at the expense of grain II and vice versa. In other words, the GB migration transforms the shrinking grain into the growing grain by rotational transformation. The motive force (F) for grain boundary migration is the minimisation of free energy G of the system (Dimitrov, 1975), which might result from lattice defects and asymmetry between the grains abutting a grain boundary.

$$F = -\mathrm{grad}G \tag{1.18}$$

Lowering energy in the system by migration of grain boundary is achieved through reduction of a) grain boundary area (Cahn and Hoffman, 1974; Dimitrov, 1975; Gottstein and Shvindlerman, 2009a), b) difference in elastic strain energy (Dimitrov, 1975; Gottstein and Shvindlerman, 2009a; Mendelev et al., 2013), c) magnetic energy (Dimitrov, 1975; Gottstein and Shvindlerman, 2009a; Molodov et al., 1997, 1998b; Sheikh-Ali et al., 2003a,b) d) elastic distortion or change in energy accross the grain boundary due to thermal fluctuations (Bai et al., 2015; Gottstein and Shvindlerman, 2009a) e) migration by absorption of dislocations, point defects at the GB surface (Dimitrov, 1975) and f) electric energy (Dimitrov, 1975). In some special cases such as symmetric systems in which no energy gradient between adjacent grains is possible, grain boundary migration can be induced by applying external mechanical force (Janssens et al., 2006). In general, describing grain boundary evolution both quantitatively and qualitatively is of considerable practical interest. It allows determining the evolution of microstructure during thermo-mechanical processing and assessing its effect.

1.3.2.1 Driving force for grain boundary migration

The driving force for grain boundary migration is referred to such factor that triggers a grain boundary motion to decrease energy of system. For example, the force due to the curvature of grain boundary also known as capillary force. This driving force is stored in a grain boundary as the energy per unit area (Sutton, 1996; Priester, 2012). During a grain boundary migration, a grain boundary moves towards its local center of curvature to reduce the GB energy. This force F was reported by Cahn and Hoffman (Cahn and Hoffman, 1974; Hoffman and Cahn, 1972) to be a function of grain boundary energy γ, the curvature k and inclination angles θ_1 and θ_2 along the directions corresponding to the curvature.

$$F = (\gamma + \gamma'')k \tag{1.19}$$

Where γ is the surface free energy, γ'' is the second derivative with respect to the orientation of the surface normal and k is the he curvature (Du et al., 2007). This formula has been employed for various grain boundaries geometry such as a) hyperbola-like shapes (Masteller and Bauer, 1979; Sun and Bauer, 1970), quarter- and half-loops (Furtkamp et al., 1998) and even cylindrical shapes (Zhang et al., 2006a).

Difference in elastic energy

The gradient in elastic energy can be introduced in a bicrystal by exerting a strain ϵ on a bicrystal. It produces an elastic strain energy E_1 in grain one and E_2 in grain two. The driving force for migration is the difference (ΔE) in elastic deformation density (Zhang et al., 2004b).

$$\begin{aligned} \Delta E &= E_2 - E_1 \\ E &= \frac{1}{2} C_{ijkl} \epsilon_{ij} \epsilon_{kl} \end{aligned} \tag{1.20}$$

Where C_{ijkl} is the stiffness tensor, ϵ_{ij} and ϵ_{kl} are strains. It is important to note that ΔE across a grain boundary is produced whenever the orientation of the grains differs in a such way that the strain applied to both grains produces different strains in each grain. In a strained bi-crystal of asymmetric tilt grain boundary, the driving force E_2 for the upper grain rotated around $\langle 001 \rangle$ by an angle θ with respect to the lower grain and E_1 for lower grain respectively are determined from equation 1.21.

$$\begin{aligned} E_1 &= \frac{(C_{11} - C_{12})(C_{11} + 2C_{12})}{C_{11}} \epsilon^2 \\ E_2 &= \frac{(C_{11} - C_{12})(C_{11} + 2C_{12})[8(C_{11} - C_{12} + C_a) - C_a(1 - \cos(4\theta))]}{2[4C_{11}(C_{11} - C_{12} + C_a) - (C_{11} + C_{12})C_a(1 - \cos(4\theta))]} \epsilon^2 \\ C_a &= 2C_{44} - C_{11} + C_{12} \end{aligned} \tag{1.21}$$

The difference in elastic deformation density ΔE reads

$$\Delta E = \frac{(C_{11} - C_{12})(C_{11} + 2C_{12})^2 C_a \sin^2(2\theta)}{C_{11}[4C_{11}(C_{11} - C_{12} + C_a) - (C_{11} + C_{12})C_a(1 - \cos(4\theta))]} \epsilon^2 \tag{1.22}$$

ϵ is the only parameter controlling the magnitude of driving force. Thus, there is a linear correlation between the driving force and ϵ^2 as figure 21 shows. Although this force has formed the basis of the early investigations of gain boundary migration (Mendelev et al., 2013; Yan and Zhang, 2010; Zhang et al., 2006a; Zhang and Srolovitz, 2006; Zhang et al., 2007) in atomistic simulations, it has limitations. It requires the strain produced in both grains to differ. This dependence on asymmetric nature of the grain boundary limits the

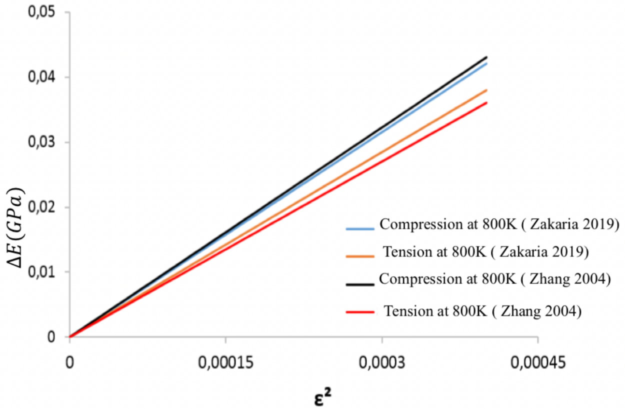

Figure 21: Elastic driving force for grain boundary migration as function of ϵ^2 (OMAR, 2019; Zhang et al., 2004b).

number of grain boundaries that can be studied this way.

Energy due to stored dislocations

A grain boundary constitutes obstacle to the motion of dislocations since the direction of the sliding from one grain to another grain is not always preserved following its passage through the interface. The resulting accumulation of dislocations at grain boundary produces an elastic force due to elastic field of dislocations which can move a grain boundary. A rough estimate of the driving force (F) is proportional to the density of dislocations ($\Delta\varrho$). With μ the shear modulus and b is Burger's vector (Priester, 2012).

$$F \propto \mu b \Delta\varrho \tag{1.23}$$

Note that some dislocations may also react with GB leading to the formation of defects at the GB surface that may promote or impede the migration of GB.

Synthetic driving force

In contrast to previous case, this is often used in atomistics, and can maybe be related to the more general generalised motive forces in theories. For symmetric grain boundaries, instead of providing a disparate driving force, a virtual force based on atomic orientation is used (Janssens et al., 2006; Olmsted et al., 2009c). It is an artificial force in a sense that it does not rely on or be directly associated with any physical source of driving force. This driving force centres on an idea that an atom being in an environment of a certain crystal orientation exhibits an anisotropic excess energy resulting from a localised bond distortion. By providing extra energy to atoms with a chosen local crystallographic orientation, a bulk driving force is imposed that moves a grain boundary to minimise energy of the system by consuming higher energy grain. This type of driving force is preferable over the conventional driving forces. Therefore virtual driving forces are very common in molecular dynamics simulations because they do not depend on anisotropic nature of a material or a grain boundary. More details information on synthetic driving force are given in section 2.5.5 of this textbook.

1.3.2.2 Mobility of grain boundary

In both experimental and computational studies, the main grain boundary property measured during migration is mobility m. Mobility describes the ratio of steady state velocity v over the applied driving force F.

$$v = mF \tag{1.24}$$

Mobility should be expected to be function of the degrees of freedom of a grain boundary (Janssens et al., 2006; Priester, 2012; Winning et al., 2002; Zhang et al., 2005), grain boundary composition (Molodov et al., 1998a), temperature (Homer et al., 2014a; Humberson, 2016; OMAR, 2019) and the magnitude of applied driving force (Priester, 2012; Zhang et al., 2004a; Deng and Schuh, 2011b; Homer et al., 2013) but not the nature of driving force (Lobkovsky et al., 2004; Mendelev et al., 2013; Gottstein and Shvindlerman, 2009b). It is not certain that the mobility is an intrinsic properties of GB, as GB structure or defect present at the GB suraface may affect mobility. The most recent calculation of mobility on a large set of grain boundaries is a work of Homer et al. (Homer et al., 2014b) who determined grain boundary mobility for a set of 388 grain boundaries and the work of El Omari and Queyreau (OMAR, 2019) on grain boundaries of type $\Sigma 7$ with misorientation axis $\langle 111 \rangle$. Since mobility depends on various aspects of GB, and experiments provide only an average measure of m at the macro-scale, atomistic simulations have been particularly useful to investigate it in correlation with elementary mechanism of grain boundary migration. We will focus on these simulation results here. For example, results from grain boundaries investigated by Homer et al. (Homer et al., 2014b) which are shown in figure 22.

Dependence of mobility on temperature

One can readily notice from figure 22 that the dependence of mobility on temperature varies from one grain boundary to another. If grain boundaries are categorised following the dependence of their respective mobility on temperature, one can notice that there are 3 main groups which are:

1. Athermal grain boundaries: these are grain boundaries with mobility that does not depend on temperature change (O'Brien and Foiles, 2016; Homer et al., 2015). Derivative of the mobility as function of temperature reads,

$$\frac{dm}{dT} = 0 \tag{1.25}$$

2. Antithermally activated grain boundaries: There are grain boundaries that are associated with mobility that decreases with temperature increasing (thermal damping) (Deng and Deng, 2017; Homer et al., 2015). The mobility is inversely proportional to temperature as equation 1.26 shows in which n is a constant.

$$m(T) \propto \frac{1}{T^n} \tag{1.26}$$

3. Thermally activated grain boundaries : these are grain boundaries with mobility that increases with temperature. Their mobility dependence on temperature follows

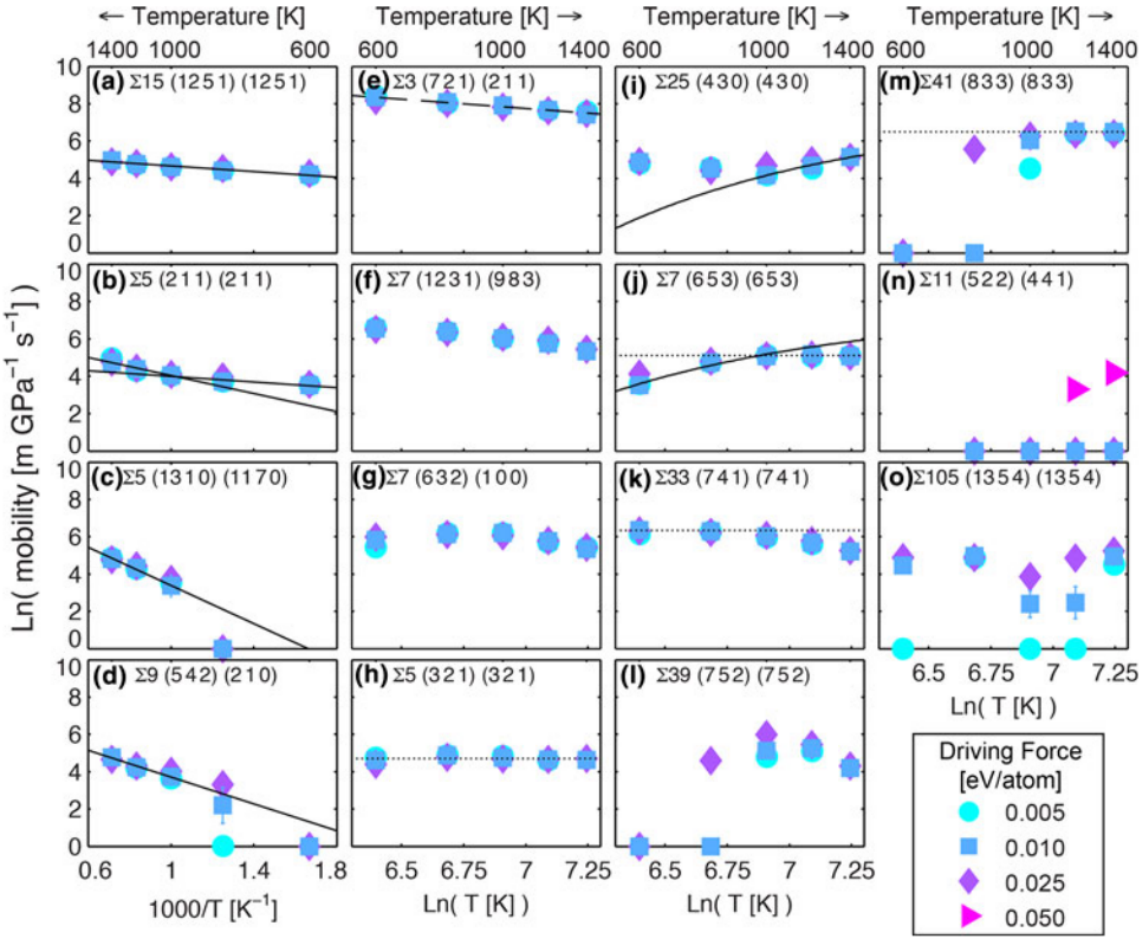

Figure 22: Temperature dependence of mobility of different grain boundaries investigated in the work of Homer (Homer et al., 2014b) a) Thermally activated b) thermally activated with two different activation energies c) thermally activated with roughening d) thermally activated with dynamic roughening e) antithermally activated f) antithermal g) antithermal h) athermal i) antithermally activated at lower temperature and thermally activated at higher temperature j) thermally activated at lower temperature and athermal at higher temperature k) athermally activated at lower temperature and antithermally activated at higher temperature I) immobile at lower temperature and antithermal at higher temperature m)immobile at lower temperature and athermal at higher temperature n)immobile o) temperature dependence is not clearly defined. The solid lines in (a), (b), (c), (d), (i) and (j) are thermally activated mobility fit. The two solid lines in (b) shows two different activation energies. The dashed line in (e) is the fit and the dotted line in (h), (j), (k) and (m) are fits as well.

Arrhenius type equation (Sutton, 1996; Priester, 2012; Race et al., 2014) which reads.

$$m(T) \propto e^{-\frac{\Delta G}{k_B T}} \tag{1.27}$$

Where k_B stands for Boltzmann's constant and ΔG the Gibbs free energy associated to the migration process (Gottstein et al., 1998; Sutton, 1996).

However, some grain boundaries from figure 22 do not show mobility with a clearly defined temperature dependence. Until now, the reason behind different temperature dependence remains mostly not understood. Some recent experimental (Cantwell et al., 2015; Gottstein and Shvindlerman, 2009b) and computational (Homer et al., 2014b, 2015; O'Brien and Foiles, 2016) studies have associated mobility with atomic structure of GB. For example, some studies have related athermal motion to low energy faceted grain boundaries (Babcock and Balluffi, 1989; Gottstein and Shvindlerman, 2009b; Hirth et al., 2006; Jung et al., 2013; O'Brien and Foiles, 2016). For some other grain boundaries, the temperature dependence may not be unique. For instance, the work of Deng et al. (Deng and Deng, 2017; Homer et al., 2015) has demonstrated that $\Sigma 5(210)$ exhibits a thermally activated motion at lower temperature while it responds differently at higher temperatures. This kind of work demonstrates once again the complex dependence of mobility on temperature and the importance of taking into account atomic structure of a grain boundary to describe mobility.

Dependence of mobility on misorientation angle θ

It is important to understand the dependence of mobility on misorientation angle between grains as this can allow to develop generic models for predicting mobility functions that take into account macroscopic degrees of freedom of a grain boundary. In the past, some attempts have been made to correlate mobility to the disorientation angle. For example, an atomistic study of Olmsted et al. (Olmsted et al., 2009c) on a set of 388 nickel grain boundaries and the work of El Omari and Queyreau (OMAR, 2019) all using a synthetic driving force molecular dynamics method. The results from both studies are shown in figure 23. Both studies have concluded that there is no simple function that can capture the correlation between mobility and misorientation angle θ.

1.3.2.3 Dependence of grain boundary mobility on driving force

Another key parameter in the mobility function is the nature and amplitude of driving forces (Bainbridge et al., 1954). In some case, the linear correlation between velocity and driving is not met. Atomistic studies of Deng et al. (Deng and Schuh, 2011b) utilising an adapted interface random walk method, and numerical study of Constantini et al. (Costantini and Marchesoni, 1999) and Lacasta et al (Lacasta et al., 2005) have reported

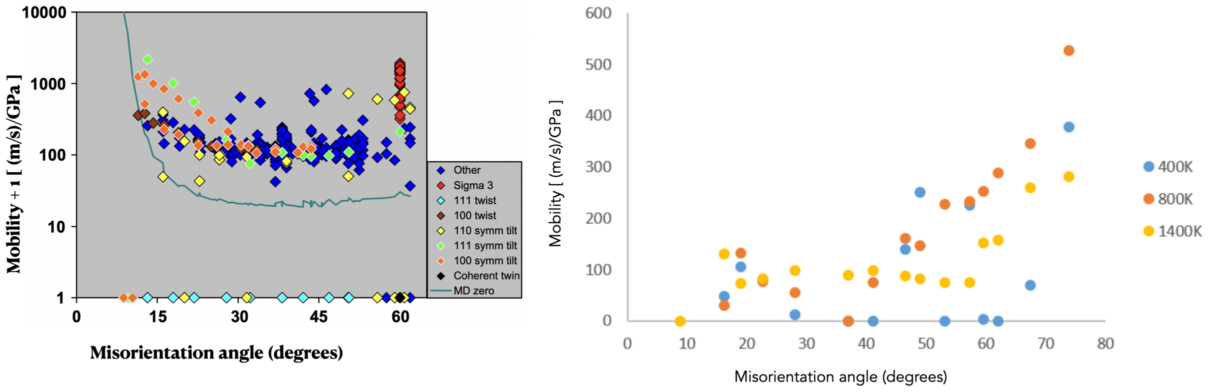

(a) **(b)**

Figure 23: a) Mobility against the misorientation angle θ for EAM Ni of 388 grain boundaries obtained at 1400 K by applying a driving force of 0.025 eV (Olmsted et al., 2009c). Note that the solid line is the mobility resolution limit of the MD simulation used in study of Olmsted et al. which is obtained by excluding unresolvable mobilities and incoherent $\Sigma3$ twin boundaries. See (Olmsted et al., 2009c) for more details on the procedure of how to obtain this resolution. (b) Mobility versus misorientation angle θ for EAM Ni symmetric $\Sigma7$ tilt grain boundaries with misorientation axis [001] obtained by applying a driving force of 0.025 eV at different temperatures (OMAR, 2019).

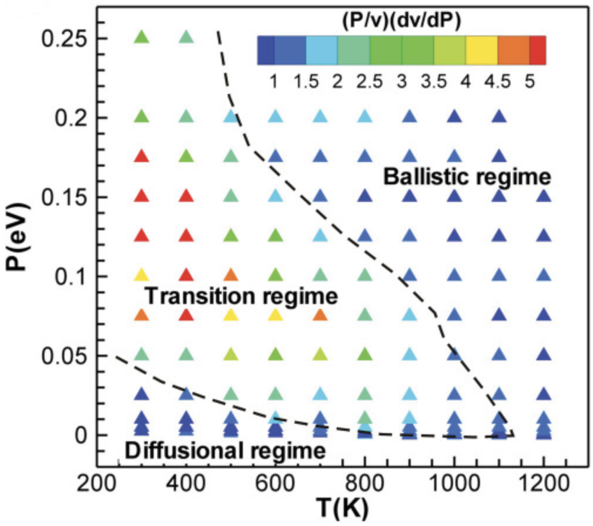

Figure 24: A map of modes of migration of symmetric $\Sigma5(310)$ tilt grain boundary. The dashed lines separate diffusional (first linear regime), transition, and ballistic (second linear) regimes of grain boundary motion. To convert the driving force from eV to Pascal, consider that $1eV \approx 1.47 \times 10^{10} Pa$. (Deng and Schuh, 2011b).

that the lack of linear dependence of velocity on driving force can originate from the magnitude of the applied motive force. Those studies have shown that the linear dependence exists in two situations. The first linear regime which is denoted difusional regime in the study of Deng et al. (Deng and Schuh, 2011b) is when the driving force is sufficiently small ($P < k_B T$). In this situation, atoms only oscillate around their equilibrium positions with occasional jump of the energy barrier back and forth in a random manner. The second linear regime denoted ballisitic regime in the study of Deng et al.(Deng and Schuh, 2011b) is when driving force is larger enough ($P > k_B T$). A large number of atoms acquires enough mechanical energy to escape energy barrier. Elsewhere there is no linear dependence of velocity on driving force and in the study of Deng et al. (Deng and Schuh, 2011b), this regime is denoted transition regime. Figure 24 shows a temperature (T) -driving force (P) map for symmetric tilt grain boundary $\Sigma 5(310)$. It is a map built using the local slope value of $\ln(v)$ vs $\ln(P)$ at various temperatures and driving forces. It shows three regimes explained above, in addition, it shows that transition from one regime to another depends on temperature and applied driving force.

1.3.3 Migration laws to predict grain boundary velocity

The mobility of GB during their migration has certainly attracted a lot attention from experimental and simulation investigations. From equation 1.24, mobility describes the ratio of the steady state velocity (v) over the applied driving force (P). Based on experimental studies (Gottstein and Shvindlerman, 2009b), mobility (m) in the exponential regime follows an Arrhenius type relation which reads

$$m = m_o f(T, P) \tag{1.28}$$

Where m_o is a constant which was reported by some studies (Race et al., 2014; Zhou and Mohles, 2011; Priester, 2012; Sutton, 1996) to depend on the distance moved by a grain boundary, attempt frequency and driving force. On the other hand, the function $f(T, P) = e^{-\frac{\Delta G}{k_B T}}$, in which k_B stands for Boltzmann's constant and ΔG for Gibbs free energy, describes all types of work (e.g. mechanical) driving a grain boundary motion (Gottstein et al., 1998; Sutton, 1996; Rajabzadeh et al., 2013). The Gibbs free energy reads

$$\Delta G(P, T) = \Delta H - T\Delta S \tag{1.29}$$

in which ΔH and ΔS are the enthalpy and entropy of activation of grain boundary migration, respectively. The function $f(T, P)$ depends on the type of grain boundary, temperature, magnitude of applied driving force and size of the simulation box (Rajabzadeh et al., 2013) (through the elastic interactions between defects, see later). Unfortunately, until now, there are no generic models to predict m_o and ΔG in a large $T - P$ parametric space. This urges a necessity of models that can work for several grain boundaries rather than for some specific grain boundaries. For example, in the past a model for predicting m_o for thermally activated grain boundaries that move by nucleation and propagation of step was devised for pure twist $\Sigma 5$, $\Sigma 13$ and $\Sigma 17$ (Sutton, 1996). It reads

$$m_o = \frac{n^2 \Omega^2 N \nu_o}{k_B T} \tag{1.30}$$

Where n is average number of atoms transferred in a shuffle, N is total number of Kinks on a step per unit boundary area, Ω is atomic volume and ν_o is Debye frequency. In addition to being specific for some particular grain boundaries, it is also difficult to implement. On the other hand, quantifying the entropy term in equation 1.29 at operational temperature required for hot working a metal is challenging. For instance, the available method which is the Nudge Elastic Band (NEB) method (Henkelman et al., 2000) is only used to provide a direct link to quantifying the activation energy ΔG associated with grain boundary migration at only 0K. This makes it less relevant, since the hot work of metal uses often temperature higher than $0.4T_m$ (T_m is melting temperature). The Entropy term is however commonly considered to be small. Most recently, a new model to predict ΔG was developed for grain boundaries whose motion is mediated by nucleation and propagation of a pair of disconnections (Rajabzadeh et al., 2013). In this model, ΔG is estimated using the elasticity theory in which the excess energy $\Delta G(w)$ associated with the existence of a pair of disconnections and their propagation under applied mechanical work is estimated as:

$$\Delta G(w) = 2\xi_{form}(r_c) + \xi_{inter}(w, r_c) + \xi_{mech}(w). \tag{1.31}$$

Where w is the distance between two disconnections, r_c is the core radius. Moreover, $\xi_{form}(r_c)$, $\xi_{inter}(w, r_c)$ and ξ_{mech} stand for energy required for formation of a pair of disconnections, energy from elastic interaction between disconnections and their image and the work of internal force, respectively. Since migration of some grain boundaries can involve the formation of configurations (known as metastable configuration) different from the ground state configurations, it is a challenge to quantify energy associated with the formation of a pair of disconnections. Consequently this model works perfectly by fitting to data points from NEB (Nudge Elastic Band) calculations.

1.3.3.1 Shear coupled grain boundary migration

The motion of some GBs is coupled with a tangential translation of grain two with respect to grain one (Sutton, 1996; Priester, 2012). Regardless the misorientation angles θ, this migration mechanism occurs in most tilt grain boundaries. The figure 25 shows the principle of shear coupled grain boundary migration which was confirmed by theoretical,

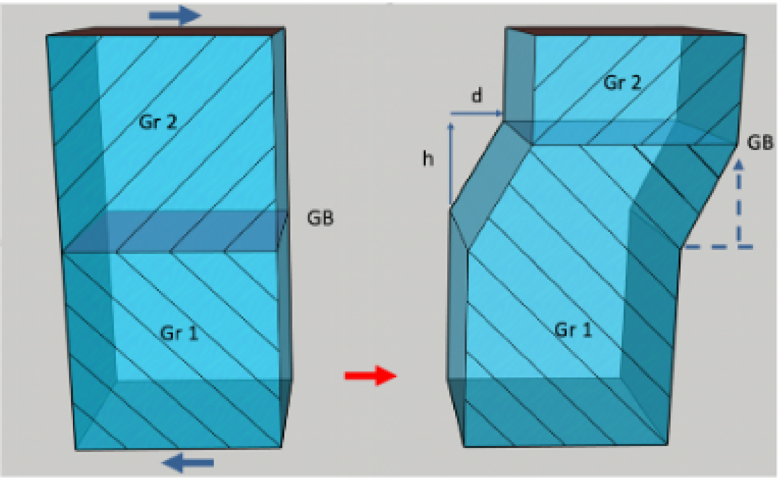

Figure 25: Migration of grain boundary by a distance h from the initial position (right figure) when a shear illustrated by blue arrow is applied. The grain 2 (G_{r2}) translates by a distance (shear displacement) d while being consumed (Gautier et al., 2021).

experimental and computational studies (Cahn et al., 2006; Caillard et al., 2009; Homer et al., 2013; Molodov et al., 2007; Mompiou et al., 2009; Thomas et al., 2017). It is the one of the most investigated grain boundary migration mechanism. The tangential velocity v_t is often related to the normal velocity as in equation 1.24 and reads;

$$v_t = \beta v \tag{1.32}$$

where β is shear coupling factor and $\beta = \frac{d}{h}$ (Gautier et al., 2021; Cahn and Taylor, 2004; Cahn et al., 2006; Rajabzadeh et al., 2013). The study of Cahn et al. (Cahn et al., 2006) has reported β to increase with the grain boundary misorientation and it might even go up beyond 50% for symmetric tilt grain boundaries in range 30° to 40° (Gorkaya et al., 2009; Ivanov and Mishin, 2008). Figure 26 shows an example of shear coupled grain boundary migration mechanism in $\Sigma 5(210)[001]$ symmetric tilt grain boundary obtained by atomistic simulations using EAM potential at 400K and 0.025 MPa (OMAR, 2019).

1.3.3.2 Elementary mechanisms of grain boundary migration

Migration usually occurs through localised processes at the grain boundary surface rather that a continuous global process. Identifying elementary mechanisms of migration is key in understanding migration and possibly obtaining general trends in migration or justifying migration function. To identify mechanism of grain boundary motion requires following each atom during grain boundary migration. This is the first advantages of molecular dynamic simulations (Kim et al., 2011; Lee and Choi, 2004; Olmsted et al., 2009b,c; Ratanaphan et al., 2015; Restrepo et al., 2014). An other advantage of molecular dynamics simulations over experimental is that spacial and temporal coordinates of each displacing

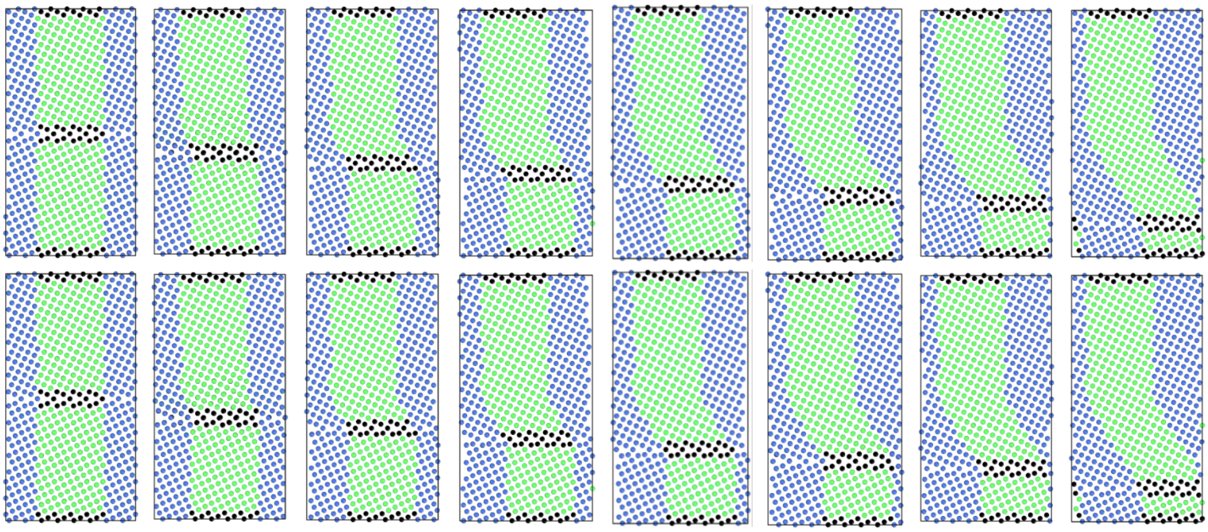

Figure 26: Shear coupled grain boundary migration in Σ5(210)[001]. The black atoms belongs to the defect and the green atoms are in perfect FCC lattice position. he blue atoms are used as reference (OMAR, 2019).

atom are stored at every time step for analysis after simulation. Therefore, molecular dynamic simulations allow to classify different mechanisms of grain boundary migration.

Migration by atomic shuffling

In this type of migration, the motion of a grain boundary occurs by the stochastic rearrangement of atoms in the grain boundary (Sutton, 1996). The motive for shuffling is the minimisation of energy of the system which is achieved by rotating one grain to produce similar orientation for both grains (Sutton, 1996; Priester, 2012). In singular grain boundaries, shuffling mechanism occurs by lateral displacement of pure steps accompanied by rotation of columns of atoms (Sutton, 1996). This mechanisms can be thermally or athermally activated.

This migration mechanism was confirmed by a number of numerical studies. For example, this migration mechanism was reported by Jhan and Bristowe (Jhan and Bristowe, 1990) from atomistic simulation of flat Σ5, Σ13, Σ17 and Σ29 pure twist in pure gold (Au) with misorientation axis [001] using an embedded atom potential for gold (Foiles et al., 1986). For Σ5, migration occurred by a shuffle of a group of 4 atoms within the coincidence site lattice unit cell (CSL) as figure 27 shows. The same mechanism was reported in pure twist copper by Schönfelder (Schönfelder et al., 2005) and latter by Yan and Zhang (Yan and Zhang, 2010; Zhang et al., 2006b) in different [100] twist boundaries in pure Nickel. The way atoms shuffle and the number of atoms involved depend on the type and atomic structure of a grain boundary.

For example, from an atomisistic study using EAM potential and difference in elastic energy as driving force, Yan and Zhang have reported the shuffle to involve a group of four

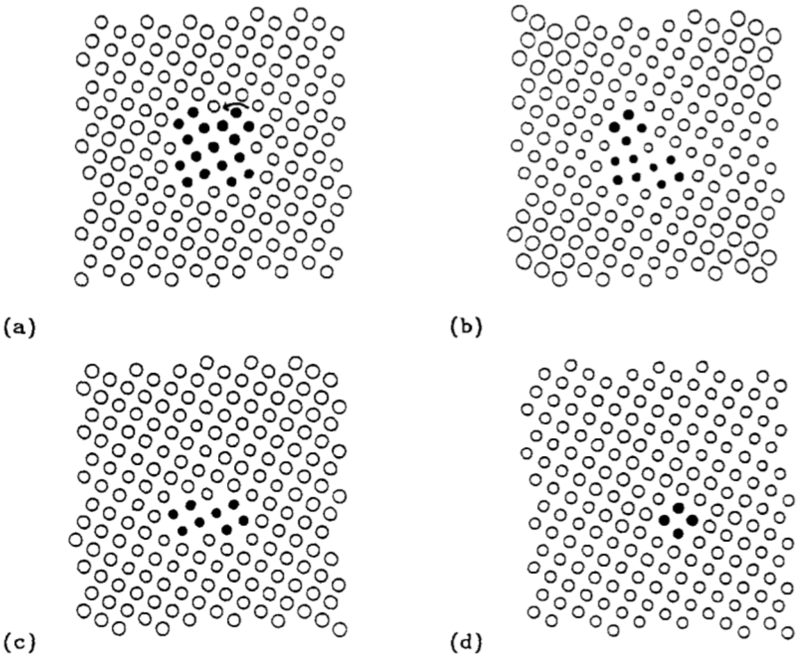

Figure 27: Shuffling of a group of four atoms in CSL unit cell of Σ5[001] pure twist as function of time a) 3ps b) 4ps, c) 5ps and d)7ps. The vertical and horizontal directions are parallel to CSL unit vectors and empty circles represent atoms in grain 1 and filled circle representing atoms in second grain (Jhan and Bristowe, 1990)

atoms in Σ5[001](36.87°) twist grain boundary in Ni where in pure Twist Σ13[001](22.63°) a string-like motion of groups of atoms propagates along the screw dislocation network. Similar migration mechanism was observed from atomistic simulation of Σ5[100] asymmetric tilt grain boundaries in pure Nickel by Zhang and Srolovitz (Zhang and Srolovitz, 2006) using EAM potential and difference in stored elastic energy as motive force for grain boundary migration.

Migration by nucleation and propagation of disconnections

Disconnections are linear defects with both dislocation and step natures (Sutton, 1996). Disconnections can be formed from the decomposition of lattice (regular) dislocations into the grain boundary, but can also spontaneously form as pair or islands at the surface of the grain boundary. Similarly to dislocations they are as well characterised by a Burger vector $\overrightarrow{b}$, and step height h (Han et al., 2018; Wei et al., 2019). Under different competing driving forces sufficient enough to overcome energy barrier for grain boundary migration; a pair of disconnections of opposite sign nucleate. They propagate along a grain boundary and once span the simulation box, a grain boundary makes a step forward. A lot can be understood from the dichromatic pattern of a grain boundary regarding the details of a disconnection to nucleate. According to Bollmann (Bollmann, 1967), the vector $\overrightarrow{b}_{dsc}$ connecting the lattice points of the Displacement shift complete (DSC) lattice is equal to

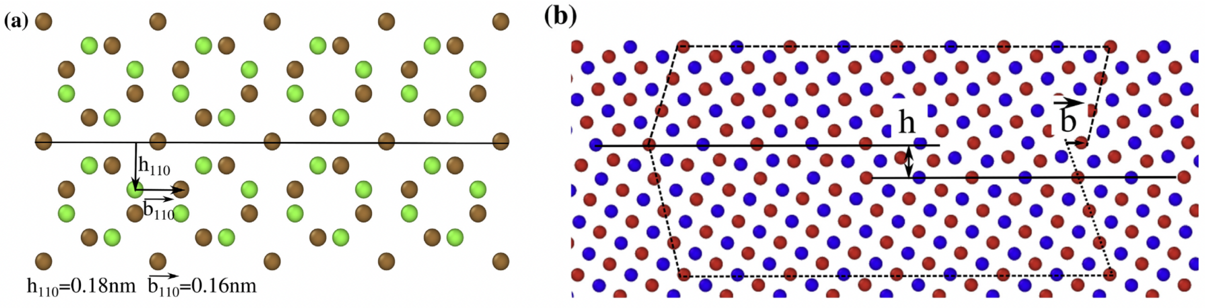

Figure 28: a)The dichromatic patterns of a **(210)** grain boundary of type Σ5. Green and brown atoms belong to the grain one and grain two of the bicrystal. $\overrightarrow{b}_{\mathbf{110}}$ and $h_{\mathbf{110}}$ are Burgers vector and step of a disconnection of type ⟨110⟩. b) The Burgers circuit built at the disconnection nucleation site in the same grain boundary. The blue and red atoms belong to different lattice planes in the y direction. h and $\overrightarrow{b}$ stands for step and Burgers vector a disconnection (Deng and Deng, 2017) as in the previous case.

the closure failure vector which is Burgers vectors always obtained from Burgers circuit around a defect (Read, 1953). The $\overrightarrow{b}_{dsc}$ vector can be obtained from the dichromatic complex. Then, the height h of a disconnection is given by

$$h = \overrightarrow{b}_{dsc}.\overrightarrow{n} \tag{1.33}$$

Where $\overrightarrow{n}$ is the normal of a grain boundary plane (Hirth et al., 2007). Figure 28 illustrates the structure of a disconnection in a bicrystal using a dichromatic pattern. It shows the height of a disconnection to form and its Burgers vector obtained from Burgers circuit around a disconnection. The grain boundary migration mechanism by nucleation and propagation of disconnections can occur in thermally activated (Combe et al., 2019) as well as in athermally activated grain boundary migration (Babcock and Balluffi, 1989; Gottstein and Shvindlerman, 2009b; Hirth et al., 2006; Jung et al., 2013; O'Brien and Foiles, 2016).

Migration by dislocation gliding

In this type of grain boundary migration, all structural units are simultaneously translated. A simultaneous translation of structural units is due to an array of grain boundary dislocations that simultaneously glide. Hence, the grain boundary moves as a whole and its surface remains flat during migration. This mechanism is often observed in low angle grain boundaries. This is due to the fact that these grain boundaries are often made of a periodic arrangement of dislocations with distant dislocation cores. It is thermally activated but in some special cases it is anti-thermally activated in which a grain boundary moves without an associated friction with the lattice (Homer et al., 2014b; OMAR, 2019).

Migration by faceting

It is a mechanism observed often in mixed grain boundaries. Mixed grain boundaries migrate by producing facets connected by other lower dimensional defects, for instance, dislocations or disconnections. Migration is produced by advancement of either those lower dimensional defects or facets. Figure 29 shows as an example, the screenshot of migration of $\Sigma 7(\overline{471})[111]$ mixed grain boundary at different time steps.

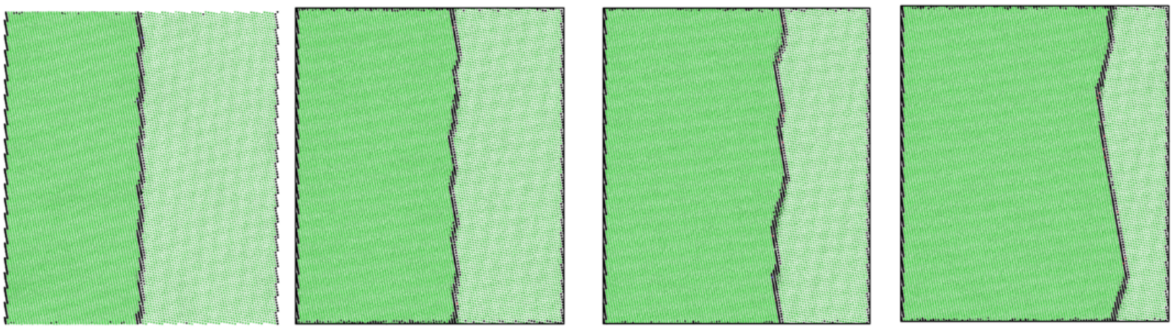

Figure 29: Migration of $\Sigma 7(\overline{471})[111]$ mixed grain boundary by faceting (OMAR, 2019).

1.3.4 Interaction of grain boundary with dislocation

In real polycrystalline materials, other defects are already present on both side of a migrating grain boundary and in particular dislocation. Dislocation can experience different interactions with grain boundary, from the distance attraction or repulsion, impeding, complete or partial absorption, partial or complete direct transmission. In turn, dislocation presence may improve or impede GB motion. The resulting overall properties of a polycrystalline strongly depends on the nature of such interaction (De Koning et al., 2003; Kacher et al., 2014; Wang and Misra, 2011; De Koning et al., 2003). In general, the mechanisms of interaction depends on local atomic structure of a grain boundary (Tucker and McDowell, 2011; Tucker et al., 2010; De Koning et al., 2003), orientation and direction of incident dislocations (Gu et al., 2014; Zhu and Gao, 2012; De Koning et al., 2003). The following section focuses on fundamental aspects of different types of grain boundary-dislocation interaction.

1.3.4.1 Dislocation pile ups at a grain boundary

During plastic deformation of polycrystalline materials, dislocations move inside grains until they reach grain boundaries. First, there is a remote interaction between the stress fields from the dislocation and the grain boundary (the one from the grain boundary usually being short range), then at close range, it is generally not easy for a dislocation to enter a grain boundary as a core reaction is required and thus activation energy. Grain boundaries impede propagation of dislocations to different degrees depending on the density of dislocations (Shen et al., 1988). Thus, dislocations form a pile up behind a grain boundary with length L as shown in figure 30. Dislocations continue to pile up until a stress concentration ($\mathscr{T}_{pileup}$) due to dislocations reaches a certain critical value (Voyiadjis and Yaghoobi, 2019).

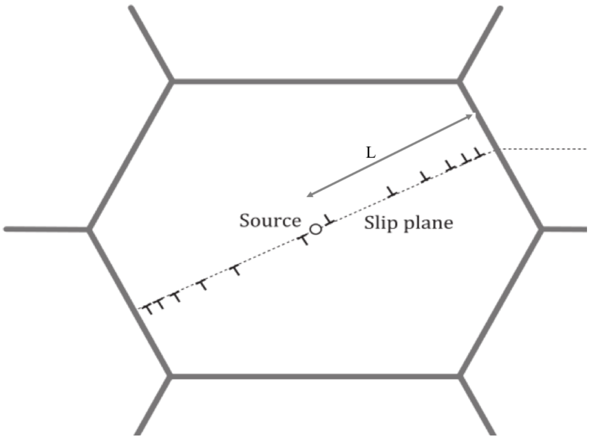

Figure 30: Dislocation pile up behind a grain boundary (Voyiadjis and Yaghoobi, 2019)

$$\mathscr{T}_{pileup} = n\mathscr{T}_s \tag{1.34}$$

With n the number of dislocations and $\mathscr{T}_s$ slip stress. This induced stress can be related to the length of pile-up by equation 1.35.

$$\mathscr{T}_{pileup} = \frac{L}{A}\mathscr{T}_s^2 \tag{1.35}$$

where $A = \frac{\mu b}{2\pi}$ for screw dislocations and $A = \frac{\mu b}{2\pi}(1-\nu)$ for edge dislocations in which μ, ν are shear modulus and ν the Poisson constant. When critical stress is reached at grain boundary, it can nucleate plastic deformation in adjacent grains or even nucleate a crack at the boundary. Dislocation pile-ups are more pronounced in processing methods aiming at improving mechanical properties of a metal by reducing the size of grains. In this processing methods, dislocation pile ups and interaction among themselves at grain boundary improve mechanical properties (Cottrell and Bilby, 1949; Eshelby et al., 1951) by what is known as Hall-Petch effect (Hall, 1951). This effect is mathematically expressed as

$$\sigma_y = \sigma_o + \frac{k_y}{\sqrt{d}} \tag{1.36}$$

Where σ_y and σ_o are resultant yield stress and initial yield stress of crystals respectively, d is grain size and k_y a constant that expresses the resistance of a grain boundary of being crossed by a dislocation. The latter depends upon material, texture, temperature, potentially extent of deformation of a material.

1.3.4.2 Combination between lattice and grain boundary dislocation

Contrary to the previous case, a reaction between lattice dislocation with Burgers vector b_m and grain boundary's intrinsic dislocation with Burgers vector b_i occurs to produce a dislocation b_e which integrates within a grain boundary.

$$b_m + b_i = b_e \tag{1.37}$$

Assuming that the Burgers vector of boundary and lattice dislocations are very close, This reaction is energetically favourable. In this particularly reaction, a sessile intrinsic dislocation reacts with a glissile dislocation from lattice to produce a glissile extrinsic dislocation as figure 31 b) shows.

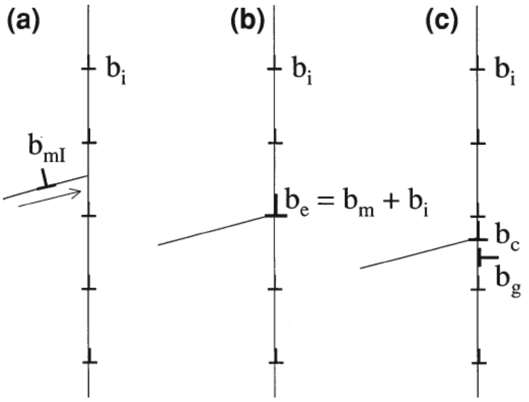

Figure 31: Types of interaction between intrinsic dislocation b_i and lattice dislocation b_m to produce an extrinsic dislocation b_e a) before reaction b) combination process c) decomposition (Priester, 2012).

1.3.4.3 Decomposition of a lattice dislocation at grain boundary

Once a lattice dislocation of Burgers vector b_m impinges a grain boundary, it produces a stress imbalance in grain boundary structure. The decomposition of lattice dislocation b_i into two (b_c and b_g) or more dislocations occurs within a grain boundary to accommodate this induced stress. The Burgers vectors (b_c and b_g) of resulting dislocations are that of DSC lattice (Dingley and Pond, 1979). This dislocation reaction is shown in figure 31 c).

1.3.4.4 Transmission of a lattice dislocation across a grain boundary

In some cases, the driving force for migration of a lattice dislocation is enough to make this incident dislocation crosses a grain boundary. This reaction is generalised as

$$\vec{b}_r = \vec{b}_1 - \vec{b}_2 \tag{1.38}$$

Where $\overrightarrow{b}_r, \overrightarrow{b}_1, \overrightarrow{b}_2$ are Burgers vectors of a partial dislocation staying in a grain boundary, incident dislocation and emitted dislocation respectively. The accommodation of resulting stress in grain boundary is achieved through three different mechanisms depending on slip planes of either side of a grain boundary.

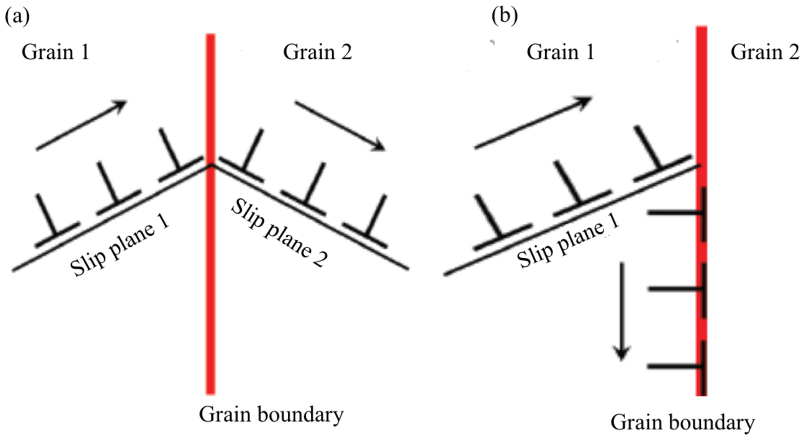

Figure 32: Total (a) transmission and (b) absorption of incident dislocation.

1. If $\overrightarrow{b}_r$ is a null vector, there is no dislocation left in a grain boundary. The incoming and emitted dislocation have parallel Burgers vectors. In this case, slip planes of incident and emitted dislocation have same trace in a grain boundary (see figure 32 (a)).
2. if $\overrightarrow{b}_r = \overrightarrow{b}_1$, there is a total absorption of incident dislocations at grain boundary (see figure 32 (b)). This special case, only happens when the incident dislocation has a Burgers vector of a DSC lattice (Priester, 2012).

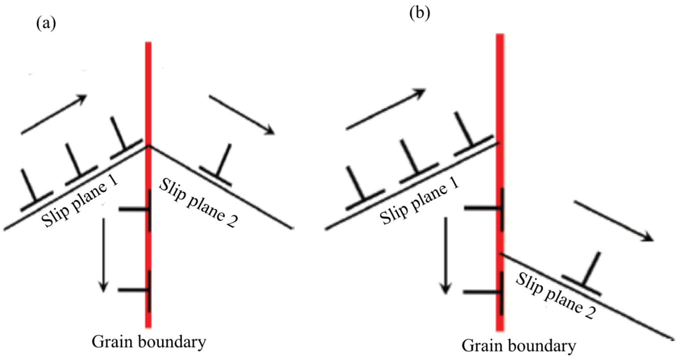

Figure 33: (a) direct and (b) indirect partial transmission of incident dislocation (OMAR, 2019)

3. if $\overrightarrow{b}_r$ is not null, there are two possible cases:

(a) Direct and partial transmission: This is a transmission mechanisms observed when the character of incident dislocation is an edge. An incident dislocation impinges a grain boundary and crosses it immediately by leaving a residual dislocation in a grain boundary (figure 33(a)). This is due to two slip planes on either side of a grain boundary which are not parallel.

(b) Indirect and partial transmission: This is a special case where incident dislocation migrates a long a grain boundary before its emission to adjacent grain(figure 33(b)).

Summary

In this chapter, we saw that a polycrystalline microstructure is made of a network of grain boundaries. Grain boundaries are mostly mobile and their rate of migration controls microstructure evolution. To successfully improve mechanical properties and durability of a polycrystalline materials requires a clear a) description of a grain boundary, b) understanding of factors that influence grain boundary migration and c) deep understanding of elementary mechanism of migration. This chapter has presented different descriptions of grain boundaries and they are based on geometrical order (CSL grain boundaries), mechanical stress order (Discrete and continuous approach to describe a grain boundary as an array of dislocations) and atomic order (structural unit) of a grain boundary. What is common for all these descriptions is that describing a grain boundary unambiguously is very challenging and requires a clear understating of its atomic structure that can only be assessed by atomisitic methods.

In addition, this chapter has demonstrated the importance of atomic structure of a grain boundary in conditioning both energy and kinetics of a grain boundary. For example, grain boundary energy and mobility vary from one misorientation angle to another and from one rotation axis to an other. In addition, atomic structure controls the response of a grain boundary to factors (temperature, driving force, interaction with dislocations, impurities etc...) that impact its motion. For instance, the dependence of grain boundary mobility on temperature ranges from thermal, athermal to antithermal. In addition, the dependence of GB on driving force can either be linear or exponential. Indeed, the elementary mechanism of grain boundary and interaction with other defects vary from one grain boundary to another. Thus, developing models that capture evolution of a grain boundary would require a deep understanding of the atomic structure of grain boundaries. Indeed, in the past some studies have attempted to develop such mobility functions. However, these models are developed for some specific grain boundaries with specific elementary mechanism of migration. Consequently, up to date, there is still a lack of a generic model that can work on several grain boundaries rather than for some specific grain boundaries.

The contents of this chapter will constitute a basis of the first part of this manuscript whose goal is a) to better understand both static and dynamic properties of grain boundaries in FCC polycrystalline materials and b) to develop generic mobility functions that work for several grain boundaries.

Chapter 2

Atomistic calculations

2.1 Introduction

Previous chapter showed that the static and dynamic properties of grain boundaries such as energy, mobility and migration mechanism depend upon their atomic structure. Thus, understanding and later predicting the GB migration is thus intimately related to GB atomic structures. Thus, an important challenge is to characterise and track individual atoms composing GB (Chookajorn et al., 2012; Jin et al., 2014; Petch, 1953). For experimental studies, tracking atoms in a moving grain boundary is a challenge. Among experimental techniques, the transmission electron microscopy (TEM) has been particularly useful for the community, however, it is limited to very special grain boundaries and in situ, high-resolution transmission electron microscopy (HREM) can not track the motion of individual atoms in a moving grain boundary (Merkle et al., 2004). Contrarily to experimental methods, the intrinsic nature of atomistic methods makes them a powerful tools for studying grain boundary evolution. In particular, the Molecular Dynamics method offer the ability of tracking the motion of individual atoms. There are several advantages of molecular dynamics for example:

1. Molecular Dynamics offers now the possibility to set up large-scale calculations that span large section of the five-parameter crystallographic phase-space of grain boundary geometry (Kim et al., 2011; Lee and Choi, 2004; Olmsted et al., 2009b,c; Ratanaphan et al., 2015; Restrepo et al., 2014).

2. Molecular dynamics allows to investigate the details of the relevant mechanisms in a well-controlled manner, which is significantly easier than in experiments with polycrystals where several mechanisms are operative simultaneously .

3. An other important advantage of molecular dynamics studies over experimental studies is the ability to provide the most detailed picture of what happens during migration and reveal more information on elementary mechanisms of migration in play.

Although, atomistic calculations offer many advantages over experimental studies, their domain of applicability is somewhat still limited in terms of time scale and length scale, despite progresses in the field. It is also important to note that atomistic systems are mostly good to simple systems, for which relevant semi-empirical interatomic potentials exist, and may be a far cry from the reallity of metals containing impurities or metallic alloys. Similarly to all simulation techniques, a trade-off must be found between physical fidelity and computational cost of the simulations.

In brief, Molecular Dynamics consists of solving equations of motion of Newtonian mechanics for N particles in the domain which results in a $3N$ set of equations to solve simultaneously. The MD community has developed over the years very user-friendly scientific codes, and it is easy to forget the complexity of doing MD simulations. In fact, MD simulations may be very touchy in the sense that the physical results and their relevant to the real materials depends upon a number of parameters as for example the size of the simulation box, the boundary conditions and the simulation environment (temperature, pressure etc..). We , therefore, start this section by presenting some key details regarding the practical MD implementation.

2.2 Molecular Dynamics

In the last four decades, many changes have been permitted by the increasing power of computational resources and reducing their associated cost. For the field of metallurgy, several computer simulation methods have arisen to allow scientist to investigate some aspects of grain boundaries that were then impossible to study with traditional research method (e.g. experimental ones). Multiscale approaches have become a powerfull tool to understand complex metallurgy and material behaviour. MD lies between at the lowest lengthscale the density functional theory (DFT), that solve the Shroedinger equation of a small set of atoms and mesoscale simulations that can be discrete in nature like Kinetic Monte Carlo (KMC) or continuous like Phase Field (see figure 34).

2.2.1 Classical molecular dynamics

MD relies upon the resolution of Newtonian equations of motion for large ensemble of classical particles whose interactions are described through a semi-empirical interatomic potential (Mishin et al., 2010; Satoh, 2010). For example, molecular dynamics can allow to look at energetics (ground state) of a possible atomic structure of GB, and allows to track atom displacements related to GB migration to understand grain boundary migration mechanisms. Molecular Dynamics relies on the formulations of classical mechanics proposed by Hamilton and Lagrange, that we present in next section.

2.2.1.1 Hamiltonian formulation

In an evolving system, even if the position and the force acting on a particle 'i' of mass m_i change, the functional form of the Newton's second law rests invariant (see equation

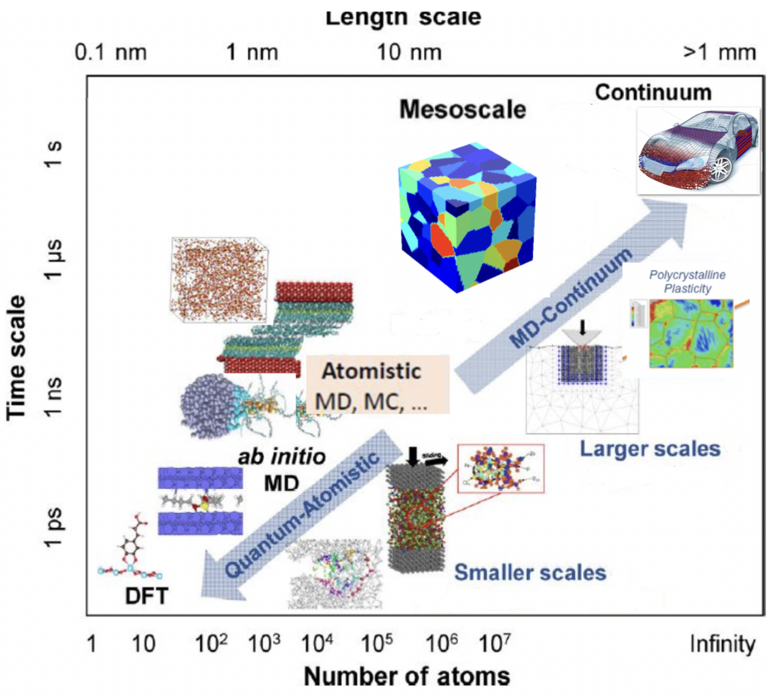

Figure 34: A representation of different scales used in simulations in materials sciences. Features are determined with DFT from the electronic structure, MD simulations are used to study systems of thousands of atoms. At larger scale, continuum methods, such as finite element method (FEM) or finite volume method (FVM) are used.

2.9). According to statistical physics, an atomistic classical system can be described by position (r_i) and velocity $(\dot{r}_i)$ (see figure 35). For an isolated system, the total energy E_{tot} (Kinetic energy plus potential energy) is conserved. This function called the Hamiltonian

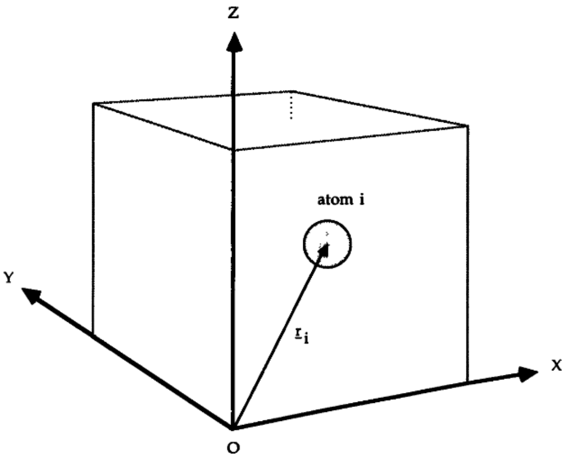

Figure 35: Definition of position vector r_i that locates particle i in the simulation box

whose value is constant in time denotes $\mathscr{H}$ (Haile, 1992).

$$\mathscr{H}(r^N, P^N) = \text{constant} \tag{2.1}$$

Where momentum on particle i is $P_i = m\dot{r}_i$. For this particular system, the Hamiltonian reads.

$$\mathscr{H}(r^N, p^N) = \frac{1}{2m_i}\sum_i P_i^2 + U(r_i) = E_{tot} \tag{2.2}$$

The general equation of motion is given by the time derivation of equation 2.1 and it reads

$$\frac{d\mathscr{H}}{dt} = \sum_i \frac{\partial \mathscr{H}}{\partial P_i}.\dot{P}_i + \sum_i \frac{\partial \mathscr{H}}{\partial r_i}.\dot{r}_i = 0 \tag{2.3}$$

By taking the time derivation of equation 2.2 gives:

$$\frac{d\mathscr{H}}{dt} = \frac{1}{m_i}\sum_i P_i.\dot{P}_i + \sum_i \frac{\partial U(r_i)}{\partial r_i}.\dot{r}_i = 0 \tag{2.4}$$

The velocity of each particle can be found by comparing equations 2.3 and 2.4,

$$\frac{\partial \mathscr{H}}{\partial P_i} = \frac{P_i}{m_i} = \dot{r}_i \tag{2.5}$$

The total force acting on a particle reads:

$$F = -\frac{\partial(U(r_i))}{\partial r_i} = -\frac{\partial \mathscr{H}}{\partial r_i} \tag{2.6}$$

2.2.1.2 Lagrangian formulation

In constrast to Hamiltonian formulation, the Lagrangian $\mathscr{L}$ is given by the difference between kinetic and potential energy (Torby, 1984). $\mathscr{L}$ reads

$$\mathscr{L}(\dot{r}_i, r_i) = K(\dot{(r)}_i) - U(r_i) = \frac{m\dot{r}_i^2}{2} - U(r_i) \tag{2.7}$$

Following a similar demonstration as in the previous subsection, the force for each atoms reads:

$$F = -\frac{\partial(U(r_i))}{\partial r_i} = \frac{\partial \mathscr{L}}{\partial r_i} \tag{2.8}$$

2.2.1.3 Newtonian formulation

For a particle i translating from one place to another due to the force F_i exerted on it by an external system. The motion and the applied force are explicitly related through Newtonian second equation of motion:

$$\overrightarrow{F}_i = m_i a_i = m_i \ddot{r}_i = -\frac{\partial(U(r_i))}{\partial r_i} \tag{2.9}$$

Where a_i is acceleration of particle i at time t. The force $\overrightarrow{F}_i$ expressions can also be obtained analytically from the gradient of potential energy as defined above, if the latter is itself an analytical function (see later). From equations 2.6, 2.8, 2.9, we can readily see that, for a multi-body system in Cartesian space, the Lagrangian and the Hamiltonian equations reduce to the familiar Newton equation:

$$\frac{\partial \mathscr{L}}{\partial r_i} = -\frac{\partial \mathscr{H}}{\partial r_i} = m\ddot{r}_i \tag{2.10}$$

This is equivalent to 3N ODEs (force, velocity and positions) of second order, that are coupled through the force $\overrightarrow{F}_i$, that needs to be solved. Consequently, this becomes increasingly computationally expensive for a bigger system.

2.2.2 Numerical integration of equations of motion

The differential equations with respect to time from previous section are discretised using various integration schemes. The quality of a Molecular Dynamics simulation strongly depends on the quality of the integration scheme used therefore they need to be presented shortly. Here we briefly give some general features of these schemes and how they are derived. Most of them derive from the Taylor expansions for the positions, the velocity and acceleration at time $(t + \Delta t)$ and $(t - \Delta t)$.

Verlet algorithm

The algorithm proposed by Verlet is one of the first introduced and it is still one of the most used today (Allen and Tildesley, 2017; Satoh, 2010). By doing Taylor expansion, one is able to derive the Verlet time integration below from equation 2.9.

$$r_i(t + \Delta t) = r_i(t) + \frac{dr_i}{dt}\Delta t + \frac{d^2 r_i}{dt^2}\frac{\Delta t^2}{2} + ... \tag{2.11}$$

$$r_i(t - \Delta t) = r_i(t) - \frac{dr_i}{dt}\Delta t + \frac{d^2 r_i}{dt^2}\frac{\Delta t^2}{2} \pm ... \tag{2.12}$$

The future position $r_i(t + \Delta t)$ of a particle i is derived from the summation of both equations (2.11 and 2.12) and rearranging the resultant which finally gives

$$r_i(t + \Delta t) = 2r_i(t) - r_i(t - \Delta t) + a_i \Delta t^2 \tag{2.13}$$

Interestingly, the calculation of the future position of atoms does not require the velocity of the particle under consideration. In a similar way, velocity of particle i is calculated from the future and previous positions as equation 2.14 derived from subtracting 2.12 from 2.11 shows:

$$\frac{dr_i(t)}{dt} = \frac{r_i(t + \Delta t) - r_i(t - \Delta t)}{2\Delta t} \tag{2.14}$$

This Verlet algorithm is very advantageous in MD simulations not only due to its simplicity but also on its capability of satisfying the time reversal symmetry contained in the Newton's equation of motion (Satoh, 2010) i.e if Δt is replaced by $-\Delta t$, equation 2.13 remains unchanged. The consequence of this symmetry is that if the course of time is reversed at an instant time t, the trajectory of a particle retraces its steps back. Unfortunately, in practice, the rounding errors accumulated during simulation limit the reversibility especially when a large number of time integration steps is used. In general, the most of the calculation time in Molecular Dynamics is consumed in force evaluations. It means that the cost of calculating new positions is marginal. The precision of calculation is estimated of about $N_t \Delta t^4$. On the other hand, there exist more sophisticated adapted Verlet algorithms to integrate the equations of motion. Some examples of these algorithms are given in the appendix A.1

2.2.3 Boundary Conditions

In molecular dynamics investigations, a material's property to study often dictates the choice of boundary conditions (BC) to utilise from a set of several existing and conventional (BC). Although in molecular dynamics simulation, the intention is to simulate a large system in order to statistically collect trends in properties over a large sample, the computation cost of atomistic simulations dictates to simulate a smaller system of limited number of atoms typically few millions of atoms (but systems up to billions of atoms are now possible). When now considering reducing the size of the considered configuration , surface effects are introduced when the size of a simulation box is too small. Once more a trade-off must be found.

Periodic Boundary conditions are often used in atomistic simulations to suppress this issue (Allen and Tildesley, 2017; Satoh, 2010). These are boundaries that approximate a large system while starting from a smaller system such that the initial smaller system becomes the basic building unit of the new bigger system. For example, if a small system (illustrated in figure 36 (a) by gray coloured particles) contained in a square box of width L. The application of Periodic Boundary Conditions (PBC) replicates the initial small box in both directions. Figure 36 (a) shows all resulting replicas illustrated with black coloured particles. Applying periodic boundary conditions generates extra 8 units in a system whereas extra 26 units result if PBC are applyed in all 3D of the system. In such a configuration, mass, energy and momentum are always conserved since the number of atoms is the same and atoms undergo identical displacement in all boxes (Haile, 1997). The conservation of the number of atoms in the system is always maintained because if an atom leaves the initial box on one side, it is immediately replaced by its image from a replica at an opposite side (this is illustrated by a black arrow in figure 36 (a)).

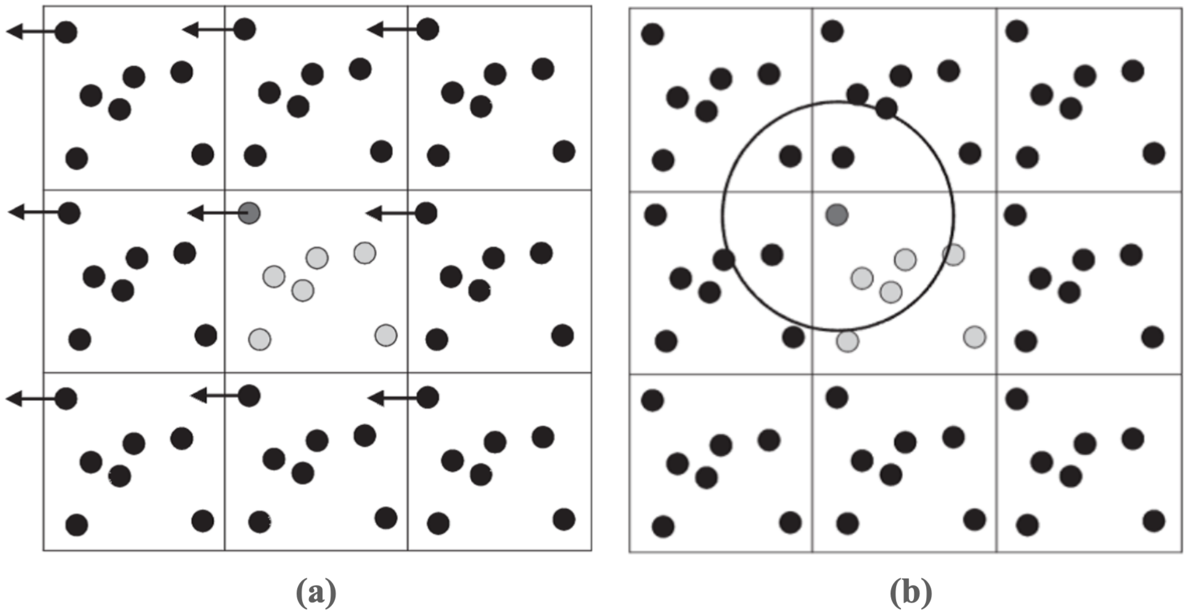

Figure 36: (a) Applying Periodic boundary condition on a square box of width L. The parent box contains gray particles and it is surrounded by its replicas with black particles. (b) Calculation of the interactions on the dark gray particle using the cut-off radius method. By using the minimum image model, only particles in the sphere of the cut-off radius are taken into account.

For the special case of bicrystals containing a GB, the usage of periodic boundary conditions virtually increases the size of the simulation box, but it also introduces an extra grain boundary in a simulation box. This new grain boundary can interact with an existing grain boundary if they are not distant enough. If there is no massive grain boundary sliding within the system, this problem is solved by increasing the separation distance up to a point where interactions are no longer significant albeit, the computing time increases.
Conversely, this solution does not solve the problem of interaction between an atom and its image. To address this problem, Metropolis et al.(Metropolis et al., 1953) have introduced the concept of the minimum image . The minimum image concept consists of counting, for each particle, only the forces coming from the neighbors located in a fictitious circular (2D) or spherical (3D) zone centered on this particle and of size identical to the original simulation box (figure 36 (b) shows). Note that, this cut off radius depends on inter-atomic potential used and it allows counting interaction of an atom in the fictitious box only once. Despite that, the utilisation of minimum image concept with periodic boundary conditions puts on a criterion of the acceptable minimum size of the simulation box (greater than twice the cut-off radius).

During simulations, grain boundary sliding can become significant. This affects measuring dynamic properties of a grain boundary, therefore, it demands a proper attention.

Grain boundary sliding is significant in low angle twists and some tilts grain boundaries due to the low density of CSL lattice (Sutton, 1996). For these grain boundaries, grain boundary sliding becomes more and more important that even 3D periodic boundary boundaries might not be the best choice (Lutsko et al., 1988; Duparc and Torrent, 1994).

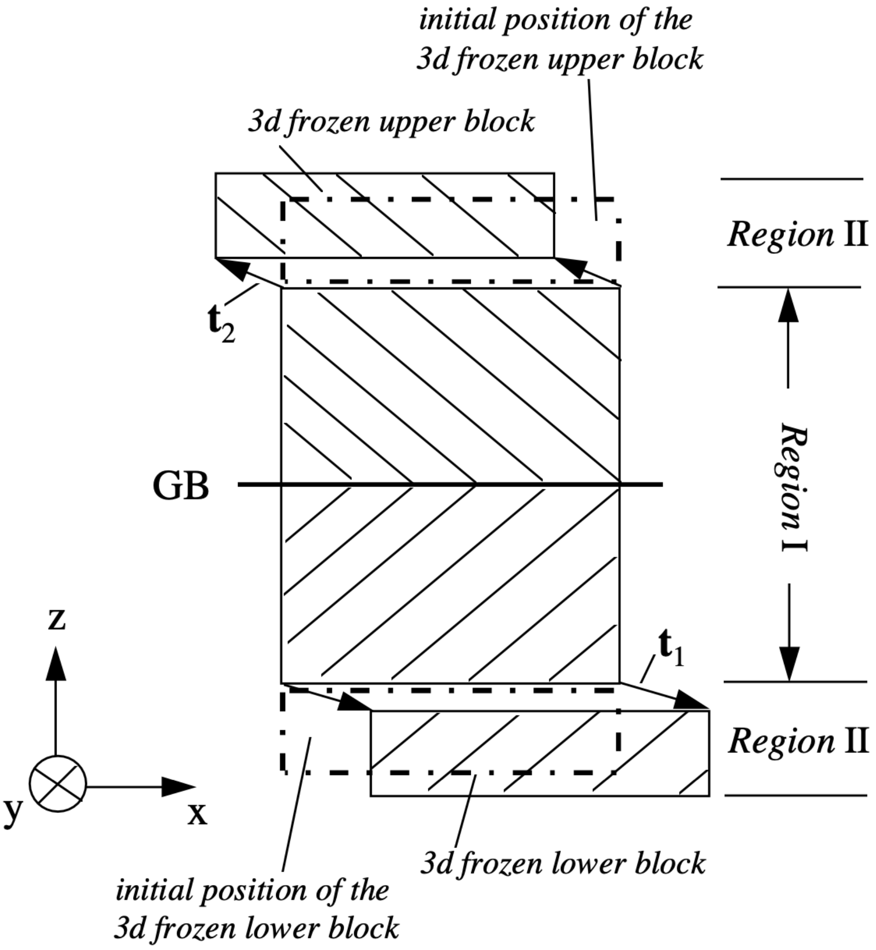

Figure 37: The simulation box is divided into two external layers of atoms I and II which are frozen and translated by vectors t_1 and t_2 (Schönfelder, 2003).

Free Surface (FS) concept in the direction orthogonal to grain boundary plane are deployed to solve this problem[1]. The use of free surfaces demands to use a robust inter-atomic potential that is able to present more realistically the free surfaces. In this work, we usefree surface in direction perpendicular to normal of grain boundary plane and Periodic boundary conditions in direction parallel to normal of grain boundary plane (see later).

---

[1] Free surfaces are surfaces that are subject to zero shear stress $\mathscr{T}$.

$$\vec{n}.\mathscr{T} = 0 \tag{2.15}$$

2.3 Geometry of simulation Box

Carefully choosing and building initial atomic structure of a grain boundary for atomistic simulations is very important for several reasons that are discussed in the following. We will focus on CSL GB to be able to use PBC. Initial atomic structure conditions energy of a grain boundary and potentially the defects that can form (Sutton, 1996) during migration when a grain boundary is exposed to an external driving force or temperature. Since atomistic studies explore a specific grain boundary configuration from an infinite set of possible configurations (if we consider all 9 degrees of freedom) of a given arbitrary character (tilt, twist or mixed), it necessitates choosing a configuration with atoms properly oriented and this orientation has to respect the underlying CSL lattice geometry. In addition, it requires to properly place the grain boundary in a simulation box in a way that a grain boundary respects the lattice periodicity of the two abutting grains.
Solving mathematically the problems related to lattice periodicity accross the Periodic Boundary Conditions amounts to solve coupled Diophantine equations. These are polynomial equations with one or more unknowns whose solutions of interest are sought among the integers. For a given bicrystal, there are two Diophantine equations (equation 2.16) for each of two grains to be solved simultaneously in each direction.

$$hx_i + ky_i + lz_i = 0 \text{ for } i = 1, 2 \tag{2.16}$$

Where (hkl) are Miller indices in an arbitrary lattice system. From a mathematical point of view, they could be solved using an Euclidean algorithm. In practice the process is simplified by taking advantage of the underlying CSL lattice as it respects the periodicity of both grains. This is achieved by properly defining the orientation of atoms and dimensions of the box from the CSL vectors. In fact, the lattice periodicity can exist if and only if there is at least one coincidence site along the grain boundary. Nevertheless, this condition has one major consequence of limiting the type of grain boundaries that can be constructed in practice. The following section presents a commonly used approach to properly orient two adjacent grains in space. This method allows to generate any rational CSL grain boundary of arbitrary geometry and of finite dimensions in a bicrystal. In this approach, the first step consists of approximating a grain boundary from misorientation angle and axis. The approximation is based on rotating one grain relative to the other until an exact coincidence is obtained (Ranganathan, 1966).
For example, considering $\Sigma 5$ with misorientation axis $T(a, b, c) = [001]$, the shortest coincidence sites are (210) and (120). From these Coincidence sites the misorientation angle θ is calculated from equation 1.2 in which $X = 2$ and $Y = 1$. It results in $\theta = 53.1301°$ and $\sigma = \sqrt{(a^2 + b^2 + c^2)} = \sqrt{(0^2 + 0^2 + 1^2)} = 1$. $(X^2 + \sigma^2 Y^2) = (2^2 + 1 * 1^2) = 5$ is odd, hence m in equation 1.3 becomes 1. By replacing, $\Sigma = \frac{X^2+\sigma^2Y^2}{m} = \frac{5}{1} = 5$.
Once the grain boundary is defined, the second step in this approach is to define a CSL

basis. It is customary preferred to work with orthogonal basis and to take the misorientation axis as one of the vectors of the CSL basis. By denoting $[a, b, c]$ as the rotation axis expressed in an orthogonal basis in a representative grain A. To constitute a CSL basis, a vector $[x_1, y_1, z_1]$ is sought such that it satisfies the condition of orthogonality with misorientation axis.

$$[a, b, c].[x_1, y_1, z_1] = 0 \tag{2.17}$$

Equation 2.17 has an infinite number of possible solutions. It is preferable to select a vector $[x_1, y_1, z_1]$ with the lowest Miller indices. The third vector $[x_2, y_2, z_2]$ of the basis is taken as the cross product of the two previous vectors

$$[x_2, y_2, z_2] = [a, b, c] \wedge [x_1, y_1, z_1] \tag{2.18}$$

It results in a vector space $\boldsymbol{G}_1$ of CSL vectors in grain one with its basis $\boldsymbol{B_{CSL1}}$ that reads

$$B_{CSL1} = \left\{ \begin{pmatrix} x_1 \\ y_1 \\ z_1 \end{pmatrix} \overrightarrow{X}_{CSL}, \begin{pmatrix} x_2 \\ y_2 \\ z_2 \end{pmatrix} \overrightarrow{Y}_{CSL}, \begin{pmatrix} a \\ b \\ c \end{pmatrix} \overrightarrow{Z}_{CSL} \right\} \tag{2.19}$$

This $\boldsymbol{B_{CSL1}}$ basis makes a data base of all possible CSL vectors in grain one. To obtain a CSL basis $\boldsymbol{B_{CSL2}}$ in grain two requires the grain boundary plane. Hence, the third step in this approach is to define a grain boundary plane from a linear combination of CSL vectors in the $\boldsymbol{B_{CSL1}}$ basis. The normal of a grain boundary plane follows this generalised equation

$$\overrightarrow{n} = \alpha \overrightarrow{X}_{CSL} + \beta \overrightarrow{Y}_{CSL} + \gamma \overrightarrow{Z}_{CSL} \tag{2.20}$$

Where α, β and γ are integers which allow to build different characters of grain boundary. For that, there are three possible categories:

1. We have a pure twist grain boundary if and only if $\alpha = \beta = 0$ that results in $\overrightarrow{n} = \gamma \overrightarrow{Z}_{CSL}$
2. We have pure tilt grain boundary if one of the following conditions satisfies:
   (a) $\beta = \gamma = 0$ then $\overrightarrow{n} = \alpha \overrightarrow{X}_{CSL}$
   (b) $\gamma = 0$ then $\overrightarrow{n} = \alpha \overrightarrow{X}_{CSL} + \beta \overrightarrow{Y}_{CSL}$
   (c) $\alpha = \gamma = 0$ then $\overrightarrow{n} = \beta \overrightarrow{Y}_{CSL}$
3. To obtain a mixed character necessitates that at least one component of tilt coexists with a twist component. Therefore, there exists a mixed grain boundary if one of the three conditions is fulfilled :

(a) $\alpha \neq 0$,$\beta = 0$ and $\gamma \neq 0$ this leads to $\overrightarrow{n} = \alpha\overrightarrow{X}_{CSL} + \gamma\overrightarrow{Z}_{CSL}$

(b) $\alpha = 0$, $\beta \neq 0$ and $\gamma \neq 0$ this leads to $\overrightarrow{n} = \beta\overrightarrow{Y}_{CSL} + \gamma\overrightarrow{Z}_{CSL}$

(c) $\alpha \neq 0$, $\beta \neq 0$ and $\gamma \neq 0$ this leads to $\overrightarrow{n} = \alpha\overrightarrow{X}_{CSL} + \beta\overrightarrow{Y}_{CSL} + \gamma\overrightarrow{Z}_{CSL}$

With the use of a rotation matrix R_{G12} that allows to pass from grain one to grain two, the CSL basis of the first grain and the grain boundary plane allow to calculate the second CSL basis. The Rodrigues rotation matrix R_{G12} reads:

$$R_{G12} = \begin{bmatrix} g + a^2(1-g) & ab(1-g) - ch & ac(1-g) + bh \\ ab(1-g) + ch & g + b^2(1-g) & bc(1-g) - ah \\ ac(1-g) - bh & bc(1-g) + ah & g + c^2(1-g) \end{bmatrix} \tag{2.21}$$

Where $g = \cos(\theta)$ and $h = \sin(\theta)$. For a grain boundary with $\overrightarrow{n} = \overrightarrow{Z}_{hkl_1}$, the CSL basis of grain one reads:

$$B_{hkl1} = \begin{cases} \overrightarrow{X}_{hkl_1}, & \text{for} \overrightarrow{X}_{hkl_1} \perp \overrightarrow{Z}_{hkl_1} \\ \overrightarrow{Y}_{hkl_1}, & \text{for} \overrightarrow{Y}_{hkl_1} \perp (\overrightarrow{Z}_{hkl_1}, \overrightarrow{X}_{hkl_1}) \\ \overrightarrow{Z}_{hkl_1} = \overrightarrow{n} \end{cases}$$

The CSL basis of grain two is calculated from B_{hkl1} and rotation matrix R_{G12} as:

$$B_{hkl2} = \begin{cases} \overrightarrow{X}_{hkl_2} = R^T_{G12}.\overrightarrow{X}_{hkl_1} \\ \overrightarrow{Y}_{hkl_2} = R^T_{G12}.\overrightarrow{Y}_{hkl_1} \\ \overrightarrow{Z}_{hkl_2} = R^T_{G12}.\overrightarrow{Z}_{hkl_1} \end{cases} \tag{2.22}$$

Now, the data base of the CSL vectors in both grains allows to properly orient atoms in both grains in a way that respects the orientation of the simulation box so that the resulting initial structure of a grain boundary lies between both grains and it respects the CSL lattice geometry.

The next step consists of defining the size of the simulation box by using the CSL vectors so that the simulation box dimensions respect the periodicity of both grains. The size of each grain reads:

$$\text{Size of grain one} = \begin{cases} L_{x1} = n_x a_o ||\overrightarrow{X}_{hkl1}|| \\ L_{y1} = n_y a_o ||\overrightarrow{Y}_{hkl1}|| \\ L_{z1} = n_z a_o ||\overrightarrow{Z}_{hkl1}|| \end{cases} \tag{2.23}$$

and the size of grain two is taken identical to the size of grain one. Here a_o is a lattice parameter of a material and n_x, n_y, $n_z \in \mathbb{N}^+$. This procedure is common in literature (OMAR, 2019; Talaei et al., 2019a). For our representative $\Sigma 5$ of misorientation angle 53.13° and of rotation axis [001], one of vectors perpendicular to [001] is [210], the third vector $[\bar{1}20]$ is a result of cross product of both vectors. The generalised CSL basis is

$$B_{CSL\Sigma 5} = \left\{ \begin{pmatrix} 2 \\ 1 \\ 0 \end{pmatrix} \overrightarrow{X}_{CSL}, \begin{pmatrix} \bar{1} \\ 2 \\ 0 \end{pmatrix} \overrightarrow{Y}_{CSL}, \begin{pmatrix} 0 \\ 0 \\ 1 \end{pmatrix} \overrightarrow{Z}_{CSL} \right\}$$

The resultant smallest CSL basis for the grain one reads

$$B_{CSL_1\Sigma 5} = \begin{bmatrix} 2 & \bar{1} & 0 \\ 1 & 2 & 0 \\ 0 & 0 & 1 \end{bmatrix}$$

By replacing θ in equation 2.21 by 53.1301° and replace R_{G12}^T in equation 2.22 by the resulting matrix gives the CSL basis in the second grain which is

$$B_{CSL_2\Sigma 5} = \begin{bmatrix} 1 & \bar{2} & 0 \\ 2 & 1 & 0 \\ 0 & 0 & 1 \end{bmatrix}$$

For this type of grain boundary and in order to obtain a tilt GB, we can either choose $\overrightarrow{n} = \overrightarrow{X}_{CSL}$ or $\overrightarrow{n} = \overrightarrow{Y}_{CSL}$. The size of the simulation of this grain boundary are:

$$\text{For grain one} = \begin{cases} L_{x1} &= n_x a_o \sqrt{2^2 + 1^2 + 0^2} \\ L_{y1} &= n_y a_o \sqrt{-1^2 + 2^2 + 0^2} \\ L_{z1} &= n_z a_o \sqrt{0^2 + 0^2 + 1^2} \end{cases}$$

2.4 Describing inter-atomic interaction

The modelling of matter at the atomic scale requires a comprehensive and clear description of interactions between constituting particles. Although, in principle, such a description must be based on quantum mechanics, in general, methods used in atomistic simulations simplify by adapting a classical point of view of representing particles as point masses interacting through forces that only depend on their separating distance. The most familiar pair interaction is the Lennard-Jones potential (Jones, 1924).

$$U(r) = 4\epsilon \left(\left(\frac{\sigma}{r}\right)^{12} - \left(\frac{\sigma}{r}\right)^{6} \right) \tag{2.24}$$

Where r is the distance between two interacting particles, ϵ is the depth of the potential well and σ is the distance at which the particle-particle potential energy is zero. However, in a metallic system, the contribution of overlapping electron clouds must be taken into account. Therefore, a multi-body potential is a more relevant potential for simulating such system. The potential energy function which describes atomic interactions is generalised as follows:

$$U(\overrightarrow{r}) = u_0(\rho)+\sum_{i_1}^{N} u_1(\overrightarrow{r}_{i_1})+\frac{1}{2!}\sum_{i_1\neq i_2}^{N} u_2(\overrightarrow{r}_{i_1},\overrightarrow{r}_{i_2})+\frac{1}{3!}\sum_{i_1\neq i_2\neq i_3}^{N} u_3(\overrightarrow{r}_{i_1i_2},\overrightarrow{r}_{i_2i_3},\overrightarrow{r}_{i_1i_3})+... \tag{2.25}$$

Where $u_o(\rho)$ is an energy term which depends only on the electronic density ρ and it describes the behaviour of electronic cloud in metallic system. The term $\sum_{i_1}^{N} u_1(\overrightarrow{r}_{i_1})$ describes the interaction between pairs, the third term $\frac{1}{2!}\sum_{i_1\neq i_2}^{N} u_2(\overrightarrow{r}_{i_1},\overrightarrow{r}_{i_2})$ describes the interaction between triplets, in a similar way, the other terms represent the multi-body character of the function by bringing into play the interactions between several atoms in the system. The two-body interaction takes precedence over other interactions. The embedded atom method (EAM) of Daw and Baskes (Foiles et al., 1986) is one example of potential that results from an empirical implementation of equation 2.25 and is particularly well suited to metals. It reads

$$U(\overrightarrow{r}) = \sum_{i} f_{s_i}(\overline{\rho}_i) + \frac{1}{2}\sum_{i,j(i\neq j)} u_{s_i s_j} \tag{2.26}$$

For

$$\overline{\rho}_i = \sum_{i\neq j} \rho_{sj}(r_{ij}) \tag{2.27}$$

The first term to the right in equation 2.26 describes embedding energy of atom i in the host of electron density $\overline{\rho}_i$ induced at site i by other atoms. The second terms describes the pair interaction between atom i and j. The ρ_{sj} describes the electron density function assigned to atom j.

There are other potentials in literature such as FS (Finnis Sinclair) (Finnis and Sinclair, 1984),

$$U_{FS}(\overrightarrow{r}) = U_n + U_p = \frac{1}{2}\sum_{ij} V_{ij} - A\sum_{i}\sqrt{\overline{\rho}_i} \tag{2.28}$$

$$V_{ij} = \begin{cases} (r-ij-c)^2(c_0+c_1r_{ij}+c_2r_{ij}^2 & \text{if } r_{ij}\leq r_{cutoff} \\ 0 & \text{if } r_{ij} > r_{cutoff} \end{cases}$$

Where r_{ij} is inter-atomic distance and c_0, c_1, c_2, A are fitting parameters and Modified Embedded Multi-body Method (Lee et al., 2003) etc... EAM and FS potentials are widely used in atomistic simulations, thus, there are some of them which have been tested and validated for a large number of elemental FCC metals for instance potentials for Nickel (Voter and Chen, 1987; Mishin et al., 1999; Foiles et al., 1986), Copper (Foiles et al., 1986; Mishin et al., 2001),Gold (Foiles et al., 1986), Aluminum (Voter and Chen, 1987; Ercolessi and Adams, 1994; Mishin et al., 1999). After comparing available inter-atomic potential, we have used in this project the EAM-type formalism of Daw and Baskes (Daw and Baskes, 1984; Daw et al., 1993) developed for mechanical application. More details on this EAM potential are given in section 2.5.5.

2.5 Simulation environment

In atomistic calculations, it is possible to maintain a constant energy, temperature, pressure, volume, chemical potential or any combination of the them. These conditions correspond to three commonly used thermodynamical ensembles (Allen and Tildesley, 1988; Evans and Sarman, 1993; Frenkel and Smit, 2001; Martyna et al., 1994).

2.5.1 The Canonical ensemble (NVT)

In this ensemble, which is used in this project, the number (N) of particles and the volume (V) and the macroscopic value of temperature (T) remain constant. The constancy is achieved by controlling the temperature through either direct temperature scaling during the temperature initialisation stage or by coupling a temperature-bath during the data collection phase. However, some fluctuations can occur but this depends on the size of the system. For example, a definite temperature T applied to the system results in a specified average macroscopic value in the system whereas the instantaneous observable parameter representing the total energy (such as the Hamiltonian $\mathscr{H}$) of the system can slightly fluctuates. By considering a system with the average energy E_{tot}, the root mean square fluctuations $\mathscr{H}_{rmsE_{tot}}$ of $\mathscr{H}$ around this average value E_{tot} can be related to the average temperature value through the heat capacity of the system c_v as:

$$\mathscr{H}_{rmsE_{tot}} = \sqrt{\langle \mathscr{H}^2 \rangle_{NVT} - \langle \mathscr{H} \rangle_{NVT}^2} = T\sqrt{k_B c_v} \tag{2.29}$$

Where k_B is Boltzmann constant. The fluctuation of the instantaneous temperature τ is quantified using the root means square $\tau rmsE_{tot}$ as follows :

$$\tau_{rmsE_{tot}} = \sqrt{\langle \tau^2 \rangle_{NVT} - \langle \tau \rangle_{NVT}^2} = T\sqrt{\frac{2}{N_{idof}}} \tag{2.30}$$

Where N_{idof} and τ is the number of internal degrees of freedom and instantaneous temperature in the system respectively. N_{idof} is calculated from the total number of particles in a system as :

$$N_{idof} = 3N - N_{geom} - N_{edof} \tag{2.31}$$

in which N_{geom} is number of geometrical constraints such boundary conditions and N_{edof} is number of external degrees of freedom (they correspond to the rigid body translation of the system) . It is evident that as the number of particles increases in the system, thermal fluctuation vanishes. This points out once again the importance of carefully choosing the size of the simulation of box.

2.5.2 The isothermal isobaric constant (NPT) ensemble

In this ensemble, the number of atoms remains constant whereas the pressure and temperature have a specified average value. The instantaneous volume υ of the system has to fluctuate. For the system at equilibrium, the root mean square fluctuations υ_{rmsv} of the instantaneous volume around its average value V is calculated as

$$\upsilon_{rmsv} = \sqrt{\langle \upsilon^2 \rangle_{NPT} - \langle \upsilon \rangle^2_{NPT}} = \sqrt{V k_B \beta_T} \tag{2.32}$$

Where β_T is the isothermal compressiblity and k_B is the Boltzmann's constant. The fluctuation in volume goes simultaneously with the fluctuation in instantaneous enthalpy $(\zeta + P\upsilon)$ of the system around its average value H. These fluctuations can be quantified in a similar way as before through the root-mean-square fluctuations of enthalpy ζ_{rmsH}

$$\zeta_{rms_H} = \sqrt{\langle (\zeta + P\upsilon)^2 \rangle_{NPT} - \langle \zeta + P\upsilon \rangle^2_{NPT}} = T\sqrt{k_B C_p} \tag{2.33}$$

Where C_p is the isobaric heat capacity of the system. In this ensemble, the magnitude of instantaneous fluctuations on P and T vanishes in the limit of macroscopic system as well.

2.5.3 The Micro-canonical ensemble (NVE)

In the Micro-canonical ensemble (NVE), the number of particles, volume and energy are fixed in the system but fluctuations in the specific heat may be obtained by examining fluctuations in the kinetic energy (κ) and potential energy (ν). In this case the root mean square of the instantaneous fluctuation in the kinetic energy (κ_{rmsNVE}) and potential energy (ν_{rmsNVE}) (Lebowitz et al., 1967) read:

$$\nu_{rms_{NVE}} = \kappa_{rms_{NVE}} = k_B \langle \tau \rangle_{NVE} \sqrt{\frac{3N}{2}\left(1 - \frac{3Nk_B}{2C_v}\right)} \tag{2.34}$$

Where C_v is isochoric heat capacity. Whereas the root mean square of instantaneous fluctuation (P_{rmsNVE}) in pressure P is quantified as,

$$P_{rms_{NVE}} = \sqrt{\frac{k_B \langle\tau\rangle_{NVE}}{V}\left(\frac{2Nk_B\langle\tau\rangle_{NVE}}{3V} + \langle P\rangle_{NVE} - \frac{1}{\beta_c} + \frac{\langle\chi\rangle_{NVE}}{V}\right)} \tag{2.35}$$

Where $\langle\tau\rangle_{NVE}$ is instantaneous temperature β_c is compressiblity coefficient of the system and χ is inter-particle pair virial function. It is evident as the volume or number of particles of the system increases, these fluctuations vanish.

2.5.4 Thermostat

One of the difficulties in statistical ensemble at constant temperature or pressure is to keep temperature T or pressure T constant on average even if the instantaneous values of T and P may fluctuate without impacting too much the natural dynamics of the atoms. For example, in the canonical ensemble (NVT), the constant temperature can be maintained through the approach of rescaling velocity of particle at each time step. In this approach, the velocity and temperature are related as follows

$$\left\langle \sum_i \frac{1}{2} m_i v_i^2 \right\rangle = \frac{3}{2} N k_B T \tag{2.36}$$

The velocity of particle at time step i is re-scaled by a factor of $\sqrt{\frac{T}{T_i}}$. In this expression T is the desired temperature whereas T_i is the instantaneous temperature. An other approach is to use an extended Lagrangian approach in modifying newton's equation of motion as proposed by Anderson (Andersen, 1980).

The Nosé – Hoover thermostat

The Working principle of this approach is based on the assumption that the simulation system is in contact with a thermal reservoir so that an exchange of energy between the system and the reservoir is allowed. In addition, the thermal reservoir has a certain thermal inertia to prevent thermal fluctuation in the system. A damping parameter specified in time units determines how rapidly the temperature and pressure are relaxed. If this damping parameter is too small, the temperature and pressure can fluctuate wildly; if this damping parameter is too large, the temperature and pressure will take too long to equilibrate. We have chosen this thermostat because the total energy in the system and in reservoir is always conserved (Andersen, 1980; Nosé, 1984; Hoover and Holian, 1996).

Anderson thermostat

This stochastic approach of Anderson consists of periodically choosing a random particle in the system and assigning it a velocity following the Boltzmann distribution law (Andersen, 1980). This amounts to consider that at periodic interval of time, a randomly chosen particle of the system collides with an imaginary particle of the heat reservoir. The time between collision is sampled from Poisson's distribution. Unfortunately, the total energy in the system is no longer conserved.

2.5.5 Synthetic driving force for grain boundary migration

Grain boundary motion is caused by a driving force. In Molecular Dynamics, it is desirable to use a driving force that can be applied identicaly to the large variety of GB configurations that will be explored, including both symmetric and asymmetric grain boundaries, flat or curved grain boundaries. This is where the synthetic driving forces (Janssens et al., 2006; Schönfelder et al., 2006; Coleman et al., 2014; Ulomek and Mohles, 2014; Yang and Li, 2015) can be particularly relevant thanks to their versatility. In this section will go through the working principle of different synthetic driving force current used for atomistic simulations.

Synthetic driving force of Janssens

The most recent development in artificial driving forces, is the Janssens's driving force (Janssens et al., 2006) which is at the center of this project. It is a driving force produced from per-atom order parameter describing the local crystallographic orientation. Let us consider a bicrystal with a grain A and B with crystallographic orientation I and J respectively. In a crystal with specific orientation I, each atom i with position vector r_i has nearest neighbour atom j at position r_j^I. Any local deviation forces its nearest neighbour atom to occupy a new position r_j. The order parameter ξ_i associated with this deviation is calculated following equation 2.37.

$$\xi_i = \sum_j^n |r_j - r_j^I| \tag{2.37}$$

It is zero if the local orientation is exactly I. Here, n is the number of nearest neighbour atoms j of i which is 12 for FCC materials, r_j^I is the nearest ideal lattice site of crystal I to r_j. The same order parameter is calculated for lattice sites in crystal J that have the nearest neighbour atom i. The orientation difference between crystal I and crystal J is then expressed as

$$\xi_{IJ} = \sum_j |r_j^J - r_j^I| \tag{2.38}$$

The difference in orientation between crystal I and J creates an extra potential energy $(u_\xi(r_i))$ to the atoms across grain boundary which reads:

$$u_\xi(r_i) = \begin{cases} 0, & \text{if } \xi_i < \xi_l \\ \frac{u_0}{2}\left[1 - \cos(2\omega_i)\right], & \text{if } \xi_l < \xi_i < \xi_h \\ u_0, & \text{if } \xi_h < \xi_i \end{cases}$$

and the resulting driving force $\overrightarrow{F}(r_i)$ follows

$$\overrightarrow{F}(r_i) = -\frac{\partial u_\xi(r_i)}{\partial r_i} = -\frac{\pi u_o}{2(\xi_h - \xi_l)}\left(\left[\sum_j \frac{\delta_{ij}}{|\delta_{ij}|}\right]\sin(2\omega_i) + \sum_j \left[-\frac{\delta_{ij}}{|\delta ij|}\sin(\omega_j)\right]\right)$$

Where f in equation 2.39 is a material and temperature dependent parameter which is used to exclude thermal vibration on the normalised order parameter ω_i which varies from 0 in grain A to 1 in grain B. The value of f by default is 0.25 (Janssens et al., 2006).

$$\begin{aligned} \xi_l &= f\xi_{IJ} \\ \xi_h &= (1 - f)\xi_{IJ} \\ \omega_i &= \frac{\pi}{2}\frac{\xi_i - \xi_l}{\xi_h - \xi_l} \end{aligned} \tag{2.39}$$

However, even with the parameter f thermal fluctuations may still be large enough to cause atoms in grain A to have an order parameter greater than 0 and or less than 1 in grain B. This may affect the determination of actual driving force because the average

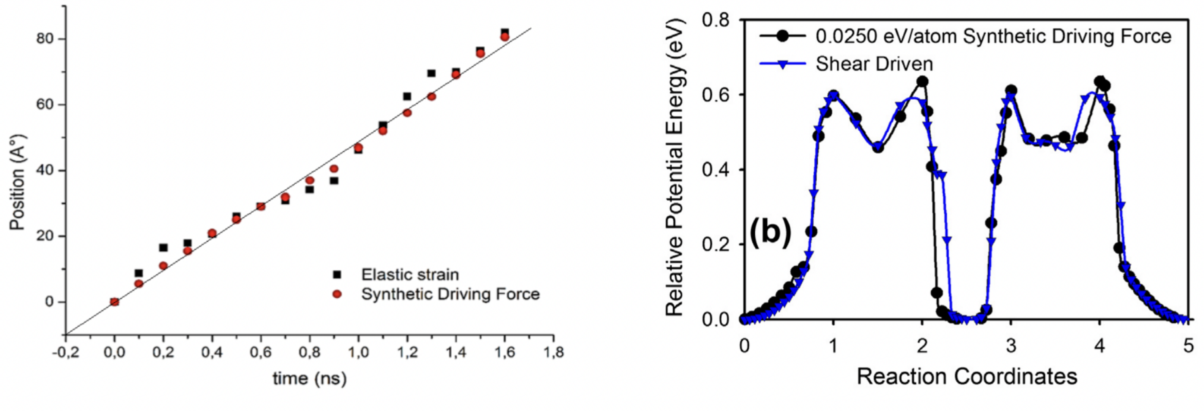

(a) **(b)**

Figure 38: **(a)** Comparison of grain boundary position vs. simulation time for migration induced by elastic and synthetic driving force for Σ5 ⟨010⟩ asymmetric tilt grain boundary at 1200 K (Zhang et al., 2007) **(b)** CINEB calculations from Σ37(570)[001] Nickel symmetric tilt grain boundary comparing energy barrier and grain boundary path for migration driven by synthetic force and shear (Coleman et al., 2014)

energy change as an atom's local orientation changes from I to J is no longer equal to u_0. This effect might be more pronounced at high temperature and when θ (misorientation angle between grains) is small. At a given temperature and θ to accurately determine the true driving force thermodynamic integration is used to calculate the amount of free energy per atom added to each grain by virtual force (Olmsted et al., 2009c). Despite the virtual nature of this synthetic force, it compares favourably with other mechanical driving forces. For example figure 38 (a) compares the path history of grain boundary motion triggered by synthetic and elastic force.

In addition, Coleman et al. (Coleman et al., 2014) has also conducted a study to verify if the non physical nature of this force does not alter the migration of a grain boundary. Coleman compared the motion of grain boundaries driven by the Jansens's driving force and shear. In this work, slip-vector analysis and continuum based deformation metrics were used to examine micro-rotation and strain. This work concluded that the nonphysical nature of Jansen's driving forces does not affect the fundamental mechanisms associated with grain boundary migration. Furthermore, by using climbing image nudged elastic band (CINEB) to compare transition path and energy barrier, the work concluded that the path and deformation history from grain boundary motion was indistinguishable from both shear and artificial driving force (see figure 38 (b)). Therefore, we can conclude that the artificial driving force migrates a grain boundary in similar way to real physical forces. For more example of synthetic driving force used in the atomistic simulation see section A.2.

Objectives and methodology

Objectives

The first objective is to identify and characterise defects on surface of a relaxed grain boundary. This will allow to describe atomic structure of a grain boundary in terms of arrays of dislocations. The resulting dislocation density which is unique for each grain boundary will be imported in the continuum scale model in the second part of this work. The second objective is to develop self-sufficient generic models capable of predicting mobility of CSL grain boundaries at any temperature and driving force. Having in place this model can serve many roles, including but not only, a) reducing consumption of computational resource and time spent in atomistic calculations b) mobility function can allow to rationalise the origin of some particular phenomena observed during grain boundary migration and c) mobility function can be used to inform large scale models, in particular, at continuum scale. Therefore, having mobility functions can be seen a step forward to bridging atomistics and continuum scale models.

Methodology

In this work, we will perform MD simulations to investigate the motion of [001] grain boundaries in FCC material. Here we will use Nickel as a model system for other FCC materials because it exhibits intermediate values for stacking fault energy and because there is a literature to compare with (Homer et al., 2013, 2014b; OMAR, 2019). The configurations to investigate in this study will encompass both low and high angle grain boundaries with different characters (tilt, twist and mixed), thus, covering a large part of the fundamental zone of the corresponding Σ GB. The initial configuration of a grain boundary will be carefully chosen (as we will see later) because it conditions energy of a grain boundary.

Differently to what was done in the literature to investigate migration of a grain boundary, we will span a very broad range of temperatures and motive forces. We will systematically explore the T-P parametric space and a detailed map of T-P space will allow to find major trends that are common for several grain boundaries rather than some particular behaviours for a specific grain boundary. We will see that this will allow to identify dynamic transition of kinetic regimes. Based on observed trends and dynamic transitions, we will rationalise our results and propose migration laws of grain boundary. All simulations will be carried in LAMMPS (Large-scale Atomic/Molecular Massively

Parallel Simulator) (Plimpton, 1995). It is a high-performance code, regularly maintained and updated. It offers a good computing facility required in this work. To visualise outputs from LAMMPS, we will deploy an other adapted tool known as Open Visualisation Tool (OVITO) (Stukowski, 2009). To post-process raw data specific to GB, OVITO does not have this functionality, consequently, we will develop our own codes. This chapter is organised as follows. We will start by setting up the simulation box, after, we will explain the choice of inter atomic potential to describe atomic interaction, in the next section, we will explain the methodology used to obtain a ground state of a grain boundary, in the fourth section we will give methodology for running MD simulations and in the final section we will explain the post treatment of raw data obtained from MD simulation.

Setting up the simulation box

In order to perform a systematic study of the GB migration with possibility to compare from data points reported in literature, we reprise the bi-crystalline geometry employed in a number of simulation studies (Olmsted et al., 2009a,b; Homer et al., 2013, 2014b, 2015; O'Brien and Foiles, 2016; Hadian et al., 2018). A planar GB is introduced in the centre of the simulation box with a normal direction along the y-axis of the simulation cell. The use of Periodic Boundary Conditions (PBCs) along x and z axes allows representing a semi-infinite domain at the cost of possible periodicity effects as discussed in section 2.2.3. Free Surface (FS) is employed on y simulation faces, and for that, we made sure that the y cell dimensions are larger enough to neglect image forces between grain boundary and free surfaces. The simulation box setup is illustrated in figure 39.

In molecular dynamics, it is very important to choose the initial structure of grain boundary. For that a great care is taken to construct this atomistic structure. We used our own tool to build CSL GB with arbitrary orientation. This tool relies upon determining the CSL vectors of the considered Σ structure and they are used to orient both grains with respect to the simulation box. These vectors are also used to properly place the PBC faces in order to preserve the continuity of atomic structure across PBC. This can also be seen as a practical way to solve the underlying and coupled sets of Diophantine equations associated to PBC on both adjacent grains. This tool is similar to the seminal work of Patala et al.(Banadaki and Patala, 2015), with the difference that steps are done in a slightly different order to be able to preserve rectangular geometry of the simulation box. Figure 40 shows grain boundaries that we have built with this tool in fundamental zone representation of their grain boundary normal.

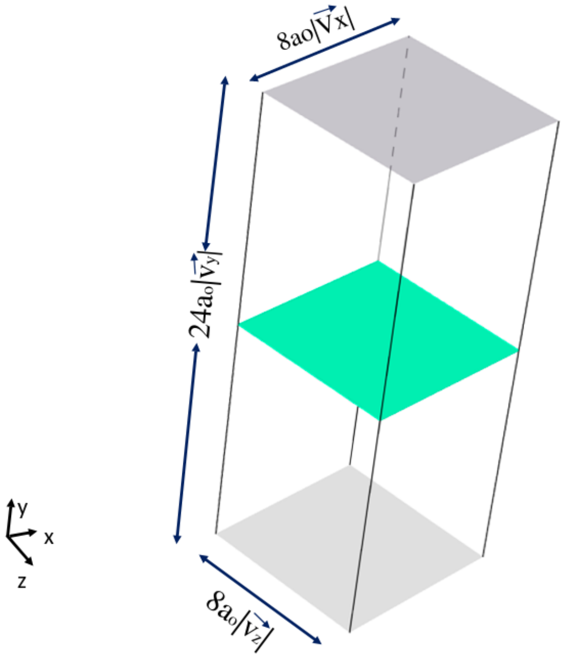

Figure 39: The simulation box setup used in this work. $\overrightarrow{v}_X, \overrightarrow{v}_Y$ and $\overrightarrow{v}_Z$ stand for the CSL vectors along the X, Y and Z directions respectively and a_o is the lattice parameter. Free surface are shown in a grey colour and the grain boundary is shown in a green colour.

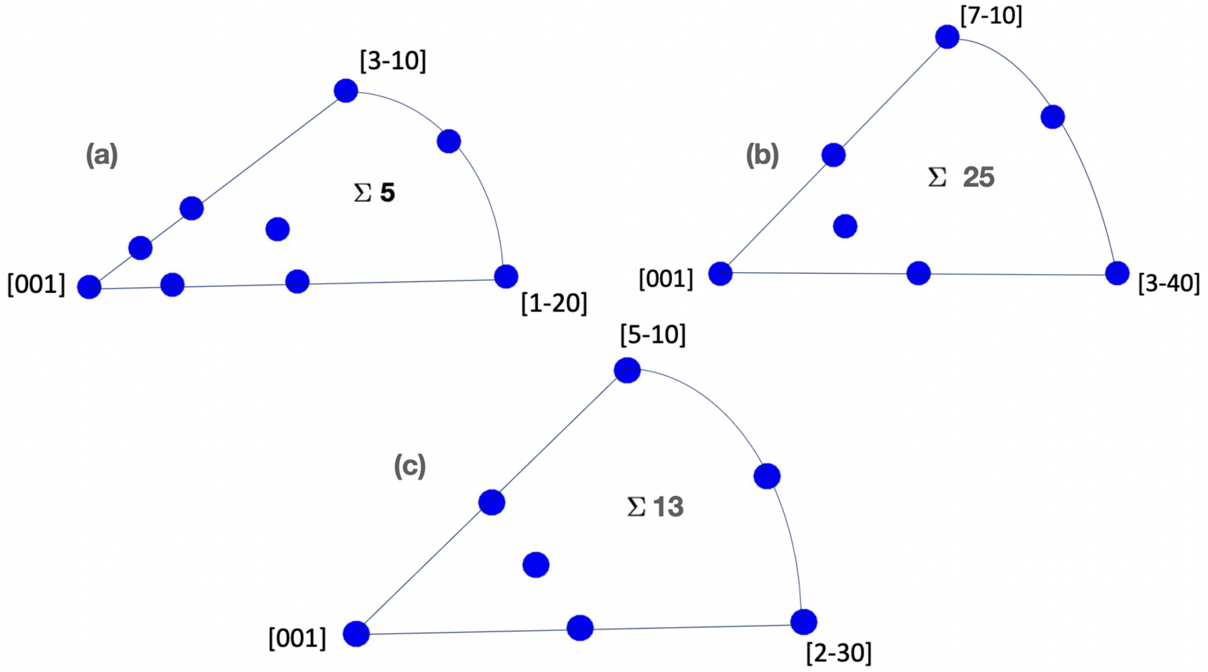

Figure 40: List of all investigated grain boundaries of (a) Σ5, (b) Σ25 and (c) Σ13, shown using the fundamental zone representation of their grain boundary normal.

Inter-atomic Potential

The quality of atomistic simulation relies on algorithms and a proper description of atomic interactions. For that, we have carefully selected the atomic potential to describe interactions among Ni atoms. We picked a well established multi-body semi-empirical potential (Foiles and Hoyt, 2006) for Ni developed specifically for mechanical applications. In what follows, we present in more details the formalism of this potential.

Atomic interactions are described following an EAM-type formalism of Daw and Baskes (Daw and Baskes, 1984; Daw et al., 1993) as presented in section 1.2. The functions used are those proposed by Voter and Chen (VOTER). To mimic the electrostatic interactions between two spherical charge densities, the pair interaction is described utilising a Morse potential,

$$u(r_{ij}) = E_o\left[e^{-2b(r_{ij}-r_o)} - 2e^{-b(r_{ij}-r_o)}\right] \tag{2.40}$$

in which $E_o = 1.39664eV$, $r_o = 2.14146A^\circ$ and $b = 1.22848/A^\circ$. The electron density function reads:

$$\rho_{sj}(r_{ij}) = \rho_o r_{ij}^n \left(e^{-ar_{ij}} + 2^{n+3}e^{-2ar_{ij}}\right) \tag{2.41}$$

Where $\rho_o = 1$, n=8, $a = 3.58321/A^\circ$ and the embedding function follows

$$\overline{\rho_i} = \sum_{(j\neq i)} \rho(r_{ij}) \tag{2.42}$$

A cut-off radius of $4.85A^\circ$ is used for calculating pair-interaction and density function following the procedure proposed by Voter and Chen (VOTER). The embedding function is determined such that the energy versus volume reproduces a Rose's equation of state (Rose et al., 1984; Foiles, 1985) which correlates the cohesive energy (E_{coh}) to lattice parameter a at a given temperature. The equation of state reads:

$$E_{coh} = -E_{sub}(1 + a^*)\exp(-a^*) \tag{2.43}$$

Where the sublimation energy $E_{sub} = 4.45eV$, $a^*{=}\left(\frac{a}{a_0} - 1\right)/\sqrt{\frac{E_{sub}}{9B\Omega}}$, lattice parameter of Ni at 0K $a_o = 3.52A^\circ$, the bulk modulus $B = 1.8037\text{x}10^{12}erg/cm^3$ and the atomic volume $\Omega = \frac{4\pi r_{ws}^3}{2}$ in which r_{ws} is Wigner-Seitz radius (Rose et al., 1984). The figure 41 shows comparison between equation of state and cohesive energy for different materials. This potential is in an excellent agreement with experiments. Table 2.1 shows a comparison for elastic constant, stacking fault energy, etc... between this potential and experimental data points. One can readily see from the table that this potential reproduces well elastic constants C_{ij}, sublimation energy E_{sub}, and stacking fault energy γ_{SF}. As a result, it has been successfully employed in several studies of grain boundary in pure Ni (Homer et al., 2013, 2014b; O'Brien and Foiles, 2016). Therefore, this potential is a

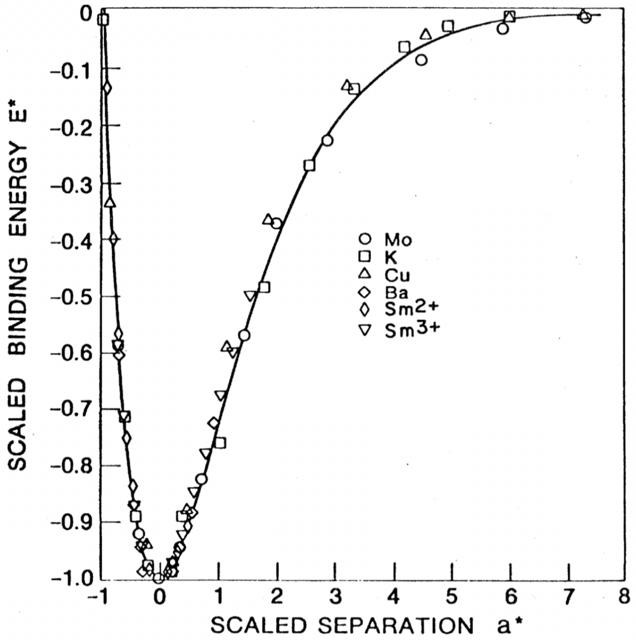

Figure 41: The cohesive energy of different materials against a reduced lattice parameter $a*$. The continuous curve corresponds to the state equation whereas the rest is DFT results from the literature for different metals (Rose et al., 1984).

Table 2.1: Comparison between the predictions of Foiles potential and experimental results for material constants (Foiles and Hoyt, 2006)

Parameters	E_{sub} $\left[\frac{eV}{atom}\right]$	a $[A°]$	B [GPa]	C_{11} [GPa]	C_{12} [GPa]	C_{44} [GPa]	E_v^f [GPa]	γ_{SF} $[\frac{mJ}{m^2}]$
Foiles	-4.45	3.52	180.4	233	154	128	1.63	127
Experiment	-4.45	3.52	181	247	148	125	1.60	125

great pick for this kind of work.

Grain boundary relaxation

Up to date, finding the atomic structure corresponding to the most stable state of a grain boundary from the initial construction described above remains a challenging task. This is due to existing additional microscopic degrees of freedom of grain boundaries. Thus, several atomic configurations are possible for a given macroscopic configuration (Sutton, 1996; Tschopp and McDowell, 2007). To address this, Frolov and Mishin (Frolov et al., 2016) and Banadaki et al.(Banadaki et al., 2018) have performed semi-grand and grand canonical Monte Carlo (MC) simulations, respectively; and they have shown that one grain boundary can have many atomic structures that may differ from the previously known structures of a grain boundary.

To find the most probable ground state of a grain boundary, we have sampled at least 100000 initial grain boundary structures of the same macroscopic degrees of freedom for each grain boundary. This is achieved by using a more practical solution, commonly used in literature (Homer et al., 2015; Olmsted et al., 2009a; Tschopp and McDowell, 2007) as a trade off between numerical cost and accuracy.

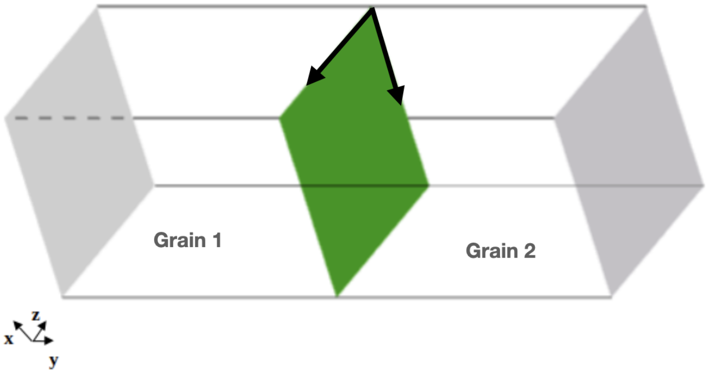

Figure 42: Schematic diagram showing shift of grain 2 relative to grain 1 following CSL vectors (illustrated by black arrows) in plane of a grain boundary.

We have shifted grain 2 with respect to grain 1 along the CSL basis vectors within the grain boundary plan as figure 42 shows and that would correspond to two of the microscopic degrees of freedom. A rigid body body translation of one lattice relative to its adjacent lattice is an important mode of relaxation of grain boundary (Sutton, 1996). During translation steps, abutting grains may contain atoms that are physically too close. The overlapping atoms are resolved by removing one of the atoms from the system. The smallest acceptable distance between atoms is determined based on convergence test. To determine energy of the most stable grain boundary configuration, we performed conjugate-gradient minimisation for all sets of initial grain boundary structures at 0K.

In all simulations, we have used equation 1.16 to calculate energy. From a list of different atomic configuration for a given grain boundary, we have selected the lowest energy configuration as the most probable ground state of a grain boundary. This was done in the interest of the dynamics of a grain boundary which is very demanding on the configuration to use. To validate our selection, we compared our grain boundary energy measures from values reported in literature when available.

MD simulations

The simulation environment was carefully set. In MD calculations, we have used an NVT ensemble since there is no clear dependence of grain boundary mobility on thermodynamic ensemble (Janssens et al., 2006). The selected stable configurations at 0K were heated and expanded to the desired temperature and respective lattice parameter over a period of 125ps. After, the selected configurations were equillibrated to the desired temperature for 125ps before applying a motive force. To keep the correct dynamical atomic structure during simulation (see references (Deng and Deng, 2017; Race et al., 2014) for more details), we performed a convergence test to determine the size of our simulation cell in each direction within the GB plane. Using a larger simulation box can be viewed as a way of keeping a constant converged temperature in the simulation box as explained earlier in section 2.5.1. The simulation box was at least 8 ($n_x = 8$ and $n_z = 8$ see equation 2.23) replicas of smallest GB structure in the GB plane that is respecting the PBC.

To move a grain boundary, we employed the synthetic driving force method developed by Janssens et al. (Janssens et al., 2006) implemented within LAMMPS (Plimpton, 1995). This method has been tested, validated and used in many studies (Homer et al., 2014b; Janssens et al., 2006; Olmsted et al., 2009b,c; O'Brien and Foiles, 2016). The choice of this type of driving force is motivated by the fact that, its results compare favourably with results obtained by other motive forces (Deng and Schuh, 2011a; Janssens et al., 2006; Olmsted et al., 2007). We applied synthetic motive forces that should correspond to stresses in a range of 50 to 500 MPa. Simulations were allowed to run for 200ps, or until the boundary reaches the end of a simulation box. For each grain boundary, we considered 3 or 4 different temperatures from 100K up to 1000K while remaining well below the melting point of Nickel which is 1726K (Porter and Easterling, 1992). In total, we performed 1250 simulations of GB motion.

Raw data analysis and post processing

To investigate dynamic properties, MD simulations were run long enough and regardless of the applied stress and temperature, configuration data were extracted every one picosecond to statistically collect enough data points. This allows to record more atomistic details occurring during grain boundary motion and to precisely keep track of all position of a gain boundary in a simulation box.

However, to locate a grain boundary in a simulation box is yet challenging. One of the challenges is to separate, with certainty, atoms belonging to a defect from atoms in perfect FCC positions. Although some theoretical metrics (Honeycutt and Andersen, 1987; Stukowski, 2012; Kelchner et al., 1998) to identify atoms belonging to a defect, are reported in literature, they still have some challenges associated with. For example, at higher temperatures required to move grain boundaries, atomic vibration can become significant enough so that atoms in perfect FCC positions can even be detected as zero dimension defects. This significantly deteriorates accuracy in measured positions of a grain boundary in a simulation box. For some grain boundaries that move by nucleation and propagation of disconnections and or facetting, it is difficult to measure with precision the exact positions of a grain boundary. One of the difficulties is that at high temperatures required for the migration of thermally activated grain boundaries, atomic vibrations are sometimes detected as point defects and that interferes with the grain boundary position measurement. Another difficulty is related to the dynamic behaviour of some grain boundaries which can present steps or facets and that makes the measurement of the average grain boundary position more difficult.

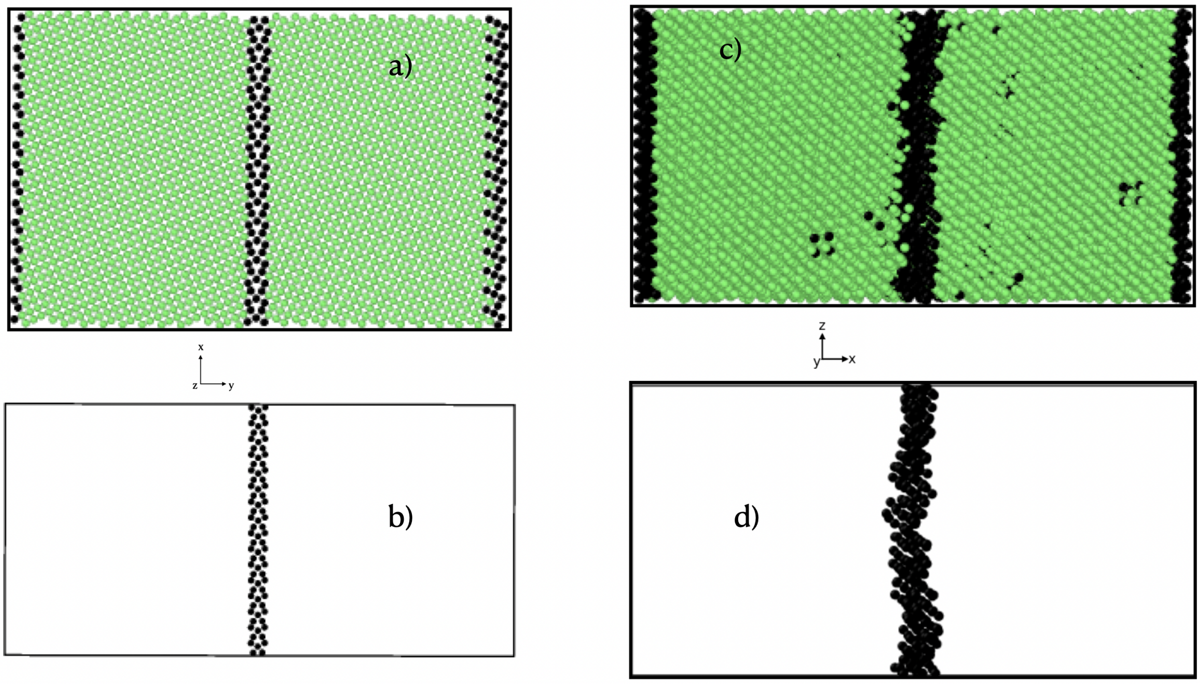

Figure 43: An example of cluster analysis. a)-b) $\Sigma 5(1\bar{2}0)$ at 100K and c)-d) $\Sigma 5(1\bar{2}2)$ at 600K as representatives of all other grain boundaries investigated in this study. a) and c) show identification of atoms not belonging to the perfect FCC positions. Here atoms that belong to the defect are shown in black colour and atoms in perfect FCC position are shown in green colour. One can notice that due to thermal vibrations some atoms in c) not belonging to grain boundary are also detected as defect. b) and d) Keeping only atoms belonging to grain boundary.

Therefore, we have developed our own code written in Python and it allows to identify atoms belonging to grain boundary, thus, locating a grain boundary. The algorithm follows three main steps. In the first step, we have used algorithm of Common Neighbour Analysis, developed by Stukowski (Stukowski et al., 2012), implemented in the Open Visualisation Tool (OVITO) (Stukowski, 2009) to identify all atoms which are not in the perfect FCC position (see figure 43 a).

The second step is a cluster analysis of these atoms to keep only atoms belonging to the grain boundary (see figure 43 b). This means, excluding atoms in perfect FCC positions and atoms belonging to free surfaces. In a perfect FCC structure, each atom has 12 neighbors otherwise it is considered as a point defect. To exclude vibration effects due to high temperature, we have added a negligible distance $\mathscr{D} \approx 3\% a_o$ to each atomic position. An atom which is still detected as a defect after adding this distance is, indeed, confirmed as a defect. This turned out to be an efficient way to separate atoms deviating from their perfect position due to thermal vibration from actual point defect at a GB.

The third step focuses on calculating positions and average speed of a grain boundary. The position (x_i) of each atom i belonging to the defect was then recorded every time t_j. The average position (X_{t_j}) of a grain boundary is calculated as

$$X_{t_j} = \frac{1}{n} \sum_{i=1}^{n} x_i \tag{2.44}$$

X_{t_j} is barycenter of atomic positions of n atoms belonging to a grain boundary at time t_j. For grain boundaries forming disconnections and or faceting during migration, a decomposition of the grain boundary into several smaller slices is envisageable. An average grain boundary position from each slice is measured and then an average grain boundary position is given by the average of the averages of grain boundary positions from all slices. In investigation of grain boundary migration, the main grain boundary property measured is its velocity. In MD, a steady state velocity is instantaneously reached. Therefore, from grain boundary positions extracted in the third step of the algorithm, velocity is extracted as the derivative of the displacement-time curve at each temperature and applied stress.

Chapter 3

Results

In this section, we present static and dynamic properties of [001] CSL grain boundaries. The number of important relationships and results are derived which will be of use in the following sections of this PhD manuscript. In this chapter, we will begin by illustrating the effect of grain boundary relaxation. For that, we will show the influence of microscopic degrees of freedom of grain boundary in properly defining an energetically stable grain boundary structure. After, we will report the details of thermodynamic and kinetic properties of grain boundaries from a systematic exploration of the $T - P$ parametric space. Since the purpose of dynamic simulations is to find trends that are common for several grain boundaries, we will show that these details are of profound interests, especially in devising generic mobility functions that can be imported in the phase field model.

3.1 Static properties of grain boundaries

3.1.1 Energy of grain boundaries

Rigid body translation at grain boundary is an important mode of atomic relaxation of grain boundary. In general, this translation has components in both direction parallel and perpendicular to grain boundary plane. In this study, we only translated one grain relative to its adjoining grain following directions within the grain boundary plane. In this section we present results from a systematic static study of grain boundaries. We will see that the results presented here reconfirm the role played by microscopic and macroscopic degrees of freedom in the relative stability of a grain boundary in agreement with existing literature (Sutton, 1996; Olmsted et al., 2009b; Priester, 2012).

3.1.2 Dependence of energy on microscopic and macroscopic degrees of freedom

It has been reported in several publications (Priester, 2012; Sutton, 1996) that the energy of a grain boundary strongly depends on microscopic parameters for otherwise fixed five macroscopic parameters. Microscopic degrees of freedom lead to multiple unequivalent atomic structures, however, there is still to date no consensus on how to obtain and what should be the groundstate of a GB. We thus have made a classical assumption that the one with the lowest energy is the most probable. In practice, we have generated several configurations of the same macroscopic degrees of freedom but of different microscopic degrees of freedom (dof) and then compare their energies. The atomic structure and corresponding GB energy may vary wildly as function of the microscopic parameters, in particular with respect to the in-plane displacements. Results are displayed as GB energy maps as function of the two microscopic dof, in a way similar to gamma surfaces for stacking faults. Figure 44 shows maps of GB energy for grain boundaries of type $\Sigma5$ and $\Sigma13$ of different characters, these maps are representative of all other investigated grain boundaries. The role of microscopic and macroscopic parameters of a grain boundary becomes evident.

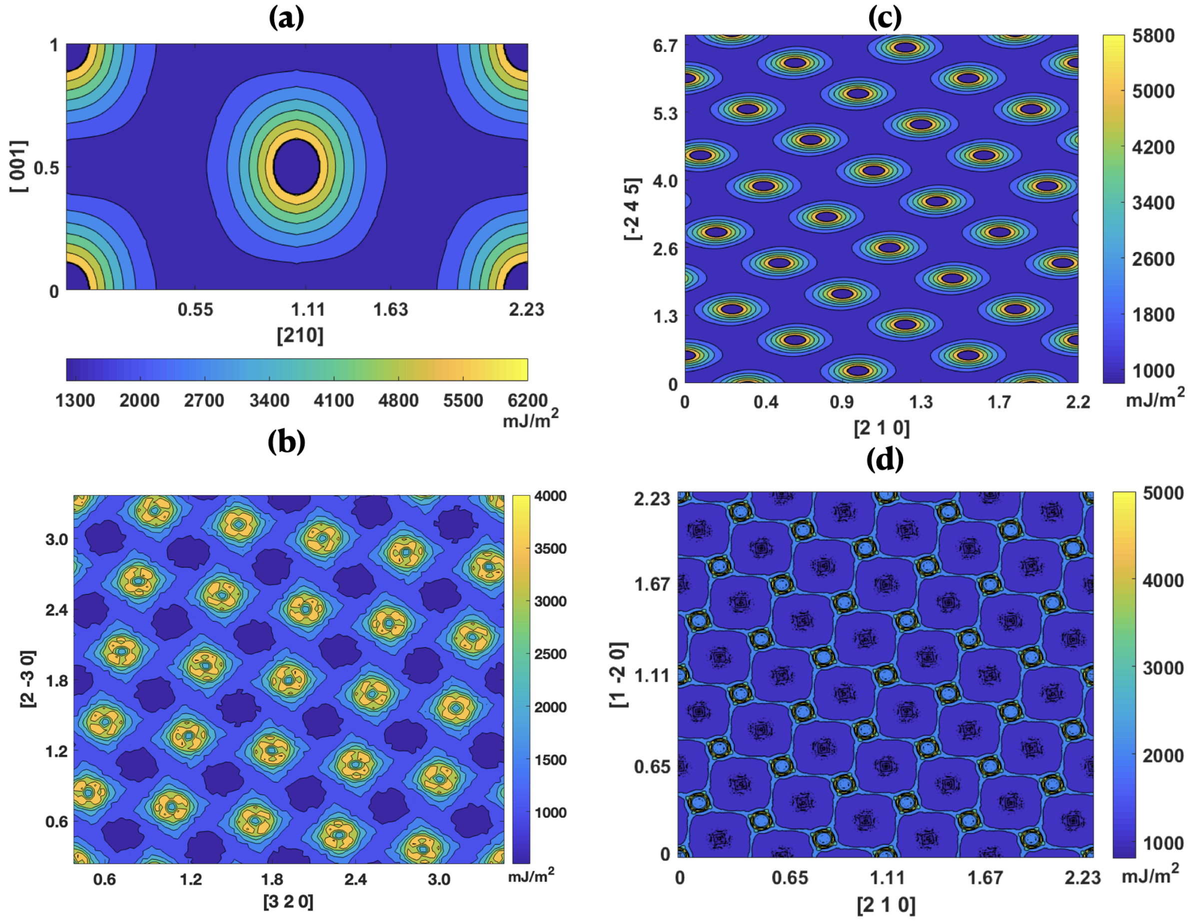

Figure 44: Representation of the GB energy obtained as function of the two microscopic dof (transverse displacement along CSL in plane vectors) for symmetric (a) tilt $\Sigma5$ $(1\bar{2}0)$ (b) twist $\Sigma13(001)$ (c) mixed $\Sigma5$ $(1\bar{2}2)$ and (d) twist $\Sigma5$ (001) GBs represented with a colour code, from blue (low energies) to yellow (high energies), as the top grain is translated relative to the bottom grain by CSL vectors along the grain boundary plane.

These energy maps differ strongly among GB type ($\Sigma5$ vs $\Sigma13$) and character (tilt vs twist vs mixed). These GB energy maps consist of a landscape of low energy valleys and high energy region (hills). In the center of high energy regions, there is usually a blu region of lower energy certainly resulting from the removal of close atoms procedure, that prevent the GB energy reaching unrealistically large values. Here, since have translated the upper grain by a maximum of 1 CSL vector amplitude, the GB maps cover only one periodicity of the underlying CSL lattice in both CSL direction. From these maps the most probable configuration for the GB can be easily identified from the energy minimum, and corresponds to precise microscopic dof.

In literature (Sutton, 1996; Priester, 2012; Talaei et al., 2019a), map of grain boundary energy as function of the two degrees of freedom was reported to depend on many factors including atomic density of a grain boundary. In order to check these ideas and better understand the GB maps differences observed among a priori similar GB, we have examined atomic positioning in the same grain boundaries. Therefore, we have compared atomic structure of Σ5, Σ13 and Σ25pure twist grain boundaries. Figures 45 a) to c) show that the inplane positioning of few layer of atoms at a grain boundary. As the misorientation angle θ increases the density of atoms increases as well at least for the investigated grain boundaries. As expected volume of the CSL lattice volume decreases with the increase in the Σ value. . It seems also that the thickness of a grain boundary depends on the type (Σ). Overall, figure 44 and 45 confirm once again that the most probable ground state configuration of a grain boundary is achievable if a grain boundary relaxation method is deployed. Figures 46a) to f) show an example of a comparison between unstable and the most probable stable configurations of representative grain boundaries. Here we can notice the difference in atomic configuration in a grain boundary. It is evident that the atomic arrangement of the most probable configuration is more compact than that of less probable configurations (based on its energy) for the same macroscopic degrees of freedom. To quantify the extent at which grain boundary relaxation affects the geometrical

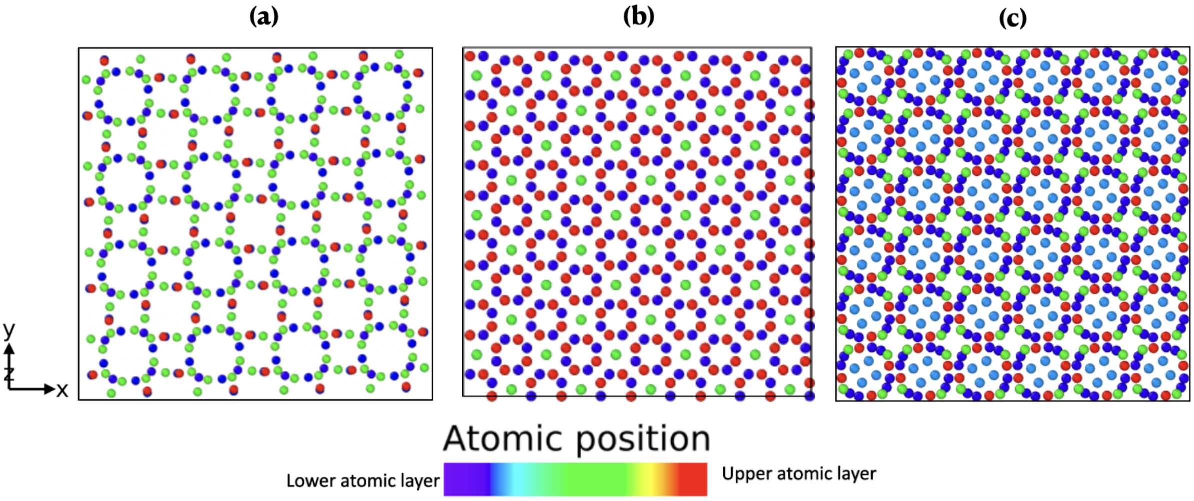

Figure 45: Atomic density in relaxed pure twist grain boundaries (a) Σ25 (b) Σ5 and (c) Σ13 in which the normal of grain boundary plane is parallel to Z axis. Atoms are coloured function of their position in a grain boundary. Blue and red colour correspond to lower and upper atomic layer respectively.

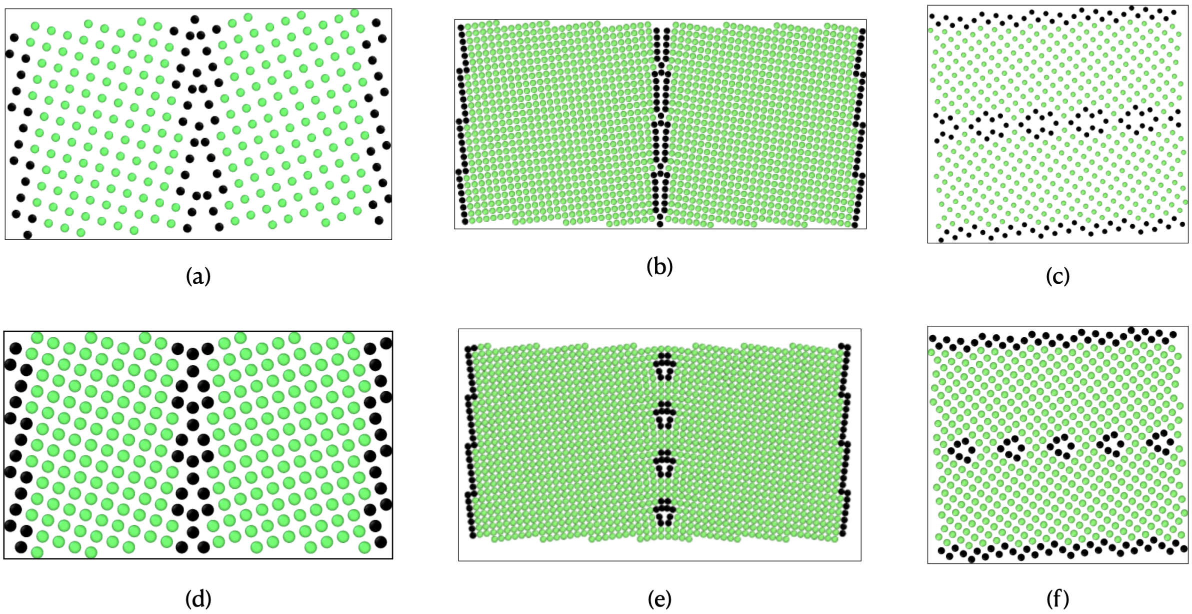
(a) (b) (c) (d) (e) (f)

Figure 46: Illustration of the atomic relaxation allowed by the Conjugate Gradient relaxation (a) $\Sigma5(3\bar{1}0)$, (b) $\Sigma25(7\bar{1}0)$, (c) $\Sigma25(3\bar{4}0)$ and after relaxation (d) $\Sigma5(3\bar{1}0)$ (e) $\Sigma25(7\bar{1}0)$ (f) $\Sigma25(3\bar{4}0)$.

configuration of grain boundary, we have measured the reduction in the excess volume by using equation 1.16. We compared the relaxed and unrelaxed grain boundary configuration. The table 3.1 shows the percentage of volume reduction following relaxation of the constructed grain boundary. It shows that the relaxation is followed by a significant reduction of the excess volume of the grain boundary.

Table 3.1: Reduction in excess volume following grain boundary relaxation for representative grain boundaries

hkl	$(3\bar{1}3)$	$(3\bar{1}0)$	$(1\bar{2}0)$	$(2\bar{3}0)$	$(5\bar{1}0)$	$(7\bar{1}0)$	$(3\bar{4}1)$	(001)	(001)
Σ	5	5	5	13	13	25	25	5	13
% of excess volume	8.2	7.2	7.5	5.5	7.2	7.4	9.9	4.3	4.1

Now we have demonstrated the impact of the microscopic dof on the atomic GB structure and on the resulting GB energy, we have discussed the GB energy of the most probable structure (e.g. lowest GB energy). For that we have selected the lowest energy configuration from a 2D energy map in figures 44 a) to d) as the most probable ground state of a grain boundary. In order to validate our procedure, we have compared our grain boundary energy measures from values reported in literature when available. Table 3.2 compares our data results from data points of Olmsted et al. (Olmsted et al., 2009a; Homer et al., 2013) obtained by using the same inter-atomic potential in FCC Ni. It is evident that our results are in a good agreement with existing data from the literature, which allows to validate our own tools and methodology to build and obtain the ground state of GB .

Table 3.2: Comparison between energy evaluations from Olmsted et.(Homer et al., 2013) and our results reported in mJ/m^2.

hkl	$(3\bar{1}0)$	$(1\bar{2}0)$	$(2\bar{3}0)$	$(5\bar{1}0)$	$(7\bar{1}0)$	$(3\bar{4}0)$	(001)	(001)
Σ	5	5	13	13	25	25	5	13
Olmsted et al.	1218	1285	1091	1201	1099	939	978	774
Our results	1195	1273	1098	1200	1087	946	997	769

Figure 47 shows energy of all selected most probable ground state configurations of grain boundaries of type a) Σ5, b) Σ13 and c) Σ25 mapped in their fundamental zone representation. Overall, energy of the most stable grain boundary configurations depends on orientation of a grain boundary plane. In all Σ families investigated, there is a rough common trend. The GB energy increases or decreases monotonically across the fundamental zone. Pure tilt and twist grain boundaries typically represent maximum and minimum GB energies, respectively. However, in all investigations carried out, we have found no clear correlation between grain boundary energy and Σ value. The same goes for the excess volume. Despite the rough correlation between grain boundary character and energy, the details of this correlation is complicated, and the link with Σ values is also unclear. This is in agreement with other large scale investigations on hundreds of GB (Olmsted et al., 2009c,b; Homer et al., 2014b, 2015), which justifies a posteriori the need of investigation like the present one, as the GB energy can only be apprehended from the atomic structure.

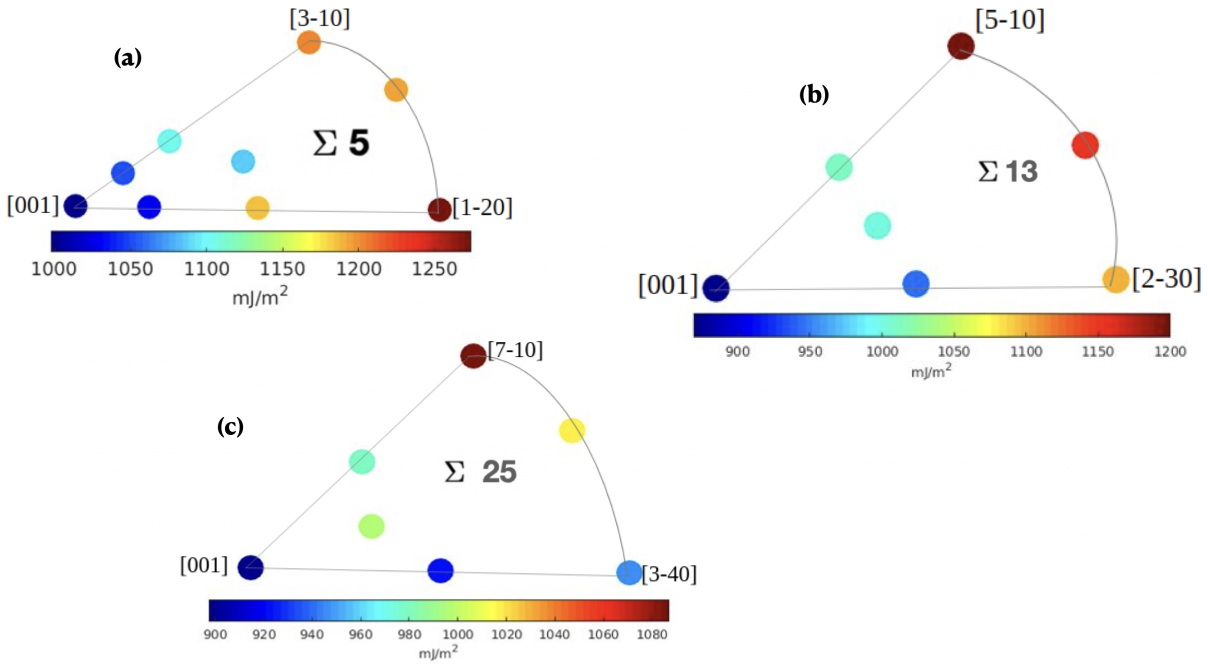

Figure 47: Energy of all investigated grain boundaries of type a) Σ5, b) Σ13 and c) Σ13, shown using the fundamental zone representation of their grain boundary normal.

3.2 Dynamic properties of grain boundaries

3.2.1 Migration velocity of grain boundaries

We have seen in section 1.3.2.2 that, regardless of the nature of driving force (P), velocity of a grain boundary is proportional (to the first order when activation energy is constant with Pressure) to the applied motive force. In addition, it strongly depends on temperature (T), type (Σ) and character (whether tilt, twist or mixed) of a grain boundary, thus, on nine degrees of freedom. Despite the fact that, the effect of motive force on migration of a grain boundary during thermo-mechanical processing of a metallic polycrstalline was recognised long ago, up to date there is no clear understanding of the evolution of a grain boundary in T-P parametric space. This is due, in part, to the fact that, in the past, most numerical studies have focused on finding general trends in grain boundary evolution for a fixed magnitude of motive force and varying temperature value and thus only partially explored the $P - T$ parametric space (Homer et al., 2014b, 2015).

The objective of the dynamic simulations that will be presented in what comes next is thus to fill this gap. For this, we investigated the migration of a large panel of GB in the large range of T-P parametric space, starting from ground state configurations of GB determined previously. For this, we did a systematic study of grain boundaries of type $\Sigma 5$, $\Sigma 13$, and $\Sigma 25$ as representative of other Σ grain boundaries. Some of these Σ(s) have been investigated in the literature, they cover very different GB structures from low to High Angle Grain Boundaries (LABG and HAGB), for example $\Sigma 5$ is a HAGB, and $\Sigma 25$ is LAGB. The character of GB was also varied. This systematic approach on very varied GB configurations will allow to capture clear and common mobility trends as function of the full P-T parametric space, these trends are expected to be found in other GB not considered here. In this section, we first report the raw measure of the migration velocity, then we classify the GB migration as function of the temperature dependence of the corresponding mobility. The GB migration velocity often exhibits different behaviour as function of the driving force applied. This was only partially understood in the existing literature, and may explain the complexity of migration behaviour observed until now for many GBs. As we systematically explore the P-T space, a phenomenological model can be proposed at the mesoscale and capture well the simulated GB migration behaviour. This mesoscale model will allow for a simple connection with larger scale simulations such as Phases Field simulations..

3.2.1.1 Extracting velocity of a grain boundary from raw atomistic data

In MD simulations, the GB migation reaches instantaneously a steady state velocity when the motive force is applied. Regardless of the value of the applied motive force and temperature, velocity is extracted as the derivative of the grain boundary displacement-time curve. Thus, velocity at a given constant temperature and driving force is a slope of the steady displacement-time curve at that temperature and motive force. Figure 48 shows displacement-time curves of $\Sigma 5(1\bar{2}2)$ mixed grain boundary as an example representative of others. It shows that temperature and magnitude of motive force applied can significantly affect the slope. Next, we will present the impact of temperature, dirving force and GB type on the observed GB migration behaviour.

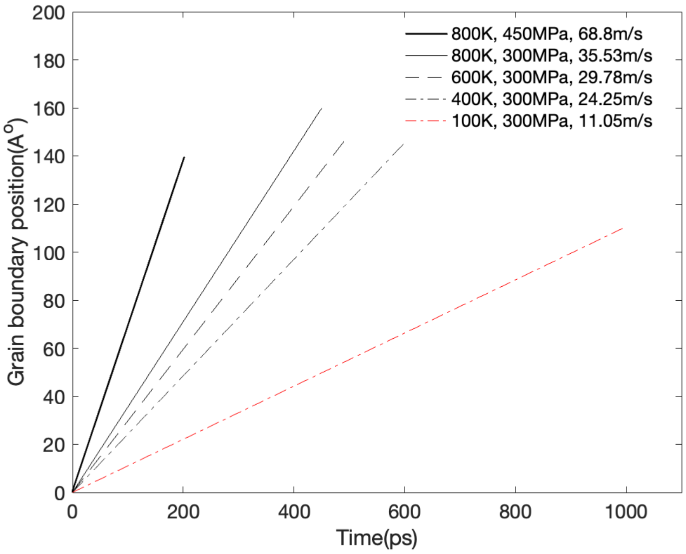

Figure 48: GB displacement versus time of $\Sigma 5(1\bar{2}2)$ at different temperatures and motive forces. The grain boundary velocity is slope of the curve.

3.2.1.2 Dependence of velocity on macroscopic degrees of freedom

The measured migration velocity varies wildly among Σ family, and as function of the grain boundary character. To show the extent of this variation, we plot grain boundary velocity in the stereographic projection of the grain boundary plane. Here, we show in figures 49 velocity at 600K with a driving force of 250MPa of all investigated grain boundaries in their respective fundamental zones. Figures 49 (a) to (c) show that grain boundaries of the same Σ family and character but with different misorientation angle, for example $\Sigma 5(1\bar{2}0)$ and $\Sigma 5(3\bar{1}0)$ have different velocity values.

Despite the fact that index values (Σ) of investigated grain boundaries are close, the difference in velocity can vary significantly. From figures 49 (a) to (c) we also notice that grain boundaries of low velocity ($< 35ms^{-1}$) are the most frequent. Overall, they are pure twist and mixed grain boundaries in any one fundamental zone. The same trend is observed for other temperature and driving force explored in this study. However, there is no clear correlation between velocity and the boundary's five macroscopic degrees of

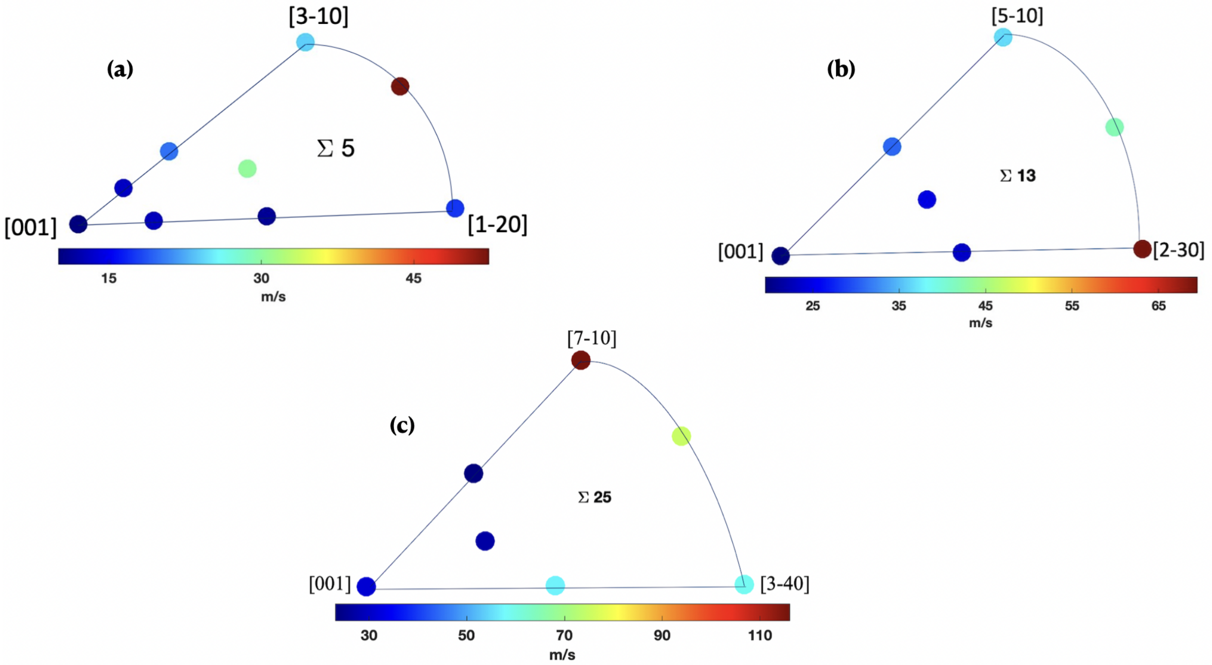

Figure 49: Velocity of investigated grain boundaries of type (a) $\Sigma5$, (b) $\Sigma13$ and (c) $\Sigma25$ at 600K with a driving force of 250MPa. Data points are presented in colour coding, from deep blue (low velocity) to deep red (high velocity).

freedom observed. It is also evident, by comparing figures 47 (a) to (c) with figures 49 (a) to (c), that velocity does not correlate with the grain boundary energy in the grain boundary plane fundamental zone. Indeed, the same observation was reported in literature (Olmsted et al., 2009c,b; Homer et al., 2015). The lack of a clear correlation between velocity, five macroscopic degrees of freedom, and energy highlights the fact that the atomic structure control mostly the static and dynamic properties of GB.

3.2.1.3 Dependence of grain boundary velocity on temperature

The applied temperature may impact differently the migration velocity of GB. This is why, the migration mobility dependence upon temperature is seen, as a convenient scheme of classifying the migration behaviour of investigated grain boundaries. Regardless of the magnitude value of applied motive force, all post-processed data were qualitatively classified into four main groups. The first group contains **Thermally activated grain boundaries**. These are grain boundaries with a velocity that increases with increasing temperature for the same applied motive force. Grain boundaries that behaved in this fashion account for ≈ 78.2% of all investigated grain boundaries. They are shown in a red colour in figure 50 (a) to (c). The second group contains **athermally activated grain boundaries**: In this group, the velocity remains insensitive to temperature change. In all grain boundaries investigated, only $\Sigma5(3\bar{1}3)$ mixed grain boundary behaved in this way. It is shown in figure 50 (a) with a black colour. The third group contains **antithermal**

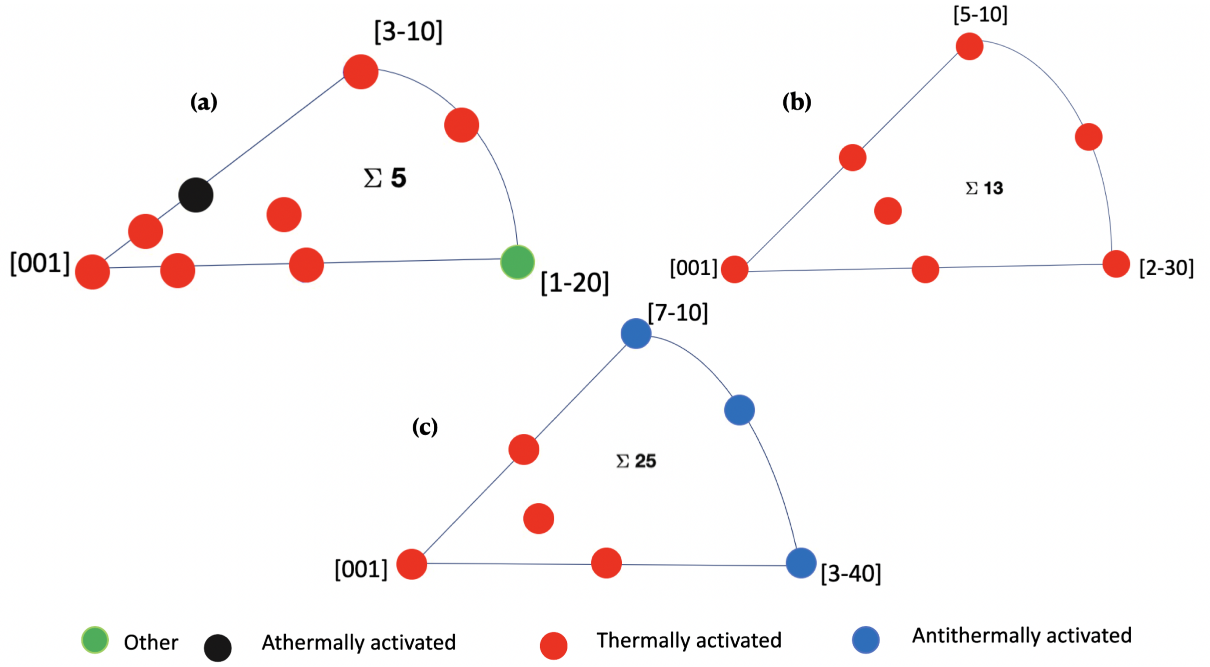

Figure 50: The dependence of migration velocity on temperature of all investigated grain boundaries of type (a) Σ5, (b) Σ13 and (c) Σ25.

grain boundaries. It comprises grain boundaries with velocities that decrease with increasing temperature. All pure tilt grain boundaries belonging to Σ25, counting 13% of all studied grain boundaries, behaved in this fashion. They are marked by a blue colour in figure 50 (c). The last group contains grain boundaries denoted **others**. This group contains one exceptional grain boundary $\Sigma5(1\bar{2}0)$. $\Sigma5(1\bar{2}0)$ behaved in a fashion that could not be classified in any previous general trends for the whole range of motive force and temperature. At lower temperature, it is thermally activated whereas it is antithermally activated at higher temperature. It is shown in green colour in figure 50 (a).

3.2.1.4 Dependence of grain boundary velocity on magnitude of driving force

In this study, we have observed that the dependence of velocity of a grain boundary on magnitude of applied motive force varies from one grain boundary to another. Regardless of the applied temperature, all investigated grain boundaries are classified into three groups. The first group which counts for 82.6% of all investigated grain boundaries contains grain boundaries whose velocity dependence on magnitude of applied motive force is exponential for the entire range of motive force explored. The second group contains grain boundaries which exhibit both exponential and linear regimes. This group contains 8.7% of all investigated grain boundaries. An exponential regime occurs at lower driving forces whereas a linear regime manifests itself at higher motive forces. The last group contains the rest of grain boundaries. These are grain boundaries whose velocity dependence on magnitude of applied motive force remained linear in the T-P parametric space explored

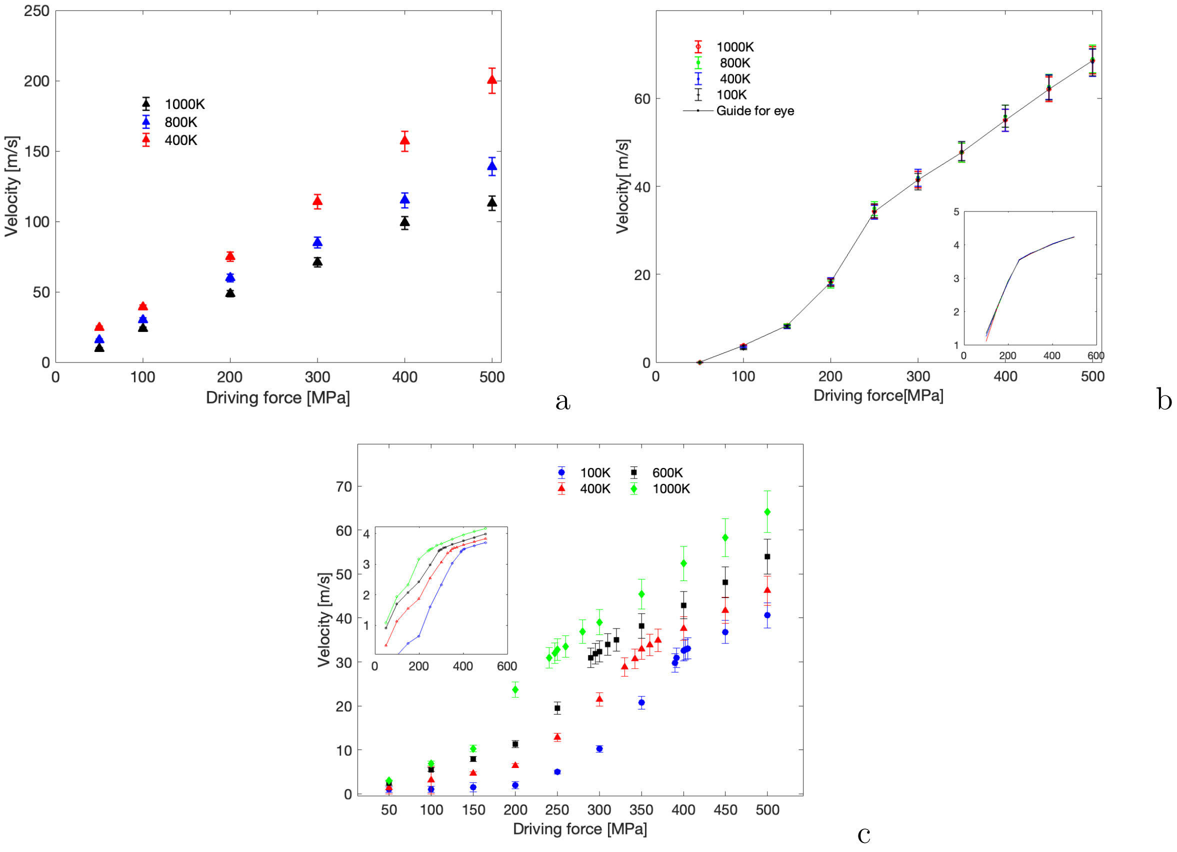

Figure 51: Velocity versus motive force of a) symmetric tilt $\Sigma25(7\bar{1}0)$ b) mixed $\Sigma5(3\bar{1}3)$ and c) pure twist $\Sigma5(001)$ grain boundaries at different temperatures. The insets to figure b) and c) shows the same data points on a semi-logarithmic scale for a better identification of the transition. We have used error bars to show an estimate of standard deviation in the measured velocity.

here. This group contains all antithermally activated grain boundaries reported in the previous section.

Figure 51 a) shows curves of velocity versus applied motive force for $\Sigma25(7\bar{1}0)$. It is clear that the velocity remains linearly proportional to applied driving force for the entire T-P range. On contrary, figures 51 b) and c) show the same physical quantities for other GB but we can visually identify both regimes. Initially, an exponential relationship at lower driving forces followed by a linear relationship at higher motive forces. To facilitate identification of this dynamic transition, the same data points in figure 51 b) and 51c) are plotted, in a semi-logarithmic scale, in the insets to figures 51 b) and 51 c) respectively. From a mathematical point of view, this transition is due to the change in local derivative of velocity function of motive force. For that, the transition stresses and velocities mark the starting point at which the velocity function changes from exponential to linear. It is not surprising that the transition stress and velocity depend on the grain boundary atomic structure considering the role played by macroscopic and microscopic degrees of

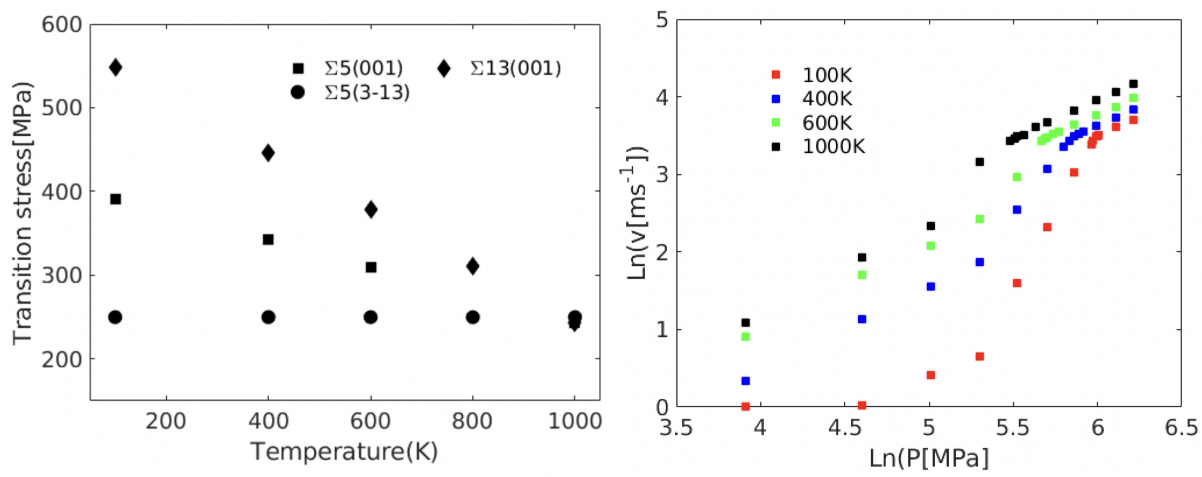

(a) **(b)**

Figure 52: (a)Transition stress against temperature for mixed $\Sigma5(3\bar{1}3)$, pure twist $\Sigma5$ and $\Sigma13$ grain boundaries.(b)The log log scale of velocity of $\Sigma5(001)$ pure twist against applied stress at various temperatures.

liberty of a grain boundary in the static and dynamic properties explained before. As an example, this transition stress is insensitive to temperature change for $\Sigma5(3\bar{1}3)$ whereas it decreases linearly with increasing temperature for $\Sigma5$ and $\Sigma13$ as figure 52 (a) shows. In contrast, the transition velocity increases with increasing temperature for thermally activated grain boundaries. By doing linear fitting on data points from all investigated grain boundaries, we have realised that this transition stress (P^*) follows a linear equation in which α_γ and α_{γ_o} are constants for a single grain boundary.

$$P^*(T) = -\alpha_\gamma T + \alpha_{\gamma_o} \tag{3.1}$$

Although, the lack of linear correlation between velocity and applied stresses contrasts with the generally assumed linear relationship at the low driving force limit, on the other hand, the effect of temperature is apparent, at least, for the thermally activated grain boundaries. As temperature increases exponential regime of thermally activate grain boundaries straightens up as figure 52 (b) shows. This might imply that at temperature high enough beyond the range investigated, the dependence of velocity on stress of thermally activated grain boundaries might possibly become linear for the entire stress range investigated. To facilitate the visualisation of this, data points in figure 51 (c) are represented in a log-log scale in figure 52 (b). Overall, pure tilt grain boundaries exhibited a longer exponential regime compared from other grain boundary characters. However, the origin of exponential regime observed for athermally activated grain boundary will be explained later. It is very important to note that the range of driving force explored [50-500 MPa] is very reasonable here, corresponding to what dislocations could generate when accumulating on a GB.

Identification of these kinetic regimes allowed developing robust and generic migration laws for predicting velocity as function of motive force and temperature. These functions are highly needed because up to date there is no model that can capture the dependence of velocity on motive force and temperature for the entire T-P parametric space. Having a single model in place can tremendously reduce the cost associated with atomistic calculations. In addition, these laws can serve as input in a continuum scale model of microstructure evolution which requires atomistic details of a grain boundary as it will be explained in part II of this PhD manuscript. Surprisingly enough, we will see in the following that the migration law can even help to rationalise the origin of the transition observed. In what follows, we will propose migration laws based on the details from the explored T-P parametric space. For the sake of clarity and simplicity, we will start with grain boundaries whose velocity-motive force curves manifest both regimes in the range of temperature and motive force investigated.

3.3 Migration laws to predict grain boundary velocity

3.3.1 Devising phenomenological migration laws

Referring to experimental studies (Gottstein and Shvindlerman, 2009b) and by recalling from section 1.3.3, m in the exponential regime can be described by Arrhenius relation that follows

$$m = \frac{A}{P*}\exp(-\frac{\Delta G(P,T)}{k_B T}) \tag{3.2}$$

in which $\Delta G(P,T)$ is given in equation 1.29. Our data suggest that the $\Delta H(P,T)$ in equation 1.29 may be reduced provided some mechanical work by P. To account for this effect, we reemploy the phenomenological empirical relation of Kocks, Argon and Ashby (Kocks et al., 1975), which was intially derived to model the actvation energy associated to double kink formation on screw dislocations in bcc metals. It reads:

$$\Delta H = \Delta H_o \left[1 - \left(\frac{P}{P*}\right)^p\right]^q \tag{3.3}$$

For ΔH_o standing for the activation enthalpy at zero effective stress and p, q are parameters such that $0 < p \leq 1$ and $1 \leq q \leq 2$ (Kocks et al., 1975). Of course, this is based on the assumption that, migration of a dislocation is controlled by a single migration mechanism for example the double kink formation in BCC metals. Here we can readily see than ΔH takes into account the mechanical work applied to the system. The work of Spitzig (Spitzig and Keh, 1970) has later shown that ΔS is negligible compared from ΔH. Consequently, ΔS can be discarded from equation 1.29 ($\Delta G \approx \Delta H$). This phenomenological function (ΔH) has been successfully used in several studies on dislocations (Tang et al., 1998; Rodney and Proville, 2009; Naamane et al., 2010; Gilbert et al., 2011; Queyreau et al., 2011). This has been an inspiring idea to our model. At atomistic scale and qualitatively speaking, a grain boundary may be seen as a periodic array of dislocations (Frank, 1950a; Read, 1953; Bollman, 1972; Sutton, 1995), for instance, figure 53 shows periodic arrangement of dislocations in $\Sigma 13(2\bar{3}0)$ symmetric tilt grain boundary. Besides, some GB migrated through the nucleation and propagation of disconnections, that need to overcome an energy barrier. Thus, the same function can be used for grain boundaries with the presumption that the overall properties is the summation of property of one dislocation over the n dislocations existing in a simulation box. In what follows, we explain concisely how we have determined the values of parameters appearing in this equation.

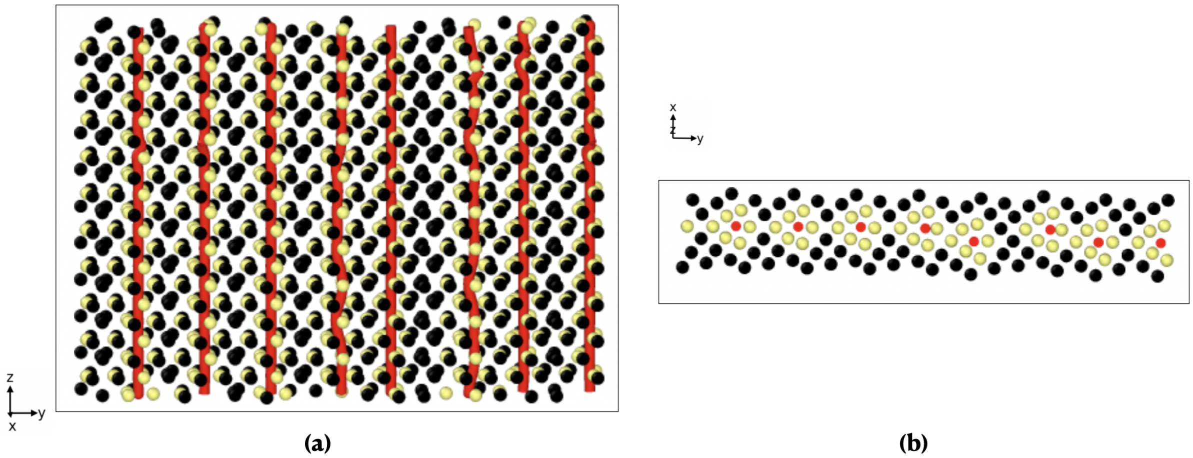

(a) (b)

Figure 53: Periodic arrays of dislocations in a disconnected $\Sigma 13(2\bar{3}0)$ STGB. Dislocations are shown in red and the triangles that are shifted towards are certainly associated to disconnections as shown in b). Here atoms belonging to the defect are shown in pale yellow and the atoms in perfect FCC positions are shown by a black colour.

3.3.1.1 Determining parameters in law of migration

To determine p and q, we have performed a global least squares fit to the raw data points of ΔH calculated from Molecular Dynamics simulations. ΔH_o was regarded as ΔH at zero effective stress for each temperature. Interestingly, we obtained almost similar values of $p \approx 0.5$ and $q \approx 1.5$ for all grain boundaries. ΔH_o can take a wide range of values for the set of GB considered. Grain boundaries with Athermal mobility exhibit lower values. ΔH_o, like ΔH and ΔG, depends on temperature as well. The relationship between ΔH_o and temperature was observed here to be linear and follows equation

$$\Delta H_o(T) = \alpha_H T + \alpha_{H_o} \tag{3.4}$$

in which α_H and α_{H_o} are constants for a given GB. This expression emphasises that thermal energy is important as well as mechanical energy in facilitating a grain boundary to overcome the energy barrier. Furthermore, it depends as well on macroscopic degrees of freedom as figure 54(a) shows. In all investigated grain boundaries, we observed no clear correlation between ΔH_o and grain boundary character. In other respects, the prefactor A is dependent on macroscopic degrees of freedom as figure 54 (b) shows. We can readily see that pure tilt grain boundaries have roughly higher values compared from the rest. However, the prefactor A is insensitive to temperature as figure 55(c) shows. Overall, activation enthalpy ΔH and ΔH_o increase with increasing temperature. Increasing magnitude of motive force decreases the activation enthalpy ΔH until the transition stress P^* is reached where it drops to zero. Figures 55(a) and (b) shows a comparison between estimated and raw MD data of ΔH for $\Sigma5$ pure twist and mixed $\Sigma13(5\bar{1}3)$ respectively. It is evident that estimated ΔH agrees well with ΔH from MD data. The apparent difference between $\Sigma5(001)$ and $\Sigma13(5\bar{1}3)$ is that the applied motive force is far less than the motive

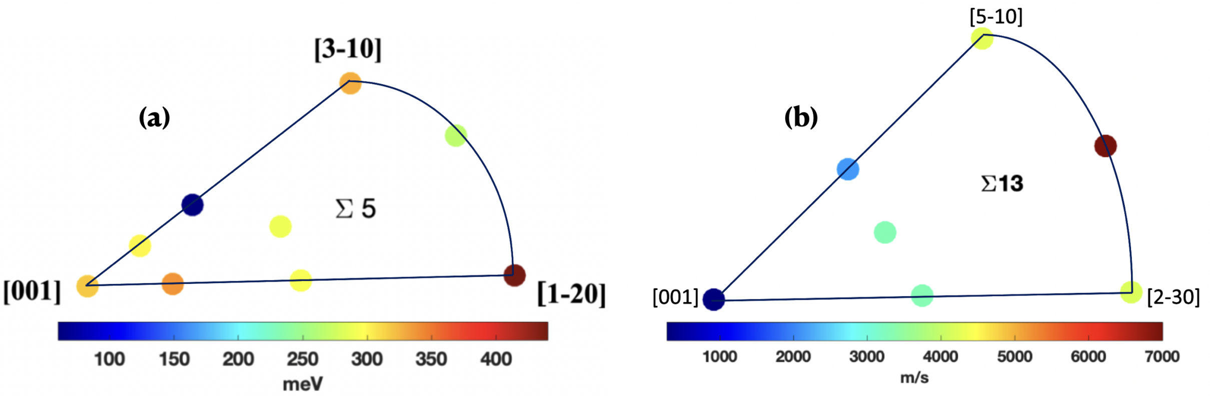

Figure 54: The dependence of (a) ΔH_o of $\Sigma5$ type grain boundaries at 1000K and (b) A prefactor of $\Sigma13$ on macroscopic degrees of freedom of a grain boundary.

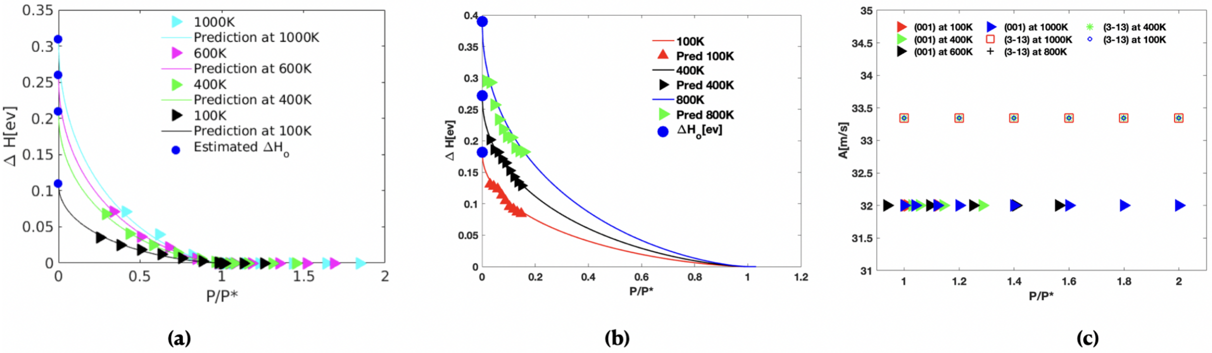

Figure 55: Comparison between MD and predicted enthalpy of activation (ΔH) of (a) $\Sigma5$ pure twist and (b) mixed $\Sigma13(5\bar{1}3)$ grain boundaries at different temperatures.(c) Plot of the value of constant A versus the normalised stress for $\Sigma5(001)$ pure twist and $\Sigma5(3\bar{1}3)$ mixed grain boundary at different temperatures.

stress required by $\Sigma13(5\bar{1}3)$ to undergo a dynamic transition. Again, from Figures 55 (a) and (b), it is clear that past P^*, the Arrhenius type relationship between mobility and motive force loses its validity, hence this linear regime could be fitted by a linear equation of the type equation 3.5.

$$v_p(P,T) = A\left(\frac{P}{P*}\right)^k \tag{3.5}$$

Where k is a constant which does not depend on temperature nor on magnitude of applied driving force. To check the suitability of this linear equation we have fitted equation 3.5 on linear data set past P^*. Indeed, $k \approx 1$ was confirmed, consequently, $v_p(T, P)$ in linear regime can be estimated by

$$v_p(P,T) = \frac{AP}{P*} \tag{3.6}$$

Now, the general closed-form velocity function of stress and temperature that results from combining the final equations from both exponential and linear regimes reads

$$v_p(P,T) = \begin{cases} \frac{AP}{P*}\exp\left(-\frac{\Delta H_o}{k_B T}\left[1-\left(\frac{P}{P*}\right)^p\right]^q\right), & \text{if } P < P^* \\ \frac{AP}{P*}, & \text{if } P \geq P^* \end{cases}$$

As we can notice from this equation, it is evident that the prefactor $\frac{A}{P*}$ is indubitably important in this equations and it could be linked to the atomic structure of a grain boundary. To investigate this, the prefactor is plotted in the FZ to see if there are some noticeable trends in its dependence on macroscopic degrees of freedom. Figure 56) shows the dependence on macroscopic degrees of freedom for grain boundaries of type $\Sigma5$ and $\Sigma13$. It is evident that in both fundamental zones, grain boundaries of character tilt boundaries have roughly higher values compared to the rest. On the other hand, for antithermal grain boundaries, we have taken advantage of the linearity between velocity

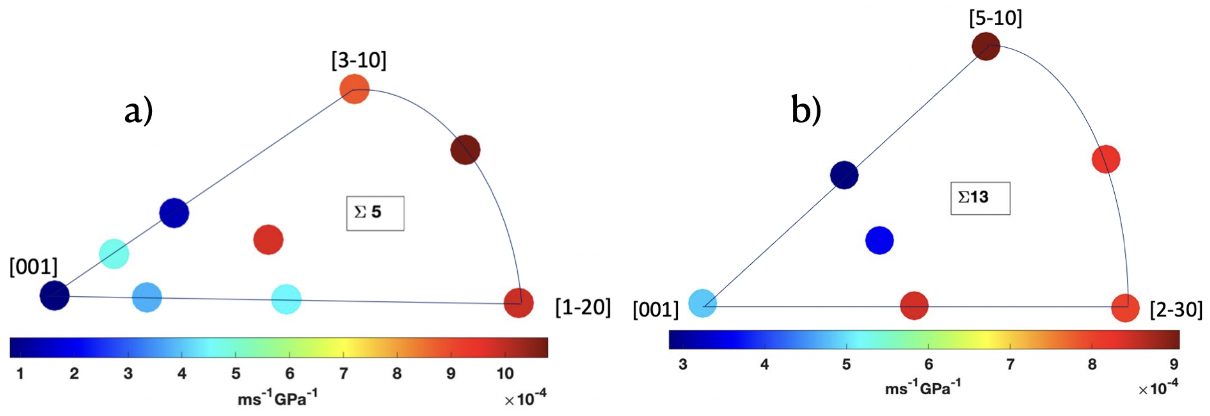

Figure 56: The dependence of the prefactor $\frac{A}{P*}$ on macroscopic degrees of freedom at 0K a)$\Sigma5$ and b)$\Sigma13$.

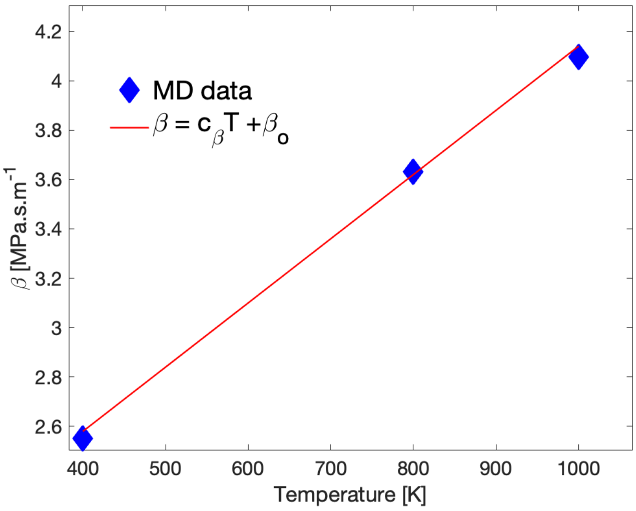

Figure 57: β against temperature for pure tilt $\Sigma 25(7\bar{1}0)$ grain boundary.

and motive force. We have fitted a linear equation 3.7 to MD velocity data points for all temperatures and motive force. β^{-1} is a constant that might depend on grain boundary.

$$v_p(P,T) = \frac{P}{\beta} \tag{3.7}$$

Interestingly, β is a constant that linearly depends on temperature and it reads

$$\beta = c_\beta T + \beta_o \tag{3.8}$$

in which c_β and β_o are all constants. Figure 57 shows a good agreement between MD data points and the predictions of the slope (β) of symmetric $\Sigma 25(7\bar{1}0)$ tilt grain boundary. Table 3.3 summarises all parameters appearing in equations of dependence of transition stress P^* and enthalpy of activation at zero effective stress ΔH_o on temperature along with the values of other constants in the proposed phenomenological law for all investigated grain boundaries of type $\Sigma 5$ and $\Sigma 13$.

3.3.1.2 Comparison of MD raw data from model predictions

Figures 115(a) to (d) (see the appendix A.3) show comparison between MD and predicted velocity of thermally and athermally activated grain boundaries. Figure 115(a) shows plots of velocity of pure twist $\Sigma 5$ grain boundary against the applied motive forces. Figures 115(b) and (c) shows the same data plots for mixed $\Sigma 5(3\bar{1}3)$ and pure tilt $\Sigma 13(2\bar{3}0)$ grain boundaries. Figure 115 (d) shows plot of velocity of pure tilt $\Sigma 13(2\bar{3}0)$ grain boundary against the normalised applied motive force. The latter clearly show that the stress range considered in this study was far less than the stress required by velocity-motive force curve of this grain boundary to undergo transition from exponential to linear regime.

Table 3.3: All parameters involving in equations describing the transition stress and enthalpy of activation ΔH_o at zero effective stress along with the parameters involved in the closed-form velocity function of grain boundaries of type $\Sigma 5$, $\Sigma 13$ and $\Sigma 25$.

$\Sigma 5$					
Plane	$\frac{\alpha_H}{10^{-4}}$	$\frac{\alpha_{Ho}}{10^{-3}}$	α_γ	$\frac{\alpha_{\gamma o}}{10^3}$	$\frac{A}{10^2}$
(001)	2.0	117.4	0.17	0.4	0.32
$(1\bar{2}0)$	4.2	20.0	0.42	4.30	42.40
$(1\bar{2}1)$	2.5	43.5	2.70	6.52	29.20
$(1\bar{2}2)$	3.2	17.9	1.30	5.82	22.00
$(3\bar{1}0)$	3.0	27.3	1.17	5.04	44.30
$(3\bar{1}8)$	2.7	29.3	0.54	4.42	20.70
$(3\bar{1}3)$	0.6	0.00	0.00	0.25	0.34
$(4\bar{3}0)$	3.5	15.0	2.50	3.41	36.80
$(4\bar{3}3)$	2.1	80.0	0.150	2.40	23.40

$\Sigma 13$					
Plane	$\frac{\alpha_H}{10^{-4}}$	$\frac{\alpha_{Ho}}{10^{-2}}$	α_γ	$\frac{\alpha_{\gamma o}}{10^3}$	$\frac{A}{10^2}$
(001)	20	13.3	0.34	0.58	2.80
$(2\bar{3}0)$	2.0	34.3	0.7	4.70	42.60
$(2\bar{3}3)$	2.0	33.5	1.2	7.50	21.20
$(5\bar{1}0)$	3.0	27.2	1.8	5.23	41.90
$(5\bar{1}3)$	3.0	15.4	0.3	3.44	33.20
$(7\bar{4}0)$	2.9	15.1	2.5	8.50	70.00
$(7\bar{4}6)$	3.0	18.4	4.5	9.30	33.20

$\Sigma 25$							
Plane	$\frac{\alpha_H}{10^{-4}}$	$\frac{\alpha_{Ho}}{10^{-3}}$	α_γ	$\frac{\alpha_{\gamma o}}{10^3}$	$\frac{A}{10^3}$	$\frac{c_\beta}{10^{-3}}$	β_o
$(3\bar{4}0)$						9	0.52
$(3\bar{4}1)$	1	39.6	0.5	4.40	2.1		
$(7\bar{1}1)$	3	29.6	0.8	7	2.5		
$(2\bar{1}0)$						7	0.45
$(7\bar{1}0)$						2.6	1.54
$(10\bar{5}2)$	2	39.8	0.5	4.4	2.1		
(001)	2.7	18.3	0.63	0.188	0.7		

From all figures, we readily see that the proposed model is an excellent agreement with the MD data. Figure 116, in appendix A.3 shows comparison between MD and predicted velocity for $\Sigma 25(7\bar{1}0)$ representative of other antithermal grain boundaries at different temperatures and motive forces. For a better comparison, we have calculated the relative error which is given by

$$error = \left| \frac{V_p - V_{MD}}{V_p} \right| \tag{3.9}$$

It is clear that the predicted and MD velocities are in a good agreement since the error remains less that 0.01. It must be emphasized that the various parameters of the model were not directly fitted from the velocity-P curves but rather from postreatement of these curves leading to measures of the activation energy, transition stress and exponential prefactor...

3.3.1.3 Reliability of the proposed functions

In this section, we discuss the suitability of proposed functions. The inspiration for this work is the phenomenological function to estimate ΔH that has been widely used for dislocations (Gilbert et al., 2011; Naamane et al., 2010; Queyreau et al., 2011; Rodney

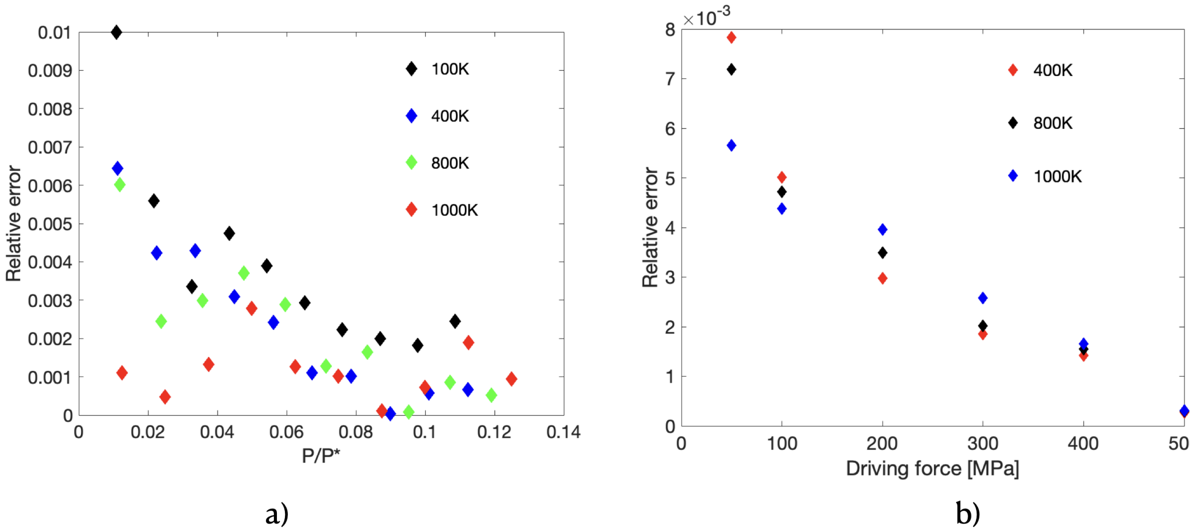

Figure 58: Relative error a)$\Sigma 13(2\bar{3}0)$ b)$\Sigma 25(7\bar{1}0)$

and Proville, 2009; Tang et al., 1998). From a kinematic point of view like the one from Bilby, we can describe any GB as dislocation arrays (see example in figures 53 and 62), hence the same functions can be used for grain boundary considering that total amount of any kinematic quantity is a summation over the number of dislocations present in a simulation cell (Priester, 2012) model on low angle grain boundaries for the case of grain boundary energy.

The ΔH_o is regarded as the total free energy for a grain boundary to move without the aid of external work. This may again justify why it is lower for athermally than that of thermally activated grain boundaries. In agreement with Race (Race et al., 2014), as driving force increases, less enthalpy of activation (ΔH) is required for a grain boundary to move.

The choice of P^* as normalising stress is justified since it is a limiting stress past which the applied mechanical work is sufficient enough for all grain boundary atoms to overcome energy barrier. For instance, in our simulations we have realised that as the ratio $\frac{P}{P*}$ increases, the number of nucleation sites for disconnections for thermally activated grain boundaries increases as well. This is reasonable, since the pre-exponential factor usually accounts for the nucleation site density.

As a consequence, if $\frac{P}{P*} \geq 1$, the grain boundary moves as a whole. On the other hand, the effect of thermal energy is evident. As temperature increases P^* decreases. This is reasonable since energy barrier decreases with increasing temperature, thus requiring lower stress to be overcome. Overall, the estimated values of p and q were within the range reported in theoretical work of Kocks, Argon and Ashby Kocks et al. (1975). With regards to linear regime, the choice of fitting function is physically justified since for $P \geq \Delta G$ the velocity is proportional to applied driving force (Lacasta et al., 2005; Costantini and Marchesoni, 1999).

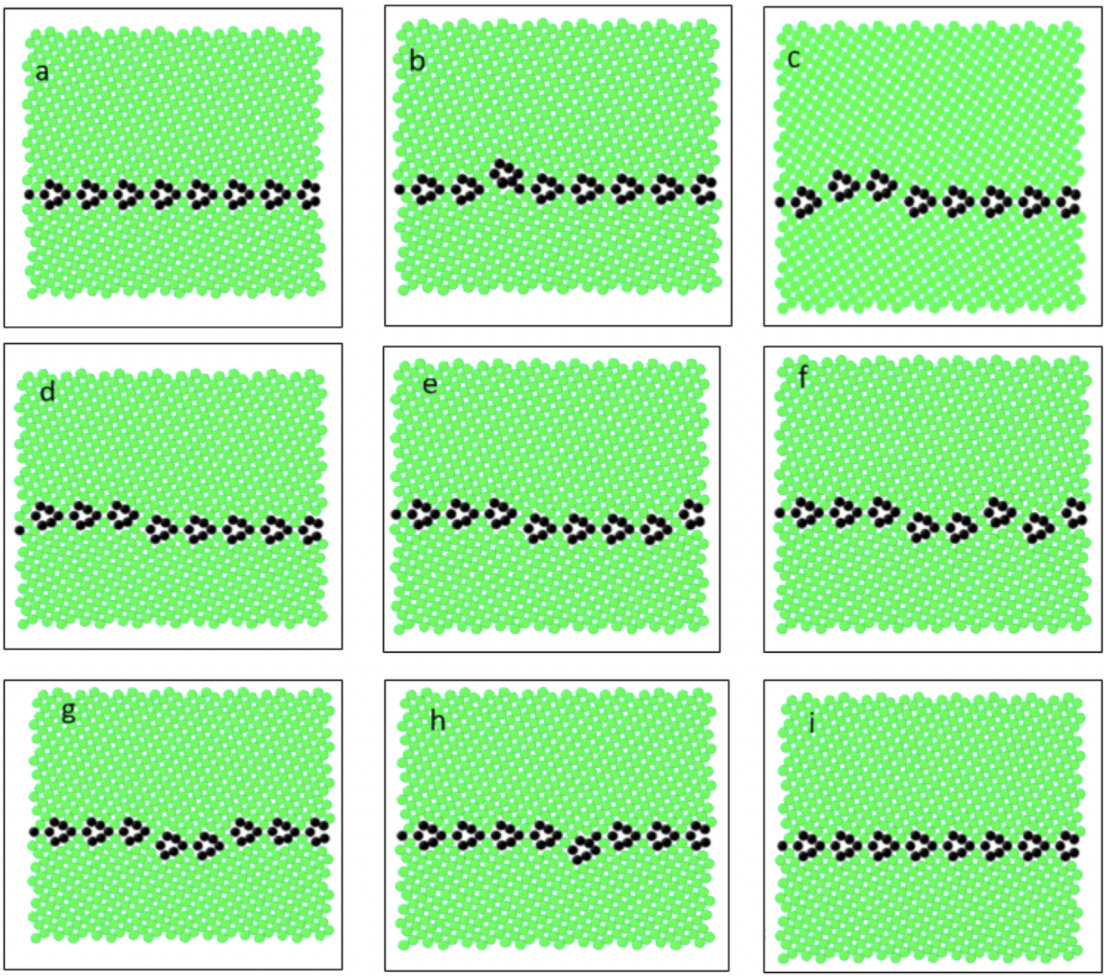

Figure 59: a) Initial relaxed structure of $\Sigma 13(2\bar{3}0)$ tilt grain boundary, its migration is mediated by b) nucleation and c) to i) propagation of disconnection. Atoms are coloured by CNA where green atoms are in perfect FCC positions and black atoms belong to the defect.

3.4 Migration mechanism

Categorising adequately migration trends in grain boundary creates the hope of finding a clear correlation with the underlying elementary mechanisms. For that, we have studied grain boundary migration mechanisms by analysing their atomic structure as they move. In general, grain boundary displacement is mediated by the deformation and either rotation or translation of its structural units. As a result, it moves by jumping from one most energetically stable structural unit to another. This explains once again why it is very important to start with the most probable ground state of a grain boundary. Interestingly, the duration of such jumps depends on temperature and magnitude value of applied driving force. The migration mechanism of grain boundary strongly depends on its atomic structure.

3.4.1 Nucleation and propagation of disconnections

For some grain boundaries, the motion is not always planar over a large area. In many cases, a critical area of the grain boundary disconnects, goes ahead and propagates. Here we give two examples, from pure tilt $\Sigma 13(2\bar{3}0)$ (figure 59) and pure twist (figure 60) grain boundaries.

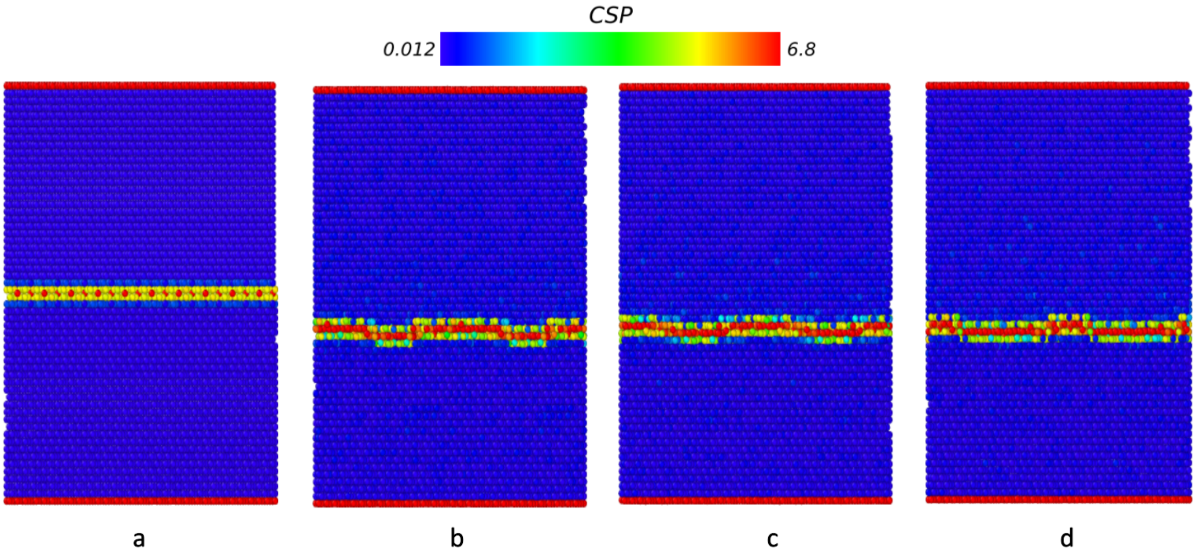

Figure 60: Pure twist $\Sigma 5$ in which atoms are coloured by centro-symmetric Parameter (CSP). Blue atoms are in perfect FCC positions and the rest belongs to the defect. The migration of this type of grain boundary is mediated by nucleation and propagation of disconnections. Figures show a) initial structure of this grain boundary b) nucleation of opposite disconnections c) and d) propagation of disconnections. mediated by nucleation and propagation of disconnections.

The nucleation of a disconnection is caused by a local atomic shuffling (see section 3.4.1.1). The later causes a relatively small-in plane atomic displacements which is accommodated by either transformation or translation of structural unit depending on the atomic structure of a grain boundary. Once all structural units undergo this transformation, the propagating disconnections span the simulation box within the GB plane. A grain boundary makes a step forward. In our study, 82.6%, mostly Σ5 and Σ13, of all investigated grain boundaries move by nucleation and propagation of disconnections.

3.4.1.1 Localised atomic shuffle

A careful examination of our simulations allowed to identify several distinct types of atomic motions that occur during the migration of a grain boundary. Here we have only focused on pure twist grain boundaries to study atomic shuffling mechanism. The main reason is until now it is still challenging to separate shear displacement from localised atomic shuffle. As we will see in section 3.4.3 pure twist grain boundaries do not undergo a shear coupled migration. Consequently they are right candidates for this study. In all investigated grain boundaries, we have observed two groups of atomic shuffle. The first group containing Σ5. As figure 61 (a) shows the displacements shown by a dotted black arrows are motion between coincidence site lattices. The displacements shown by red arrows are primarily in the plane perpendicular to the normal of a grain boundary for pure twist grain boundaries. The displacement shown by green arrows occurs in direction perpendicular to the grain boundary plane. Consequently, they are geometrically necessary component of grain boundary motion. This displacement is the one at origin of transformation of the local structural unit described previously. This displacement is

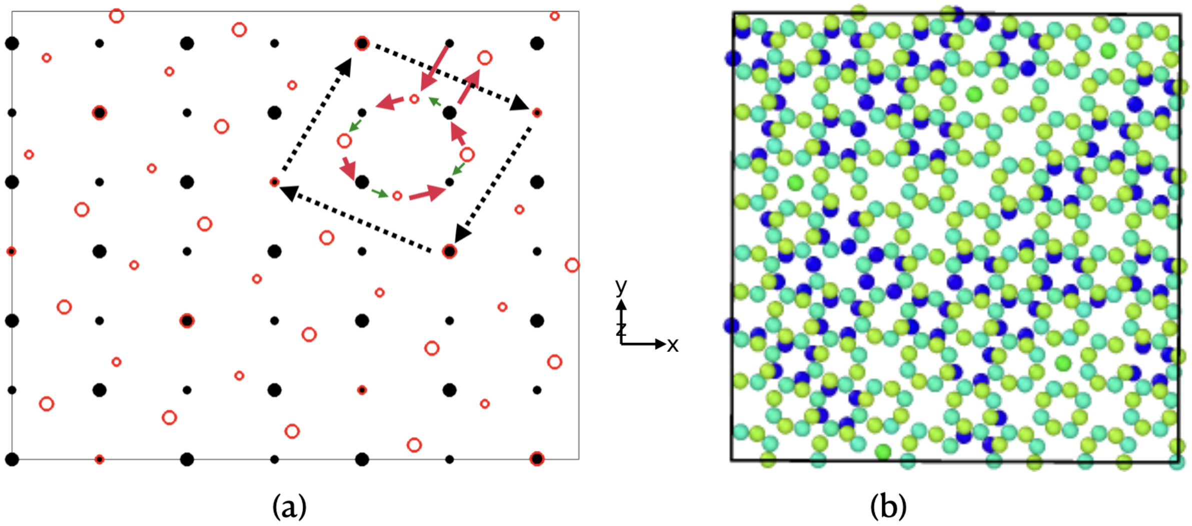

Figure 61: (a) The possible atomic jump path for Σ5 type grain boundary. The two grains (in black and red) are superimposed (in dichromatic complex). The smaller and bigger dots correspond to lower and upper atomic layer in the atomic stacking respectively. (b) A simultaneous motion of 4 atoms shown in blue colour in Σ5 pure twist grain boundary at 10ps of simulation at 100K for a motive force of 200MPa.

highly cooperative. For Σ5, this displacement involves simultaneous motion of four atoms as figure 61(b) in the direction along the normal of a grain boundary. The motion of these four atoms is a geometrically necessary component of the grain boundary motion and it is at origin of localised transformation of the local structural units of a grain boundary. The second group contains Σ13 and Σ25. For these grain boundaries no 4 atomic shuffling motion was observed instead the jumps are of mostly single atoms. On the other hand, as dynamics properties of grain boundary depend strongly on macroscopic degrees of freedom of a grain boundary, we can only consider atomic structure of a grain boundary to explain the difference observed here. Σ5 has higher symmetry compared from Σ13 and Σ25. This is due to the fact that, it is one of the lowest possible CSL with misorientation axis [001] that can be obtained in FCC materials. This symmetry allows it to have a relatively simple atomic shuffle along the displacement shift complete lattice compared with its counterparts. Since this subject is beyond the scope of this work, we did not go into more details but for more details see the textbook of Sutton and Balluffi (Sutton, 1996). These mechanisms may be investigated in the future.

3.4.2 Dislocation gliding

For some grain boundaries, the translation of structural units during migration occurs simultaneously in all grain boundary structural units. In our simulations, we have observed two groups. The first group contains all antithermal grain boundaries. These grain boundaries are made of equidistant arrays of dislocations as figure 62 shows. These dislocations simultaneously glide and this is the origin of a simultaneous transformation of all structural units said before. The grain boundary surface remains flat during grain boundary migration since the local distribution of grain boundary dislocations remains unaffected by grain boundary migration. In other words, the crystal misorientation associated with the boundary accompany the moving grain boundary. Although, a grain boundary moves forwards, the migration was observed to be associated with a macroscopic shape change accommodated by shearing (see section 3.4.3 for details). Here we give two examples of Σ25(3$\bar{4}$0) in figures 63 a) to c) and Σ25(7$\bar{1}$0) in figures 64 a) to c) in which the shape

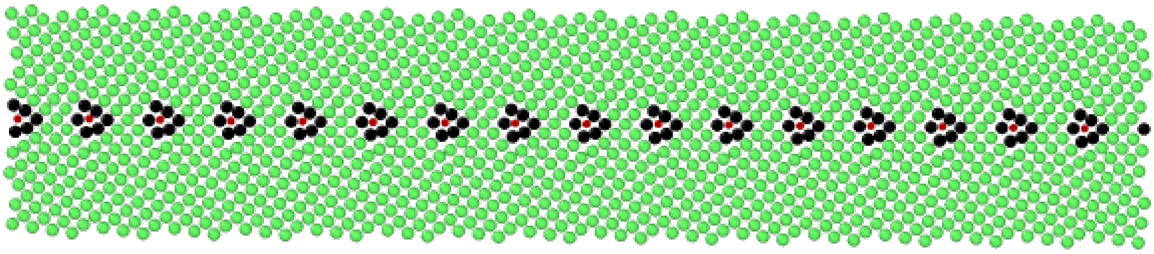

Figure 62: Equidistant dislocations in Σ25(3$\bar{4}$0) shown in red colour. Atoms in perfect FCC position are shown in green and atoms belonging to the defect in black colour.

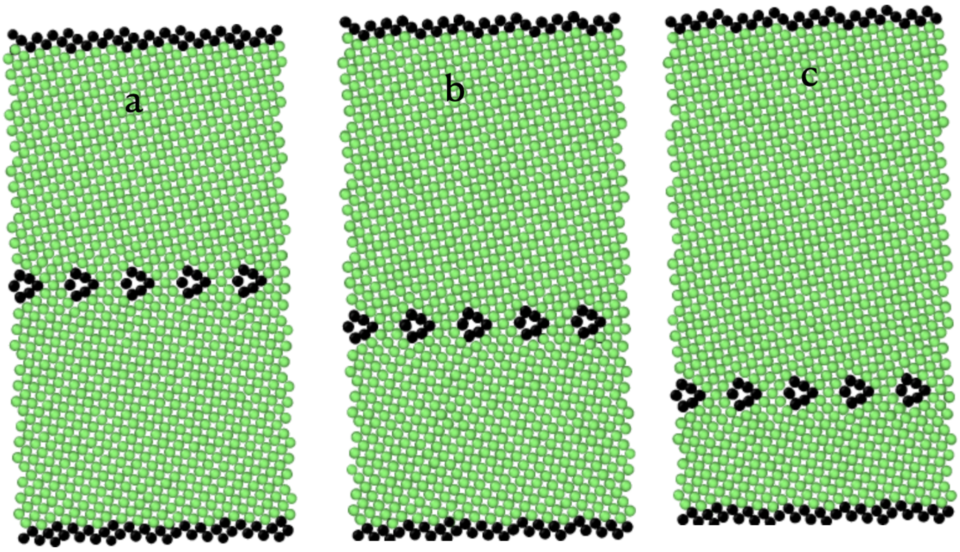

Figure 63: Dislocation gliding in $\Sigma 25(3\bar{4}0)$ at 100K for 150MPa. Atoms in perfect FCC positions are in green and black colours for atoms identified a belonging to a defect.

change was observed to be controlled by the correlated atomic displacement throughout the simulation box.

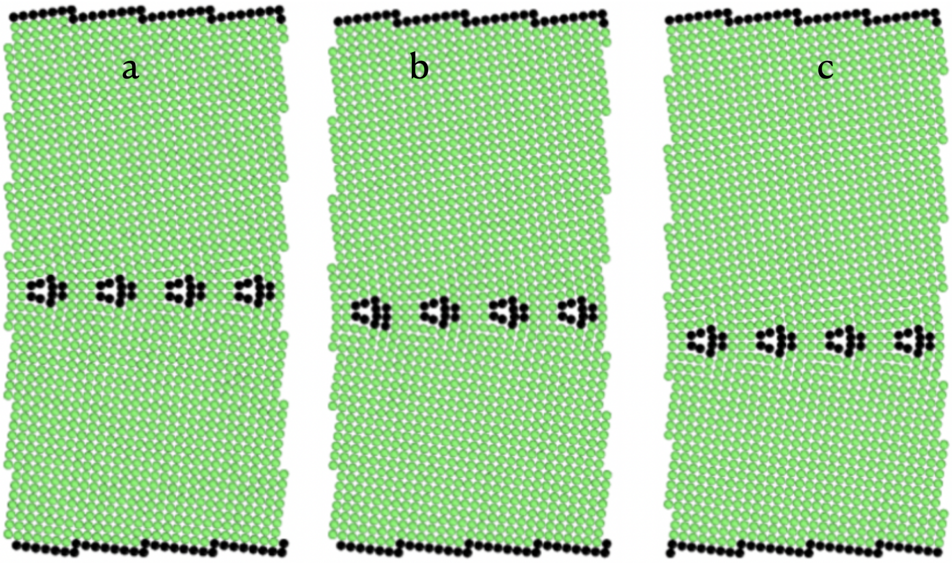

Figure 64: Dislocation gliding in $\Sigma 25(7\bar{1}0)$ at 100K for 200MPa. Atoms in perfect FCC positions are in green and black colour for atoms belonging to a defect.

The second group contains athermal $\Sigma 5(3\bar{1}3)$ grain boundary. This grain boundary is arguably special as we believe that defects -disconnections- are already existing on its surface from the beginning. The same grain boundary is shown in figures 65a) to d) which show propagation of the disconnections. In these figures, atoms are coloured by the Centro-Symmetric parameter (CSP) with dark blue atoms corresponding to the atoms in perfect FCC positions and the differently coloured atoms belongs to the grain boundary. The configuration 65a that corresponds to the initial configuration shows that

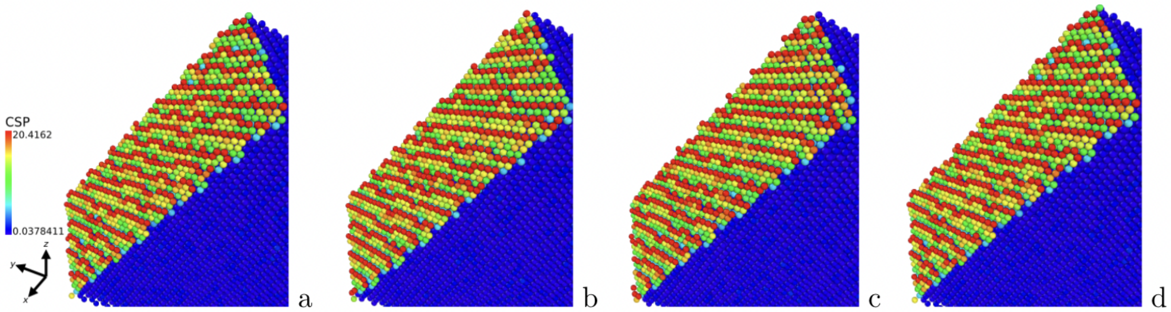

Figure 65: Migration of $\Sigma5(3\bar{1}3)$ mixed GB at 200MPa for 400K. Atoms are coloured by the centro-symmetry parameter(CSP, atoms in perfect FCC positions are shown in blue and the rest belongs to the defect a) shows the grain boundary containing disconnections before migration b) and c) during propagation of disconnections d) across the entire periodic box.

disconnections are already in the GB surface before propagation. The applied driving force serves to propagate the existing disconnections across the entire periodic box as shown in figures 65b and 65c) to reach a next stable configurations in figure 65d by making a complete step forward. Consequently, this grain boundary requires thermal or mechanical energy to activate and propagate these existing disconnections (figures 65 b to d) rather than nucleating and propagating new disconnections which is common for other grain boundaries whose evolution is mediated by motion of disconnections. Once disconnections have propagated across the entire periodic box a grain boundary copes with by making a step forward. Due to these existing multiple disconnections, this grain boundary moves almost as a whole.

3.4.3 Shear coupled grain boundary migration

Particularly for all pure tilt grain boundaries (39% of studied grain boundaries), the change in grain boundary surface and the jump from one structural unit to another in the normal direction of a boundary plane are associated with a relative in-plane translation of the shrinking crystal. Figures 66 a) to f) show shear coupled migration of $\Sigma5(1\bar{2}0)$ symmetric tilt grain boundaries at 100 K and 400 MPa which is representative of all other shear coupled grain boundaries. On contrary, no such shear coupling migration was observed for mixed and pure twist grain boundaries. This may be due to the atomic structure of the GB or to BC. For instance, for pure twist grain boundaries, atomic layers above and below a grain boundary are identical. Figure 67 shows atomic structure of $\Sigma5$ pure twist. Green atoms are in a perfect FCC position and the black atoms belong to a defect. It is clear that the atomic layer in green above a grain boundary is similar to the one below a grain boundary. This is reasonable since, (001) is a mirror plane of the DSC. Consequently, applying motive force in any direction is not expected to lead to grain boundary shearing. As figures 67 shows the grain boundary displacement in opposite

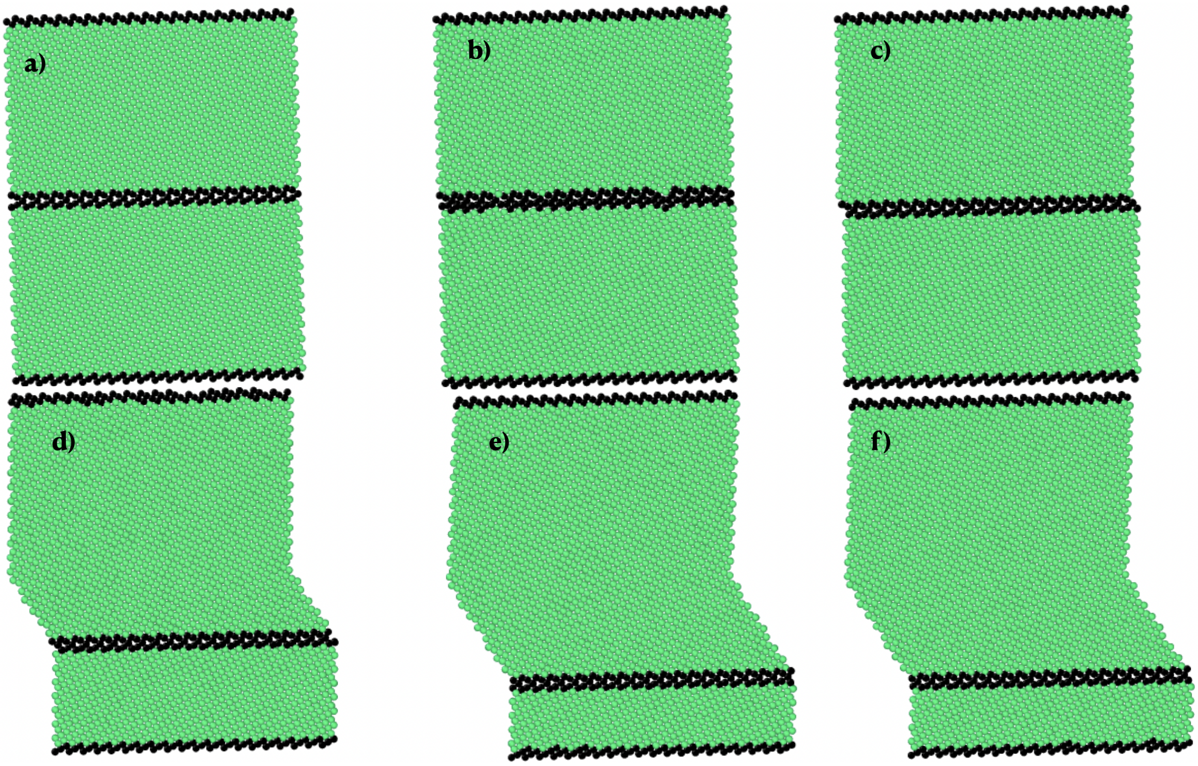

Figure 66: Mechanical response of $\Sigma5(1\bar{2}0)$ to applied driving force of 400MPa at 100K. Atoms in green are in perfect FCC position and black atoms belong to the defect a) before applying motive force b) during migration, showing rearrangement of the atomic configuration in plane of the GB accommodated by a relatively smaller in plane translation of growing grain. c) when all structural units have undergone this transformation, a grain boundary copes with by making one step forward d) to f) show the effect of the shear-coupled migration as the grain boundary advances.

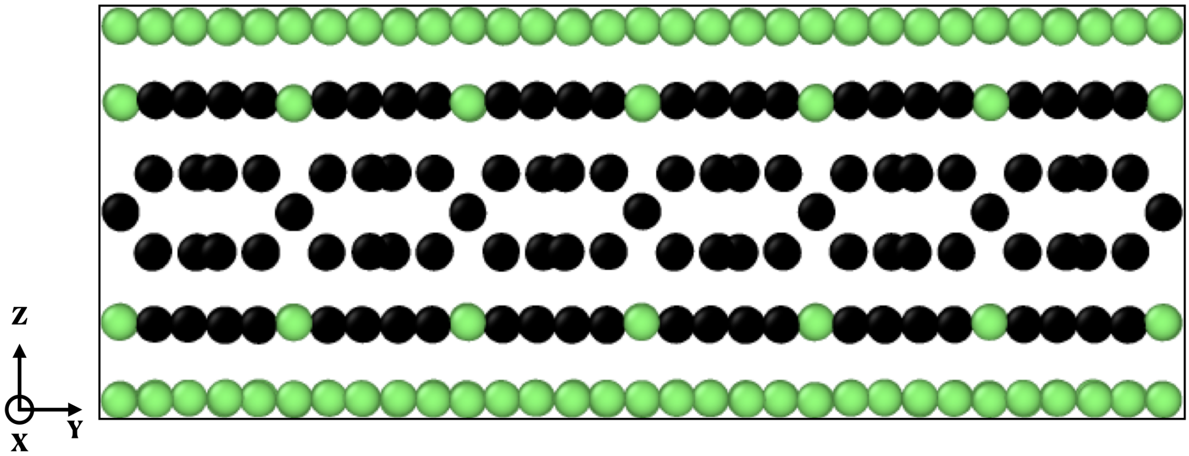

Figure 67: The atomic structure of $\Sigma5$ pure twist grain boundary. Atoms in perfect positions are shown by green colour and black atoms belong to the defect.

directions is totally equivalent. From figure 45 b), it is clear that for any applied motive force, the average lateral position of a grain boundary will not evolve with time since atoms will shift by DSC vector within grain boundary plane. This results from the fact that the shear elastic energy is relaxed by sliding of both grains abutting a grain boundary.

3.5 Characterisation and identification of defects on surface of a grain boundary

As we have seen in the previous sections, Thermodynamics and kinetics of a grain boundary may vary wildy among GB. This could be due to the difference in properties of either constituent lower dimension defects, specifically, dislocations or nucleated defects during migration. A clear understanding and categorising of these defects can allow to rationalise the difference in grain boundary energy and migration mechanisms observed in the previous sections. For instance, dislocations condition energy and interactions of grain boundary with dislocation emerging from the bulk of the crystal whereas nucleated disconnections and their propagation controls evolution of a microstructure. Therefore, obtaining the spatial distribution of defects on a surface a grain boundary can improve modelling of grain boundaries at both higher and lower scales. In particular in the present PhD work, being able to describe GB in terms of dislocation distributions may be very usefull to connect with mesoscale PF simulations II. In this section, we will first investigate the atomic structure of a stationary relaxed grain boundary and then the atomic structure of a moving grain boundary. As the phase field model is a 2D model, we will only investigate pure tilt grain boundaries which are simple enough for building two dimensional simulation cells.

In crystalline materials, characterisation of defects on the surface of grain boundary is based on constructing the Burgers circuit around a grain boundary following the methodology of Hirth and Pond (Hirth et al., 2007). A resulting closure failure is the Burgers vector of a crystalline defect (Frank, 1951; Stukowski and Albe, 2010; Hirth et al., 2007; Stukowski et al., 2012). There is a dislocation extraction algorithm (DXA) (Stukowski et al., 2012) already implemented in OVITO which analyses dislocations in crystals. However, this module does not allow the analysis of grain boundaries other than those where the dislocations are significantly distant. For grain boundaries with closer dislocations, we have developed our own tool referring to DXA for inspiration (OMAR, 2019).

This tool starts first by building the list of neighbour atoms to each atom contained in the simulation box. By using the cut off radius, we limited ourselves to 12 neighbors for an FCC materials. In the second step, we used the list of neighbors to separate atoms belonging to the core of defect from atoms in perfect FCC positions. Here the criterion is that, an atom belongs to a perfect position if and only if it has 12 neighbors otherwise it belongs to a defect. To identify these two categories of atoms, we have used the Common Neighbor Analysis algorithm already (Honeycutt and Andersen, 1987) implemented within OVITO (Stukowski, 2009). After identifying the defect, a circuit is constructed by surrounding the defect. To optimise the search of optimum path, we have used the commonly known A* algorithm (Hart et al., 1968). Figure 68 a) shows an example of a circuit constructed around a dislocations. Finally, the obtained Circuit is redrawn on the reference configuration as figure 68 b) shows. As we can see from 68 a) the Burgers circuit is composed of a set of vectors $\overrightarrow{\Delta x}$ such that $\sum \overrightarrow{\Delta x} \approx 0$ for the closed atom to atom path. If we map vector $\overrightarrow{\Delta x}$ to a vector $\overrightarrow{\Delta X}$ in the perfect crystal 68 b), the true Burgers can be calculated as

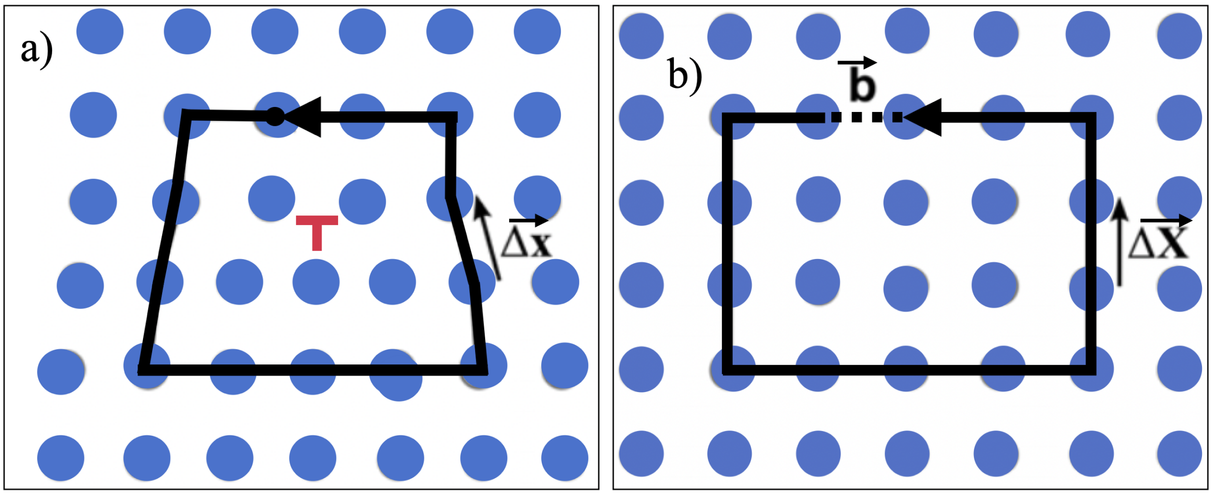

Figure 68: The Burgers circuit in a discrete domain a) containing a dislocation (shown in a red colour) b) perfect crystal.

$$\overrightarrow{b} = \sum \overrightarrow{\Delta x} \tag{3.10}$$

3.5.1 Structure of relaxed grain boundaries

Although structural units of a grain boundary might become compressed or expanded (Han et al., 2017b) due to atomic relaxation process, surprisingly enough, the determination of Burgers vector of these dislocations is not affected by relaxations. To validate our model, we have compared obtained Burgers vectors with the prediction of Frank-Bilby equation that returns the Burgers vector of dislocations to realise the compatibility at grain boundary (Priester, 2012).

$$\overrightarrow{b}_i = (I - R^{-1})\overrightarrow{k} \tag{3.11}$$

Where $\overrightarrow{b}_i$ is the Burgers vector content of defects crossed by the probing vector $\overrightarrow{k}$ and R is a deformation matrix that converts grain one into grain two. Consequently, $\overrightarrow{k}$ must satisfy the equation of grain boundary plane. Some relaxed grain boundaries were shown as examples in figure 46. They show the characteristic structural unit of grain boundaries. The properties investigated for simple grain boundaries studied here are grouped in Table 3.4 which provides information on Burgers vector $\overrightarrow{b}$ and the line vector $\overrightarrow{l}$ of extrinsic dislocations.

Σ	$\overrightarrow{n}$	$\overrightarrow{b}$	$\overrightarrow{k}$	$\overrightarrow{l}$
5	(120)	$\frac{a}{2}[110]$	$\frac{a}{4}[2\bar{1}0]$	[001]
5	(130)	$\frac{a}{2}[110]$	$\frac{a}{4}[3\bar{1}0]$	[001]
13	(150)	$\frac{a}{2}[110]$	$\frac{a}{4}[5\bar{1}0]$	[001]
13	(230)	$\frac{a}{2}[110]$	$\frac{a}{8}[3\bar{2}0]$	[001]
25	(430)	$\frac{a}{2}[110]$	$\frac{a}{11}[3\bar{4}0]$	[001]
25	(170)	$a[100]$	$\frac{-a}{4}[\overline{17}0]$	[001]

Table 3.4: Characterisation of relaxed symmetric tilt grain boundaries.

3.5.2 Structure of a moving grain boundary

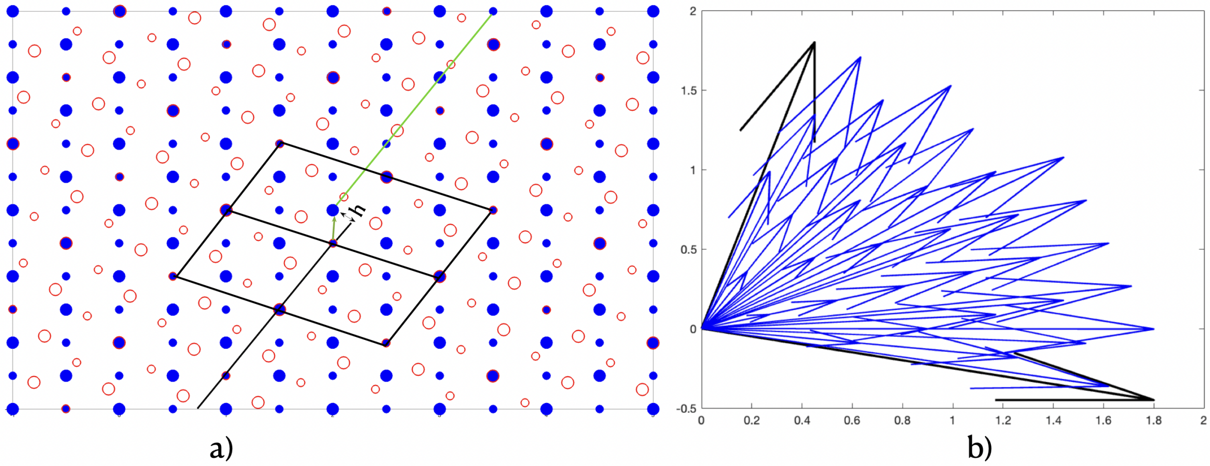

Figure 69: Identification of a structural defect for $\Sigma 5(1\bar{2}0)$ symmetric tilt grain boundary a) a disconnection of height h shown by a green line b)shows the possible DSC vectors.

According to Bollmann (Bollmann, 1967), the vector connecting the lattice points of the DSC lattice is equal to the closure failure vector due to existence of a climbed intrinsic dislocations. The latter is Burgers vectors always obtained by comparing the Burgers circuit in reference and defective configurations (Read, 1953) as illustrated in the previous sections. The same procedure as before was used to determine the Burgers vector ($\overrightarrow{b}_{dsc}$) of these dislocations. The only difference is that, since we are dealing with the DSC vectors, we have used the dichromatic complex as the reference configuration.
Figure 69 a) shows a dichromatic complex for $\Sigma 5(1\bar{2}0)$ as representative for all other grain boundaries investigated. The open circles correspond to atoms of grain one and the blue filled circles correspond to atoms of grain two. The smaller cycles and bigger circles

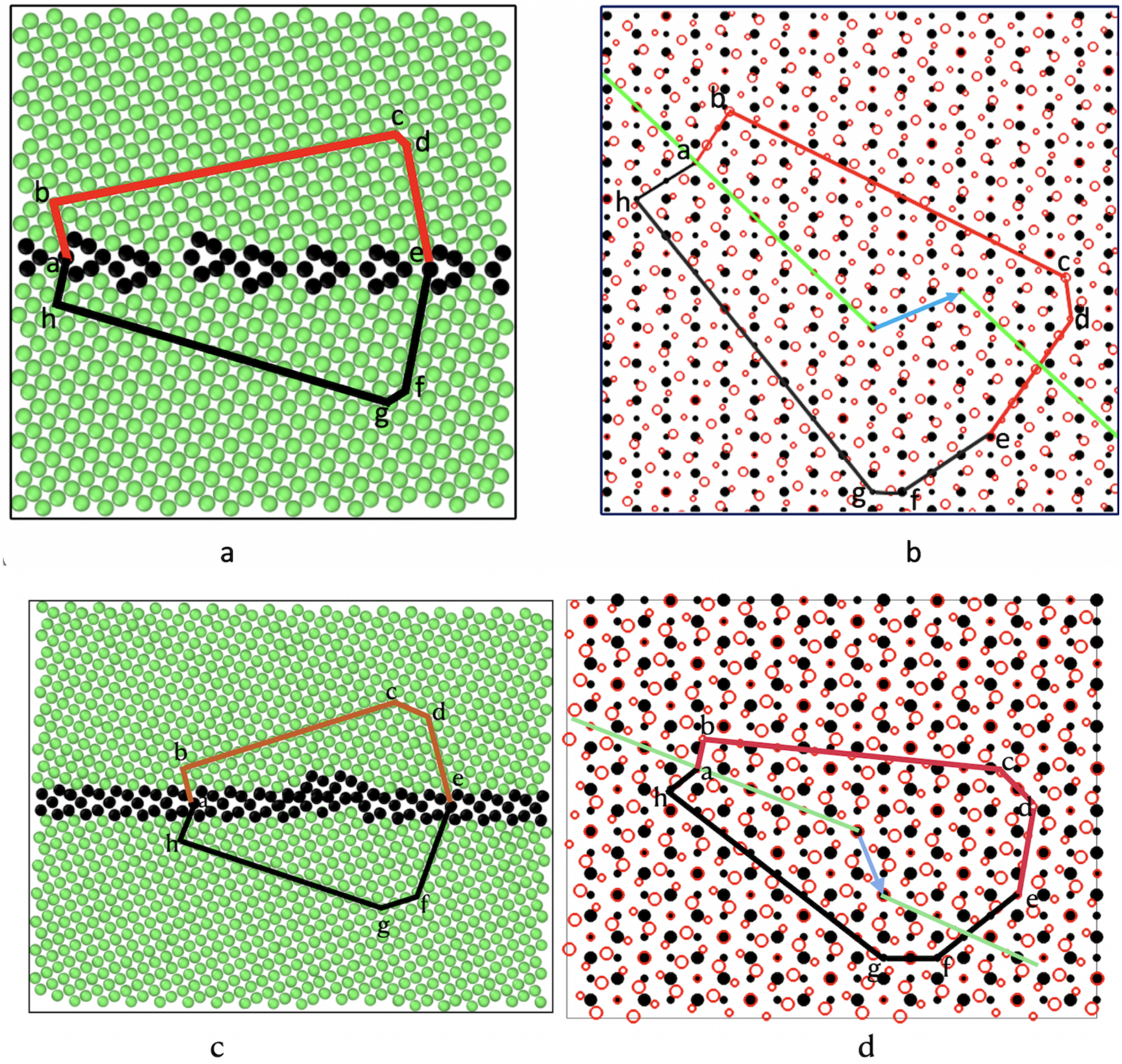

Figure 70: Burgers circuit around a disconnection in a) $\Sigma 13(2\bar{3}0)$ and c) $\Sigma 5(1\bar{2}0)$ symmetric tilt grain boundary with misorientation axis [001] b) and c) illustrate the same grain boundaries in a dichromatic complex in which red atoms belong to grain one and black atoms belong to grain two. The smaller and larger circles belong to A and B stacking layers in FCC Nickel. The green line shows location of a grain boundary and the pale blue arrow is a vector connecting two coincidence sites.

correspond to layer A and layer B of atomic stacking in FCC materials. The green colour line shows the next position of a section of a grain boundary that disconnects with a height (h) from initial position of a grain boundary shown by a long black line. Figure 69 b) shows all possible disconnection ($\overrightarrow{b}_{dsc}$) vectors for $\Sigma 5(1\bar{2}0)$. To demonstrate our procedure, we give two examples, $\Sigma 5(1\bar{2}0)$ and $\Sigma 13(2\bar{3}0)$ symmetric tilt grain boundaries in figure 70 as representative of other grain boundaries. As figures 70 a to d show, we constructed our circuit starting from point a by surrounding disconnections to reconnect the circuit to the same starting point a. The height (h) of a disconnection is calculated as:

$$h = \overrightarrow{b}_{dsc}.\overrightarrow{n} \tag{3.12}$$

Where $\overrightarrow{n}$ is the normal of a grain boundary plane (Hirth et al., 2007). Table 3.5 gives Burgers vector and step height of disconnections of $\Sigma 5$ and $\Sigma 13$ grain boundaries. As the height of disconnection operating during GB migration may appear explicitly in the exponential prefactor of the mobility function, these data are valuable for future investigation.

Table 3.5: Identification and characterisation of disconnection on surface of a moving grain boundary.

Σ	$\overrightarrow{n}$	$\overrightarrow{b}_{dsc}$	h $[A°]$
5	(210)	$\frac{a_o}{5}[120]$	2.8
5	(310)	$\frac{a_o}{10}[130]$	2.1
13	(510)	$\frac{a_o}{13}[150]$	2.7
13	(320)	$\frac{a_o}{13}[230]$	3.2

Part II

Continuum scale

The first part of the manuscript showed that atomistic methods allow an accurate and efficient study of grain boundaries by capturing atomistic details in the five dimensions of a GB orientation parametric space. However, atomistic methods are limited in both time and length scales. This constrasts with macroscopic methods that can capture the complexity of microstructure evolution at the scale of polycrystals. In the literature there exist many of such methods, for example discrete disclination based models (Taupin et al., 2015; Sun et al., 2016), which profit the kinematic equivalency between equidistant arrays of dislocations and dipoles of disclinations to investigate grain boundaries, the vertex method (Piękoś et al., 2007) that tracks grain boundary as a sharp front and Phase Field method (Warren et al., 2003). The latter technique is formulated based on a set of field variables that are assumed to be continuous accross the interface regions (Elder and Grant, 2004; Elder et al., 2002) and they are used to model microstructure evolution.

The main challenge of macroscopic methods is to capture multiple phenomena concurrently occurring during microstructure evolution and preserve at the same time most of the physics observed in atomistics. Available macroscopic methods capture either evolution of microstructure or deformation but not both at the same time (Raabe, 2002; Steinbach and Pezzolla, 1999; Krill Iii and Chen, 2002; Kobayashi et al., 2000, 1998). There exist, in literature, some reformulations which are based on coupling models that capture grain growth with models that capture crystal plasticity (Raabe and Becker, 2000; Takaki et al., 2008; Bernacki et al., 2011; Abrivard et al., 2012b,a; Popova et al., 2015; Li et al., 2016; Zhao et al., 2016; Zhou et al., 2017). The working principle of these coupled methods is that dislocation density is updated by models that capture crystal plasticity and it is passed to the models that capture grain boundary evolution. Then, the dislocation density is used in a penalty function to steer grain boundary evolution to areas with high accumulated plastic strain. Consequently, the deformation is only due to bulk crystal plasticity and grain boundary motion does not contribute to macroscopic deformation which renders these model unable to capture shear induced grain boundary migration.

We will now mostly focus upon Phase Field approach. Recently Ask et al. (Ask et al., 2018) and Admal and Marian (Admal et al., 2018) proposed Phase Field models where the coupling between plastic mechanisms and GB mechanisms is more organic . The Admal and Marian's model, will be the main focus of the present manuscript. This model derives from coupling the Kobayashi Warren Carter PF model, which describes only crystal growth, to more conventional crystal plasticity to account for plastic activities that take place during grain boundary evolution (Kobayashi et al., 2000, 1998). The central idea of this model is to regard the transformation processes that transform grain one into grain two as a conventional plastic process induced by the Geometrical Necessary Dislocations (GND). This model is described in details in section 5.3.

While this model makes it possible to model concurrently grain growth and crystal plasticity, the comparison of this model to atomistic data for example has still to be performed, and the manner to make this model quantitative and predictive is still unclear. Therefore, a dialogue must be made between this PF model and atomistics to transfert the necessary physics to the larger scale. Connecting atomistics and mesoscale PF is challenging and few studies have attempted to connect both approaches in the past. For example, in (Hoyt et al., 2001) interface energies are extracted from atomistic molecular dynamics simulations and imported in a phase-field model, in (Denoual et al., 2010) to study martensitic transformation, in (Reina et al., 2014) to investigate grain boundary in Germanium, in (Bergmann et al., 2017) to study anisotropic solid–liquid interface kinetics in silicon and in (Bragard et al., 2002) for predicting the dendrite growth velocity function of under-cooling rate in pure Ni. Despite these efforts, there is still to date no generic physically-based model really capable of predicting microstructure evolution at polycrystalline length-scale in FCC materials.

The ultimate goal of this second part of my PhD manuscript is to provide a path on how to connect qualitatively and then quantitatively Admal and Marian's Phase Field Model to the atomistic data presented in previous part. It starts by recalling the classical phase field approach. Chapter 4 provides a review of the basic ingredients of phase field method in terms of energy and dynamics and the corresponding fundamental interpretation of the phase field dynamic equations along with their route origin from statistical mechanics. Chapter 5 introduces the KWC and the unified formalism of Admal and Marian's model, in addition, it gives examples of some of algorithms to solve phase field equations. Then, we will give our objectives and methodology. Finally, in chapter 6, we will propose a parametric study of Admal and Marian's Phase Field model to fully grasp, the features and capability of this model. Then, we will perform simulations of the GB stability and migration of symmetric tilt GB identical to the one considered in MD simulations. We will see that with its intial parametrization, the Model naturally captures some trends of the MD results like the GB energy or two of the migration behaviour observed in atomistics. Finally, to be able to quantitatively connect MD and a phase field, we will propose a fully analytical closed form solution of the 1D KWC model. This will be the cornerstone to future parametrization of the PF model allowing for an exact agreement between scales.

Chapter 4

Introduction to phase field method

A suitable computational model for investigating microstructure evolution at microscopic scale must be able to describe accurately the complexity of a real microstructure and be able to capture multiple mechanisms taking place during microstructure evolution. Such models must have solid foundations in physics. The relatively new modelling methods of phase field methods may fill these requirements. Phase-field methods describe a microstructure with a set of field variables which are assumed to be continuous across the grain boundary regions. These field parameters ϕ_i (for $i = 1, 2, ..., n$ where n is the number of grains in a microstructure) are introduced alongside the usual temperature field (T). Recalling that microstructures are developed during the process of solidification and thermo-mechanical processing. These processes are governed by phase transformation kinetics. For example nucleation of crystal grains is followed by a competitive growth of these grains under the drive to reduce the overall free energy of the system. Phase transformations can be categorised as first and second order transformations. The **first order transformation** is characterised by a non-continuous first order derivative of total free energy of the system (see section 4.2.4 for more details) with respect to a thermodynamic quantity (Langer, 1986; Fix, 1983). In addition, it is characterised by a release of latent heat. Examples of such transformation include solidification of liquids and condensation of vapour.

On the other hand, the **second order transformation** is characterised by a continuous first order derivative of the total free energy of the system with respect to thermodynamic quantity and it does not release the latent heat. The second derivative of the total free energy of the system is discontinuous. Such transformation are generally triggered by thermal fluctuation in the domain. Examples of such transformation include spinodal decomposition in metallic alloys, spontaneous ferromagnetic magnetisation of iron below the Curie temperature (Archer and Rauscher, 2004). Such thermal fluctuations can induce a spatial fluctuation in material ordering (in ϕ_i), for instance, it can induce grain boundary migration, therefore both fluctuations play a dominant role in modelling the evolution of thermodynamic quantities. We will see later in section 4.2 that since evolution of a thermodynamic quantity is driven by the minimisation of the total energy of the system, the total free energy of the system is expressed in terms of ϕ and T parameters in order to allow describing and quantifying any fluctuation in these quantities during evolution of the system.

4.1 Phase-field variable

In PF simulations dedicated to phase transformations, phases are described using the order parameter ϕ. The ϕ describes the change of symmetry from disordered to ordered phase as the transformation evolves. In order words, ϕ describes the degree of crystalinity in a simulation cell (Landau, 1980; Moelans et al., 2008). For example, to describe a polycrystal, ϕ is customary chosen to be one in a crystalline material region and $\phi \neq 1$ in a non crystalline material region such as grain boundaries. During phase transformation, the spatial variation of ϕ occurs on a very specific length scale. This correlation length sets the scale over which the order changes from one phase to another. For example κ is taken to be the thickness of interface during grain boundary migration. In practice, this correlation length is taken to be many times larger than the lattice constant of a material but small enough to describe the spatial variations characterising a particular pattern in a system.

In general, there are two types of field parameters (Binder, 1987). Order parameter that evolves with global conservation of a quantity is called **conserved order parameter**. The conserved order parameter describes a local composition of quantities such as concentration of a chemical species (Nigro, 2020). In contrast, **non conserved order parameters** do not evolve constrained to a conservation law. Here we can give an example of a grain boundary migration. The temporal evolution of the conserved and non conserved phase field variables follows different kinetics (see later 4.3).

In the real world, systems usual seek to achieve an equilibrium state by minimising their free energy. For a system modelled using a phase field method, a dissipative minimisation of free energy controls the evolution of dynamic equation of order parameters, heat and mass transfer which are usually expressed as partial differential equations. Phase field models are connected to thermodynamics via a phenomenological free energy functional which is usually expressed in terms of ϕ and other fields such as temperature, strain etc...

4.2 Free energy functional

In phase field, the phenomenological free energy functional of Ginzburg-Landau (equation 4.1) serves a starting point of the formulation for the modeling of microstructure evolution (Huang, 1987; Gurtin, 1996; Provatas and Elder, 2011).

$$F\left(\phi(x,t), T(x,t)\right) = \int_v \left[\frac{1}{2}|\alpha_o \nabla\phi(x,t)|^2 + f\left(\phi(x,t), T(x,t)\right)\right] dx \tag{4.1}$$

Where v is volume of a material under consideration, x is the spatial coordinates and α_o is the gradient coefficient which is connected with surface energy. $\phi(x,t)$ is a continuous function that describes the uniformity/non-uniformity of a material at each spatial coordinate x and temporal coordinate t. The spatial variation of $\phi(x,t)$ is often assumed to be small in order, this avoids introducing higher-order gradient terms in the $\phi(x,t)$ function because they are more computationally demanding. $f\left(\phi(x,t),T(x,t)\right)$ is regarded as a local free energy density (free energy per unit volume) also known as the bulk free energy density.

4.2.1 Approximating $f\left(\phi(x,t),T(x,t)\right)$

Following the Landau theory $f\left(\phi(x,t),T(x,t)\right)$ can be approximated (Landau, 1980; Provatas and Elder, 2011). By considering the fact that ϕ vanishes ($\phi \neq 1$) in the disordered state and that there is a phase transition in the vicinity of the critical point at which ϕ undergoes a small jump from $\phi \neq 1$ to $\phi = 1$, $f(T,\phi)$ is assumed to be a polynomial function of the form

$$f(T,\phi) = f(T,\phi = 0) + \sum_{n=2}^{M} \frac{H_n}{n}\phi^n \tag{4.2}$$

Where H_n are coefficients that depend on temperature and other thermodynamic variables. This free energy may then be tailored to several practical use. For example, this free energy functional can be chosen to be symmetric or non symmetric by carefully selecting the coefficients H_n (Provatas and Elder, 2011).

4.2.2 Multi-phase field models

For some applications a phase field model can contain many field parameters (Chen, 1995). For example, phase field models to simulate eutectic solidification (Steinbach et al., 1996; Nestler and Wheeler, 2002; Nestler et al., 2005; Eiken et al., 2006). In these models containing many phase field variables, each phase or grain is represented by one field variable ϕ_i for $i = [1,2,3,...,n]$ where n describes the number of phase or grains in a system.
For example, the phase field model of Chen and Yang (Chen, 1995). This model is used to simulate the growth of a single phase polycrystalline microstructure whose grains possess the same chemical composition and lattice structure but with different local crystalline orientations. As figure 71 shows each grain i is presented by a non conserved order parameter ϕ_i. In grain i, $\phi = \pm 1$, while all other field variables equal zero for $\phi_{j\neq i}$. In this model, the energy functional is viewed as a generalisation of the free energy of the phase field model with only one phase field variable. It reads:

$$F = \int \left[f(\phi_i) + \sum_i \frac{\alpha_i}{2}\left(\vec{\nabla}\phi_i\right)^2 \right] dv \tag{4.3}$$

By comparing this model from the single field variable model described earlier, one can easily notice the similarities. For example, the gradient term relating to existence of a

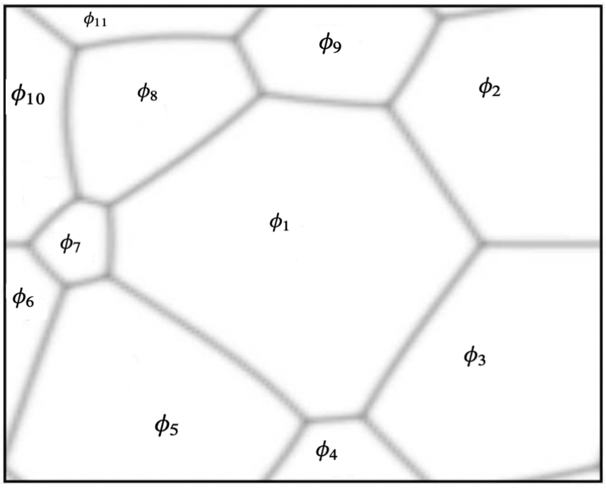

Figure 71: Schematic representation of a polycrystalline microstructure. Grains are of different orientation, consequently, are represented by different phase-field variables ϕ_i.

grain boundary. With this gradient, the properties of individual grain boundary can be adapted by varying the constant α_i. In addition, for isotropic grain boundary properties α_i takes the same value for all grain boundaries. As figure 72 (a) shows, the free energy density $f(\phi_i)$ is a double well potential for each grain i and it is chosen to be

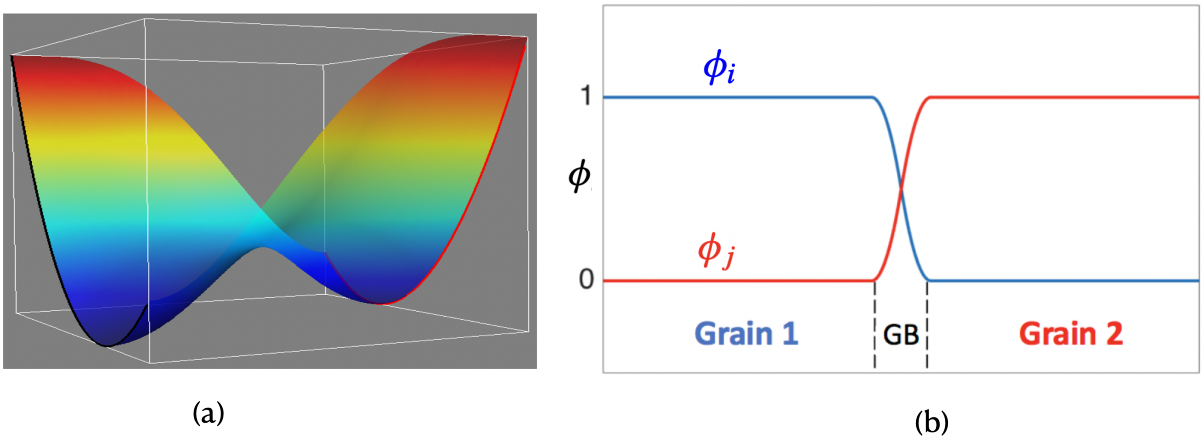

(a) (b)

Figure 72: (a) Example of double well potential visualised as a surface which relates the local free energy density. (b) The order parameter profiles accross a grain boundary. In grain one , $\phi_i = 1$. As the value of ϕ_i decreases accross a grain boundary, ϕ_j of grain two simultaneously increases, consequently, $\phi_i = 1$ for $\phi_j = 0$ and $\phi_i = 0$ for $\phi_j = 1$.

$$f(\phi_i) = \sum_i \left(-\alpha\phi_i^2 + \beta\phi_i^4\right) + \gamma \sum_i \sum_{j\neq i} \phi_i^2\phi_j^2 \tag{4.4}$$

in which α, β and γ are constant with physical meaning. With this choice of $f(\phi_i)$, the free energy is always minimised when $\phi_i = \pm 1$ and all other field variables equal zero. As figure 72 (b) shows, going from grain i ($\phi_i = 1$, $\phi_j = 0$) to grain j ($\phi_i = 0$, $\phi_j = 1$), there is a simultaneous gradual decrease in value of ϕ_i and increase in value of the field ϕ_j at grain boundary. The variation of ϕ_i and ϕ_j accross the grain boundary increases the free energy. This energy increase is due to the excess energy resulting from the existence of grain boundary. In few words, the grain boundary energy strongly depends on the model parameters and can be defined in dependence on the crystalline orientations associated with grains. The grain boundary energy has to be taken into account when quantifying the total free energy of the system.

As it will be shown in chapter 5.2, the grain boundary energy has, however, to be inserted in the model manually. Indeed, the grain boundary energy does not arise naturally instead it is a phenomenological functional tailored for a given system. In general a microstructure in polycrystalline materials is made of several thousands of grains with different orientations. With this model, each grain should be represented by a different field variable ϕ_i which makes this model computationally expensive.

4.2.3 Phase-field models with orientation field

One common problem for single and multi phase field models described previously is to describe grain rotation during microstructure evolution, to quantify the consequences of grain rotation and to realistically capture the nucleation of new sub-grains with different crystalline orientations. In other words, these models do not consider the macroscopic degrees of freedom of a grain boundary in consideration. A grain boundary is described by the crystallographic misorientation angle θ between two abutting grains and an inclination angle Θ. Therefore, a phase field model should be able to take into account these two parameters in order to realistically describe a grain boundary.

In the literature, few models attempted this, in both two and three dimensions, and have been developed for different purposes (Warren et al., 2003; Kobayashi et al., 1998, 2000; Lobkovsky and Warren, 2001; Gránásy et al., 2004, 2005; Pusztai et al., 2005a; Kobayashi and Warren, 2005; Pusztai et al., 2005b). These models contain at least one phase field variable ϕ ($0 \leq \phi \leq 1$) to describe the degree of crystalinity in the domain where minimum value locates in the core of a grain boundary and a field variable θ that is used to measure a change in local orientation with respect to a fixed coordinate system. To calculate angle difference numerically a crystal is considered to have an $n-$fold symmetry so that $-\frac{\pi}{n} \leq \theta \leq \frac{\pi}{n}$ (Warren et al., 2003). The main challenge here is to develop a potential functional that includes both θ and ϕ and that covers the natural physics of an evolving dynamic property under study (Admal et al., 2018; Kobayashi and Warren, 2005). Similarly to the previously described cases, this potential functional must be a double well potential with minima existing at $\phi = 1$ and at $\phi = 0$, in addition, this free energy functional must contain θ which describes the change in orientation between two adjacent grains and the inclination of a grain boundary plane Θ. It is important to note that for grain boundary orientation, we consider the angle difference between adjacent grains because there are no preferred grain orientations. Therefore free energy functional can not explicitly depend on θ. Consequently, to obtain a localised interface, the lowest order gradient term $|\nabla\theta|$ is included which leads to cups in the free energy and singularities that are treated adequately in the numerical simulations. The basic form of this free energy functional of the $(\phi - \theta)$ formalism was developed by Kobayashi (Kobayashi et al., 1998, 2000; Warren et al., 1998) and later extended by Warren (Warren et al., 2003). The Kobayashi formalism will be discussed in more details in section 5.2.

4.2.4 Total free energy of the system

The total free energy of the system $F\ (\phi(x,t), T(x,t))$ can be a complex or a relatively simple functional. For instance, for grain boundary evolution, $F(\phi(x,t), T(x,t)$ can be reformulated to include $\nabla\theta$, which describes a change in local orientation between two adjacent grains (Kobayashi et al., 1998, 2000) as a grain boundary migrates or to include a function describing an inclination of the grain boundary plane. The total free energy $(F((\phi(x,t), T(x,t)))$ of the system can be additively decomposed into contributions from different parts in a system, thus, it is expressed as a sum that reads:

$$F = f(T,\phi) + F_{gb} + F_{el} + ... \tag{4.5}$$

Where $F_{gb} = \int_v f(\nabla\theta, T, P)dv$ is grain boundary energy and accounts for the presence of interfaces through $\nabla\theta$ term, v is the volume of the system, T is temperature, P is pressure, $f(T,\phi)$ is the bulk free energy described above and F_{el} relates to elastic energy stored in a system subjected to stresses or undergoing elastic deformation. The bulk free energy $f(T,\phi)$ is related to the compositions or volume fractions of the phases in equilibrium, whereas grain boundary energy (F_{gb}) and strain energy (F_{el}) affect the equilibrium compositions and volume fractions of the coexisting phases.

4.3 Kinetic equations for microstructure evolution

In general, the functional F is used to characterise thermodynamic properties of an evolving system (Moelans et al., 2008). By neglecting thermal fluctuations, dynamic evolution of the field variables and of material is, in general governed by kinetic equations. The time derivative of a phase-field parameter is correlated to the functional derivative of the total free energy (F) of the system with respect to the phase-field variable. The resulting kinetic equation depends on the nature of the field variable whether locally conserved or not.

For locally conserved field variable, the kinetic equation follows the **Cahn-Hilliard equa-**

tion (Cahn, 1961) that reads

$$\frac{\partial \phi_i(x,t)}{\partial t} = -\nabla.\left(-M_{ij}\frac{\partial F}{\partial \phi_j}\right) \tag{4.6}$$

This is also similar to the diffusion equation or **Fick's equation** in which the term $\left(-M_{ij}\frac{\partial F}{\partial \phi_j}\right)$ describes diffusion flux of the j^{th} component and the term $\frac{\partial F}{\partial \phi_j}$ is the driving force for diffusion of the j^{th} component and M_{ij} is diffusion coefficient.

On the other hand, the **time-dependent Ginzburg-Landau equation**, also known as **Allen-Cahn equation** (Allen and Cahn, 1979), is used to model the evolution of non-conserved phase-field variables. It reads

$$\frac{\partial \phi_i(x,t)}{\partial t} = -M_{ij}\frac{\partial F}{\partial \phi_j} \tag{4.7}$$

In this equation M_{ij} is referred to as mobility. As M_{ij} is a positive definite matrix, both kinetic equations (eqs. 4.6 and 4.7) minimize the total free energy of the system as time evolves, thus, allowing the dynamic evolution of the microstructure towards the state of equilibrium (Gurtin, 1996).

4.3.1 Thermal fluctuation of thermodynamic quantities

In a thermally activated transformation, thermodynamic quantities of a system are continuously fluctuating in space and in time in way which is consistent with statistical thermodynamics. Thanks to Langevin dynamics, the kinetic equations above are reformulated to include thermal fluctuations ($\mathscr{G}_{\phi_j}(x,t)$) also known as the Langevin noise (Gunton and San Miguel, 1983) in order to properly model the evolving system. Consequently, equations 4.6 and 4.7 become

$$\frac{\partial \phi_i(x,t)}{\partial t} = -\nabla.\left(-M_{ij}\frac{\partial F}{\partial \phi_j}\right) + \mathscr{G}_{\phi_j}(x,t) \tag{4.8}$$

$$\frac{\partial \phi_i(x,t)}{\partial t} = -M_{ij}\frac{\partial F}{\partial \phi_j} + \mathscr{G}_{\phi_j}(x,t) \tag{4.9}$$

The noise $\mathscr{G}_{\phi_j}(x,t)$ is Gaussian distributed and its mean value satisfies [2]

$$\left\langle \mathscr{G}_{\phi_j}(x,t) \right\rangle = 0 \tag{4.10}$$

---

[2] In this PhD manuscript, $\left\langle . \right\rangle$ denotes a mean value in space of a given variable.

and correlation are

$$
\begin{aligned}
\left\langle \mathscr{G}_{\phi_i}(x,t)\mathscr{G}_{\phi_j}(x',t') \right\rangle &= -2k_B T \nabla . \mathscr{T}_{ij} \nabla \left[\delta(x-x')\delta(t-t') \right] \\
\left\langle \mathscr{G}_{\phi_i}(x,t)\mathscr{G}_{\phi_j}(x',t') \right\rangle &= 2k_B T \mathscr{T}_{ij} \delta(x-x')\delta(t-t')
\end{aligned}
\tag{4.11}
$$

Where $\mathscr{T}_{ij}$ is the symmetric part of the matrix M_{ij} and (x,t) denotes the reference state x at time t whereas the new state at time t' is denoted by x'.

4.4 Reliability of phase field dynamic equations

Cahn-Hilliard and Allen-Cahn equations are often seen as phenomenological, however, they are indeed physically-based models. Since these equations has set stage for other phase field models, it is important to understand their connection with statistical mechanics. The demonstrations are given in the appendix B.1.

4.5 Phase field dynamic and heat flow equations

To simulate the evolution of a dynamic quantity in a thermo-mechanically processed polycrystalline, requires tracking the evolution of temperature field T. Therefore the equation of motion described in section 4.3 are coupled with the heat conduction equation and it reads

$$\frac{\partial T}{\partial t} = M\nabla^2 T + \frac{L}{c_p}\frac{\partial \phi}{\partial t} \tag{4.12}$$

Where L is the latent heat and c_p is the specific heat. This equation can be reformulated to reproduce a particular phenomena, for example the solidification in which it takes the form

$$\frac{\partial T}{\partial t} = M\nabla^2 T + \frac{L}{c_p}\frac{\partial \phi}{\partial t} + c(T_{cool} - T) \tag{4.13}$$

Where M, c and T_{cool} are constants. The Laplace operators and the directional derivatives in equations above are approximated with appropriate numerical integration techniques which are explained in appendix C.1.7. Figure 73 shows snapshot of microstructure evolution in which the heat is extracted to freeze the simulation box (Warren et al., 2003). These are snapshots from the work of Kobayashi (see (Warren et al., 2003) for more details). One can note that temperature diffusion is allowed leading to nucleation of dendritic microstructures which grow as time passes by. The dendrites grow by approaching each other and finally recoalesce. They merge forming a network of grains that coarsen.

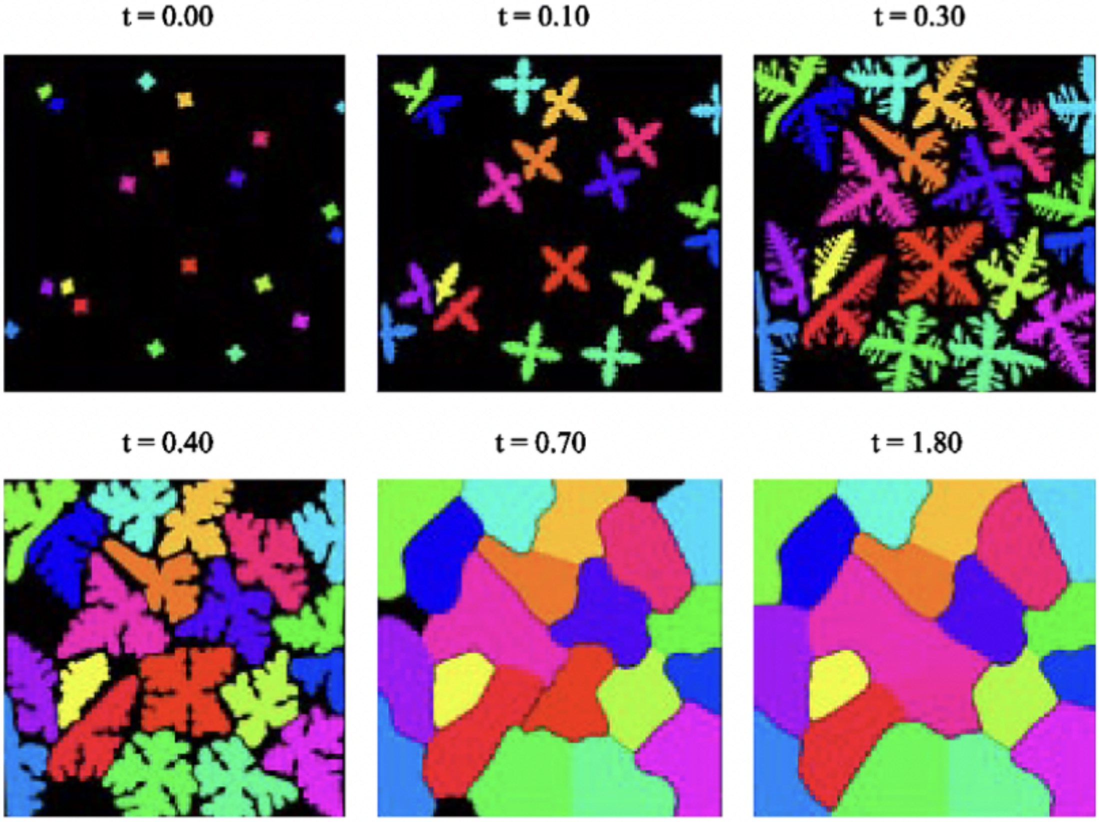

Figure 73: Microstructure evolution by solidifying grains from their under-cooled melt. Grains are crystallographically oriented differently and they are coloured function of their orientation (Warren et al., 2003).

Chapter 5

Phase Field models for grain boundary migration

After presenting the basics and few general example of Phase Field, we now present successful example of PF simulations to model and investigate grain boundary evolution. In this section, we discuss examples of phase field model available in literature, in particular, phase field models that take into account disorientation between two adjacent grains. Thus, it mainly focuses on phase field model of Kobayashi Warren Carter and the new phase field model of Admal and Marian, both of them are at the heart of my work, and may be used to investigate both sharp and diffuse interfaces. Then, we will show the difference in GB energy functional of Admal et al.'s model and Asks et al.'s model. Since this project is only concerned with diffuse interface, this chapter starts by elucidating the difference between sharp and diffuse interface. The section C.1.7 in appendix discusses practical algorithms to solve dynamic equations of these phase field models, as numerical resolution techniques are also important to simulations.

5.1 Description of diffuse and sharp interface

Recalling from section 1.2 that a grain boundary is described in a (at least) five dimensional parametric space. Thus, a grain boundary can be described in terms of a misorientation between grain one of orientation $\boldsymbol{R}^1$ and grain two of orientation $\boldsymbol{R}^2$, and an inclination of the grain boundary plane. The misorientation between grain one and grain two is $\left(\boldsymbol{R}^1\right)^{\boldsymbol{T}} \boldsymbol{R}^2$. This misorientation accounts for three degrees of freedom of the grain boundary space. In a similar way as in section 1.2, the orientation of the grain boundary plane accounts for the remaining two degrees of freedom.

A flat grain boundary with a **sharp-interface** defined by a scalar misorientation angle θ_0 between adjoining grain one and grain two with a misorientation axis denoted by a unit vector $\overline{w} \in \mathbb{R}^3$ and an inclination i is described by a piece-wise constant rotation field that reads

$$R(X; \theta_0, \overline{w}, i) = \exp\left\{\theta(X; \theta_0, i)[w\times]\right\} \tag{5.1}$$

in which $\theta(X; \theta_0, i)$ is a piece-wise constant scalar-valued function that reads

$$\theta(X;\theta_0,i) = \begin{cases} -\frac{\theta_0}{2}, & \text{if } X.i < 0, \\ \frac{\theta_0}{2}, & \text{if } X.i \geq 0 \end{cases}$$

Where **i** is the unit vector describing the grain boundary normal and it is parallel to $\nabla\theta$. Note that , $[w\times]$ in equation 5.1 denotes the second-order anti-symmetric tensor with axial vector w [3]. On contrary, for a **diffuse-interface** with a width ε represented in figure 74,

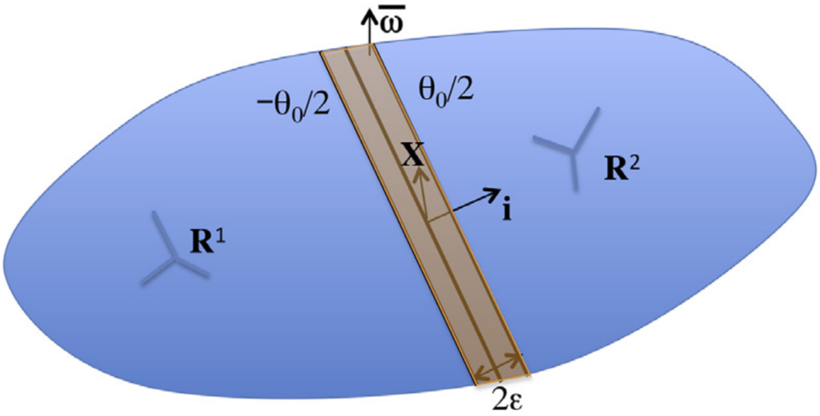

Figure 74: Schematic illustration of diffuse interface of boundary width ε (Admal et al., 2019).

the smooth rotation field reads

$$R(X;\varepsilon,\theta_0,\overline{w},i) = \exp\{\theta(X;\theta_0,i)[w(X)\times]\} \tag{5.3}$$

in which $\theta(X;\theta_0,i)$ is smoothened as follows

$$\theta(X;\varepsilon,\theta_0,i) = \begin{cases} -f\left(\frac{2X.i}{\varepsilon}\right)\frac{\theta_0}{2}, & \text{if } 2X.i \in [-\varepsilon,\varepsilon], \\ -\frac{\theta_0}{2}, & \text{if } 2X.i < -\varepsilon, \\ \frac{\theta_0}{2}, & \text{if } 2X.i > -\varepsilon \end{cases}$$

Where f is a continuous smoothening function such that

$$f : [-1,1] \to [-1,1] \text{ with } f(1) = -f(-1) = 1$$

and w is a vector-value function such that $w(X) = \overline{w}$ if $2X.i \in \mathbb{R}\backslash(-\varepsilon,\varepsilon)$. It is evident that by construction if $\varepsilon \to 0$ the rotation field of the diffuse interface (equation 5.3) converges to equation 5.1. This is shown in figure 75 which shows a comparison between sharp and diffuse interface plus the curve of the step-wise θ functions described above. It

---

[3] The second-order anti-symmetric tensor is described as

$$[w\times]_{ij} := \varepsilon_{ijm}w_m \tag{5.2}$$

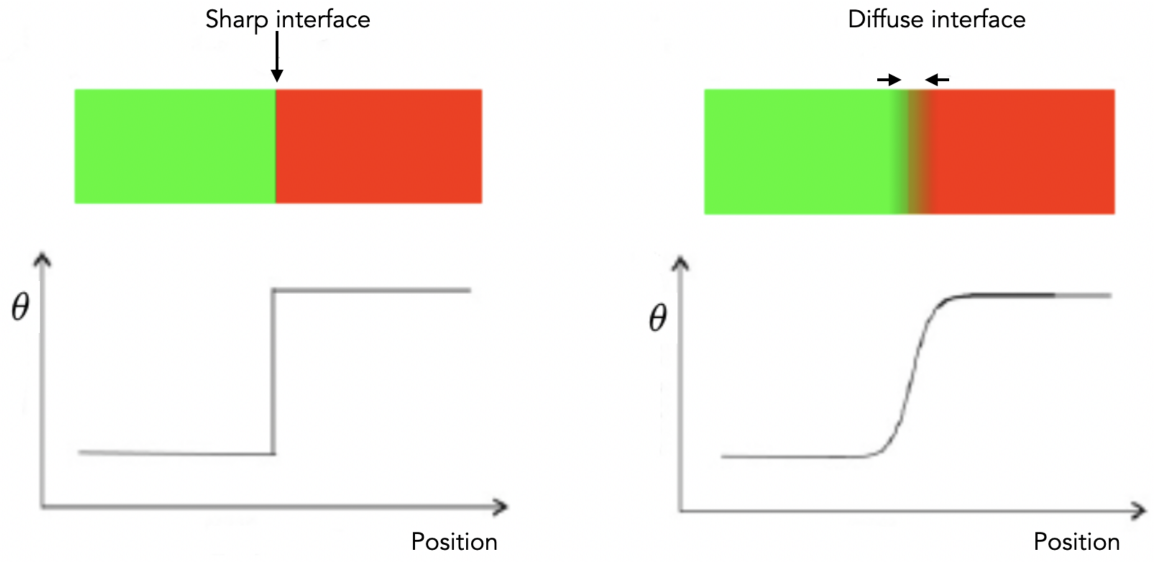

Figure 75: Comparison between the sharp and diffuse interface showing the difference in θ field.

is evident that in sharp interface, contrary to diffuse interface, the orientation parameter θ changes sharply accross the grain boundary. Therefore, a sharp interface is regarded as a singular surface that is explicitly tracked during microstructure evolution. Note that, here, a singular surface describes a surface in the body across which jump discontinuities are allowed for various fields and their derivatives which otherwise are continuous in the body. For example the jump of the field θ accross a singular surface is denoted

$$|\theta| = \theta^{+} - \theta^{-} \tag{5.4}$$

On the other hand, the orientation order parameter changes rapidly but smooth accross the diffuse interface. Consequently, the position of interface is implicitly given by the gradients of the order parameters. Therefore, contrary to sharp interface, explicit tracking of the grain boundary is no longer required (Rokkam et al., 2009).

5.2 The Kobayashi Warren Carter model

The work of Kobayashi, Warren and Carter (Kobayashi et al., 1998, 2000; Warren et al., 2003) has set stage to modelling the evolution of a microstructure of a pure polycrystalline material by taking into account the orientational order parameter. They proposed a phase field model to study evolution of grain boundary in a two dimension polycrystalline ($\Omega_0 \in \mathbb{R}^2$). The model consists of three scalar field parameters θ, ϕ both described earlier (see section 4.2.3) and temperature T. T is not often explicitly written, but it is understood to enter the free energy parameters. The KWC free energy function F_{KWC} reads

$$F_{KWC}[\phi,\theta] = \int_{\Omega_0} \Psi_{KWC} dV \tag{5.5}$$

Where

$$\Psi_{KWC}(\phi,\nabla\phi,\nabla\theta) = \frac{\alpha^2}{2}|\nabla\phi|^2 + f(\phi) + g(\phi)s|\nabla\theta| + \frac{\varepsilon^2}{2}|\nabla\theta|^2 \tag{5.6}$$

and

$$\begin{aligned} f(\phi) &= e(\phi-1)^2 \\ g(\phi) &= \phi^2 \end{aligned} \tag{5.7}$$

Where α, e, s and ε are constants. $\nabla\theta$ is the rotationally invariant expression that describes interface energy due to orientational mismatch between two rotated grains. The term $g(\phi)s|\nabla\theta|$ localises the interface whereas the term $\frac{\varepsilon^2}{2}|\nabla\theta|^2$ diffuses it. Therefore, both terms in $\nabla\theta$ plays an important role for a grain boundary to have a finite width. In addition, the term ε plays an important role in a mobility of a grain boundary as it will be shown later in this manuscript.

5.2.1 Mobility function of field variables

In phase field methods for grain boundary problems, it is difficult to maintain angle variable constant or almost constant within each grain during grain boundary migration. One can solve this by creating local minima in the energy space according to the number of grain orientations (Morin et al., 1995; Chen and Yang, 1994; Kobayashi and Giga, 1999). Unfortunately, this solution is physically undesirable since it breaks the rotational invariance of the model. On the other hand, if the leading term of the energy with respect to $\nabla\theta$ is $|\nabla\theta|^2$ and if there is no local minimum assumed in the energy space, the angle variable is hardly kept constant in interior of each grain during migration (Kobayashi et al., 1998; Warren et al., 1998; Lusk, 1999), especially without the help of boundary conditions. Therefore, the following equations containing $|\nabla\theta|$ instead of $|\nabla\theta|^2$ for the dynamic evolution of field variables ϕ and θ are derived by taking independent variation of Ψ_{KWC} with respect to ϕ and θ which results in [4]

$$\tau_\phi \frac{\partial\phi}{\partial t} = \alpha^2\Delta\phi - f'_\phi(\phi) - g'_\phi(\phi)s|\nabla\theta| \tag{5.8}$$

$$\tau_\theta \frac{\partial\theta}{\partial t} = \nabla.\left[\varepsilon^2\nabla\theta + g(\phi)s\frac{\nabla\theta}{|\nabla\theta|}\right] \tag{5.9}$$

Where τ_ϕ and τ_θ are kinetic time constant with respect to ϕ and θ and for a function $M(\varphi,\vartheta)$, its derivatives are $M'_\varphi(\varphi,\vartheta)$ and $M'_\vartheta(\varphi,\vartheta)$ with respect to φ and ϑ. Note that

---

[4] Note that Δ denotes Laplacian operator, ∇ denotes the gradient operator and $\nabla.$ denotes the divergent operator.

$M_\phi^{\dot{\phi}} = \tau_\phi \frac{\partial \phi}{\partial t}$ and $M_\theta^{\dot{\theta}} = \tau_\theta \frac{\partial \theta}{\partial t}$ are inverse mobilities of ϕ and θ respectively. This model includes θ only in $\nabla\theta$ form, therefore the model retains a symmetry in evolution of ϕ under rotation. The main idea behind the formulation of energy functional (equation 5.6) and mobility function (equations 5.8 and 5.9) by including $|\nabla\theta|$ is to keep angle variable constant by means of singular diffusivity in each grain. In this way, the jump of the angle variable can inevitably appear at the grain boundary, consequently, the singular $|\nabla\theta|$ term appears in equations 5.6, 5.8 and 5.9. Therefore the term $\frac{\nabla\theta}{|\nabla\theta|}$ makes equation 5.9 a singular diffusive equation (Admal et al., 2018). By this singularity, the graph of ϕ decreases gradually to pick downward at the core of grain boundary, while $\phi = 1$ in interior of each grain. For more details on the derivation of such equations see (Kobayashi and Giga, 1999).

5.2.2 Numerical implementation of KWC model

Numerical implementation of the KWC model requires to properly treat the singular term because the singular term makes the model mathematically difficult to converge. In the following section, we explain the approximation of the singular term.

5.2.2.1 Numerical convergence of the mobility equations

The presence of the singular term makes equations numerically difficult to converge. Kobayashi and Giga (Kobayashi and Giga, 1999) proposed an elegant method of replacing the singular term with non singular term without compromising the physics.

$$p(|\nabla\theta|) := \frac{\ln(\cosh(\gamma|\nabla\theta|))}{\gamma} \tag{5.10}$$

Where γ is an adjustable parameter such that

$$\lim_{\gamma\to\infty} p\left(|\nabla\theta|\right) \approx |\nabla\theta|$$

By replacing $|\nabla\theta|$ by $p\left(|\nabla\theta|\right)$, the Euler–Lagrange equations 5.8 and 5.9 become:

$$M_\phi^{\dot{\phi}} = \alpha^2 \Delta\phi - f^{'}(\phi) - g^{'}(\phi) sp \tag{5.11}$$

and

$$M_\theta^{\dot{\theta}} = \nabla . \left[\varepsilon^2 \nabla\theta + gsp^{'}_{|\nabla\theta|} \frac{\nabla\theta}{|\nabla\theta|} \right] \tag{5.12}$$

A comparison of the numerical and analytical solution of the KWC model is given in appendix B.2 and B.3.

5.2.3 Energy of a grain boundary

Energy γ_{gb} of a grain boundary is a key element in assessing relative stability of a grain boundary. In addition, γ_{gb} takes part of an important motive force for grain boundary migration, through the expressions of GB stiffness. In the continuous PF model, the γ_{gb} is expected to include a contribution from Ω_0^p and Ω_0^{GB}. Warren and Co-workers (Warren et al., 2003) have proposed a methodology to calculate the excess energy of a grain boundary (Warren et al., 2003). The procedure is to integrate the steady state form of equations 5.8 and 5.9 and substitute the resulting equations into the free energy functional. after the temperature dependent reference bulk energy (f_{ref}) is subtracted from the resultant ($f(\phi_o(x))$ functional.

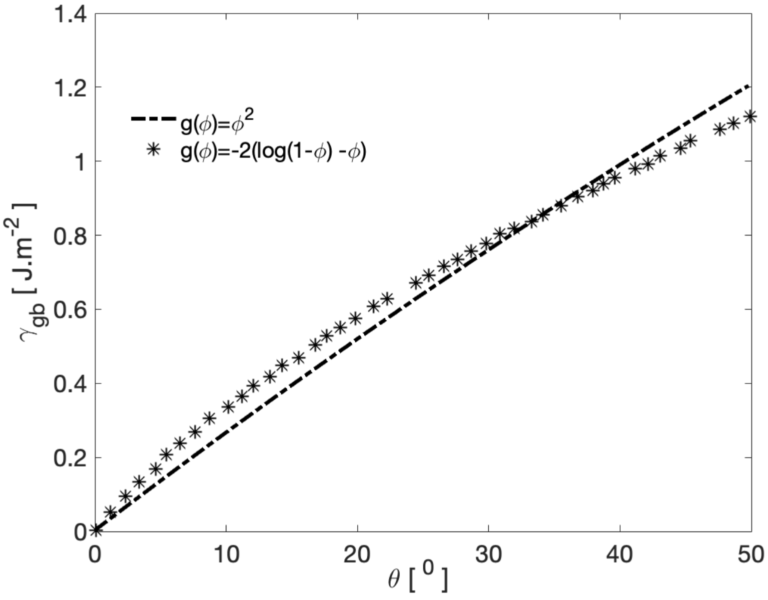

Figure 76: Grain boundary energy (γ_{gb}) against misorientation angle (θ) for different $g(\phi)$ functions (Admal et al., 2018).

$$\gamma_{gb} = sg(\phi_{min})\Delta\theta + 2\alpha \int_{\phi_{min}}^{1} \left(f(\phi_o(x) - f_{ref}\right) dx \tag{5.13}$$

For low angle grain boundaries, grain boundary energy is approximated as

$$\gamma_{gb} \approx -s\Delta\theta \ln(\Delta\theta) \tag{5.14}$$

Since the energy contribution from the terms containing ϕ is very negligible relative to the contribution from terms containing $(\nabla\theta)$. This is the Read-Shockley model for low angle tilt grain boundaries (Read and Shockley, 1950). $\Delta\theta$ is the misorientation across the bicrystal and ϕ_{min} is the value of the $\phi_0(x)$ field, in the centre of the grain boundary with a width W_{GB} and ϕ_{min} (the global minimum of $\phi_0(x)$) reads

$$\begin{aligned}
\phi_{min} &= 1 - \frac{\Delta\theta}{\Delta\theta_c} \\
W_{GB} &= \frac{2\alpha}{e}\ln\left(1 - \frac{\Delta\theta}{\Delta\theta_c}\right) \\
\Delta\theta_c &= \frac{\alpha e}{s}
\end{aligned} \tag{5.15}$$

For more details on the derivation of these functions see in (Warren et al., 2003). In general, $g(\phi)$ is chosen to increase monotonically in ϕ, for example equation 5.7. However, in some cases, for example in the work of Kobayashi (Kobayashi et al., 2000) and Admal et al. (Admal et al., 2018) it is chosen to follow

$$g(\phi) = -2\left(\ln(1-\phi) - \phi\right) \tag{5.16}$$

The Work of Admal et al.(Admal et al., 2018) has shown that the choice of $g(\phi)$ from equation 5.16 yields a grain boundary energy of the Read–Shockley form (Read and Shockley, 1950) as figure 76 shows, whereas Kobayashi and Giga (Kobayashi and Giga, 1999) realised that the choice of $g(\phi)$ from equation 5.7 results in a linear dependence of the grain boundary energy on misorientation as figure 76 shows.

5.2.4 Limitation of KWC model

The main advantage of KWC model is that it is possible to model both grain rotation and shrinkage simultaneously. Despite the fact that the KWC model models qualitatively grain boundary migration, it is purely phenomenological with no connection with underling plastic mechanisms. For that, it does not provide a detailed picture of plastic activities due to dislocations during microstructure evolution.

5.3 Admal and Marian's phase field model

A quantitative and qualitative prediction of microstructure evolution requires tracking factors that affect the displacement of a grain boundary such as its interaction with dislocations and understanding how plastic activities from these dislocations affect the motion of a grain boundary. One of the recent model to simulate grain boundary evolution with plastic activity of dislocations was recently proposed by Admal and Marian (Admal et al., 2018). It is a model based on modelling a grain boundary as a continuum collection of dislocations. Its basic form originates from the free energy functional of Kobayashi Warren Carter model (Kobayashi et al., 1998, 2000). Therefore, it might inherit the computational challenges of the KWC model, especially, originating from the singular diffusive nature of its governing equations. In this section we discuss this model in more details since it is at the center of the present work.

5.3.1 Kinematics of polycrystal plasticity

The kinematic of polycrystal plasticity is essentially concerned with the change of shape of microstructure due to plastic deformation activities. Note that change in shape are observed on both macroscopic and microscopic scales. It is of great importance to describe this microstructure shape change in order to be able to quantify how it affects properties of an evolving microstructure, in particular mobility of a migrating grain boundary. This section gives fundamental insights of kinematics behind a continuum polycrystal plasticity model of Admal and Marian (Admal et al., 2018). Thus, it starts by describing useful kinematic variables required to successfully describe grain boundary plasticity. Since this model originates from the theory of single crystal plasticity, we start by describing the kinematic of a single crystal and then later, we will introduce a grain boundary in a crystal as a continuum array of geometrically necessary dislocations.

5.3.1.1 Macro and micro-scopic kinematics of bulk polycrystal

Here, we describe a body as an open subset $\beta \subset \mathbb{R}^3$. In circumstances when a body undergoes deformation, its deformation is described relative to a reference body $\beta_t \subset \mathbb{R}^3$ identified with the bounded regions of $\mathbb{R}^3$ it occupies. β_t is customary assumed to be homogeneous. In order words, each point $X \in \beta_t$, referred to as a material point, is associated with a reference lattice that does not vary from point to point. During deformation of the body, the description of the resulting $x \in \beta$ relative to the material point $X \in \beta_t$ follows a one to one mapping

$$x = y(X, t) \tag{5.17}$$

Where $y(X, t) = X + u$ is a deformation function of X at each time t where u is a displacement of any point in β. The deformation gradient F reads,

$$F = \nabla y = \nabla u \tag{5.18}$$

The gradient is expressed with respect to the material coordinates. The determinant of F ($\det F$) satisfies the following condition

$$\det F \neq 0 \tag{5.19}$$

In general, the micro-kinematical hypotheses of classical theory of crystal plasticity are based on the multiplicative decomposition of the deformation gradient F into its elastic

F^e and plastic F^p components (Lee, 1969; Kröner, 1959; Reina and Conti, 2014; Gurtin, 2000).

$$F = F^e F^P \tag{5.20}$$

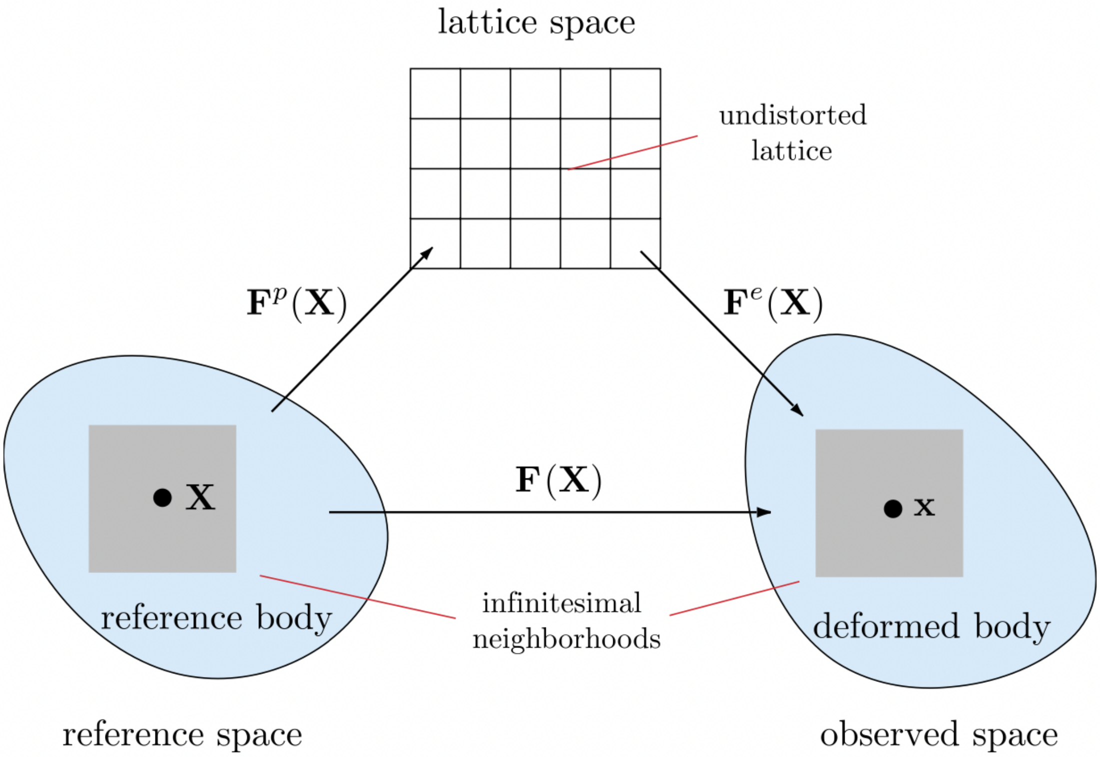

Figure 77: Schematic diagram illustrating the decomposition of deformation gradient into elastic distortion F^e and plastic distortion F^p(Kröner, 1959; Gurtin, 2008).

F^e represents elastic stretching and rotation of the atomic lattice and F^p describes the plastic distortion of atoms due to dislocation slip. Both tensors F^e [6] and F^p are invertible and they can be viewed as describing deformation of infinitesimal neighbourhoods. This means that they are not necessary gradient of motions. In order words F^p maps the infinitesimally small material element $\mathbf{dX}$ to $F^p dX$. In this framework, the lattice configuration is used to describe the collection of infinitesimal configurations obtained by applying either F^e locally to reference increment $\mathbf{dx}$ or F^p locally to reference increment $\mathbf{dX}$. Thus, F^p and F^e fields are very different. Here F^e maps the lattice configuration to the deformed configuration whereas F^p maps the reference configuration to the lattice configuration. Furthermore, F and F^T maps as well the reference configuration to the deformed configuration (see figure 77 for visualisation). The velocity gradient L (∇v) is important when describing F^e and F^p. ∇v can also be decomposed into its elastic and

---

[6] Note that F^e and F^l carry the same description.

plastic components by using the Kroñer–Lee decomposition technique

$$\begin{cases} \nabla v = L = L^e + F^e L^p F^{e-1} \\ L^e = \dot{F}^e \big(F^e\big)^{-1} \\ L^p = \dot{F}^p \big(F^p\big)^{-1} \end{cases}$$

The terms L^e and L^p denote the elastic and plastic components of the velocity gradient. In classical single crystal plasticity, the presumption that plastic flow takes place though slip manifests itself in the description of the evolution of the deformation gradient F^p. It is determined from the plastic flow rate $\dot{F}^p$ which is expressed in terms of plastic velocity gradient L^p and the plastic deformation gradient F^p as

$$\dot{F}^p = L^p F^p \tag{5.21}$$

Since the motion of dislocations takes place on prescribed slip systems, the overall plastic velocity gradient considers the contribution from each slip α $(\alpha = 1, 2, ..., A)$. For more on slip system in FCC materials see section 1.1.2. Therefore L^p becomes

$$L^p = \sum_{\alpha}^{A} v^{\alpha} \mathscr{V} \tag{5.22}$$

where v^{α} is microshear rates in order words the slip rate and

$$\mathscr{V} := s^{\alpha} \otimes m^{\alpha}$$

is Schmid tensor that projects the amount of slip on each system with respect to the frame of reference. Here, s^{α} describes the dislocation slip glide direction and m^{α} is the normal of dislocation slip plane. s^{α} and m^{α} are vectors in the lattice configuration. Due to orthogonality existing between s^{α} and m^{α}, $tr(L^p) = 0$ consequently

$$\det(\dot{F}^p) = \det\Big((F^p) tr(L^p)\Big) = 0 \tag{5.23}$$

On the other hand, $F^e > 0$ and from classical plasticity F^e can be decomposed into rotation field R^e and the right stretch tensor U^e

$$F^e = R^e . U^e \tag{5.24}$$

For

$$U^e = \sqrt{(F^e)^T F^e} \tag{5.25}$$

The right Cauchy-Green lattice deformation tensor C^e and the lattice Lagrangian strain

$\boldsymbol{E}^e$ are obtained from $\boldsymbol{F}^e$

$$C^e = (F^e)^T F^e$$
$$E^e = \frac{1}{2}(C^e - \mathbf{I}) \tag{5.26}$$

Where $\mathbf{I}$ is the identity matrix. The crystal plasticity framework successfully describes materials deformation.

5.3.2 Kinematic framework to include grain boundary plasticity

The grain boundary plasticity is centered on describing a grain as an array of periodic arrangement of Geometrically Necessary Dislocations (GND) (Admal et al., 2017; Cermelli and Gurtin, 2002; Admal et al., 2018). In this way each grain boundary is described in terms of its own GND with unique characteristics (e.g. properties, densities etc...) sufficient enough to precisely define it. In this way, during any deformation mechanism, plastic distortion due to climbing or sliding of the GND dislocations emerges naturally and follows the plastic flow rule in equation 5.21. During the flow of geometrically necessary dislocations, their Burgers vectors is characterised by the closure failure of referential circuits as mapped by $\boldsymbol{F}^p$ or of deformed circuits as mapped by $\boldsymbol{F}^e$. By means of characterising the Burgers vector, a tensor field referred to as the Burgers tensor $\boldsymbol{G}$ is derived from $\boldsymbol{F}^p$ or $\boldsymbol{F}^e$(Cermelli and Gurtin, 2002) and reads,

$$\begin{aligned} G &= F^p \mathrm{curl} F^p \\ &= J^e F^{e-1} \mathrm{curl} F^{e-1} \end{aligned} \tag{5.27}$$

Where $J^e = \det F^e$. Considering the fact that, a grain boundary is planar defect, it is worthy noting that $\boldsymbol{G}$ is not a function, instead it is a distribution supported by the surface of a grain boundary. $\boldsymbol{G}$ allows to measure the net Burger vector in each surface from the collection of grain boundary surfaces that support the distribution of $\boldsymbol{G}$ (Acharya, 2008; Gurtin et al., 2010). For instance, if we consider the normal n of a given surface in a lattice configuration, the net Burger vector G_n of dislocation lines per unit area passing through a plane of normal n in the lattice configuration is given by

$$G_n = G^T.n \tag{5.28}$$

This method of interpreting a grain boundary as a continuum periodic array of geometrically necessary dislocation was previously used in both atomistic simulations (Lim et al., 2009; Warrington and Bollmann, 1972) and in elastic models (Saada, 1979). In atomistic simulations, $\boldsymbol{G}$ is expressed in terms of the number (n_i) of arrays of geometrically necessary dislocations, their dislocation line L_i and their net Burgers vector b_i and the volume of the domain V (Cermelli and Gurtin, 2001).

$$G = \frac{1}{V}\sum_{i}^{n_i} L_i \otimes b_i \tag{5.29}$$

or by a equation of Frank-Bilby (Priester, 2012), where $\mathbf{I}$ is the identity matrix and $\overrightarrow{k}$ is a probing vector within the GB plane.

$$G = \left(R^0(\theta(X)) - \mathbf{I}\right)\overrightarrow{k} \tag{5.30}$$

For flat diffusive tilt interface, G tensor has two non zero components G_{31} and G_{32} which are expressed in terms of the smoothened step function $\theta(X)$ describing the orientation of the two grains. Evaluation of G tensor with $F^p = R^{0T}(\theta(X))$ using equation 5.27 returns

$$\begin{aligned} G_{31} &= -\cos(\theta(X))\frac{\partial\theta(X)}{\partial\theta_1} \\ G_{32} &= -\sin(\theta(X))\frac{\partial\theta(X)}{\partial\theta_1} \end{aligned} \tag{5.31}$$

and the rest of the components are zeros. Figure 78 shows the plots of the components of $|G|$ tensor against the position x along the x axis. From here, one can easily notice

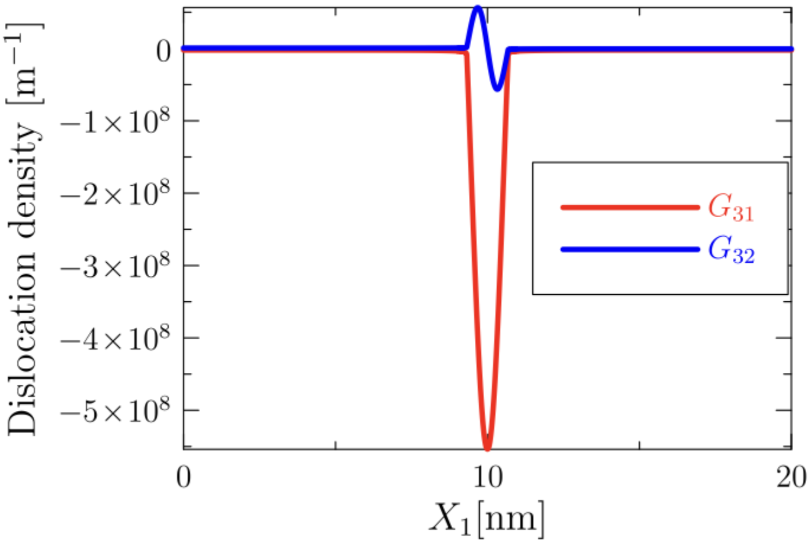

Figure 78: Dislocation density obtained from one dimension steady state simulation modelling of a flat symmetric tilt grain boundary of misorientation angle $\theta_0 = 30°$ with misorientation axis [001] located at the center of a simulation box of $20nm$ long (Admal et al., 2018).

the importance of interpreting a grain boundary as an array of dislocations. The major advantage is that the evolution of tensor G tracks simultaneously the bulk dislocation activities and grain boundary activities through $\dot{F}^p$ field.

5.3.2.1 Building a grain boundary

To build a grain boundary we take advantage of the multiplicative polar decomposition of $\boldsymbol{F}$ in equation 5.20. The main advantage of building a grain boundary based on this polar decomposition is that it offers an immediate access to $\boldsymbol{G}$ tensor. As figure 79 shows, a strain free ($F \equiv I$) single crystal with initial states below is considered as a reference configuration.

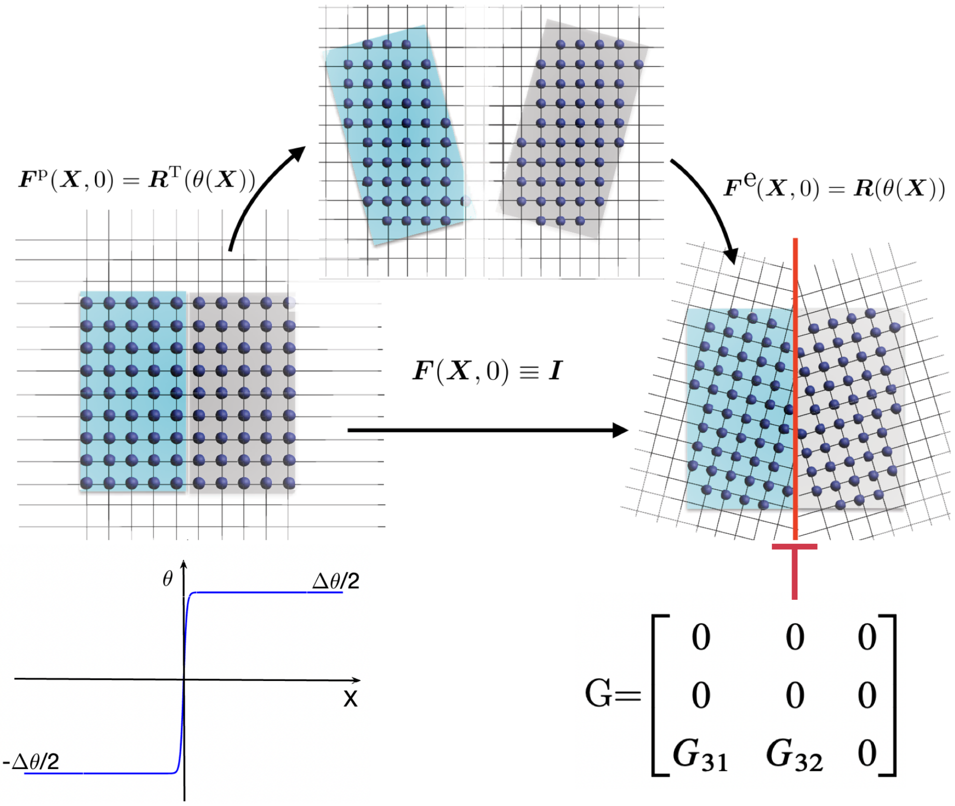

Figure 79: Constructing a grain boundary by utilising polar decomposition of the deformation gradient (Admal et al., 2018, 2017).

$$
\begin{aligned}
F^{e}(X,0) &= R\left(\theta(X)\right) \\
F^{p}(X,0) &= R\left(\theta(X)\right)^{T}
\end{aligned}
\tag{5.32}
$$

In the second step, this single crystal is plastically deformed by applying a step-wise rotation $R\big(\theta(X)\big)$, a functional representing a lattice rotation field in bicrystal. This rotation field is a piece-wise constant value (Admal et al., 2017, 2018) functional. Apparently, the resulting plastic deformation gradient F^{p} deforms the material leaving the lattice fixed. In the next step an elastic deformation is applied. On contrary to plastic deformation, elastic deformation deforms the lattice. This results in a total deformation gradient that is compatible

$$
F(X,0) = F^{e}F^{P} \equiv \mathbf{I} \tag{5.33}
$$

This method results in a relaxed bicrystal which is strain free since the resulting Lagrangian strain is zero. Figure 80 shows the plot of a components a) of plastic distortion and b) lattice Lagrangian strain obtained from a steady state simulation of a flat symmetric tilt grain boundary with a misorientation angle 30° and disorientation axis [001]. Thus, this procedure produces bicrystal with the right amount of slip in each grain. However, this seems contradictory from a visual comparison between the resulting bicrystal and the initial single crystal in figure 79. This apparent contradiction results from interpreting $F^P = R^T$ in an absolute sense for a discrete lattice (Admal et al., 2017). To circumvent this apparent contradiction, F^P should be viewed in an average sense using the theory of weak convergence (Admal et al., 2017; Rudin, 1991). For more details on this theory see appendix C.1.1.

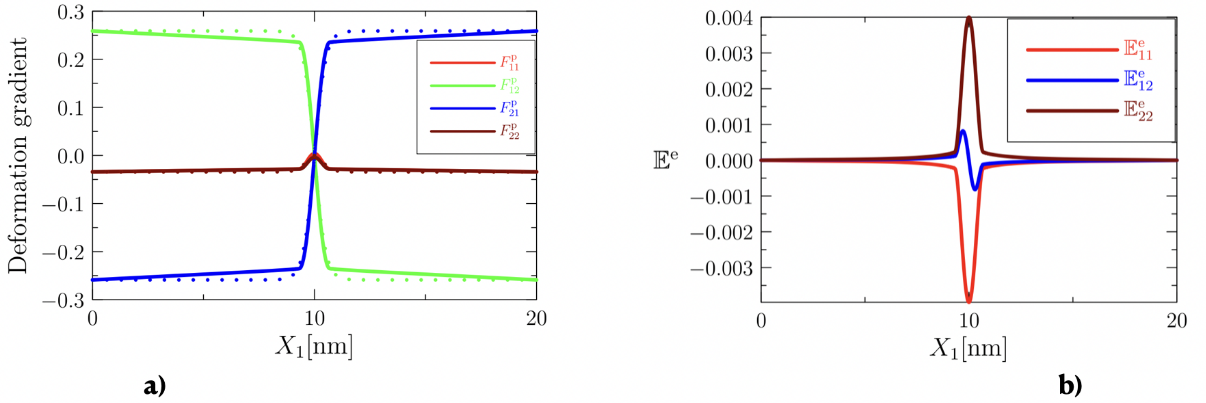

Figure 80: Plots of components of a) plastic distortion F^p and b) Lattice Lagrangian strain $\mathbb{E}^e$ for a flat symmetric tilt grain boundary with a misorientation angle 30° around [001] misorientation axis located in centre of the simulation box of $20nm$ long (Admal et al., 2018).

5.3.3 Macroscopic and microscopic force balance

To arrive at the force balance equations requires taking independent variation of equation C.10 (in appendix) with respect to $\dot{y}$, $\dot{\phi}$ and $v^\alpha(\alpha = 1, ..., n)$. Here we list all macroscopic and microscopic force balance equations obtained:

1. Macroscopic force balance equations are

$$\begin{cases} \mathrm{Div} P = 0, & \text{in } \beta_t \\ t = PN, & \text{on } \partial\beta_t \end{cases} \tag{5.34}$$

2. Microscopic force balance for each slip system α reads

$$\begin{cases} \mathrm{Div}\xi^\alpha - \Pi^\alpha = 0, & \text{in } \beta_t \\ \Xi^\alpha = \xi^\alpha . N, & \text{on } \partial\beta_t \end{cases} \tag{5.35}$$

3. Microscopic force balance equations for ϕ reads

$$\begin{cases} \mathrm{Div}\varrho - \pi = 0, & \text{in } \beta_t \\ s = \varrho.N, & \text{on } \partial\beta_t \end{cases} \tag{5.36}$$

The details of the model as proposed by Admal and his collaborators is left in appendix C.1 for the sake of conciseness.

5.3.4 Grain boundary energy ψ_{gb}

By taking advantage of $\boldsymbol{G}$ tensor described in section 5.3.2, grain boundary energy is expressed in terms of $\boldsymbol{G}$. The Admal and Marian's model is inspired by the KWC model in a sense that the gradient of lattice rotation is replaced by $\boldsymbol{G}$ which is a frame-invariant tensorial quantity that includes the misorientation axis, angle and the inclination of a grain boundary.

$$\psi_{gb}(T, \phi, \nabla\phi, G) = \frac{\alpha^2}{2}|\nabla\phi|^2 + f(\phi) + g(\phi)s|G| + \frac{\varepsilon^2}{2}|G|^2 \tag{5.37}$$

Where α, s and ε are constants that depend on temperature. This is natural since $\boldsymbol{G}$ is unique for each grain boundary. In addition, under the assumptions of small strain, Nye (Nye, 1953) has shown that tensor $\nabla\theta \approx |G|$ can be related to the gradient of lattice rotation. We may refer the reader to the appendix C.1 for more on derivation of this energy functional.

5.3.5 Bulk elastic energy ψ_{bulk}

The bulk elastic energy is assumed to depend on $\boldsymbol{T}$ and $\boldsymbol{E^e}$ through the lattice constants. It is described by a polyconvex energy density for isotropic materials proposed by Ciarlet and Geymonat (Ciarlet et al., 1982).

$$\begin{aligned} \Psi_{bulk} &= a\left(3 + 2Tr(E^e)\right) + b\left(3 + 4Tr(E^e) + 2Tr^2(E^e) - 2Tr\left((E^e)^2\right)\right) \\ &\quad + c\det\left(2E^e + I\right) - \frac{1}{2}d\log\det\left(2E^e + I\right) - (3a + 3b + c) \end{aligned} \tag{5.38}$$

For

$$\begin{aligned} a &= \mu - \frac{1}{2}\left(\mu + \frac{\lambda}{4}\right) \\ b &= -\frac{\mu}{2} + \frac{1}{2}\left(\mu + \frac{\lambda}{4}\right) \\ c &= \frac{\lambda}{8} \\ d &= \mu + \frac{\lambda}{2} \end{aligned}$$

Where λ and μ are the Lame's constant. Figure 118 (in appendix) shows curve of elastic energy function of the $x-$coordinates for a flat symmetric tilt grain boundary of misorientation angle 30° around a misorientation axis [001] obtained from a steady state simulation at $0K$.

5.3.6 Mobility function of Admal & Marian's model

The Euler-Lagrange equations resulting from taking independent variations of ψ_{gb} with respect to ϕ and G are

$$\begin{aligned} M_\phi^{\dot{\phi}} &= \alpha^2\nabla^2\phi - f_\phi'(\phi) - g'(\phi)s|G| \\ M_G^{\dot{G}} &= g(\phi)s + \varepsilon^2|G| \end{aligned} \tag{5.39}$$

Similar to KWC model, $|G|$ in the functions above is approximated by $p(|G|)$ where the function p is given in equation 5.10. $M_\phi^{\dot{\phi}}$ and $M_G^{\dot{G}}$ are inverse mobility function with respect to ϕ and G. For more on the derivation of these equations, we may refer the reader to the section C.1 in appendix.

5.4 The phase Field model of Anna

This is another recent model devised to capture simultaneously grain boundary evolution in unison with plastic activities. As for Admal and Marian's model, this model derives from the extension of KWC model (Warren et al., 2003). The difference with Admal and Marian model described in previous sections is that this model is formulated using the Cosserat crystal plasticity to incorporate plastic activity induced by a moving grain boundary (Ask et al., 2018). The resulting grain boundary energy functional reads

$$\begin{aligned} \Psi(\eta, \nabla\eta, e^e, \kappa, \tau^\alpha) = f_0\Big[f(\eta) + \frac{a^2}{2}|\nabla\eta|^2 + sg(\eta)||\kappa|| + \frac{\varepsilon^2}{2}h(\eta)||\kappa||^2 \Big] \\ + \frac{1}{2}\varepsilon^e : \mathbb{E}^s : \varepsilon^e + 2\mu_c(\eta)\, \overset{x}{e}{}^e . \overset{x}{e}{}^e + \Psi_\rho(\phi, \tau^\alpha) \end{aligned} \tag{5.40}$$

Where η is order parameter, $\overset{e}{e}$ elastic deformation tensor , κ is the curvature tensor, τ^α internal variable that is function of the dislocation densities, f_0 is a normalisation parameter, $h(\eta)$ is an interpolation function , ε^e plastic strain tensor, $\mathbb{E}^s$ is elasticity tensor, μ_c is the coupling modulus, $\overset{x}{e}{}^e$ is skew-symmetric deformation tensor and all others have(s, $g(\eta)$, =g(ϕ), $a^2 = \alpha^2$, ε) the same meaning as in the KWC or Admal's model presented before.

This model capture successfully the moving grain boundary and plastic activity associated with. For example, figures 81 a) and b) shows initial profiles of θ, e^* (the Eigen-deformation tensor) and η (at $\bar{t} = 0$) and after the grain with a high content of stored dis-

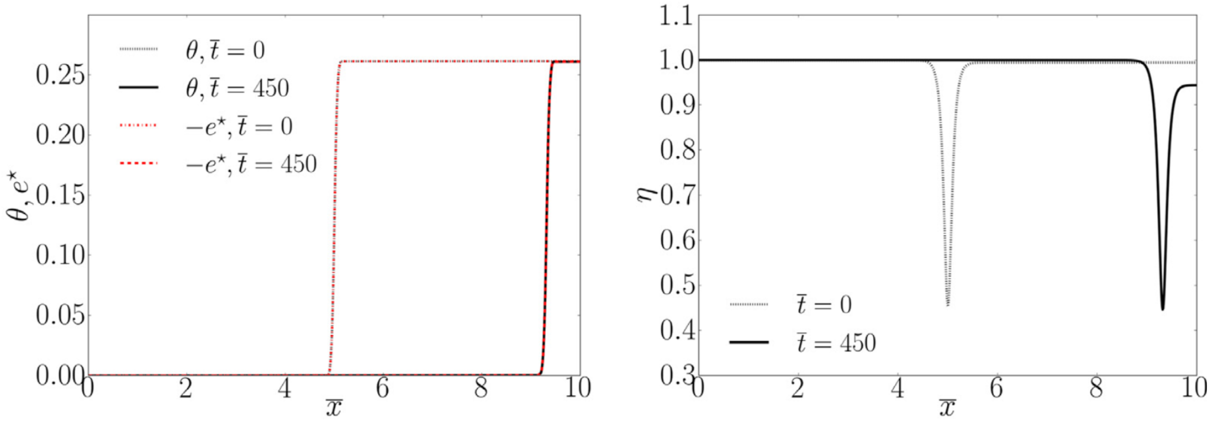

a) b)

Figure 81: Profiles of a) θ and e^{*} and b) η of a moving grain boundary at initial position ($\bar{t} = 0$) and after $\bar{t} = 450$ (Ask et al., 2018).

locations is almost entirely consumed by a growing dislocation free grain (after $\bar{t} = 450$). For more in the model see in (Ask et al., 2018).

5.5 Algorithms to solve phase field equations

The quality of phase field simulations roots in both carefully choosing algorithm to solve partial differential equations appearing in phase field equations and on properly meshing the simulation domain. Therefore, it is important to compare available algorithms in order to make a proper choice on which one to use. In this literature review we have assessed different algorithms used for discretisation and numerically solving phase field equations and related partial differential equations. Since in this project, we simulated only two dimensional phase field equations, we have limited ourselves to algorithms that are applicable to a two dimensional system. For that reason, we have assessed the finite difference and finite element methods. In addition, we have assessed the implicit and explicit algorithms for time marching and compares their stability. To capture the whole theoretical backgrounds of these schemes we may refer the reader to the section C.1.7 in appendix of this manuscript.

Objectives and methodology

Objectives

The ultimate objective of this work is to develop a physically based model capable of predicting microstructure evolution at the scale of FCC Nickel polycrystals. This has been a challenge for several decades now. In the general introduction we identified two main challenges that must be overcome at the mesoscale to reach this objective. 1) One of the major difficulties lies in the fact that many mechanisms are occurring concurrently, ranging from Grain Boundary (GB) migration, accompanied -or not- by GB rotation and shear coupling, existence of multiple driving forces, to GB interaction with crystal dislocations. The relative contribution of each of these mechanisms is difficult to assess with most of the currently available models. 2) Because the details of GB migration and of their interaction with crystal dislocations depend upon the atomic details of GB structures, and can only be assessed by atomistics, a successful predictive model for microstructure evolution should retain the key atomistics data like these obtained by Molecular dynamics in the first part of this manuscript. In the previous chapters, we reviewed the basics of PF and demonstrated that the PF model proposed by Admal et al. (Admal et al., 2018) could be a good framework to include all the necessary physical mechanisms. In this chapter, we will implement and assess the capability of this model to produce the mechanisms that hopes to reproduce. We will start by a sensitivity study, to fully understand all the role of the parameters and terms in the model, then we will investigate the stability and migration of the symmetric tilt GB around [001] corresponding to the configuration of the first part of this part, and we will see that the model captures spontaneously with the existing parametrization many of the qualitative and even some quantitative features observed in MD. Finally at the end of the chapter, we will propose an explicit analytical solution of the KWC model in 1D, upon which the Admal et al. model is based. This analytical solution allows for the first time to rigorously and unambiguously identify the PF parameters.

Methodology

In this section, we will perform numerical simulation to investigate migration of two dimensional [001] diffuse symmetric tilt grain boundaries from a list of grain boundaries investigated by atomistic method in the first part of this thesis. The list of grain boundaries investigated here which are shown in table 3.4 encompasses both symmetric tilt grain boundaries with low and high misorientation angle. All simulations will be carried in

COMSOL Multi-physics V5.6 which is a cross-platform finite element analysis, solver and multi-physics simulation software. The choice of this software is centred on the fact that it is a high performance code which features faster and more memory-lean solvers for multicore and cluster computations and more efficient CAD assembly handling. It is a regularly maintained and updated code. COMSOL Multiphysics is seamlessly integrated with MATLAB to extend our modelling with scripting programming in the MATLAB environment. This will allow us to utilise the full power of MATLAB and its toolboxes in pre-processing, scripting and post-processing of raw data.

Dynamic equations to solve

During numerical simulation, we will solve the following force balance equations 5.34,5.36,5.35 (for P, ϱ, ξ^{α}, Π and π), for the unknowns ϕ, u, $v^{\alpha}(\alpha = 1, .., A)$ and the plastic flow equation for the unknown F^{p} using finite element analysis methods. For each equation an appropriate boundary condition was applied. For instance,

1. $\mathrm{div} P = 0$ in Ω with boundary conditions on u as shown in figure 82.
2. $\mathrm{div} \varrho - \pi = 0$ in Ω with boundary conditions on ϕ (see figure 82).
3. $\mathrm{div} \xi^{\alpha} - \Pi^{\alpha} = 0$ in Ω with boundary condition on v^{α}
4. $\dot{F}^{p} = L^{p} F^{p}$ in Ω with $F^{p}(.,0) = \tilde{R}^{OT}$ in Ω

To solve these equations we have reprised the methodology devised by Admal (Admal et al., 2018), we have used the MUMPS (Multifrontal Massively Parallel Sparse direct Solver which is used to solve large sparse systems of linear algebraic equations on distributed memory parallel computers) and BDF (Backward Differential Formula) time stepping algorithm due to its versatility (it is described in appendix section C.1.9.4) both implemented in COMSOL V5.6 and both with a tolerance of 10^{-8}.

Input parameters to the governing equations

To solve force balance equations (eqs.5.34, 5.35 and 5.36 derived in appendix C.1.3), grain boundary energy equation (eq.5.37), bulk elastic energy equation (eq. 5.38) and thermodynamic constitutive equations (eq.C.35) require input parameters and/or functions. For instance, the presence of a linear term $g(\phi)s|G|$ in equation 5.37 results in a singular diffusive terms in both microscopic force balance equation 5.35 and mobility function, therefore for numerical convenience, the terms $|G|$ is approximated with $p(|G|)$ with a function p defined in equation 5.10. However, γ has to be carefully chosen because if γ increases the gradient of plastic distortion tends to zero in the bulk (Admal et al., 2018).

For the function $g(\phi)$ we have used

$$g(\phi) = -2\Big(\ln(1-\phi) - \phi\Big) \tag{5.41}$$

which results in non-convex grain boundary energy as predicted by Read and Shockley (Read, 1953; Kobayashi and Giga, 1999). For other constants appearing in grain boundary energy functional such as α, e, s and ε, we have initially used the value from KWC model and they are given in table 5.1, and then after we have redone the convergence test to determine the suitable values for our cases (see section 6.1.1 for more details). For parameter B^α associated with ξ^α_{diss} in equation C.35, we have used the value provided by Admal (Admal et al., 2018). In addition we have assumed that plastic distortion evolves due to the presence of four slip systems with slip directions $s^{\alpha=(1,2,3,4)}$ which are also given in table 5.1. For the initial value of $|G|$ we have used the values in table 3.4 to calculate the initial values of the components of G following equation 5.30. For a material, we have imported elastic constants entering the bulk elastic energy functional for Nickel from a data base of COMSOL V5.6.

Table 5.1: List of parameters used for the implementation of the Admal & Marian model (Admal et al., 2018).

ε^2 $\times 10^{-10}$ $[Jm^{-1}]^2$	α^2 $\times 10^{-9}$ $[Jm^{-1}]^2$	s $[Jm^{-2}]$	e $\times 10^{-8}$ $[Jm^{-3}]$	B^α $\times 10^{-15}$ $[J.s.m^{-1}]$	γ $\times 10^{-7}$ $[m]$	s^1	s^2	s^3	s^4
3.1999	7.95	1.7	3.5	1	5	$(1,0)$	$(0,1)$	$\frac{1}{\sqrt{2}}(1,1)$	$\frac{1}{\sqrt{2}}(\bar{1},1)$

Geometry setup and initial conditions

We have used the bi-crystalline geometry employed in atomistic simulations. A planar grain boundary is introduced in the centre of the simulation box by following procedure described in section 5.3.2.1. A smoothened step-wise function $\theta(x)$ is used to describe orientation of the crystal lattice. As described in section 5.1 a diffuse interface bicrystal is generated by regularising $\theta(x)$ into a smooth function as follows

$$\theta(x) = -\frac{\theta_0}{2} + \frac{\theta_0}{1+\exp[-4(x-L/2)]} \tag{5.42}$$

Where θ_0 is a misorientation angle between adjacent grains. Note that this expression for θ is not exactly solution of the KWC model as we will see at the end of the chapter, and few iterations are required to fully relax the initial fields. A strain free bicrystal is obtained by starting with $F^p(X,0) = R^{0T}(\theta(x))$ where R is a regularised rotation field. Contrary to atomistic part, we will use only a two dimensional domain Ω since the primary focus here is to provide a working and reliable model of simulating grain boundary evolution that is able to preserve the physics observed in atomistic simulations. Similarly to atomistic simulation box, we have used the same length along the x and y axis. The use of similar box size will allow to compare directly both methods. Figure 82 shows the simulation box setup in which the grain boundary is shown by a dotted green line in the middle of the box.

Boundary conditions

We will use both periodic and Dirichlet Boundary conditions (see section C.1.10 in appendix for more details). Periodic Boundary Conditions are shown in black. The use of periodic boundary conditions allows to simulate a semi-infinite domain which is large enough to statistically collect general trends on a large sample. Dirichlet boundary conditions are shown in red and blue. On the Dirichlet boundary conditions in red $x = -L$, we will impose solutions to our unknowns (u, ϕ and v^α) as follows:

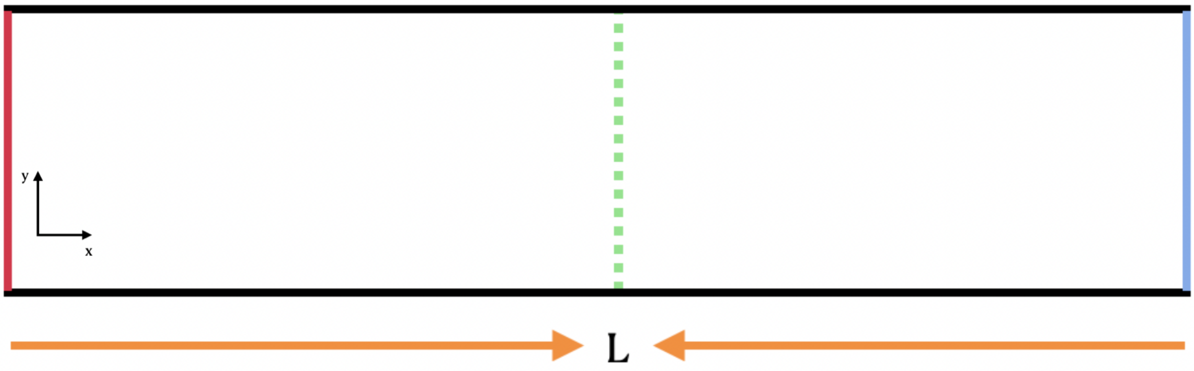

Figure 82: A schematic of a bicrystal used to study grain boundary migration. The grain boundary is shown as a dotted line. Dirichlet boundary conditions are shown in red and blue, the periodic boundary conditions are shown in black.

$$\begin{cases} (u_1, u_2) = (0, 0) \\ \phi(-L) = 1 \\ v^\alpha(-L) = 0 \end{cases}$$

On the Dirichlet boundary conditions in blue ($x = +L$), we will apply driving force for grain boundary migration. This motive force is exerted by translating the surface $x = +L$ upwards (along the y axis) with a constant velocity $c[m.s^{-1}]$ for a time duration $t_0[s]$ and then held fixed in that position for the duration of a simulation. Consequently, the following solutions are imposed to unknowns at $x = +L$

$$\begin{cases} (u_1, u_2) = \left(0, ct\mathbb{I}_{[0,t_0)} + ct_0\mathbb{I}_{[t_0,\infty)}\right) \\ \phi(+L) = 1 \\ v^\alpha(+L) = 0 \end{cases}$$

Where $\mathbb{I}(x,t)$ is an indicator function defined for $x \in \mathbb{R}^d$ $(d = 1, 2)$ and $A \subset \mathbb{R}^{d+1}$ as

$$\mathbb{I}(x,t) = \begin{cases} 1 \text{ if } (x,t) \in A, \\ 0 \text{ otherwise} \end{cases} \tag{5.43}$$

Isoparametric representation of the simulation box

Creating a high-quality mesh is one of the most critical factors that must be considered to ensure accuracy in numerical simulations. Consequently, the displacement variables u_1 and u_2, the slip rate v^α and order parameter ϕ will be interpolated using the Lagrange quadratic finite elements due to a dominant second derivative term in kinetic equations. A convergence test was carried out in order to choose the shape and size of an element to use in meshing the simulation box. Figure 83 shows an unstructured mesh with quadratic triangular elements used in our simulations in which the region around a grain boundary is finely meshed to improve accuracy in the grain boundary region. Note that we have taken advantage of the Adaptive Mesh Refinement (AMR) method implemented in COMSOL Multiphysics in order to mitigate computational time while maintaining precision. It is also important to note that since F^p is a smooth rotation field at $t = 0s$, it satisfies the orthogonality conditions (to mean ${F^p}^T F^p \equiv I$). Since it does not satisfy requirements to be interpolated using the Lagrange finite element, it has been replaced by its components R^p and U^p by using the polar decomposition as follows $F^p = R^p U^p$ Where R^p is plastic component of rotation field and it depends only on θ^p. U^p is the positive definite

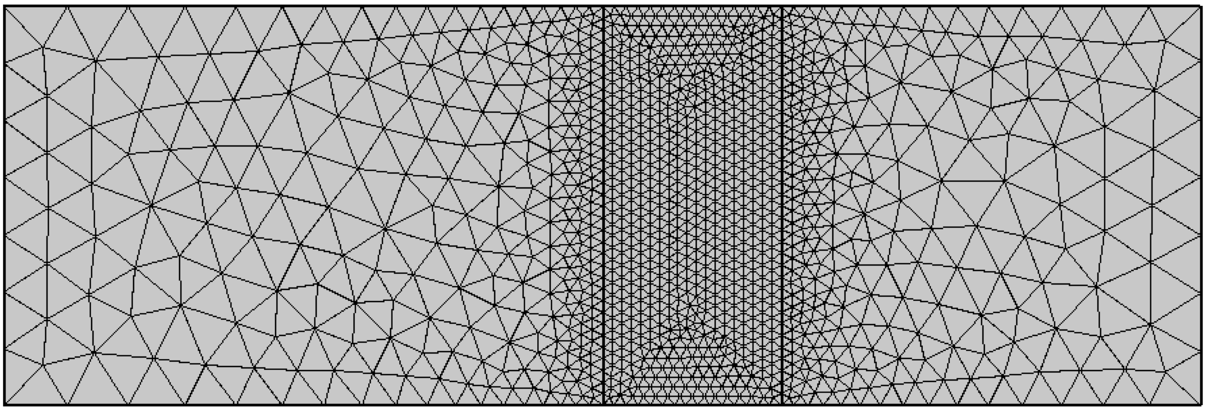

Figure 83: An adaptive mesh of triangular elements used in out simulation.

symmetric stretch tensor. Therefore $\boldsymbol{F^p}$ is interpolated using the Lagrange quadratic finite element interpolation of θ^p, U_{11}^p, U_{12}^p and U_{22}^p thus guaranteeing to circumvent this orthogonality conditions.

To move a grain boundary, a shear stress is applied on the blue surface of the simulation box (figure 82). The shear stress is imposed by translating the blue surface upwards at a constant velocity c in a range $[0-30] \times 10^{-4} ms^{-1}$ for a time $t_0 = 2 \times 10^{-5} s$ and it was held in that position for the rest of the simulations. From section C.1.5 in appendix, we did not solve energy balance equation in this study because all simulations are performed at a constant temperature. All simulations were allowed to run long enough ($2 \times 10^5 s$). In order to investigate the influence of temperature on migration of a grain boundary, we have applied temperature in a range $[0, 1000]K$ which will allow to compare directly with the MD results. In our simulations we have used the inverse mobility ($M_\alpha^{\dot{\alpha}}$) function used by Admal and Marian (Admal et al., 2018). It reads, for $\alpha = [1, 2, 3, 4]$,

$$M_\alpha^{\dot{\alpha}} = m_{min}^\alpha + \left(1 - 10\phi^3 + 15\phi^4 - 6\phi^5\right)\left(m_{max}^\alpha - m_{min}^\alpha\right) \tag{5.44}$$

Where the minimum mobility is attained when $\phi = 1$ is $m_{min}^\alpha = 1 \times 10^{-12} m^3 J^{-1} s^{-1}$ and the maximum mobility is attained when $\phi = 0$ is $m_{max}^\alpha = 1 \times 10^{-3} m^3 J^{-1} s^{-1}$. It is important to note that if $m_{max}^\alpha \gg m_{min}^\alpha$, it ensures that the simulation is only restricted to modelling grain boundary mediated plasticity otherwise reversing m_{max}^α and m_{min}^α in equation 5.44 leads to modelling bulk plasticity.

Chapter 6

Results

In this chapter, we present static and dynamic properties of all investigated grain boundaries that are listed in table 3.4. The curves are plotted from phase fields and fields collected from a dashed red horizontal line passing through the center of the simulation domain as figure 84 shows. In this chapter, important relationships and results are derived. We will start by doing a sensitivity test on the parameters and terms appearing in the phase field model to investigate a role they play. This will allow us to find suitable values of these parameters to be used in this project.

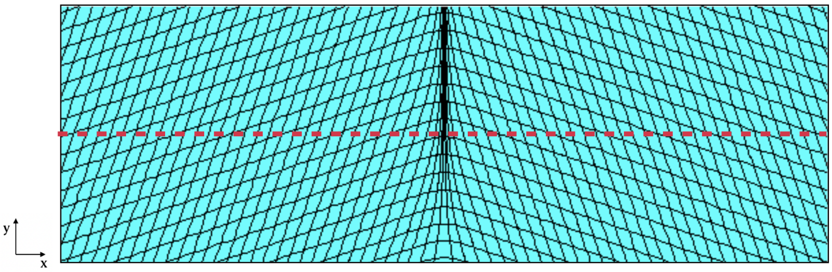

Figure 84: All data points are collected on the horizontal red line passing through the center of the simulation box.

6.1 Static study of grain boundary properties

6.1.1 Parametric sensitivity analysis

In the first step, we have analysed the role played by different parameters in the phase field equation. We know from the analysis made on KWC model that ε and α in particular are expected to be parameters that set the strength of the penalties for gradients in misorientation and degree of crystalline orientational order, respectively. In addition, ε and s are expected to have an opposing effect in setting the width of a grain boundary. In order words, decreasing s increases the width of a grain boundary whereas decreasing ε decreases the width of a grain boundary. Importantly, if $\varepsilon = 0$ and $s \neq 0$, a grain boundary becomes a sharp interface and if $\varepsilon \neq 0$ and $s = 0$, the misorientation field θ becomes a linear function in steady state. Therefore, the terms with $|G|$ are expected to act together to set the finite width of a grain boundary. From equation 5.15, one can readily notice that α, e and s play an important role in defining the width of the grain

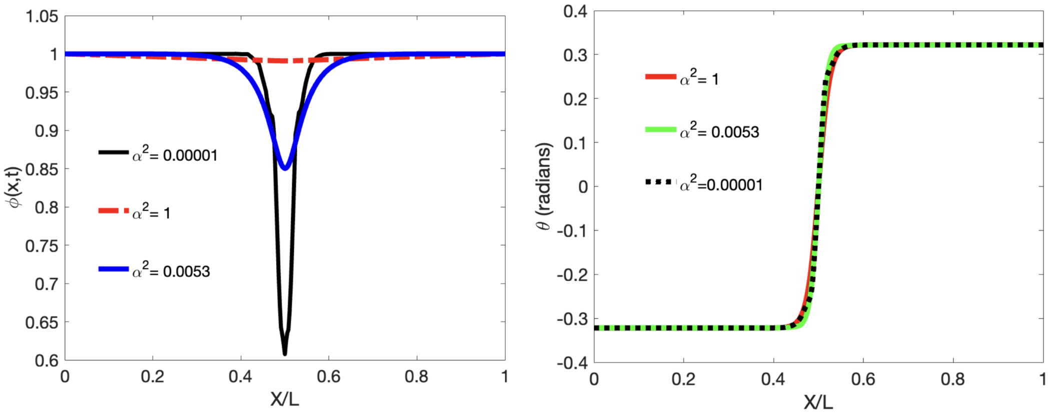

a) b)

Figure 85: Effect of varying values of α on field a) ϕ and b) θ in $\Sigma5(3\bar{1}0)$ symmetric tilt grain boundary.

boundary and from equation 5.14 that s plays an important role in describing energy of a grain boundary. As we will see later, it is also expected that ε plays an important role in the mobility of a grain boundary. According to Kobayashi et al. (Kobayashi and Giga, 1999), the role played by different parameters can be examined by studying the steady state solution. Therefore, in this study our system was allowed, in the absence of driving force for migration, to evolve $2 \times 10^{-3}s$ long enough to reach a static equilibrium configuration. The values of these constants were varied in a range given in table 6.1. To study influence of a given parameter, we have kept other parameters constant with the

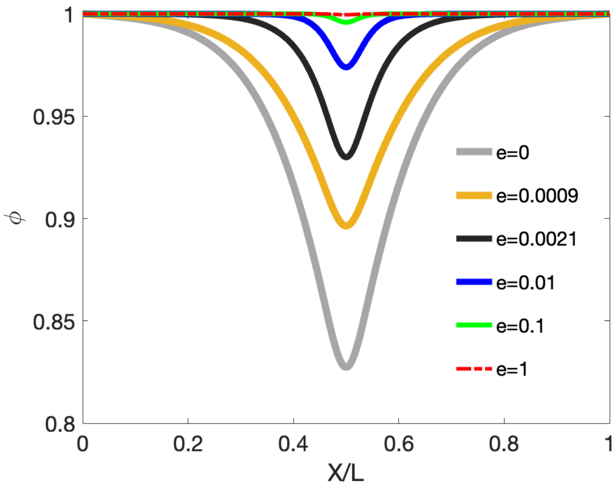

Figure 86: Effect of varying values of e on field parameter ϕ for $\Sigma25(7\bar{1}0)$ symmetric tilt grain boundary.

Table 6.1: Range of values used for sensitivity test

Parameter	$\alpha^2[fJ/nm]^2$	$s[fJ/nm^2]$	$\varepsilon^2[fJ/nm]^2$	$\gamma[nm]$	$e[J.m^{-3}$
Range	$[0-1]$	$[0-1]$	$[0-1]$	$[1-2000]$	$[0-1]$

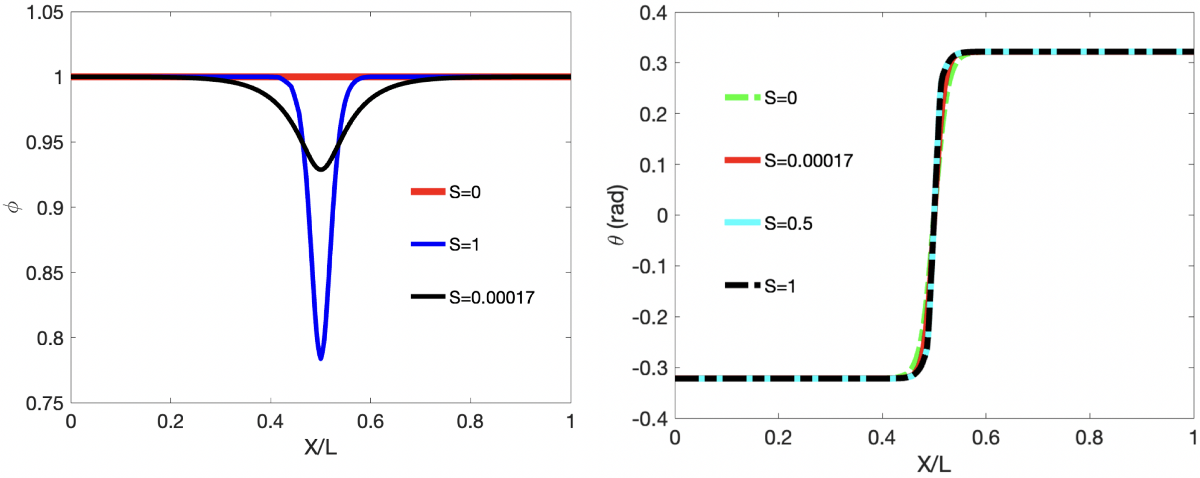

a) b)

Figure 87: The effect of varying s on a) ϕ and b) θ (in radians) solutions of $\Sigma5(3\bar{1}0)$.

values from the Admal et al. (Admal et al., 2018) and vary a parameter of interest. Since the field ϕ and the width of a grain boundary controls energy of a grain boundary, in the first time, we have investigated how parameter α affects the solution of ϕ and the width of a grain boundary. From figure 85a) one can notice how significantly α influences the solution of ϕ. As the value of α decreases the solution of ϕ picks downward in the region Ω_0^{GB} (grain boundary region) and the width of the Ω_o^{GB} region decreases. This is reasonable considering the solution of ϕ given in appendix D.1 and equation 5.15.

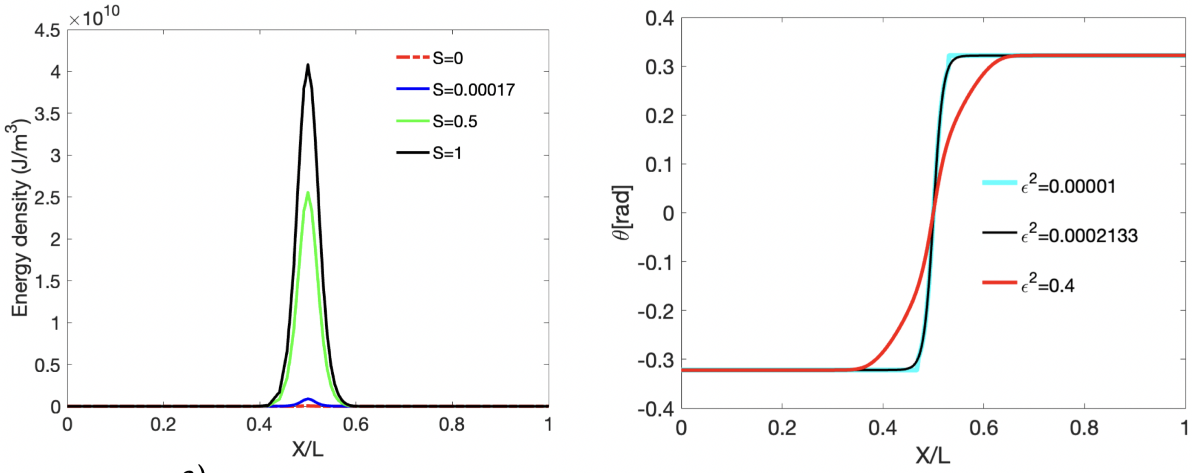

a) b)

Figure 88: a) The Effect of varying a) s on the energy density of $\Sigma5(3\bar{1}0)$ b) ε on the misorientation field θ.

This means that:

$$\begin{cases} \textbf{If } \alpha \to +\infty \textbf{ then } \phi_{min} \to 1 \\ \textbf{If } \alpha \to 0 \textbf{ then } \phi_{min} \to 0 \end{cases}$$

One can also see that the changes in the value of α manifest themselves in the solution

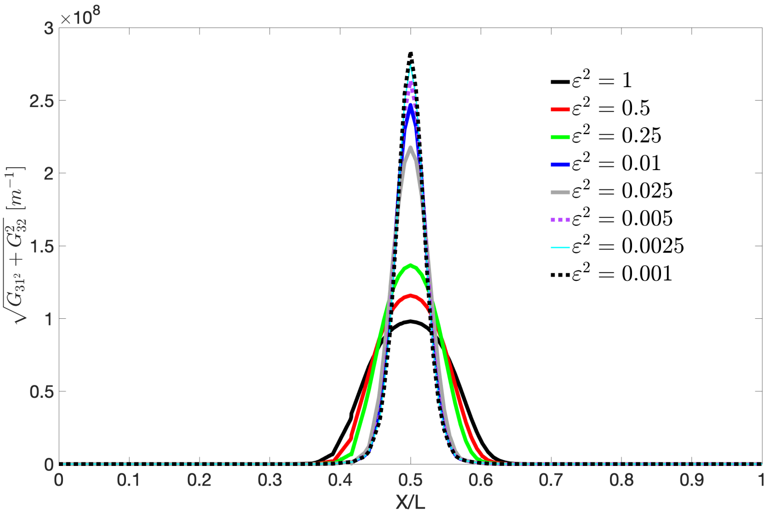

Figure 89: The effect of varying ε on norm of density of geometrically necessary dislocations in $\Sigma 25(7\bar{1}0)$ symmetric tilt grain boundary at $100K$ with a shear rate of $\dot{\gamma} = 2 \times 10^{-4} m.s^{-1}$.

of θ as figure 85b) shows, however, there is no clear trend. Here, it is important to note that for all values of α, a simulation domain is still divided into two regions Ω_0^p and Ω_0^{GB}, this is reasonable since the terms containing $|G|$ are not affected by changing α. In this study we have observed that the change in total energy of the system is not significantly affected by varying α. This is due to the fact that, depending on the relative weight of the other parameters in the energy equation, the contribution of the terms containing ϕ to the total energy of the system is negligible compared from contributions of terms containing $|G|$ (see figure 102). In the second step, we have examined the role of e. Figure 86 shows the dependence of ϕ field on the value of e. As the value of e decreases ϕ picks downwards and the width increases. This observation agrees with the formula 5.15 from KWC model. On the other hand from figures 87a) and b) one can notice the influence of s on numerical solution of ϕ and θ. It is evident that

$$\begin{cases} \textbf{If } s \to +\infty \textbf{ then } \phi_{min} \to 0 \\ \textbf{If } s \to 0 \textbf{ then } \phi_{min} \to 1 \end{cases}$$

The value of s decreases energy density decreases (see figure 88 a)). This is reasonable since ϕ_{min} tends to one leading to an increase in crystalinity in the domain. In the third case study, we have varied ε in a range given above. Figure 88 b) shows the influence of

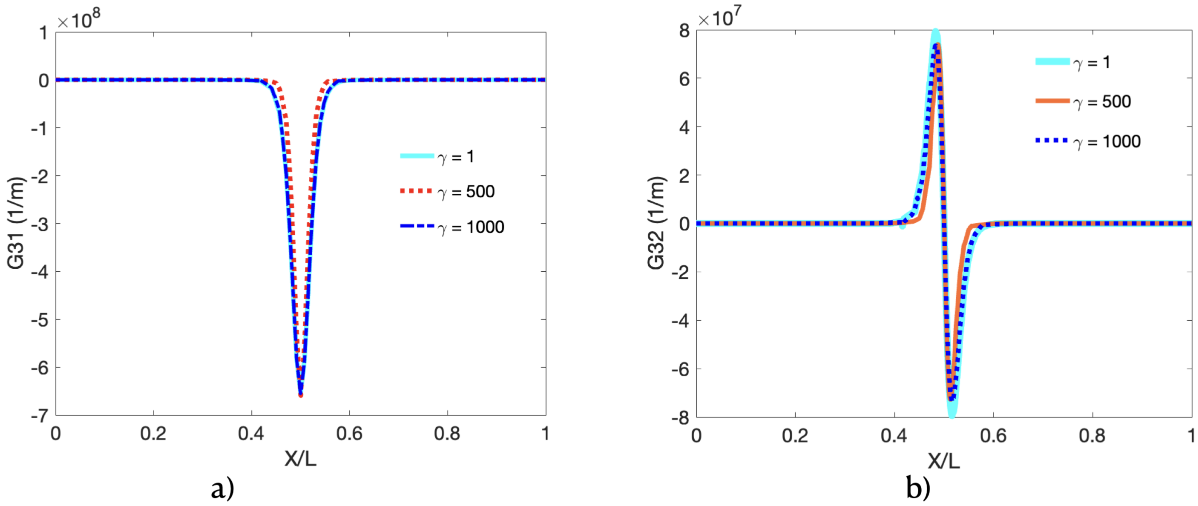

Figure 90: Effect of $\gamma[m]$ on the components of the dislocation density $|G|$ in $\Sigma5(3\bar{1}0)$ symmetric tilt grain boundary.

ε on the solution of θ. We see that:

$$\begin{cases} \text{If } \varepsilon \rightarrow 0,\ \theta \text{ function becomes a sharp step wise function} \\ \text{If } \varepsilon \rightarrow \infty,\ \theta \text{ function tends to be a linear function} \\ \text{At intermediate value of } \varepsilon,\ \theta \text{ is a step wise smooth function.} \end{cases}$$

The sharpwise nature of θ for $\varepsilon \rightarrow 0$ is shown by a curve in cyan colour.When the value of ε decreases the width of a grain boundary decreases. The increase of value of ε increases the width of a grain boundary until the field θ looses its step-wise nature and becomes a linear function as illustrated in figure 88 b). The same grain boundary width variation by changing the value ε manifests itself in plot of density of geometrically necessary dislocations. Figure 89 shows the dependence of the norm of $|G|$ on ε in $\Sigma25(7\bar{1}0)$ symmetric tilt grain boundary. It shows that as the value of ε^2 increases the width of a grain boundary increases and as the value of ε^2 decreases the curve picks upwards. Plus, one can remark also that the

$$\int |G_{ij}|dx = \sum \overrightarrow{b}_i$$

where $\overrightarrow{b}$ is the Burgers vector in the Franck Bilby model. Thus for a given grain boundary, $\sum \overrightarrow{b}_i$ is a constant and changing epsilon only changes the width of the grain boundary. By comparing the effect of varying s and ε^2, one can conclude that the term $g(\phi)s|G|$ plays a role of localising a grain boundary in the simulation box whereas the term $\frac{\varepsilon^2}{2}|G|^2$ tends to diffuse a grain boundary. Since $|G|$ is approximated by $p(|G|)$ as shown in equation C.42 in appendix, we have investigated how varying the value of γ affects $|G|$. This is necessary since it allows assessing the quality of approximation we are making.

Table 6.2: Parameter used in our calculations.

Parameters	α^2 $[fJ/nm]^2$	s $[fJ/nm^2]$	ε^2 $[fJ/nm]^2$	γ $[nm]$
values	0.0053	0.0017	0.0002133	510

One can notice from figures 90a) and 90 b) that the components of $|G|$ are slightly affected by varying γ. This is supported by the fact that varying γ does not affect the misorientation field between abutting grains which is reasonable since it is only used to remove the singularity. However, in our calculations, we have realised that as the value of γ increases the stiffness of the governing equations increases therefore consuming much computational resources. In conclusion, we have chosen to use, in the next calculations, the values of these parameters that produce the step-wise nature of θ function. These values are listed in table 6.2.

Here recalling that, the rotation field described in equation 5.42 has been used as an initial input to describe misorientation between grain one and grain two. Here we show its plots for symmetric $\Sigma5(3\bar{1}0)$ tilt grain boundary as a representative of all other grain boundaries investigated. Figure 91a) shows a colour coded steady state $\theta(x)$ field from $\theta(x)$ function and figure 91b) shows the same $\theta(x)$ function for only points collected from an horizontal line passing through the center of the simulation box (see figure 84). As expected, the KWC model (and by extension Admal et al. model) localised the GB in a finite region where $\nabla\theta \neq 0$ and a prefect crystalline region surrounding a grain boundary where $\nabla\theta = 0$. This localization of the GB, has been exploited to propose a path for an analytical solution of the 1D KWC problem, as will be seen latter. $\theta(x)$ acts as a regularised step function that returns a diffuse interface with a characteristic width. In the region Ω_0^p, $\forall x \in \Omega_0^p$, $\theta(x) = -18.43°$ in grain one and $\theta(x) = +18.43°$ in grain two, whereas it increases smoothly from grain one to grain two in the region Ω_0^{GB} [15].

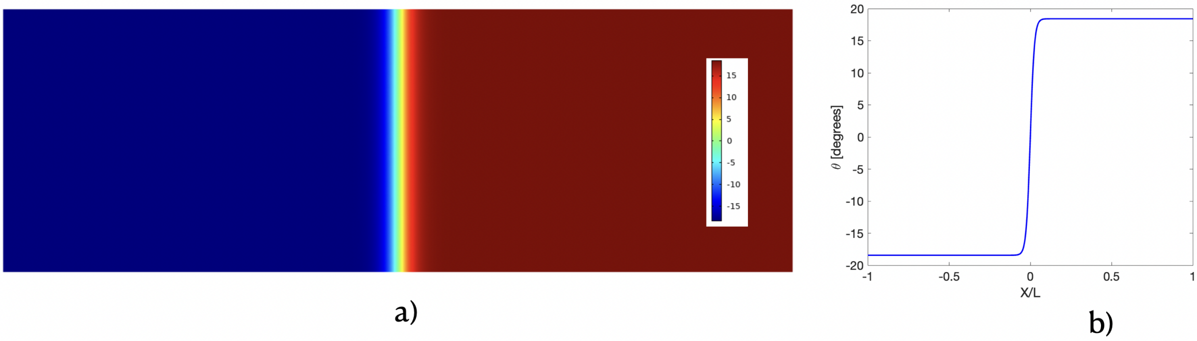

Figure 91: a) Colour plot of $\theta(x)$ over the domain for $\Sigma5(3\bar{1}0)$ tilt grain boundary (units in degrees) and b) curve of $\theta(x)$ function of the x-coordinates. The data points are collected from a horizontal line passing through the center of the simulation box.

In the next step, we have plotted the numerical solution of $|G|$ and ϕ. We have observed

---

[15] Note that we have denoted our domain $\Omega_0 = [-L, L]$ and the region containing a grain boundary is denoted $\Omega_0^{GB} = [-l, l]$ and the perfect crystalline region is denoted by $\Omega_0^p = \Omega_0 \backslash \Omega_0^{GB}$.

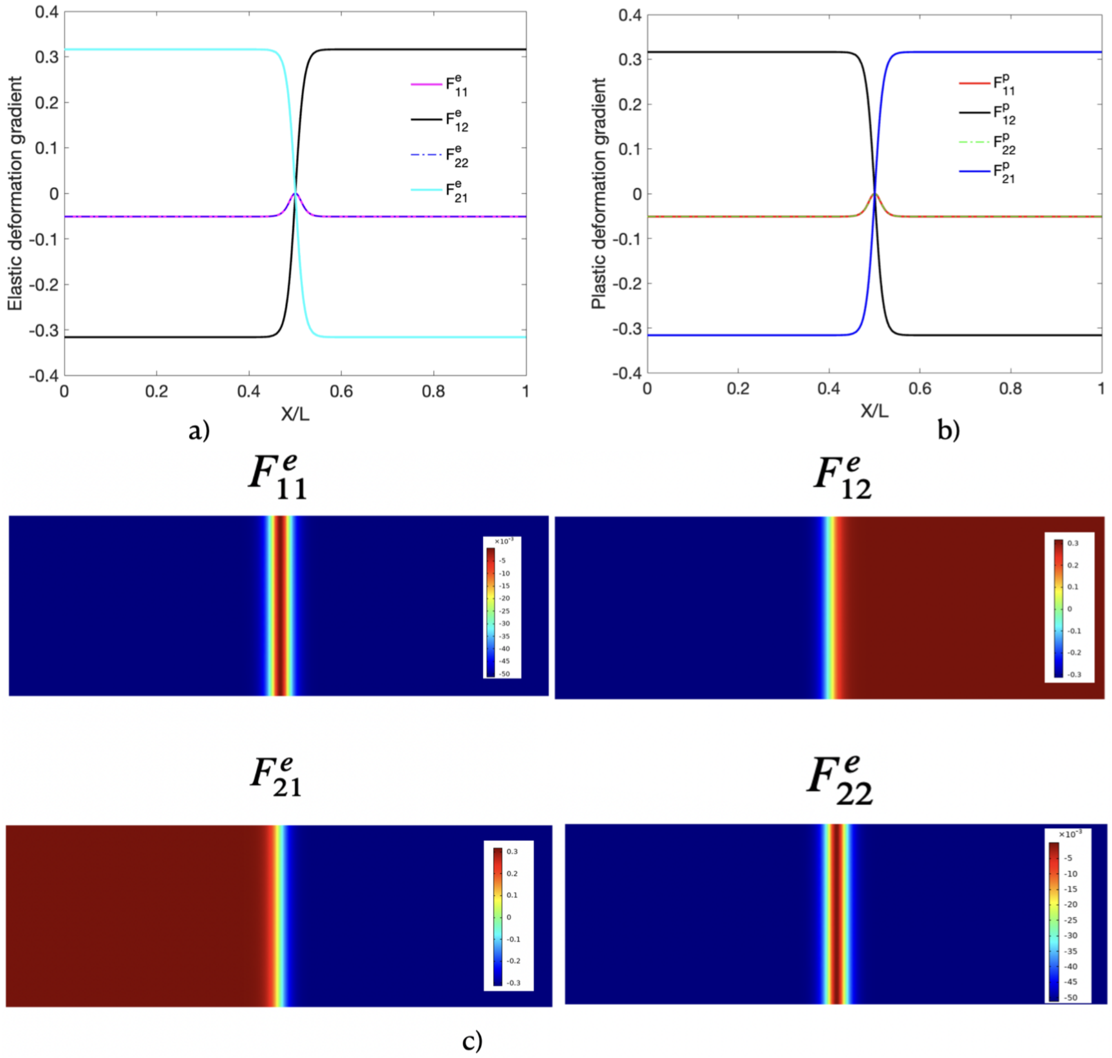

Figure 92: Plots of components of a) elastic deformation gradient $\boldsymbol{F}^e$ and b) plastic deformation gradient $\boldsymbol{F}^p$ in $\Sigma5(3\bar{1}0)$ grain boundary c) colour map of $\boldsymbol{F}^e$ components for the same grain boundary.

that within each grain $|G(x)| = 0$ and $\phi(x) = 1$. This indicates a perfect crystalline region.

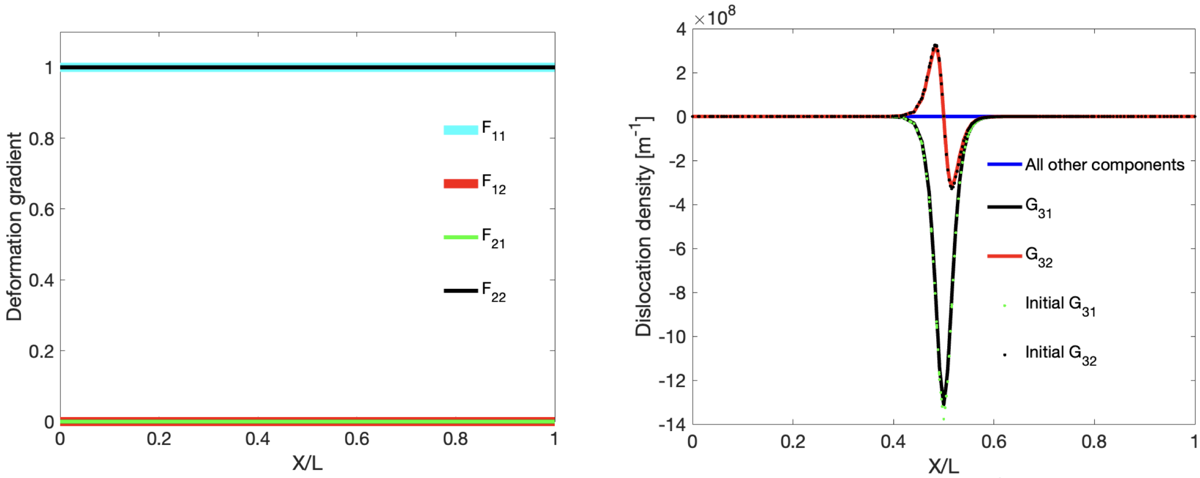

a) b)

Figure 93: a) Deformation gradient F for $\Sigma5(3\bar{1}0)$ symmetric tilt and b) plots of one dimensional simulation modelling of a flat $\Sigma25(4\bar{3}0)$ symmetric tilt grain boundary under steady state conditions.

$\phi(x)$ drops at the grain boundary indicating a decrease in crystallanity and in the same time $|G(x)|$, which is equivalent to the presence of geometrically necessary dislocations at grain boundary. Next, we considered the distribution of different components of the deformation gradient. Note, here, that the regularised $\theta(x)$ shown above has been used to describe initial rotation field $R^o(\theta(x))$ in the bicrystal as described in section 5.3.2.1. Recall here that $R^o(\theta(x))$ satisfies the condition of orthogonality, therefore, the total

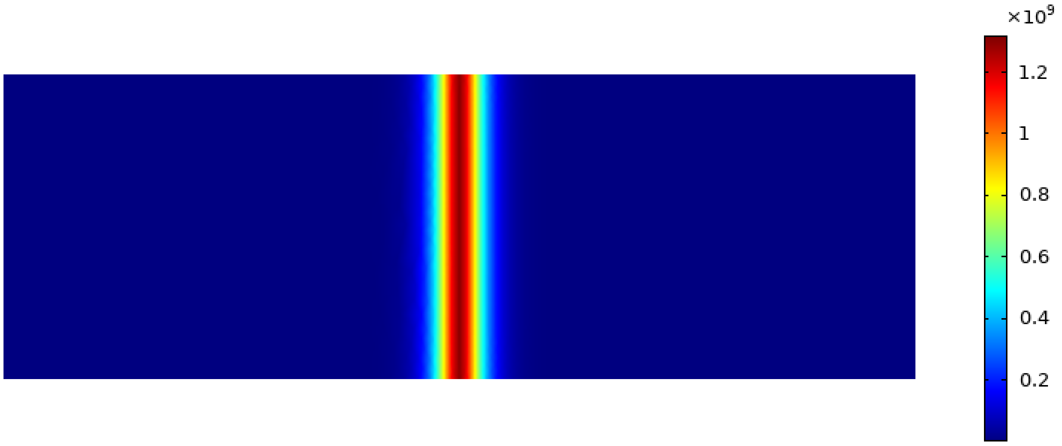

Figure 94: Map of the norm of the density of the Geometrically necessary dislocations (in units of m^{-1}) in the un-deformed flat $\Sigma25(4\bar{3}0)$ symmetric tilt grain boundary.

deformation gradient F satisfies $F \equiv I$ and both elastic and plastic deformation gradients read

$$\begin{cases} F^e = R^0\Big(\theta(x)\Big) \\ F^p = R^{0T}\Big(\theta(x)\Big) \\ F = F^e F^p \end{cases} \tag{6.1}$$

Figure 92 a) to c) show the resulting steady state profiles for components of elastic (F^e), plastic deformation (F^p) gradient and the colour code map for the F^e components respectively for $\Sigma5(3\bar{1}0)$ symmetric tilt grain boundary. One can see from figure 92 a) to c) that all components remain constant in each grain and vary only at the grain boundary. In addition, one can notice that F^p is a inverse of F^e.

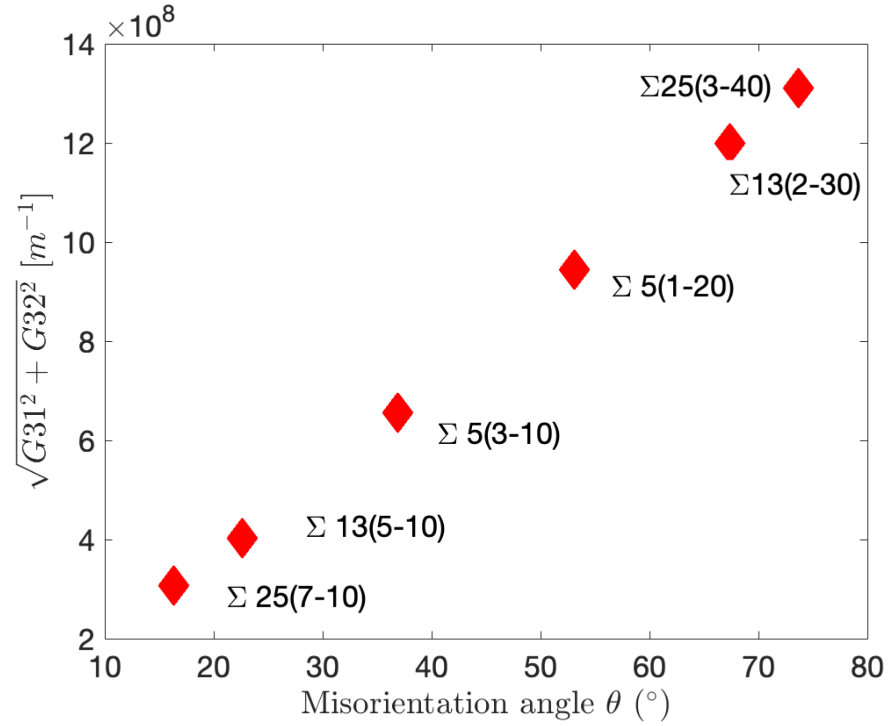

Figure 95: Dependence of the maximum value of $\sqrt{G_{31}^2 + G_{32}^2}$ on misorientation angle θ.

For instance, Fe_{12} increases at grain boundary to reach a maximum value while F_{12}^p decreases in a similar way to reach a minimum value. The F^e being an inverse of F^p and vice versa manifests itself in the curves of components of F shown in figure 93a). They show that all diagonal components of F $(F_{11}$ and $F_{22})$ equals one, whereas F_{12} and F_{21} are zero in each grain and at grain boundary.

Although there exist both elastic and plastic distortion in the vicinity of a grain boundary as explained in section 5.3.1.1, there is a conservation of the mass densities in the reference and the deformed configurations. This comes from the fact that det F

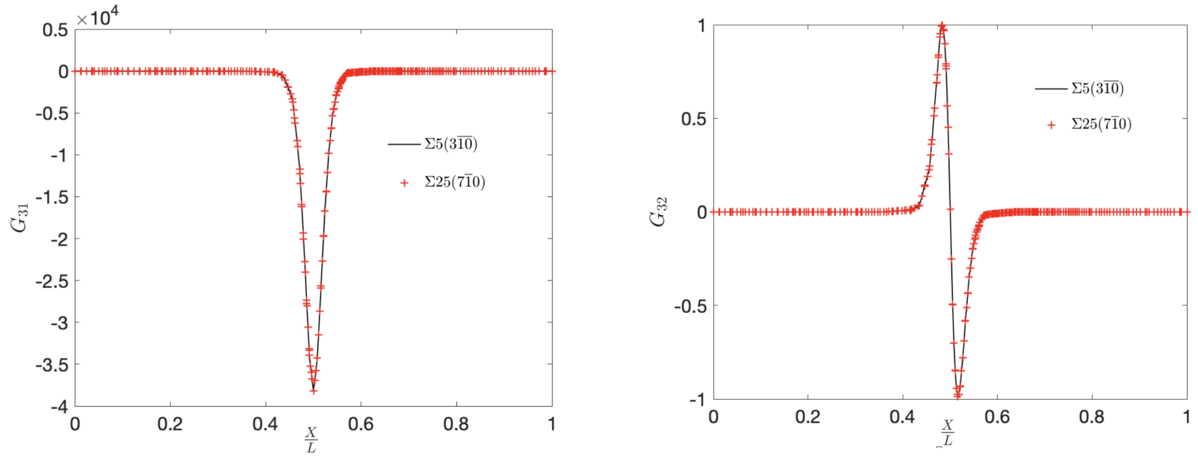

a) b)

Figure 96: The normalised distribution of G31 and G32 in S25(710) and S5(310).

describes the volumetric part of the deformation which reads

$$J = \det F \equiv \frac{\rho_0}{\rho} \tag{6.2}$$

where ρ_0 is the mass density in the reference configuration and ρ is the mass density in the deformed configuration. In addition, the symmetric nature of curves of components of F^e and F^p indicates that both grains are equally distorted. On the other hand, it is important to note that both F^e and F^p were expected to be zero in the interior of both grains. The non zero value is a consequence of approximating $|G|$ by $p(|G|)$ in term $g(\phi)s|G|$.

Next, we discuss the distribution of $|G|$ (see figure 94) since $|G|$ depends upon F. But first a precision is required. The model of Admal et al. is based on the kinematic equivalence of a rotation transformation described by a matrix $R^{G_1G_2}$ and an array of discrete dislocations. The Frank-Bilby equation states this equivalence as:

$$\sum \mathbf{b_i} = \left(\mathbf{R^{G_1G_2}} - \mathbf{I}\right) \cdot \mathbf{k}, \tag{6.3}$$

where $\mathbf{I}$ is the identity matrix, and $\sum \mathbf{b_i}$ the sum of Burgers vectors intersected by the probing vector $\mathbf{k}$ contained within the interface. This is equivalent, to a GND tensor $\mathbf{G}$:

$$\mathbf{G} = \sum \frac{\mathbf{L_i} \otimes \mathbf{b_i}}{\mathbf{V}} \tag{6.4}$$

Where, L_i is a dislocation line and V is a volume of a domain. For a STGB around the z axis and a plane along x the dislocation array is made of edges, which correspond to a GND component G_{31}. Admal's model not only deals with GND but with the GND's spatial distribution, taken first as a Dirac $\delta(x)$:

$$\mathbf{G} = \begin{bmatrix} 0 & 0 & 0 \\ 0 & 0 & 0 \\ \Delta\theta_0\delta(x) & 0 & 0 \end{bmatrix} \tag{6.5}$$

, where $\Delta\theta_0$ is the misorientation across the GB. The model, after relaxation will in 2D, have two non zero distributions:

$$G_{31} = -\cos(\tilde{\theta})\nabla\theta(x) \tag{6.6}$$

$$G_{32} = -\sin(\tilde{\theta})\nabla\theta(x) \tag{6.7}$$

with $|G| = \nabla\theta(x)$ However, we can notice that the distribution of G_{32} is antisymmetrical and will not contribute to the overall rotation of the grains. Figure 93b) shows plots of components of $|G|$ tensor versus normalised x coordinates obtained from a steady state simulation of $\Sigma25(4\bar{3}0)$ symmetric tilt grain boundary which is shown as a representative of all other investigated grain boundaries.

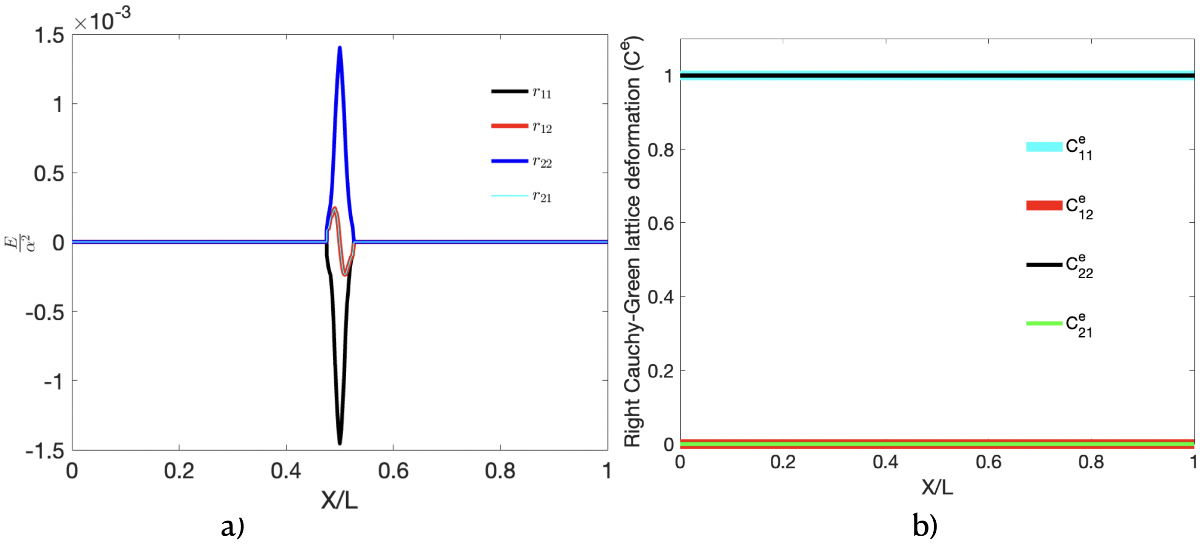

Figure 97: Plots of a) lattice Lagrangian strain E over the constant α^2 where r_{ij} stands for the $\frac{E_{ij}}{\alpha^2}$ component b) Right Cauchy-Green lattice deformation in $\Sigma25(4\bar{3}0)$.

The obtained results are compared from initial inputs obtained from using initial $\theta(x)$ values. It is clear that they are in a good agreement. In addition, figure 93b) confirms that all components of $|G|$ are zero except G_{31} and G_{32}. One sees that in interior of the grains all components are zero indicating the lack of dislocation inside the grains this is re-shown in the colour plot of the norm of the density of the geometrically necessary dislocations in figure 94 in which the dark blue and dark red corresponds to the lowest and highest dislocation density respectively.

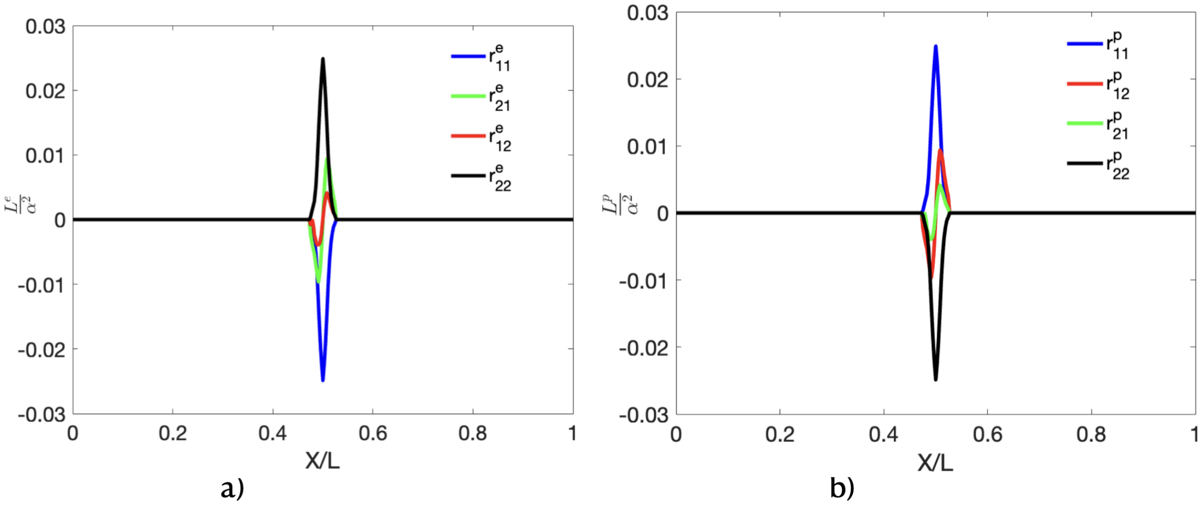

Figure 98: a) Elastic and b) plastic component of velocity gradient over α^2 for $\Sigma 25(4\bar{3}0)$ symmetric tilt grain boundary.Where r^e_{ij} and r^p_{ij} stand for $\frac{L^e_{ij}}{\alpha^2}$ and $\frac{L^p_{ij}}{\alpha^2}$ respectively.

To assess the change in GND distribution for the various STGB we have considered, we plot first the maximum of $|G|$ (which corresponds mostly to the maximum of G_{31}) as a function of the misorientation angle. This is shown in Figure 95, and we see the maximum of $|G|$ linearly increases with misorientation $\Delta\theta_0$. When, considering the two previous equations 6.5 and 6.7, it becomes clear, that the GND distribution may be the same. This is what is checked in figure 96, for two GBs with respectively small and large misorientation angles. We see that the -rescaled- spacial distribution for G_{31} and G_{32} are rigorously identical. This is a key feature of the Admal et al. model, that could be very interesting to exploit for future modelling and theoretical developments.

Since the time dependent simulations of flat symmetric grain boundary requires to start with a relaxed configuration, we have made sure that both crystals are equally deformed in order to avoid favouring one grain over an an other. As we want to deploy a strain free bicrystal, we have started by examining the strain distribution in the bicrystal. Figure 97a) shows curves of components of the lattice Lagrangian strain (E^e) versus the normalised $x-$ coordinate of the simulation box.
One can see that E^e is zero away from grain boundary and negligibly oscillates about zero in the vicinity of a grain boundary even if it was expected to be zero. This expectation comes from the fact that representing a grain boundary as a continuum dislocation distribution instead of a discrete array of dislocations results in no Lagrangian strain near a grain boundary. However, the presence of negligible E^e in the vicinity of a grain boundary shown in figure 97a) can be attributed to the construction of grain boundary that uses $|G|$ instead of the exact lattice gradient tensor $R^{eT}\text{curl}R^{eT}$. This Lagrangian strain is insignificant, in fact, a measure of the deformation independently of the rotation

has confirmed a deformation free bicrystal as shown in figure 97b.

Figure 97b) shows that there is no right Cauchy green lattice deformation $\boldsymbol{C^e}$ in the bicrystal, consequently, there is no stretching of the lattice. $\boldsymbol{U^e} \equiv \mathrm{I}$ can be explained by the fact that in the case where micro-rotation follows elastic rotation such that $\boldsymbol{R} = \boldsymbol{R^e}$ the resulting microstructure coincides with the frame of the reference microstructure and the associated elastic stretches are significantly small. We have also verified that the factors that contribute to the micro or macro stress during grain boundary migration are inactive in static simulations. We have first verified that the components of elastic and plastic velocity gradients are both inactive. Since, time dependant simulations of flat symmetric grain boundary requires to start with equal amount of slip in each grain to avoid favouring one grain over an other, in the second step, we have that the resolved shear stress τ is equal for both grain one and grain two. Figure 99a) shows the resolved shear stress τ on α slip plane expressed in equation C.18 (in appendix). It is clear that τ is zeros in the interior of each grain whereas it is not at grain boundary. In addition One can see that there is an equal amount in both grains. In addition, it is important to verify if both grains in a bicrystal are subjected to similar magnitude of the stress due to slip system. Figure 99b) shows microscopic stress ξ^α on each slip system α expressed in equation C.31. One can once again see that there is an equal amount of stress on each side of a grain boundary core and that the stress is zero in interior of grain one and two. This means that, the bicrystal is obtained from a reference single crystal by the right amount of slip in each grain such that both grains undergo a relative rotation but the underlying lattice in the bicrystal remains strain free as equation 6.1 shows. One can recall that ξ^α is addi-

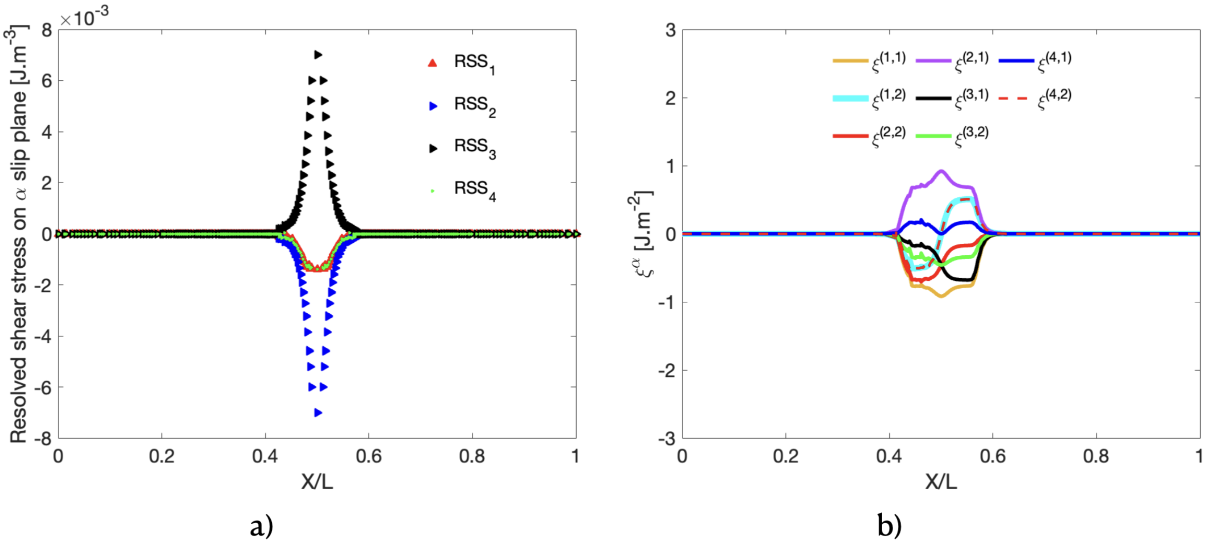

a) b)

Figure 99: a)Resolved shear stress τ on $\alpha = [1, 2, 3, 4]$ slip plane expressed in equation C.18, RSS for $\alpha = [1, 2, 3, 4]$ denotes resolved shear stress due to slip plane $\alpha = 1$ b)Plots of micro-stress ξ^α due to slip activity in flat symmetric tilt grain boundary $\Sigma 5(3\bar{1}0)$. Note that the $\xi^{\alpha,b}$ indicates the back stress of slip $\alpha = [1, 2, 3, 4]$ with a slip direction $b = [1, 2]$ for $b = 1$ in $x-$direction and $b = 2$ in $y-$direction.

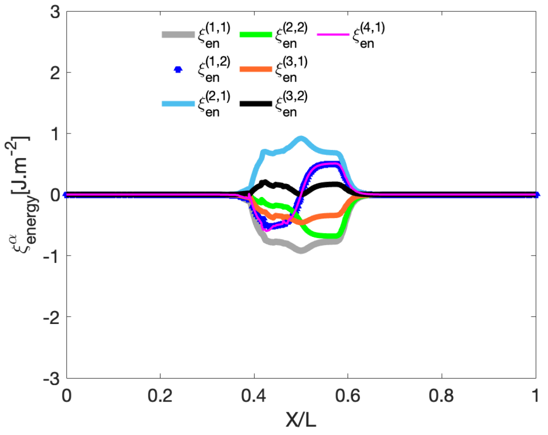

Figure 100: Plots of energetic component of the micro-stress ξ^α due to slip activity in flat symmetric tilt grain boundary $\Sigma5(3\bar{1}0)$. Note that the $\xi^{\alpha,b}$ indicates the back stress of slip $\alpha = [1, 2, 3, 4]$ with a slip direction $b = [1, 2]$ for $b = 1$ in $x-$direction and $b = 2$ in $y-$direction.

tively decomposed into energetic part which is described by equation C.33 and dissipative part described by equation C.35. It is important to understand the contribution of both parts to the total energy due to slip systems. Since we want one grain to be exactly a mirror image of the other, it is also important to verify if the force due to dislocations (Peach-Koehler force) is identical on both sides of the grain boundary.

Figure 100 shows curves of the Peach-Koehl force (ξ_{energy}^{α}) versus normalised $x-$ coordinate. One can notice that the Peach-Koehler force is zero in each grain but change at grain boundary this is due to the existing geometrically necessary dislocations at grain boundary. In addition, if one compares both figures 99 b) and 100 one can notice that the contribution of the dissipative component is very negligible compared from the energetic

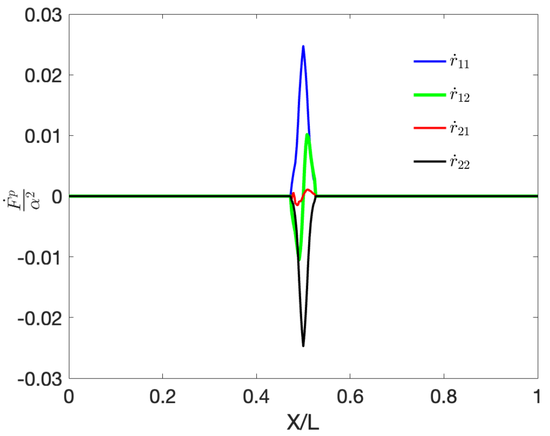

Figure 101: Plots of components of the plastic flow rate $\dot{F}^p$ (described in equation 5.21) over constant α^2 for a flat symmetric tilt $\Sigma25(4\bar{3}0)$ grain boundary.Where $\dot{r}_{ij}$ stands for $\frac{\dot{F}_{ij}^p}{\alpha^2}$

component.

This is reasonable since a grain boundary is stationary and ξ^{α}_{diss} depends on micro-shear rate ∇v^{α} due to slip (see equation C.35) which is inactive since a grain boundary is stationary. During dynamic simulation, $\boldsymbol{F}^p$ is updated from $\dot{\boldsymbol{F}}^p$ as section 5.21 shows, it is imperative to be sure that there is no localised plastic flow prior to applying driving force for grain boundary migration. Therefore, in our static simulation, we have made sure that there is no active localised plastic flow. In the next step, we can compare the relative contributions of the different energy terms (with the current parameters used), from section 4.3, one can recall that this energy functional will be connected to the driving force for the grain boundary migration. As discussed in section 4.2.4, the total energy of the system is a summation of contributions from different terms in the equation of total energy of the system (see equation 4.5). Figure 102 shows, the contributions to total energy of the system from different terms in the total energy functional at 0K for a relaxed GB. One can easily see that the major contribution comes from the terms containing dislocations density tensor and the contribution from the terms that depend on the order parameter ϕ is insignificant. This agrees fair well with the work of Admal and Marian (Admal et al., 2018).

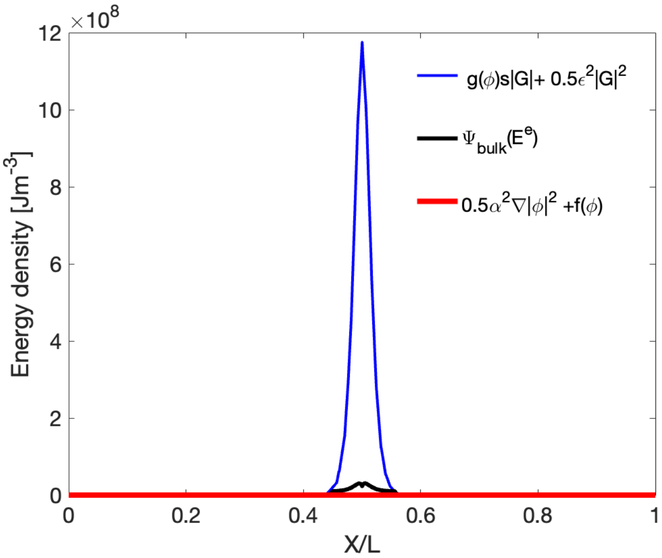

Figure 102: Contributions of the three parts of the total energy density of the symmetric $\Sigma 25(7\bar{1}0)$ tilt grain.

6.1.1.1 Comparison between the GB energy obtained from MD and PF

It is now possible to compare the GB energy predicted by the Phase field method from the GB energies measured by molecular dynamics in part I. However, simulations made using the phase field method are performed in a two-dimensional domain, whereas atomistic simulations were performed in a three-dimensional domain. Therefore to compare grain boundary energy on equal footing, grain boundary energies from MD is expressed per unit length, by multiplying by the appropriate length. The table 6.3 shows this comparison and the GB energies obtained by the two approaches are found to be in a nice agreement. This result is very surprising as the PF parameters used until now have no connections with MD data except for the initial input of the G tensor. The values are however close to the values (α, ϵ, s, e) suggested in (Warren et al., 2003) where the materials parameter are scaled with respect to a typical value for the latent heat L per unit of volume, $L = 2 \times 109 J/m^3$ of metals. The PF model accounts for the elastic distortion induced by the GBs. Alternatively, this nice agreement could means that for the simple GB included here, including elasticity as the main part of the GB energy is sufficient. This should be investigated in more details.

Table 6.3: Comparison of grain boundary energy from Molecular Dynamics (MD) and Phase Field (PF).

GB plane	$(3\bar{1}0)$	$(1\bar{2}0)$	$(5\bar{1}0)$	$(2\bar{3}0)$	$(3\bar{4}0)$	$(7\bar{1}0)$
Σ	5	5	13	13	25	25
MD energy $[J.m^{-1}]$	5.9	6.3	6	5.4	4.7	5.5
PF energy $[J.m^{-1}]$	6.1	6.4	5.8	5.8	5.5	5.3

6.2 Simulations of grain boundary migration

We now move to dynamic simulations of GB migration and compare the results to migration simulated thanks to MD in part I. For this we will mimic in the PF, the configuration and simulation conditions employed in MD. To move a grain boundary we have applied a shear stress as described in previous section and all simulations were run $2 \times 10^5 s$ and the temperature was varied between the range $[0 - 1000] K$. In the literature, it was reported that the active slip systems control the migration mechanisms of a grain boundary whether sliding or shear coupling (Admal et al., 2018), therefore in our time dependent simulations we have first run a test to investigate the influence of slip system on migration mechanism of a grain boundary.

6.2.1 Sensitivity Study

In section 6.1.1, we have proposed a sensitivity study for static simulations (immobile GB), here we are going to do the same for dynamic simulations. In the phase field, the materials parameters (α, ϵ, e and s) appears explicitly in both the static and dynamic behaviours, as it will be demonstrated clearly in the analytical model shown at the end of this part.

Effect of ε, s, e and α on migration of grain boundary

For this second sensitivity study, we reprise the methodology and value range considered in the first part of the PhD manuscript. We will see that the various parameters preserve their role observed in static simulation, with slight nuances. To investigate the role played by the parameter ε in the migration of grain boundary, we have varied the value of ε in range of $[0, 1]$ at each time we kept other parameters fixed with value reported in table 5.1. A shear rate $\dot{\gamma} = 1.5 \times 10^{-4} m.s^{-1}$ was applied to the system at 100K and it was allowed to run for $9 \times 10^5 s$. Figure 126 in the appendix D.3.1 shows the effect of varying the value of ε on diffusion of density of geometrically necessary dislocations in $\Sigma 25(7\bar{1}0)$ symmetric tilt grain boundary as a representative of all other grain boundaries investigated. As the value of ε increases the grain boundary migrates faster, and the GND distribution is wider. For $\varepsilon = 0$ and $s \neq 0$, a grain boundary becomes sharp and does not move. From all investigated grain boundary a common trend emerge as the value of ε decreases the normal of density of geometrically necessary dislocations increases. This observation agrees with the equation D.9 in the appendix D.1 as figure 89 shows. When the value of ε decreases, the curve picks upwards and the width of the grain boundary decreases.

We have also varied the value of s in range $[0, 1]$ for other parameters fixed and then after the value of s and α were allowed to vary and other parameters kept fixed. For $\alpha \neq 0$ and $\varepsilon \neq 0$, if s tends to zero the width of a grain boundary tends to zero too as discussed in section 6.1.1. If the value of s increases, the computational time increases. For $s = 0$ and , $\varepsilon = 0$, $\alpha = 0$ and e, there is no grain boundary. If s, tends to zero the width of a grain boundary decreases and a grain boundary does not move. As the value of e increases for the others fixed with the values in the table 5.1, the width of grain boundary decreases and a grain boundary tends not to move. Different tests at different values of α, e and s are listed in the appendix D.3.

6.2.1.1 Role of the different slip systems composing a GB

In the PF in static, the GBs correspond to the same continuous distribution of $|G|$ scale with the misorientation; and we will see that GB migration will correspond to the motion of GND fields (in correlation with the shift of $\phi(x)$). We started by probing the impact of the various slip system implemented in the PF as shown in the table 5.1 by turning the activity on or off. The details of these results can be found in the appendix D.2 for the sake of conciseness. From this, several observations can be made. The slip system $S^{\alpha} = (1, 0)$ was observed to be responsible of grain boundary sliding, slip systems $S^{\alpha} = \frac{1}{\sqrt{2}}(1, -1)$ and $S^{\alpha} = \frac{1}{\sqrt{2}}(1, 1)$ play an important role of keeping the diffuse nature of a grain boundary as it moves and the slip system $S^{\alpha} = (0, 1)$ is responsible for shear coupling. As the last image in figure 124 shows, all slip systems listed in 5.1 act together to allow a grain boundary to move by mechanism that involves a combination of both shear coupling and sliding motion. This decomposition of the role played by the different slip system, is still particularly useful to dissociate the different effects happening on a given GB in PF. We can also say that this decomposition, while a bit simplistic, still in a way reflects the kinematics of what is observed in MD, with shear coupling for example controlled by the in plane shear contribution of disconnections operating during migration.

6.2.2 Simulation of the migration of symmetric tilt GB

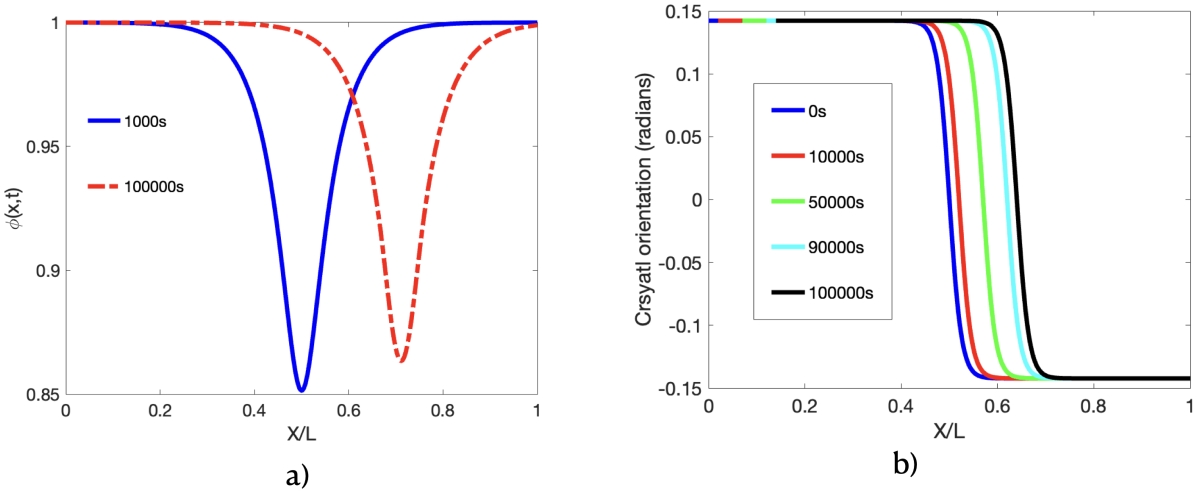

Figure 103: Evolution of ϕ with time and b) associated crystal rotation for $\Sigma 25(7\bar{1}0)$ symmetric tilt grain boundary at a shear rate $\dot{\gamma} = 8 \times 10^{-4} ms^{-1}$.

Here, we show how the PF model describes the migration of a GB in a bicrystal. Figure 103 a) shows the evolution of the field $\phi(x,t)$ with time during GB migration. We can consider that the minimum value of $\phi(x,t)$ locates in the core of a grain boundary. As expected, when applying the driving force the $\phi(x,t)$ distribution translated to the right and its shape remains mostly the same. The slight asymmetry observed on the red curve and change in width may be due to either numerical issues or due to the fact that the field exited the fine mesh region. Figure 103 b) shows the evolution of the θ field with time, as expected the front follows the $\phi(x,t)$ field due to the cross terms in the energy density functional, linking the two fields. The $\nabla\theta$ is related to $|G|$, which itself is related to $\mathbf{G} = \mathbf{F^P}\text{curl}\mathbf{F^P}$. Next we present the evolution and distribution of F^P.

Since in the model, the GB is equivalent to a distribution of dislocations, its motion leaves in its wake a plastic distortion corresponding to the transformation of grain 1 into grain 2. To illustrate the propagation of the crystal rotation change from grain 1 into grain 2, we have plotted in figures 104 a) to d) the streamlines of vectors $F^e e_1$ and $F^e e_2$. Note that, here $e_1 = (1,0)$, $e_2 = (0,1)$ and the color density corresponds to the first component of the plastic strain $\mathbb{E}^p = \frac{1}{2}(F^{p^T} F^p - I)$.

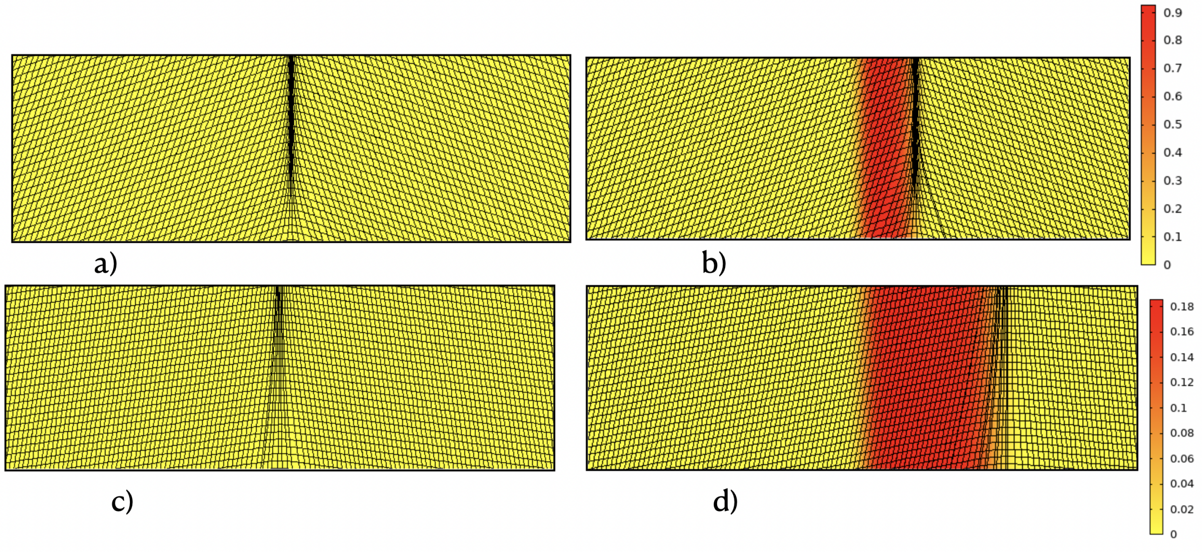

Figure 104: Streamlines tangential to the vector fields F_1^e and F_2^e describing the variations in the lattice plotted in the reference configuration. Note that the colour density here corresponds to the first component of the plastic strain a) and c) undeformed lattice of $\Sigma 5(3\bar{1}0)$ and $\Sigma 25(7\bar{1}0)$. grain boundaries respectively b) and d) deformed lattice of b) $\Sigma 5(3\bar{1}0)$ and d)$\Sigma 25(7\bar{1}0)$ respectively after $1.5 \times 10^5 s$.

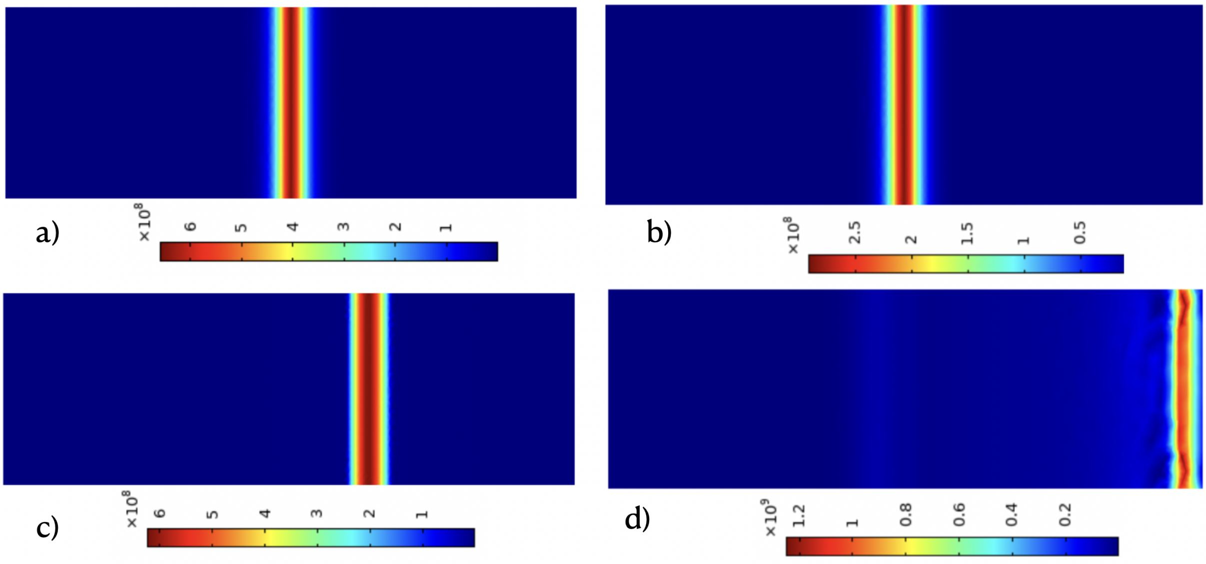

Figure 105: Colour plot of the norm of the GND density $|G|$ in undeformed (initial) configurations a) $\Sigma 5(3\bar{1}0)$, b) $\Sigma 25(7\bar{1}0)$ and deformed configurations c) $\Sigma 5(3\bar{1}0)$ after $9 \times 10^4 s$, d) $\Sigma 25(7\bar{1}0)$ after $26833 s$ at 400K with a shear rate $\dot{\gamma} = 8 \times 10^{-4} m s^{-1}$.

Since this plastic deformation must conserve the volume of the system, we also made sure that det $F^p = 1$ at all times. Figure128 a) shows the evolution of det F^p at different time steps. It is clear that the determinant remains equal 1 at all times. Here, one can notice that, this determinant means that F^p remains a piece-wise constant field, with only the discontinuity translating with time.

Finally, we considered the evolution of the distribution of the GND density constituting

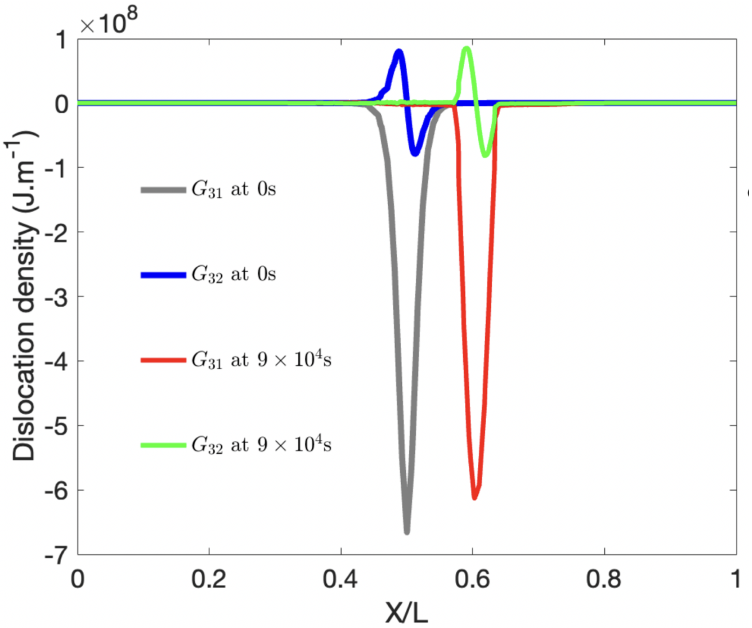

Figure 106: Plots of a) density of GNDs density components G_{31} and G_{32} and evolution of energy density at different time steps in $\Sigma 5(3\bar{1}0)$ grain boundary at a shear rate of $\dot{\gamma} = 8 \times 10^{-4} ms^{-1}$.

the GB during the GB migration. Figures 105 a) to d) show the colour plot of evolution of the norm of the GND density for two different grain boundaries. One can notice that even if the simulations of both grain boundaries are run at the same temperature with the same shear rate applied, migration of GNDs depends on the type of grain boundary as evidently, the grain boundaries did not move the same distance. In a more quantitative manner, Figure 106 a) shows the evolution of components of $|G|$ in $\Sigma 5(3\bar{1}0)$ at two different time steps. When comparing with the undeformed configuration (at $t = 0s$), the dislocation distribution are shifted to the right due to the driving force application in the deformed configuration (at $t = 9 \times 10^4 s$). The distributions are also slightly wider, again certainly due to an effect of the application of the driving force.

6.2.2.1 Influence of the temperature

Here, in preparation for the next sections, we discuss the impact of temperature on the mechanical loading of the GB (equivalent GND distribution). We have examined the Peach-Koehler (PK) contribution (calculated using equation C.33 in appendix) felt on the various slip systems possible for the dislocations. This contribution is now continuous as the GND are themselves distributions, and the PK was observed to be unaffected by the temperature. This is in contrast to the dissipative back stress (calculated in equation C.35 in appendix) shown in figure 107. These distributions are plotted as function of the slip system and for two different grain boundaries at a temperature of 400K. This is interesting to not that the dissipative back stress are rather very different for the two GB type, while we have shown earlier that the re-scaled GND distributions constituting these GB are rigorously the same.

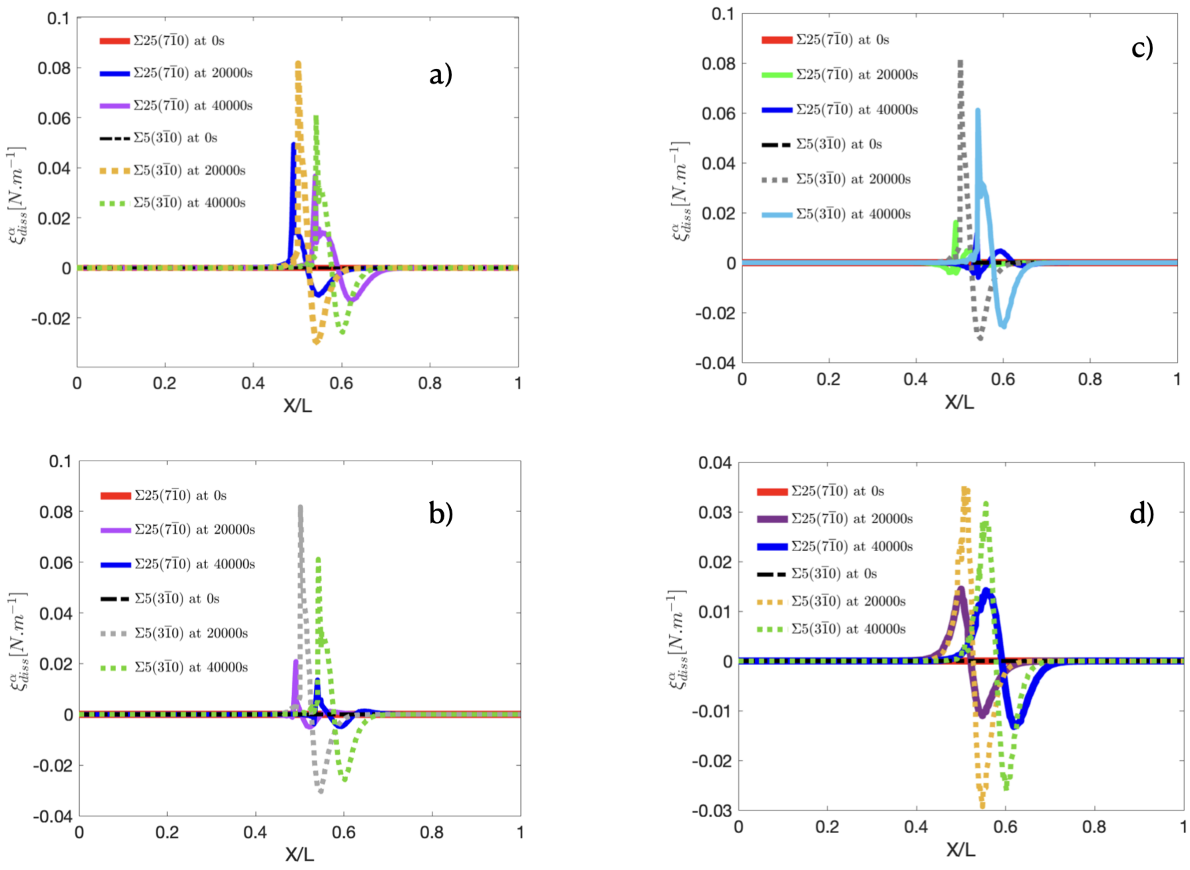

Figure 107: Dissipative energy ξ^{α}_{diss} in x direction due to slip a) S^1 b)S^2 c)S^3 and d)S^4 for two grain boundaries $\Sigma5(3\bar{1}0)$ and $\Sigma25(7\bar{1}0)$ at 400K.

6.2.2.2 Shear coupling migration

As a grain boundary described as an array of dislocations sweeps through a bicrystal, it plastically deforms a bicrystal. For all investigated grain boundary, the migration of a grain boundary in normal direction is accompanied by the translation of the grain being consumed in tangential direction with respect to the growing grain. This migration mechanism is illustrated in figure 108 for two different grain boundaries $\Sigma25(7\bar{1}0)$ and $\Sigma5(3\bar{1}0)$ at 100K. By using the shear coupling factor β which is the ratio of the distance traversed by a grain boundary along its normal direction to the vertical displacement, one can assess the extent of shear coupling in a grain boundary motion. Figure 109 a) shows the evolution of the shear coupling factor as function of time. β converges after some time-steps as in (Admal et al., 2018). This could be due to the fact that shear coupling is not a local phenomena therefore the measurement of β is also not local. Next, we have compared the obtained values from theoretical values (calculated from $\beta = 2\tan(\theta/2)$, where θ is a misorientation angle between two abutting grains (Homer et al., 2013)). The figure 109 b)

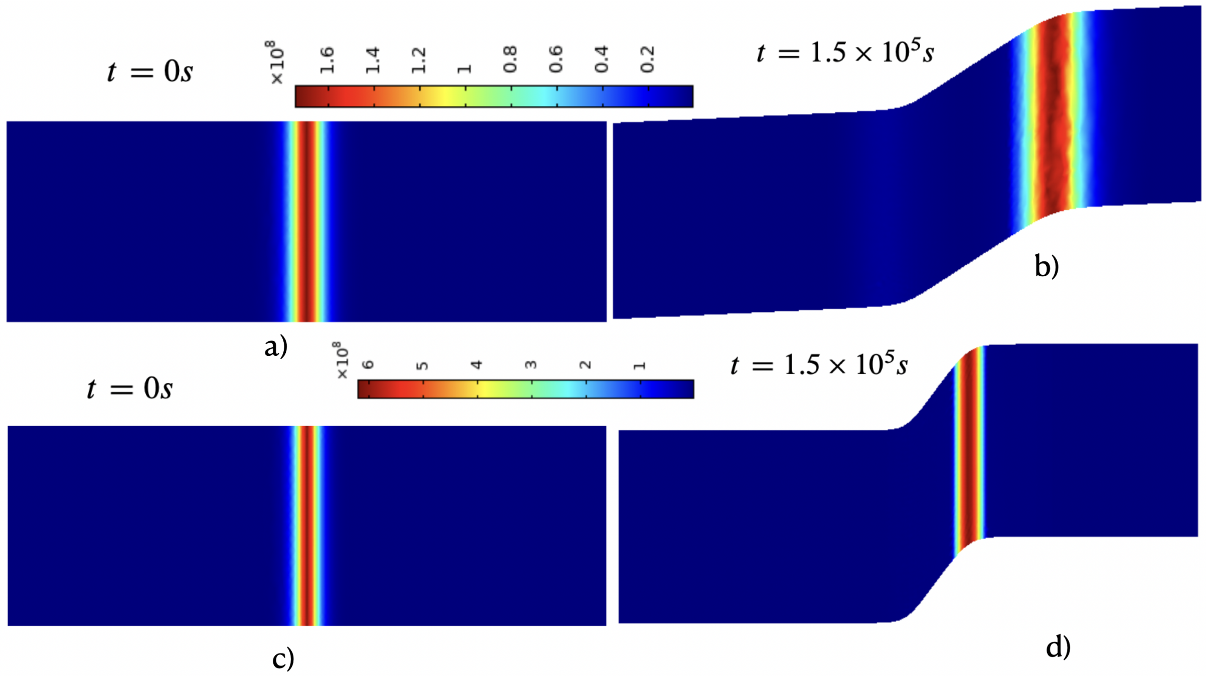

Figure 108: Colour plot of the norm of the GND density $|G|$ in a)$\Sigma25(7\bar{1}0)$, c) $\Sigma5(3\bar{1}0)$ initial and b) $\Sigma25(7\bar{1}0)$, d) $\Sigma5(3\bar{1}0)$ deformed configuration at shear rate $\dot{\gamma} = 2 \times 10^{-4} ms^{-1}$.

shows that the shear coupling factors increases with the misorientation angle. Overall, the

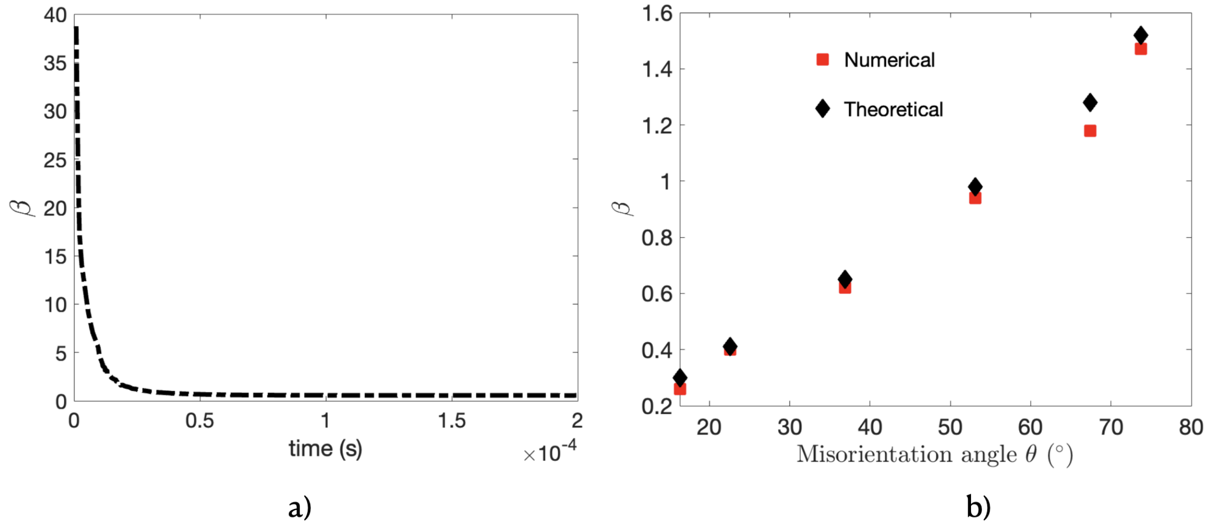

Figure 109: a) Convergence of the coupling factor β with respect to time for $\Sigma5(3\bar{1}0)$ symmetric tilt grain boundary.b) Comparison of the dependence of numerically and theoretically calculated shear coupling on misorientation angle.

simulated shear coupling factors from PF are in good agreement with the theoretical model derived from geometric arguments. The simulation slightly underestimate the theoretical values and this could be related to numerical issues. For all investigated grain boundaries, as general trends, it was observed that as the shear coupling increases the velocity of a grain boundary in the normal direction of grain boundary decreases. By comparing figure

109 b) with figure 95, it is evident that the shear coupling factor increases with the density of geometrically necessary dislocations. Figure 109 b) compares the shear coupling factor from the phase field study from theoretical values.

6.2.3 Velocity of GB migration as function of applied shear rate and temperature

In this final subsection, we plot the average velocity of GB migration in a similar manner as for the atomistic data e.g. as function of the GB type, in the 2D parametric phase space shear rate and temperature. As in the MD, and independently of the applied temperature and motive force, GB velocity reaches an instantaneous steady state and the velocity is extracted as the derivative of the grain boundary displacement-time curve. Note that, the position of a grain boundary is extracted from the evolution of the crystal lattice rotation curves in figure 103b). Figure110 shows the time displacement curve of $\Sigma25(7\bar{1}0)$ symmetric tilt grain boundary as a representative of all other investigated grain boundaries.

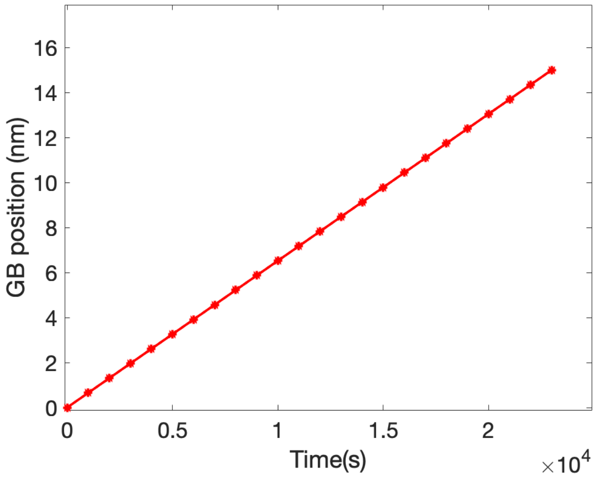

Figure 110: The position of $\Sigma25(7\bar{1}0)$ symmetric tilt grain boundary at over time at 100K and $\dot{\gamma} = 1 \times 10^{-4} m.s^{-1}$.

Before presenting the results, a remark is necessary regarding the substitution of the shear rate instead of the actual driving force employed in MD, which is harder to assess in the present PF simulations. For, this we will consider a discrete array of dislocations to describe the GB. Driving GB migration by a shear rate $\dot{\gamma}$ will correspond to using the second Orowan's law (Orowan, 1934) that reads

$$\dot{\gamma} = \rho_{mob}|b|\bar{v}$$

Where ρ_{mob} is the mobile dislocation density and $|b|$ the norm of the GB Burgers vector. For a given GB, these two quantities are fixed, the average dislocation velocity $\bar{v}$ has thus to increase to accommodate $\dot{\gamma}$. In the model, and similarly to most crystal dislocations, the dislocation velocity (v) is linearly related to the effective stress (τ_{eff}) felt by dislocations ($v = \tau_{eff}/B(T)$, where $B(T)$ is a temperature dependent coefficient) (Queyreau et al., 2011). For all investigated grain boundaries, the GB velocity depends upon the magnitude of applied driving force and temperature. Depending on the correlation between applied shear rate and the resulting velocity of grain boundary, all investigated grain boundaries are classified into different groups, in a similar manner as was done for MD results. The first group contains grain boundaries whose correlation is linear. The second group contains grain boundaries whose correlation between velocity and applied shear rate is non linear, probably exponential.

Figure 111 shows migration velocity against the applied shear rate at 400K and 1000K for the $\Sigma25(7\bar{1}0)$ and $\Sigma5(1\bar{2}0)$ STGB. First, the $\Sigma25(7\bar{1}0)$ exhibits a linear dependence of its migration velocity as function of shear rate, and the linear dependence decreases with the increase of temperature. Interestingly, this behaviour is in qualitative agreement with the viscous behaviour obtained for the same GB as simulated by MD. The quantitative values are however not comparable, in part due to the nature of graph that is function of shear rate and not driving force explicitly. Second, the $\Sigma5(1\bar{2}0)$ GB have a very different behaviour with a non linear -possibly exponential- increase of the GB migration velocity with shear rate, and the velocity increases with temperature for a given shear rate. This is again in qualitative agreement with the thermally activated clearly identified in MD for

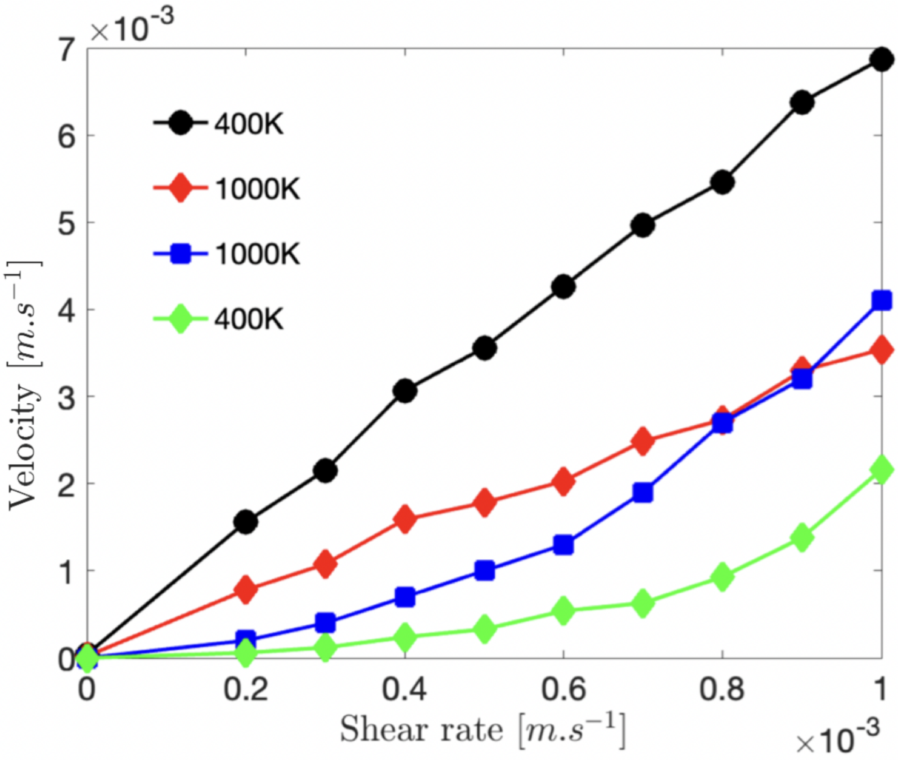

Figure 111: Plot of velocity of $\Sigma25(7\bar{1}0)$ and $\Sigma5(1\bar{2}0)$ symmetric tilt grain boundaries at different temperature against different applied shear rate.

this particular GB.

This qualitative agreement between PF and MD regarding the velocity dependence upon temperature and the GB type is really surprising. Indeed, as of right now, the PF was not particularly set to match the MD results obtained for FCC Ni. Again, the materials parameters were set close to scale with the latent heat, and Read and Shockley GB energy, but they do not account yet for the details in the atomistic structure of the GB and associated migration processes. This being said, the only feature that the PF may reproduce naturally is thus the GB structure in terms of dislocation distribution. To check that idea, we show the resolved shear stress distribution 112 and dissipative energy 107 for the two GB examples and at various temperatures. The two GB being made of different dislocation distributions on the various systems, may be activated differently and interact differently when set in motion. This need to be investigated further. In the mean time, this suggest that GB properties such as migration for such simple CSL GB could be simply more related to the GB structures in terms of defects and less the atomistic nature of the GB.

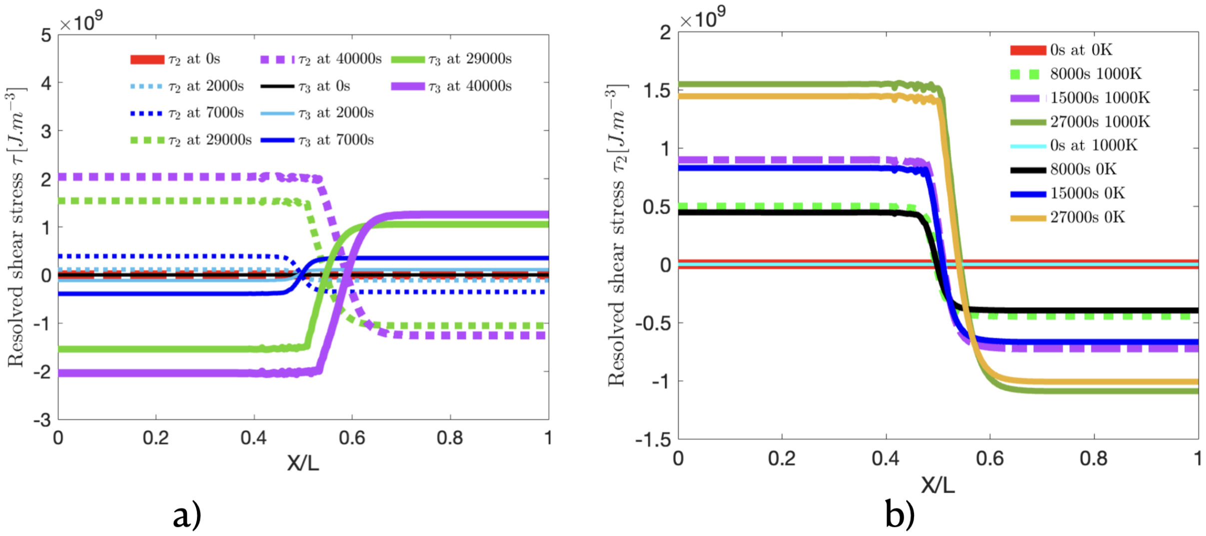

Figure 112: a) Evolution of the resolved shear stress due to slip systems S^2 and S^3 for $\Sigma25(7\bar{1}0)$ and b) Dependence of resolved shear stress on slip system S^2 for $\Sigma5(3\bar{1}0)$ grain boundary.

6.3 Towards a quantitative way to connect MD and Phase Field

In the previous chapters of part 2, we have shown that the PF from Admal et al., deriving from the KWC model could be (along with a few other models) a good candidate to include the various mutual effects between crystal dislocations and GBs that are required to fully capture microstructure evolution. This is the answer to the first challenge listed in the general introduction. The second challenge is to being able to make PF truly quantitative by using MD data. In particular, our existing MD results provide GB energies and complex mobility functions for about 30 different CSL grain boundaries with a [001] misorientation axis. While the two types of simulations are capable of describing similar mechanisms, connecting the two approaches is not straightforward. In particular, phase field relies upon continuous fields, whose direct determination from atomistic calculations seems unclear (this is particularly true for the order parameter $\phi(\mathbf{x})$ and the generalised forces). In the original form, parametrizing a KWC model with MD data, would require to run many PF simulations and a lot of trials and errors in an attempt to find the correct set of PF material parameters to match the GB energy and mobility from MD. In addition to being extremely costly in terms of time and computing resource, there is no guaranty that this procedure will converge to a unique set of PF material parameters identified this way. Here, we derive an analytical solution of the KWC phase field set of equations of the 1D problem of a single GB in a bicrystal under static and steady motion conditions.

In this section we want to provide analytical solution of $\phi(x)$ and $\theta(x)$ which were previously expressed in the inverted form in the section B.3 in appendix. Thus, the methodology relies on a formal asymptotic expansion of the model as devised by Lobkovsky et al. (Lobkovsky and Warren, 2001) and demonstrated in section B.3 in appendix for KWC model and for Marian & Admal's model in appendix D.1. The solution proposed in (Lobkovsky and Warren, 2001) while remaining general and constituting the starting point to our development, suffers the following limitations:

- The solution for ϕ and θ are expressed as integral equations (equations B.44, D.5, D.14, D.13 below), while being general, are not trivial to solve.
- Even if these equations may be solved to obtain $x(\phi)$, the solution still need to be inverted to obtain $\phi(x)$, and there is no guarantee that this is even possible.
- The $\phi(x)$ solution will ultimately depend upon its own minimal and maximal values ϕ_{min} and ϕ_{max} through some integral constants. Solving an implicit equation for ϕ_{min} and ϕ_{max} is thus required prior to obtaining the final $\phi(x)$. These parameters will depend upon the material constants and nature of the GB.

In this context, we propose a closed form analytical solution of the 1D KWC PF equations, which have the following advantages:

- The solutions $x(\phi)$ and the inverted $\phi(x)$ solutions are both analytical (semi-analytical to be exact as it relies on Elliptic integrals and Jacobi amplitude).
- The energy and inverse mobility functions are also analytical.

- The ϕ_{min} and ϕ_{max} can now be obtained using a very efficient Newton-Raphson algorithm.
- The role played by the various materials parameters can now be unambiguously investigated.
- The identification of the materials parameters, or mobility functions in PF to match MD is now very simple, as we simply have to equate physical quantities (e.g. GB energy, or migration velocity) obtained with the two approaches.

The solution is however rather long and complicated and obtaining this analytical solution was admittedly tedious.

6.3.1 Closed-form analytical static solution for the 1D KWC model

We start recalling the KWC model. The energy density can be written:

$$\psi^{KWC} = \frac{\alpha^2}{2}|\nabla\phi|^2 + f(\phi) + g(\phi)s|\nabla\theta| + \frac{\epsilon^2}{2}|\nabla\theta|^2 \tag{6.8}$$

with,

$$\begin{aligned} f(\phi) &= e(\phi-1)^2 && (6.9)\\ g(\phi) &= \phi^2 && (6.10)\end{aligned}$$

The parameters α, ϵ and s are material constants. For non conservative phase fields, the time evolution of $\phi(\mathbf{X})$ and $\theta(\mathbf{X})$ are related to the partial derivative of ψ^{KWC} with respect to ϕ and θ:

$$\begin{aligned} b^{\phi}\dot{\phi} &= \alpha^2\Delta\phi - f_{,\phi} + g_{,\phi}s|\nabla\theta| && (6.11)\\ b^{\theta}\dot{\theta} &= \operatorname{div}\left(\epsilon^2\nabla\theta + g_{,\phi}s\frac{\nabla\theta}{|\nabla\theta|}\right) && (6.12)\end{aligned}$$

It must be noted that the formulation above, which includes the term $\nabla\theta/|\nabla\theta|$ leads to a singular diffusive equation. A non-singular approximation may be found in [Kobayashi Giga, JSP 1999], but this did not seem to be initially required in the 1D solution proposed in what follows. Let us recall that both models tend to localise a grain boundary, therefore our domain $\Omega_0 = [-L, L]$ is typically separated into a grain boundary region $\Omega_0^{GB} = [-l, l]$ and a crystalline region $\Omega_0^{p} = \Omega_0 \backslash \Omega_0^{GB}$ within grains. $\forall x \in \Omega_0^{p}$, $\nabla\theta(x) = 0$ and $\nabla\phi(x) = 0$. The boundary conditions are:

$$\phi(\pm L) = 1,\ \theta(\pm L) = \pm\frac{\theta_0}{2} \tag{6.13}$$

On contrary, in grain boundary region delimited by $\pm l$, $\nabla\theta(x) \neq 0$ and $\nabla\phi(x) \neq 0$. The $\phi(x)$ field is symmetric whereas the $\theta(x)$ is anti-symmetric about the origin. Under static conditions, $\forall x \in \Omega_0^p$, $\phi(x)$ satisfies:

$$\alpha^2 \Delta\phi - f_{,\phi} = 0 \tag{6.14}$$

By multiplying both sides of equation 6.14 by $\frac{\partial\phi}{\partial x}$ and integrating the resultant equation leads to

$$\frac{\alpha^2}{2}\phi_{,\phi} - f(\phi) = c \tag{6.15}$$

where c is an integration constant. Integrating equation 6.15 leads to

$$L - x = \int_{\phi}^{1} \frac{\alpha}{\sqrt{2(f(\tilde{\phi}) + c)}} d\tilde{\phi} \tag{6.16}$$

In order to obtain a closed form analytical solution for $\phi(x)$, we have to find an analytical function for the integral in the right hand side of the equation 6.16, and then we have to be able to invert that function. Luckily, this is the case for the choice of $f(\phi)$ in equation 5.7. The solution outside the GB region, thus, becomes:

$$\begin{aligned} \phi(x) &= 1 - \sqrt{\frac{c}{e}\frac{\tanh^2(\lambda(x))}{1 - \tanh^2(\lambda(x))}} && (6.17) \\ \lambda(x) &= \frac{\sqrt{2e}}{\alpha}(x - L) && (6.18) \\ c &= \left(\frac{1 - tanh^2(\lambda(l))}{tanh^2(\lambda(l))}\right) f(\phi_2) && (6.19) \end{aligned}$$

In the region Ω_0^{GB}, $\theta(x)$ and $\phi(x)$ must satisfy the conditions:

$$\begin{aligned} \alpha^2 \Delta\phi - f_{,\phi} + g_{,\phi} s |\nabla\theta| &= 0 && (6.20) \\ \left(\varepsilon^2 \nabla\theta + g_{,\phi} s\right)_{,x} &= 0 && (6.21) \end{aligned}$$

By integrating equation 6.21 leads

$$\epsilon^2 \nabla\theta + g_{,\phi} s = \text{constant}$$

and considering boundary conditions $\phi_{,x} = 0$ at $x = l$;

$$\theta_{,x} = \frac{s}{\epsilon^2}\Big(g(\phi_2) - g(\phi)\Big) \tag{6.22}$$

Inserting equation 6.22 into equation 6.21 yields

$$\left(\frac{\alpha^2}{2}\phi_{,x} - f(\phi) + \frac{s^2}{2\epsilon^2}(g(\phi_2) - g(\phi))^2\right)_{,x} = 0 \tag{6.23}$$

Using boundary condition, $\frac{\alpha^2}{2}(\phi_{,x})^2 - f(\phi_2) = c$, equation 6.23 becomes :

$$\frac{\alpha^2}{2}\phi_{,x} - f\phi + \frac{s^2}{2\epsilon^2}(g(\phi_2) - g(\phi))^2 = c \tag{6.24}$$

By integrating equation 6.24 provide an equation in the form of an integral

$$x(\phi) = \int_{\phi_1}^{\phi} \frac{\alpha}{\sqrt{2(f(\tilde{\phi}) + c) - \frac{s^2}{\epsilon^2}(g(\phi_2) - g(\phi))^2}} d\tilde{\phi} \tag{6.25}$$

To find $\phi(x)$, one has to find an analytical and inversible solution to the RHS of equation 6.25 in order to provide a closed form expression. However, the presence of the term $\Big(g(\phi_2) - g(\phi)\Big)$ in equation 6.25 makes it harder to solve. Therefore, the equation 6.25 can be presented as an ordinary differential equation (ODE).

$$\frac{d\tilde{\phi}}{dx} = \frac{1}{\alpha}\sqrt{2(f(\tilde{\phi}) + c) - \frac{s^2}{\epsilon^2}(g(\phi_2) - g(\phi))^2} \tag{6.26}$$

Under this form, the main difficulty is that the resulting equation 6.26 is a non-linear first order ODE. We tried to solve the ODE (equation 6.26) using the Laplace Transforms without success. This is due to the presence of the terms in power of ϕ^4 and ϕ^2 in the polynomial $P(\phi)$ under the square root, for which there is no known Laplace Transform. An alternative way, is to consider tables of known integrals whose form would be similar to the form of equation 6.26. To do this $P(\phi)$ must be reworked in the following way :

$$\begin{aligned} P(\phi) &= -\frac{s^2}{\epsilon^2}\phi^4 + (2\frac{s^2}{\epsilon^2}\phi_2^2 + 1)\phi^2 - 2\phi + (2c + 1 - \frac{s^2}{\epsilon^2}\phi_2^4) && (6.27) \\ &= \frac{s^2}{\epsilon^2}\left(-\phi^4 + (2\phi_2^2 + \frac{\epsilon^2}{s^2})\phi^2 - 2\frac{\epsilon^2}{s^2}\phi + \frac{\epsilon^2}{s^2}(2c + 1 - \frac{s^2}{\epsilon^2}\phi_2^4)\right) && (6.28) \\ &= \frac{s^2}{\epsilon^2}\left(-(\phi - r_1)(\phi - r_2)(\phi - r_3)^2\right) && (6.29) \end{aligned}$$

Where r_i are roots of the polynomial $P(\phi)$ in equation 6.27. Note that, the roots of this quartic equations can still be analytically obtained using Ferrari's solution. Therefore, to find an analytical solution for the integral in equation 6.26 one can distinguish two cases:

Case One: if $P(\phi)$ admits three distinct roots

If we assume the root r_3 to be double. One can thus find an analytical solution for the integral in equation 6.26

$$x(\phi) = \frac{\alpha\epsilon}{s}\int_{\phi_1}^{\phi}\frac{1}{\sqrt{-(\tilde{\phi}-r_1)(\tilde{\phi}-r_2)(\tilde{\phi}-r_3)^2}}d\tilde{\phi} \tag{6.30}$$

$$c_1 + x = \frac{\alpha\epsilon}{s}\left[\frac{2}{\sqrt{r1-r3}\sqrt{r3-r2}}\tan^{-1}\left(\frac{\sqrt{r3-r2}\sqrt{r1-\tilde{\phi}}}{\sqrt{r1-r3}\sqrt{r2-\tilde{\phi}}}\right)\right]_{\phi_1}^{\phi} \tag{6.31}$$

Interestingly, this function is invertible, yielding a solution of $\phi(x)$:

$$\phi(x) = \frac{r_1 A - r_2\tanh^2\left(B(c_2-x)\right)}{A-\tanh^2\left(B(c_2-x)\right)} \tag{6.32}$$

$$A = \frac{r_3-r_2}{r_1-r_3} \tag{6.33}$$

$$B = \frac{s\sqrt{(r_1-r_3)(r_3-r_2)}}{2\alpha\varepsilon} \tag{6.34}$$

In this solution, the periodic tan function has been replaced by a non-periodic hyperbolic tan function. Consequently, a new integration constant c_2 was introduced.

$$c_2 = c_1 - \frac{\alpha\varepsilon}{s}F(\phi_1)$$

Where $F(\phi_1)$ is the primitive on the RHS of equation 6.31. It can be made sure that this new expression of $\phi(x)$ is indeed a solution by emerging it in the equation 6.25 and 6.26. On the other hand, the solution of $\theta(x)$ is obtained from integration of equation

$$\theta_{,x} = \frac{s}{\varepsilon^2}\left(\phi_2^2 - \phi^2(x)\right) \tag{6.35}$$

after a solution of $\phi(x)$ is inserted in. The integration leads to

$$\begin{aligned}\theta(x) &= \frac{s}{\varepsilon^2}\phi_2^2 x + \frac{s}{\varepsilon^2}\frac{1}{2(A-1)^2 B}\left[C\tanh^{-1}\left(\frac{\tanh(Bx)}{\sqrt{A}}\right)\right.\\ &\quad \left.\frac{D\tanh(Bx)}{A-\tanh^2(Bx))} - EBx\right]\\ C &= \sqrt{A}\left(A(3r_1+r_2)(r_1-r_2)+(3r_2+r_1)(r_2-r_1)\right)\\ D &= A(A-1)(r_1-r_2)^2\\ E &= 2(r_2-Ar_1)^2\end{aligned}$$

The integration constant can be implicitly defined as:

$$c = -f(\phi_1) + \frac{s^2}{2\epsilon^2}(g(\phi_2) - g(\phi_1))^2 \tag{6.36}$$

which is problematic as the solution for $\phi(x)$ depends on its own extremas. Finally, it can be checked that the two solutions for $\phi(x)$ and $\theta(x)$ can be analytically integrated to calculate the GB energy and the GB mobility.

Case two: if $P(\phi)$ admits four distinct roots

In general, $P(\phi)$ admits four different roots. The solutions are still obtainable but in a semi-analytical manner only. This is due to the fact that, it implies an incomplete Elliptic integral of the first kind where $F(x|m)$ and

$$x(\phi) = \frac{\alpha\epsilon}{s}\int_{\phi_1}^{\phi} \frac{1}{\sqrt{-(\tilde{\phi}-r_1)(\tilde{\phi}-r_2)(\tilde{\phi}-r_3)(\tilde{\phi}-r_4)}}d\tilde{\phi} \tag{6.37}$$

$$c_1 + x = \frac{\alpha\epsilon}{s}\left[\frac{2}{\sqrt{r1-r3}\sqrt{r2-r4}}\mathrm{F}\left(\sin^{-1}\left(A\sqrt{\frac{r1-\tilde{\phi}}{r2-\tilde{\phi}}}\right)\middle| m\right)\right]_{\phi_1}^{\phi} \tag{6.38}$$

$$A = \sqrt{\frac{r2-r4}{r1-r4}} \tag{6.39}$$

$$m = \frac{(r_2-r_3)(r_1-r_4)}{(r_1-r_3)(r_2-r_4)} \tag{6.40}$$

Elliptic integral of the first kind is defined as

$$F(x|k) = \int_0^x \frac{dy}{\sqrt{1-k^2\sin^2 y}}$$

Where k is the elliptic modulus k and it must satisfy $0 < k < 1$.

$$\phi(x) = \frac{r_2\mathrm{sin}^2(\lambda,k) - r_1A^2}{\mathrm{sin}^2(\lambda,k) - A^2} \tag{6.41}$$

$$\lambda = \frac{s}{\alpha\epsilon}\frac{\sqrt{(r_1-r_3)(r_2-r_4)}}{2}(c_1 - x) + F(\phi_1) \tag{6.42}$$

With, $F(\phi_1)$ is the primitive function appearing on the RHS in equation 6.38. While, the expression for $\phi(x)$ is rather short and simple, this is not the case anymore for θ field and the GB energy. However, the semi-analytical expression can still be obtained for these two terms thanks to Mathematica. It exhibits a sum of various Elliptic functions and integrals. For the sake of conciseness however, and as ϕ is well bounded between ϕ_1 and 1, ϕ is approximated using a Taylor Series on different terms. This Taylor expansion offers advantages that the remaining unknowns ϕ_1 and ϕ_2 can be obtained using the Newton-Raphson scheme to solve these non-linear equations

$$c = -f(\phi_1) + \frac{s^2}{2\epsilon^2}(g(\phi_2) - g(\phi_1))^2 \tag{6.43}$$

$$\theta_0 = \frac{\alpha s}{\epsilon^2}\int_{\phi_1}^{\phi_2} \frac{g(\phi_2) - g(\phi)}{\sqrt{2(f(\tilde{\phi}) + c) - \frac{s^2}{\epsilon^2}(g(\phi_2) - g(\phi))^2}} d\tilde{\phi} \tag{6.44}$$

$$\text{Ł} = \int_{\phi_1}^{\phi_2} \frac{\alpha}{\sqrt{2(f(\tilde{\phi}) + c) - \frac{s^2}{\epsilon^2}(g(\phi_2) - g(\phi))^2}} d\tilde{\phi} + \int_{\phi_2}^{1} \frac{\alpha}{\sqrt{2(f(\tilde{\phi}) + c)}} d\tilde{\phi} \tag{6.45}$$

Jacobian that appears in the Newton-Raphson algorithm for this multi-variable problem is calculated analytically using Mathematica.

To validate our model, we have made a direct comparison of the analytical solution with numerical calculations of the KWC model presented in (Admal et al., 2018). ϕ_1 and ϕ_2 were measured from (Admal et al., 2018). Materials parameters we have used are registered in table 6.4. At the time of writing of the manuscript, one application to a $\Sigma 5$ is performed, applying the model to other GBs is left for future work.

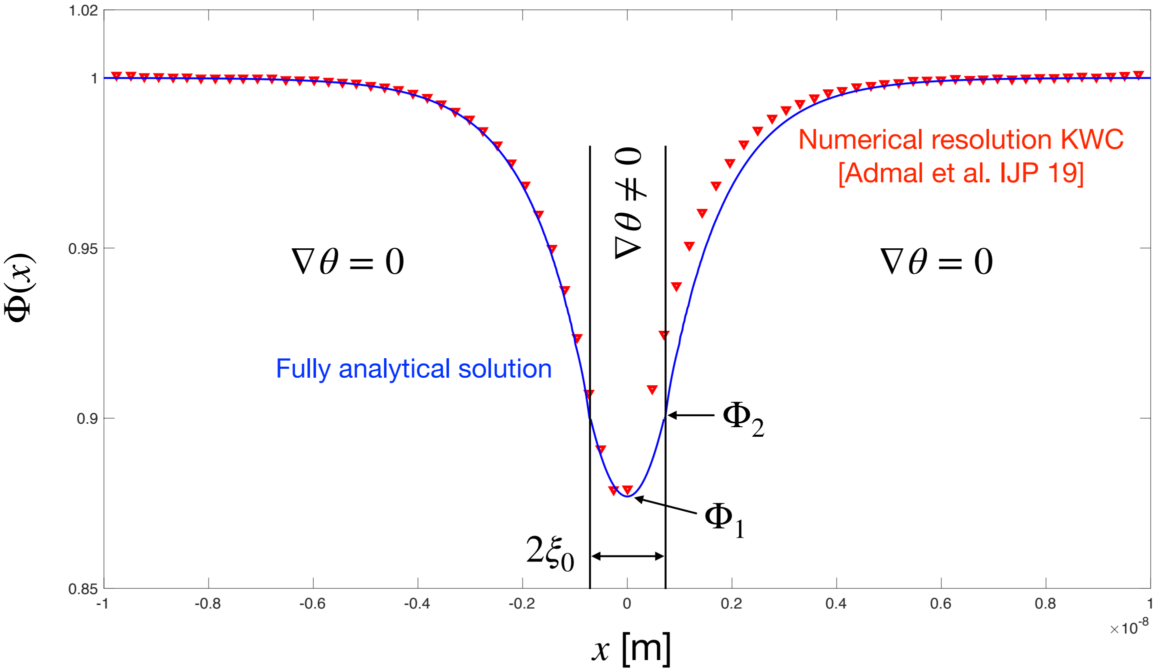

Figure 113: Validation of the analytical (1D) model with the numerical resolution of the (2D) KWC model.

However, note that s has to be greatly reduced compared from the value used in numerical solutions. This is because, the analytical model does not smooth our the $\nabla\theta$ in the grain boundary region as opposed to what is done in the numerical solve. Figure 113 shows a comparison between analytical and numerical solution of ϕ. Figure 114 shows the

Table 6.4: Materials parameters and $\phi_i (i = 1, 2)$ values used to compare our analytical solution from the numerical solution of KWC model.

α^2	ϵ^2	e	s	ϕ_1	ϕ_2	ξ_0
5.3×10^{-9}	2.1333×10^{-10}	2.1×10^9	0.17	0.875	0.9	0.7nm

normalised solution of $\phi(x)$ and $\theta(x)$ for a representative grain boundary. Note that here the purpose is to show that the proposed solutions describe qualitatively the domain into crystalline and grain boundary regions. Similar to the functional form outside the GB approximation of the polynomial when looking at the Admal & Marian's model (Admal et al., 2018) rather than the KWC model, the solution of G_{13} can be determined in a similar manner from the equation D.7 in appendix. For an analytical solution of mesoscale properties of a grain boundary, see section 6.3.2

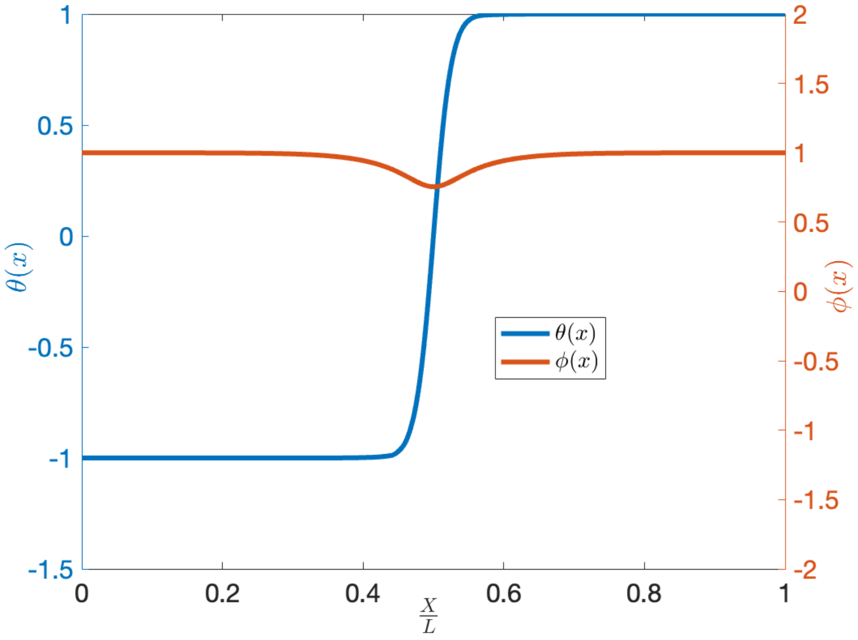

Figure 114: Plot of the normalised $\phi(x)$ and $\theta(x)$ solutions.

6.3.2 Analytical mesoscale properties of the GB

Finally, we are continuing deriving analytical solution devised in section 6.3, and at this time focusing on dynamic properties of a grain boundary. Going back to (Lobkovsky and Warren, 2001), the mesoscale properties of a grain boundary *i.e.* GB energy, velocity v

and mobility M can be expressed from the ϕ and θ fields derived in section 6.3 as

$$\begin{aligned}
\gamma &= s\Delta\theta_0\phi_2^2 + 2\alpha\int_{\phi_{max}}^{1} \sqrt{2(f(\tilde{\phi})+c)}\, d\tilde{\phi} && (6.46)\\
&\quad +2\alpha\int_{\phi_{min}}^{\phi_{max}} \sqrt{2(f(\tilde{\phi})+c) - \frac{s^2}{\epsilon^2}(g(\phi_2)-g(\phi))^2}\, d\tilde{\phi} && (6.47)\\
M^{-1} &= \int_{-L}^{L} \left(b^{\phi}\phi_{,x}^2 + b^{\theta}\theta_{,x}^2\right) dx && (6.48)
\end{aligned}$$

with b^{ϕ} and b^{θ} inverse mobility functions associated to the time variation of ϕ and θ, respectively. For the case of the 1D configuration, these mobility functions are simple constants. The velocity of a grain boundary reads

$$v = M\kappa\gamma$$

and is the result of capillarity through γ and curvature driving forces through curvature κ. However, in this present 1D model, the curvature κ is undefined. Here, will assume that mobility will be preserved when the GB migrates under other driving forces. A more complete exploit of the present model is left for future work.

General conclusions and future works of the project

6.4 General conclusions

The general context of this project was to better understand the evolution of microstructure in FCC materials under thermo-mechanical conditions. To capture the full complexity of microstructure evolution at higher temperatures and/or stresses requires to have in place more robust models capable of capturing simultaneously grain boundary migration and plastic activities associated with and preserve, at the same time, the physics observed at atomistic level. The path forward to having such models in place requires bridging both atomistics and continuum scale simulation techniques. In this work we attempted to bridge both scales by importing atomisitic data into a Phase field model of Admal and Marian (Admal et al., 2018) capable of capturing concurrently grain boundary migration and associated plastic activities.

In the first and principal part of this work, we have performed large scale Molecular dynamics simulations on a large set of [001] symmetric CSL grain boundaries of different characters in pure Nickel, encompassing pure tilt, twist and mixed GB. Since atomic structure of a grain boundary is very important in this study, we have carefully built several configurations of similar macroscopic degrees of freedom but of different microscopic degrees of freedom for each grain boundary. This was done using our own in-house tools, that are the continuation of the PhD work of Omari (OMAR, 2019). Then, we have relaxed these configurations and compare their energy values. This is seen as a practical way of finding the most stable -thus, most probable- configuration of a grain boundary. This practice has allowed us to confirm, once more, that the energy of a grain boundary has a complex dependence on both macroscopic and microscopic degrees of freedom. Therefore, both type of degrees of freedom must always be taken into account, and thus justifies aposteriori the need for such reference atomistic data. For each grain boundary, we have selected a configuration with the lowest energy value as the most stable configuration of a grain boundary.

To validate our procedure, we have compared the energy values of the most stable configurations with reference data reported in literature, which allowed to validate our methodology and tools. In addition, we have observed that the energy of the selected most stable configurations varies from one grain boundary to another and from one GB character to an other. Overall and in simplifying a bit, pure twist GB have the lowest energy whereas pure tilt grain boundaries have the highest energy. Then, we have characterised and identified the defects on the surface of the most stable configurations. This has allowed to define the density of geometrically necessary dislocations of each grain boundary that may be imported in a continuum scale model.

In a second step, we have investigated dynamic properties of a grain boundary still using MD. To trigger grain boundary migration, we have applied the synthetic driving force methodology of Janssens (Janssens et al., 2006). The objective here was to explore a large parametric space function of driving force (P) - temperature (T) in order to reveal trends that are common for a large set of grain boundaries, and clarify some contradictory results of the literature. More specifically, we have conducted a systematic study of the grain boundary migration by applying a driving force in range of $[50 - 500]$MPa and temperature in $[100 - 1000]$K. This study has revealed that velocity of grain boundary strongly depends again initially on the atomic structure of a grain boundary and vary widely among grain boundary characters and type. However, the velocity does not correlate with the grain boundary energy in the respective fundamental zone.

We have also observed very different temperature dependence of the migration velocity as was observed in the literature, with different behaviour ranging from thermally activated, athermal, to antithermal grain boundary migration, although some grain boundaries behaved in a fashion that could not be classified in any of these three general trends. In addition, we have observed that the way a grain boundary responds to an applied driving force depends on its atomic structure, thus, varies from one grain boundary to another. There were grain boundaries whose velocity correlation with driving force remained either a) linear or b) exponential for the entire stress. However, few grain boundaries on our list, exhibited both an exponential regime at lower stress and a linear regime at higher stress regime. In all investigated grain boundary, we have observed that the transition stress from exponential to linear regime varies from one grain boundary to another and linearly decreases with increasing temperature.

All these details from a systematic exploration of the P-T parametric space has allowed to propose a generic phenomenological mobility function, to capture microstructure evolution at atomic scale. This is one of the main result of the atomistic study in this work. This generic mobility function was obtained by least square fitting raw data from post-treatment of the atomistic simulations using the phenomenological empirical relation of Kocks, Argon and Ashby (Kocks et al., 1975) for the migration activation energy, which has been initially proposed for dislocation. Interestingly, for all grain boundaries investigated we have obtained very close values for $p = 0.5$ and $q = 1.5$ (in Kocks, Argon and Ashby's phenomenological function). This implies that these parameters are not influenced by the atomic structure of a grain boundary instead they may depend solely on the type of material. In addition, the enthalpy of activation for grain boundary migration varies largely among grain boundaries. To validate our post-treatment and model, we have compared raw data of mobility from predictions by this proposed model. One single mobility equation, can thus reproduce the data for the entire P-T parametric space for a given GB.

Obtaining such mobility law was key for several reasons. First, this phenomenological law allowed to rationalise results obtained from atomistic simulations. For instance, now we know that when the applied driving force equals the transition stress, the mechanical work allows to overcome the migration energy barrier, consequently the grain boundary moves as whole, and the velocity becomes linear. Moreover, having in place a generic law to capture grain boundary migration at atomistic scale can not only reduce the need for cpu-demanding MD calculations but also serve as an input to models at continuum scale, which in turn could help optimizing thermomechanical treatements.

In the second part of this work, we have investigated both static and kinetic properties of a grain boundary using now the phase field model of Admal et al., which derives from the so-called KWC model. In brief, the key idea of the model is to describe GB as GND and thus approximate $\nabla\theta = |G|$ and relate the density tensor $\mathbf{G}$ to a crystal plasticity framework. The ultimate objective, here, was to capture microstructure evolution at the length scale of microstructure. First, We have carried out a sensitivity test on the parameters of the Admal et al. model by assessing the influence of each parameter on the energetic stability of the system. In addition, this study has allowed to select values to use in our simulation. Parameters may have antagonistic effects to spread the width (through the ϕ and GND fields) of the diffuse interface that the GB represents in the model. For some extreme values, the GB becomes a singular interface and may remain immobile or numerical resolution becomes more computationally demanding. As a start point, we performed PF simulations using the initial parametrization derived in Admal et al.

We have investigated the static and dynamic behaviour of symmetric tilt grain boundaries around [001] in 2D phase field corresponding to the same CSL grain boundaries as those considered by atomistics. GB structure correspond to the spatial distribution of GND, and we found that the distribution scales with the misorientation angle and the distribution is the same for all STGB when rescaled. The rescaled GND distribution depends solely upon the materials parameters. In a very surprising manner, the PF calculation of the GB energy agree quantitatively with those measured by MD. We have investigated the migration of STGB by applying a shear rate in range $[0-30] \times 10^{-4} ms^{-1}$

and temperature in a range $[0, 1000K]$. During migration, the GND distributions are very similar in shape between the equilibrium and steady state motion, as we would want to, based on physical arguments. The PF simulations agree quantitatively well with the geometric model for the shear coupling coefficient. Interestingly, the PF recovers naturally some of the trends obtained in MD, when considering the velocity of GB migration as function of both temperature and shear rate. For some GB, the velocity is non linear as function of the shear rates and increases with the temperature, akin to the thermally behaviour observed in MD. Some other GBs exhibit a linear relationship of the velocity with driving force and the slope decreases with temperature, akin to the dragging regime observed in MD. It is possible that the existence of the two temperature behaviours in PF are related to the dynamic and dissipation associated to the motion of the slip systems (GND). Arguably, the rearrangement of slip systems in the GB may lead to a non linear regime, while the simple gliding of dislocations may explain the linear regime and may be associated to more dissipation. This needs to be further studied. Bottom line, The fact that the PF "naturally" captures some key features such as GB energy, or migration velocity trends is very striking, as no data was directly coming from atomistic at that stage. Therefore, this suggests that describing GB as dislocation arrays (or GND distribution) is very effective and promising, at least for the STGB considered here.

In the final step of this work, we have derived semi-analytical solutions of $\phi(x)$ and $\theta(x)$ of the one dimensional problem of a single GB in a bicrystal under static and steady motion conditions. This can be seen as one way to compare and validate numerical solution. Having in place an analytical solution for both θ and ϕ field parameters is more convenient than numerically evaluating these fields from implicit integral equations. In addition, this analytical solution can be used as an $ansatz$ for initial conditions or as a fit for the dynamical case where the grain boundary is moving. However, the solutions for both field parameters remain implicit because of the integral constant c that can only be identified iteratively.

6.5 Future works of the project

Atomistic simulations

- The generic phenomenological mobility function was only devised for bi-crystalline geometries of [001] flat grain boundaries, therefore, the future work will focus on validating this phenomenological mobility function on a) other misorientation axes b) curved grain boundaries and c) a more realistic polycrystalline microstructure, where differently oriented grain boundaries form a network and react differently once a driving force is applied.

- There should be also a challenging study aiming at relating different parameters in the mobility function to the atomic structure or migration mechanism of a grain boundary. For example, in literature the prefactor of mobility function was reported by some studies (Sutton, 1996) to be related to the number of nucleation site for a pair of disconnections or the number of atoms involved in shuffle at grain boundary. This requires to have in a place a code to identify and characterise a defect on a surface of moving grain boundary. Therefore the future work will also aim at developing this tool to analyse the atomic structure a moving GB.

- It will be interestingly to verify if this mobility function is transferable to other material system for example BCC materials.

Phase Field simulations

- Our analytical solution was only applied to a $\Sigma5$ is performed, for the future of this model, we will aim at applying the model to other GBs of different characters including both low and high angle grain boundaries.
- A natural extension of the work would be to import the developed atomistic mobility functions in both Admal's & Marian's phase field model and in our developed analytical solutions, for that we will do a one-to-one comparison between analytical and numerical solution for the same grain boundaries investigated in this study.
- In the next step, we will rework this phase field model for the 3D representation, which can allow a direct comparison with the atomisitic simulations conducted in this study.
- We could provide a mathematical way of comparing the physical work applied in mesoscale simulation from synthetic driving force applied in atomistic simulation.
- We would assess the capability of the atomistically informed phase field model to model a polycrystal with dozen of grains, and compare this with a MD simulation on a similar configuration.
- We could compare the prediction of this atomistically informed phase field model with experimental data.

Appendix A

A.1 Adapted Verlet algorithm to integrate equation of motion

Leap frog algorithm

On the other hand, there exist more sophisticated adapted Verlet algorithms to integrate the equations of motion. In Leap frog algorithm, velocity of a particle is calculated on $(t + \frac{\Delta t}{2})$ and $(t - \frac{\Delta t}{2})$ whereas position is collected on $(t + \Delta t)$ and $(t - \Delta t)$ as shown in the equations

$$v_i\left(t + \frac{\Delta t}{2}\right) = \frac{r_i(t + \Delta t) - r_i(t)}{\Delta t} \tag{A.1}$$

$$v_i\left(t - \frac{\Delta t}{2}\right) = \frac{r_i(t) - r_i(t - \Delta t)}{\Delta t} \tag{A.2}$$

Here we are not diving into more details of this algorithm since the fundamental features of this scheme is already demonstrated in the simple Verlet algorithm.

Predictor-Corrector algorithm

There exist also other distinct and sophisticated class of integration schemes known as Predictor-Corrector schemes. The first kind was introduced in Molecular dynamics by Rahman (Ackermann et al., 1988). As in simple Verlet algorithm, this class also relies on the Taylor series expansion method. Predictor-Corrector scheme uses temporal and spacial coordinates, velocity of a given atom and higher time derivatives to predict atomic coordinates and velocity on the next time step. The latter are then refined by a corrector procedure. An example of the commonly used method is the Gear-predictor-corrector algorithm (Allen and Tildesley, 2017) which comes from the collection of methods devised by Gear (Broughton et al., 1986). More details of this integration scheme can be found in textbook (Allen and Tildesley, 2017),(Satoh, 2010) and (Paul, 1993).
After carefully comparing all algorithms above, we have decided to use Verlet algorithm in this project.

A.2 Synthetic driving force of Schönfilder

The first virtual driving force was introduced in 2006 (Schönfelder et al., 2006) with the name of orientation-correlated driving force (OCDF). From Schönfilder, the excess energy for each atom i is a function of the structural factor $\left|S(\overrightarrow{k}_{\alpha}\right|^2$ that depends on orientation and this structural factor is calculated in the vicinity of atom i. The vicinity of atom is measured using a sphere of chosen radius known as cut-off radius which must be centred around atom i. The overall contribution of excess energy to the system (E_{corr}) is given by the summation of excess energy per atom i (e_i^{corr}).

$$E_{corr} = \sum_{i=1}^{N} e_i^{corr} = \sum_{i=1}^{N}\sum_{\alpha=1}^{2} a_\alpha . |S(k_\alpha)|_i^2 = \sum_{i=1}^{N} a_1 . |S(K_1)|_i^2 + a_2 . |S(k_2)|_i^2 \tag{A.3}$$

Where N is the number of atoms in a system, k_α is the reciprocal lattice vector corresponding to a crystallographic orientation α, a_1 and a_2 are the parameters that determine the amount of energy per atom added to crystal 1 and crystal 2 respectively. $|S(k_\alpha)|^2$ follows equation A.4 in which r_j and $\overrightarrow{r}_k$ are the real space vector of atom j and k respectively.

$$|S(k_\alpha)|^2 = \frac{1}{N^2}\sum_{j=1}^{N}\sum_{k=1}^{N} \exp(i k_\alpha (r_j - r_k)) \tag{A.4}$$

By carefully choosing a_1 and a_2 an energy difference between grain 1 and grain 2 is created which drives a grain boundary.

Results obtained from using this driving force were reported to be in a good agreement with results from the more classical elastic driving force. Schönfelder et al. compared the rate of migration of [001] grain boundaries induced by orientation correlated force and an elastic driving force. Both driving forces were reported to be in a good agreement. Schönfelder et al. reported that orientation correlation driving force was able to continuously drive grain boundaries whereas in case of elastic driving force, grain boundary sliding events happened that did not produce a steady rate of motion. This is one advantage of orientation correlated driving force over elastic force. It means that elasticity or processes that lead to plastic deformation can easily be separated from the issue of introducing driving force. One of feature that orientation correlation driving force and elastic driving force share in common is their temperature dependence.The orientation correlated driving force's magnitude for a fixed a_1 and a_2, decreases with increasing temperature. This is reasonable, since increasing temperature leads to increase in thermal fluctuations in the atomic positions which results in reducing the energy applied to each grain, hence a reduction in the driving force.

A.3 Comparison between predicted and MD raw velocity

Figures 115 a-d and figure 116 show comparison between velocity from MD and predicted velocity points at different temperature and driving force from some grain boundary representatives of all other investigated grain boundaries.

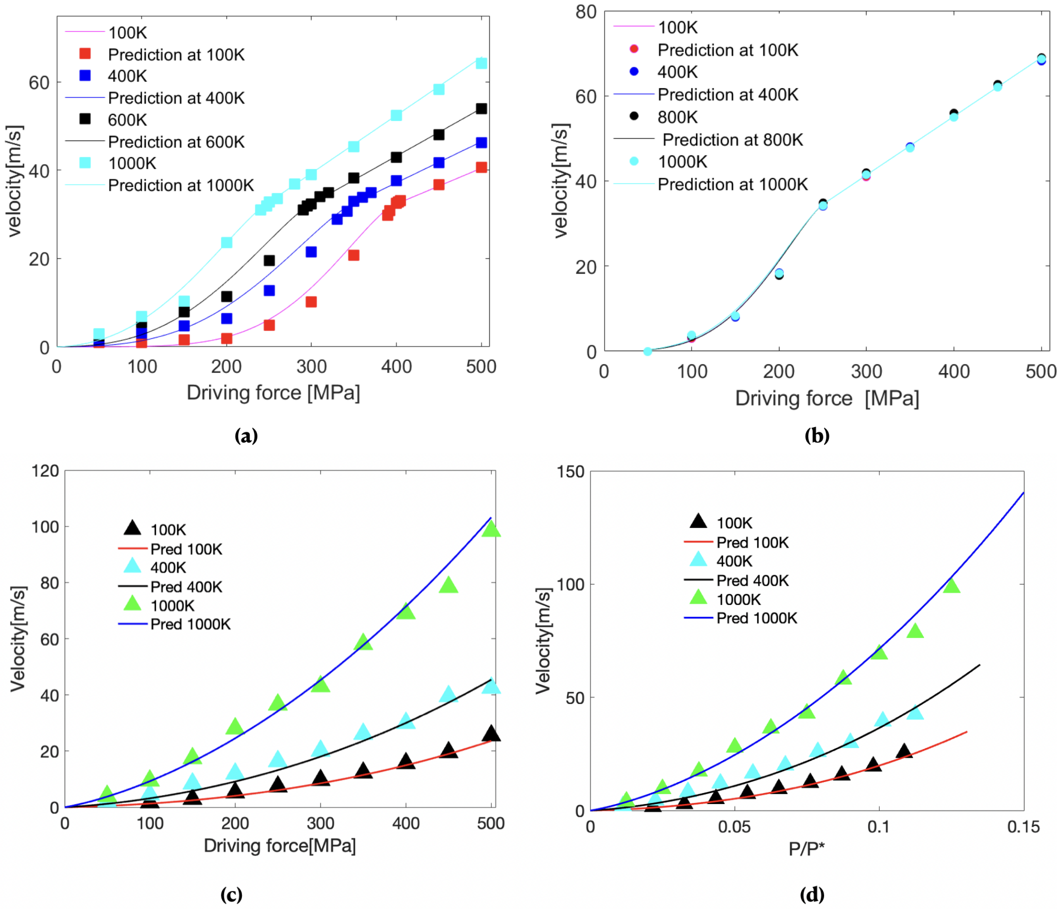

(a) **(b)**

(c) **(d)**

Figure 115: Comparison between MD and predicted velocity for a) thermal $\Sigma5(001)$ pure twist b) athermal $\Sigma5(3\bar{1}3)$ mixed and for thermally activated $\Sigma13(3\bar{2}0)$ (c) over the stress range investigated (d) over the applied stress normalised by the transition stress $P*$.

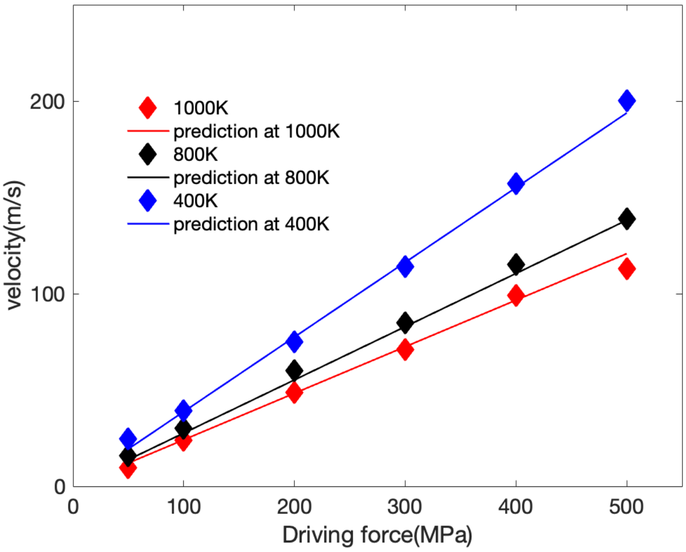

Figure 116: Comparison between MD and predicted velocity for antithermal $\Sigma25(7\bar{1}0)$ grain boundaries.

Appendix B

B.1 Reliability of phase field dynamic equations

Here, we start by recalling the Hamiltonian dynamics discussed in section 2.2.1.1 and the Langevin dynamics that explicitly separates the thermal fluctuation.

For a system containing N atoms of spatial coordinates $q = \{q_1, q_2, q_3, ..., q_N\}$ and momenta $p = \{p_1, p_2, p_3, ..., p_N\}$ of individual atoms, thus, resulting in 6N degrees of freedom, the time evolution of the system in the Hamiltonian mechanics is described by the following equation

$$\begin{aligned} \frac{\partial q}{\partial t} &= \frac{\partial \mathscr{H}}{\partial p} \\ \frac{\partial p}{\partial t} &= \frac{\partial \mathscr{H}}{\partial q} \end{aligned} \tag{B.1}$$

Where $\mathscr{H}$ is the Hamiltonian. By considering each individual atoms, this may result in 2N partial differential equations which is quite expensive to solve all numerically. In practice it is preferable to use the principle of statistical mechanics to reduce the complexity of the system. In statistical mechanics, a large number of degrees of freedom of the system is replaced by a probability function that represents an averaged consequence. This function describes a $2N$ dimensional phase space with coordinates p and q and each point in this space represents a particular state called a micro-state of the system. Temporal evolution of the system is then viewed as a trajectory connecting a sequence of micro-states. For a smaller volume of the system with coordinate (p, q) at time t, the probability $\mathscr{P}$ of finding a state (p, q) is equal to $\rho(p, q, t)dpdq$ and is normalised in a such way that

$$\int \rho(p, q, t)dpdq = 1 \tag{B.2}$$

Where $\rho(p, q)$ describes the density of the micro-states in a volume. The phase space distribution function $\rho(p, q)$ derives the observable property $\mathscr{A}_{obs}$ as the ensemble average $\Big\langle A(p, q) \Big\rangle$ of property $A(p, q)$ with explicit dependence on the micro-state (p, q). $\mathscr{A}_{obs}$

reads

$$\mathscr{A}_{obs} = \left\langle A(p,q) \right\rangle = \int \rho(p,q,t)A(p,q)dqdp \tag{B.3}$$

The dynamic equation is obtained by substituting equation B.1 into the continuity equation

$$\frac{\partial \rho}{\partial t} + \frac{\partial}{\partial x}\left(\frac{\partial x}{\partial t}\right) = 0 \tag{B.4}$$

For a conserved phase points x which is sampled such that $x = (p,q)$. The dynamic equation for $\rho(p,q)$ reads

$$\frac{\partial \rho}{\partial t} = -\mathscr{L}\rho \tag{B.5}$$

Which is commonly known as Liouville equation and $\mathscr{L}$ is the Liouville operator which reads

$$\mathscr{L} \equiv \left(\frac{\partial \mathscr{H}}{\partial p}\frac{\partial}{\partial q} - \frac{\partial \mathscr{H}}{\partial q}\frac{\partial}{\partial p}\right) \tag{B.6}$$

Although in thermodynamic problem, a system in contact with a thermal reservoir is modelled as a whole by using either Hamiltonian or Liouville equations, it is preferable to model both entities separately to reduce the complexity of the system. Thanks to Langevin dynamics, thermal fluctuation or force from a thermal reservoir $\mathscr{G}$ can explicitly be separated from the internal force $v(x)$. The dynamic evolution of the system follows a Langevin dynamic equation

$$\frac{\partial x}{\partial t} = v(x) + \mathscr{G} \tag{B.7}$$

B.1.1 Fokker-Planck's equation

Fokker-Planck equation is a very useful starting point for relating phenomenological continuum equations to the master equations[16]. Thus, Fokker-Planck equation allows to relate kinetic equations (Cahn-Hilliard and Allen-Cahn equation) to statistical mechanics. In statistical mechanics, this partial differential equation is used to describe the time evolution of the probability density function of the velocity of a particle subjected to drag and random forces. For a Gaussian distributed thermal fluctuation $v(x)$ depends only on the current state x. By considering an average over thermal noise by following equation B.3 and combining equation B.7 and equation B.4 give the Fokker-Planck equation also known as noise averaged distribution function (Pathria and Beale, 1996)

$$\frac{\partial \rho(x,t)}{\partial t} = -\frac{\partial}{\partial x}\left[v(x)\rho(x,t)\right] + \frac{\partial}{\partial x}\left[B\frac{\partial}{\partial x}\rho(x,t)\right] \tag{B.8}$$

---

[16] Master equations are a set of differential equations which are used to describe the time evolution of a system that can be modelled as being in a probabilistic combination of states at any given time. In addition, the switching between states must be determined by a transition rate matrix.

Where B is a function that depends on x. The Fokker-Planck equation is identical to the Liouville equation in Hamiltonian dynamics. To derive the Fokker-Planck equation for a general case is based on the transition state theory (Pathria and Beale, 1996). In the transition state theory, the rate of transition $P(x,x')$ from x to x' is obtained from equation again by averaging $P(x,x')$ by using equation B.3

$$\frac{\partial \rho(x,t)}{\partial t} = \int \left[-\rho(x,t)P(x,x') + \rho(x',t)P(x',x)\right] dx' \tag{B.9}$$

The two terms in the integrand represent respectively the flow of ρ that leaves and enters the state x. Consequently, their sum is the net flow of ρ that leaves the state x. If we consider the situation where the noise is low enough so that the transition only occurs between the neighbouring states, the function $P(x,x')$ becomes a sharply peaked function whose center is on x and decreases rapidly with $(x'-x)$. Considering, the transition from state x to state $(x'-x)$, the function $P(x,x')$ is rewritten as $P(x,x'-x)$. By doing a Taylor expansion of both functions $\rho(x,t)$ and $P(x,x')$ in the vicinity of state x leads to

$$\begin{aligned}\frac{\partial \rho(x,t)}{\partial t} = \int \Bigg\{ &- \rho(x,t)P(x,x'-x) + \rho(x,t) + \frac{\partial \rho(x,t)}{\partial x}(x'-x) + \frac{1}{2}\frac{\partial^2 \rho(x,t)}{\partial x^2}(x'-x)^2 + ... \\ &+ P(x,x'-x) + \frac{\partial P(x,x'-x)}{\partial x}(x'-x) + \frac{1}{2}\frac{\partial^2 P(x,x'-x)}{\partial x^2}(x'-x)^2 + ... \Bigg\} dx'\end{aligned} \tag{B.10}$$

By only keeping the terms up to second order expansion term leads

$$\frac{\partial \rho(x,t)}{\partial t} = -\frac{\partial}{\partial x}[\mu_1(x)\rho(x,t)] + \frac{1}{2}\frac{\partial}{\partial x}\frac{\partial[\mu_2(x)\rho(x,t)]}{\partial x} \tag{B.11}$$

For

$$\begin{aligned}\mu_1(x) &= \int (x'-x)P(x,x'-x)d(x'-x) = \frac{\langle \delta x \rangle}{\delta t} = v(x) \\ \mu_2(x) &= \int (x'-x)^2 P(x,x'-x)d(x'-x) = \frac{\langle \delta x^2 \rangle}{\delta t}\end{aligned} \tag{B.12}$$

Apparently, μ_1 is the rate at which the system leaves the state x therefore it is seen as a velocity term $v(x)$ and μ_2 is the fluctuation on x. For a case where μ_2 does not depend on x equation B.11 becomes identical to Fokker-Plank equation B.8. The demonstrations shown above have used the generalised form of $P(x,x')$, in some specific derivations, like ours for deriving Cahn-Hilliard and Allan-Hilliard, $P(x,x')$ can be expressed function of the free energy of the system.

B.1.2 Derivation of the phase field dynamic equations

In this section, we use the theory developed in previous sections and follow the procedure described in (Langer, 1969) and (Langer, 1971), to derive dynamic equations given in section 4.3.

Cahn-Hilliard equation

Let consider a binary system of dimension **d** containing **N** number of atoms which is in direct contact with a temperature reservoir. The system is subdivided into $\frac{N}{\nu}$ cells each containing n atoms. We further assume that the pair-exchange of atoms is the only transition mechanism between neighbouring cells. In this case, $P(X, X')$ takes the form

$$P(X,X') = \frac{1}{2}\sum_{\alpha,\alpha'}\prod_{\beta\neq\alpha,\alpha'} \delta\left(X'_\beta - X_\beta\right) M_{\alpha\alpha'} \int R(X,X')\delta(X'_\alpha - \varepsilon - X_\alpha)\delta(X'_{\alpha'} + \varepsilon - X_{\alpha'})^3 d\varepsilon \tag{B.13}$$

X and X' denote the initial and final transition states respectively whereas indices α, α' and β denote the cells. In equation, the term $M_{\alpha\alpha'}$ is the matrix with value unity if α and α' are neighbouring cell and zero elsewhere. The term $\delta(X'_\beta - X_\beta)$ plays the role of constraining the pair-exchange between cells α and α'. A change of $-\varepsilon$ in cell α, as the term $\delta(X'_\alpha - \varepsilon - X_\alpha)$ shows, is accompanied by a change of $+\varepsilon$ in cell α' as the term $\delta(X'_{\alpha'} + \varepsilon - X_{\alpha'})$ shows. It is important to note that this pair-exchange ensures a local conservation of the composition. The rate of pair exchange $R(X, X')$ reads

$$R(X,X') = \overline{\mathscr{T}}(X,X')exp\left(\frac{F(X) - F(X')}{2k_BT}\right) \tag{B.14}$$

For

$$\begin{aligned}\overline{\mathscr{T}}(X,X') = \frac{1}{\Omega}\int\Bigg\{\int & \mathscr{T}_{rr'}(X,X')\sqrt{W(X)W(X')} \\ & exp\left(-\frac{E_R(r) + E_R(r')}{2k_BT}\right)\delta\left(E_R(r) - E_R(r') + E(X) - E(X')\right)dr'\Bigg\}dr\end{aligned} \tag{B.15}$$

For a thermal reservoir which is always at equilibrium, Ω is a constant, $E_R(r)$ and $E_R(r')$ are the internal energy of the thermal reservoir at state r and r'. The internal energy of system at states X and X' are denoted as $E(X)$ and $E(X')$ respectively. $W(X)$ and $W(X')$ describe the number of possible microscopic configurations of the same macroscopic configuration X and X' respectively. Therefore $W(X)$ and $W(X')$ account for the configurational entropy from atomic scale length up to the cell length scale. $\mathscr{T}_{rr'}$ is proportional to the transition rate between states r, X and r', X'. Note that, the terms $\delta\left(E_R(r) - E_R(r') + E(X) - E(X')\right)$ ensures the conservation of the total internal energy of the system and thermal reservoir. F is total free energy of a system described previously. If we substitute equation B.14 into equation B.13 and the resultant equation into equation B.9 yield

$$\frac{\partial\rho(X,t)}{\partial t}=\frac{1}{2}\sum_{\alpha\alpha'}M_{\alpha\alpha'}\int\left\{\overline{\mathscr{T}}(\varepsilon)exp\left(F_1\right)\rho(X_{\alpha'}-\varepsilon,X_{+}\varepsilon)-\overline{\mathscr{T}}(\varepsilon)exp\left(F_2\right)\rho(X_{\alpha'},X_{\alpha})\right\}d\varepsilon \tag{B.16}$$

For

$$F_1=\frac{F(X_{\alpha'}-\varepsilon,X_{\alpha}+\varepsilon)-F(X_{\alpha'},X_{\alpha})}{2k_BT}$$
$$F_2=\frac{F(X_{\alpha'},X_{\alpha})-F(X_{\alpha'}-\varepsilon,X_{\alpha}+\varepsilon)}{2k_BT}$$

However, due to the constrained transition between X and X', as previously explained, $\overline{\mathscr{T}}(X,X')$ is rewritten as $\overline{\mathscr{T}}(\varepsilon)$ for convenience. If the system is large enough, the variation in time of X during transition is expected to be smaller, therefore, $\overline{\mathscr{T}}(\varepsilon)$ peaks at $\varepsilon=0$. By doing Taylor expansion on function $F(X_{\alpha'}-\varepsilon,X_{\alpha}+\varepsilon)$ to keep only second order terms returns

$$\begin{aligned}F(X_{\alpha'}-\varepsilon,X_{\alpha}+\varepsilon)&=F(X_{\alpha'},X_{\alpha})+\varepsilon\left(\frac{\partial}{\partial X_{\alpha'}}-\frac{\partial}{\partial X_{\alpha}}\right)F|_{X'_{\alpha},X_{\alpha}}\\&+\frac{\varepsilon^2}{2}\left(\frac{\partial}{\partial X_{\alpha'}}-\frac{\partial}{\partial X_{\alpha}}\right)^2F|_{X'_{\alpha},X_{\alpha}}\end{aligned}\tag{B.17}$$

and doing the same for $\rho(X_{\alpha'}-\varepsilon,X_{\alpha}+\varepsilon)$ gives

$$\begin{aligned}\rho(X_{\alpha'}-\varepsilon,X_{\alpha}+\varepsilon)&=\rho(X_{\alpha'},X_{\alpha})+\varepsilon\left(\frac{\partial}{\partial X_{\alpha'}}-\frac{\partial}{\partial X_{\alpha}}\right)\rho|_{X'_{\alpha},X_{\alpha}}\\&+\frac{\varepsilon^2}{2}\left(\frac{\partial}{\partial X_{\alpha'}}-\frac{\partial}{\partial X_{\alpha}}\right)^2\rho|_{X'_{\alpha},X_{\alpha}}\end{aligned}\tag{B.18}$$

By substituting equations B.17 and B.18 into equation B.16 and by considering that the first-order terms vanishes due to symmetric function $\overline{\mathscr{T}}(\varepsilon)$, equation B.16 leads to

$$\begin{aligned}\frac{\partial\rho}{\partial t}=&\left(\int\varepsilon^2\overline{\mathscr{T}}(\varepsilon)d\varepsilon\right)\sum_{\alpha',\alpha}M_{\alpha'\alpha}\left(\frac{\partial}{\partial X_{\alpha'}}-\frac{\partial}{\partial X_{\alpha}}\right)\left[\frac{1}{k_BT}\left(\frac{\partial F}{\partial X_{\alpha'}}-\frac{\partial F}{\partial X_{\alpha}}\right)\rho\right.\\&\left.+\left(\frac{\partial\rho}{\partial X_{\alpha'}}-\frac{\partial\rho}{\partial X_{\alpha}}\right)\right]\end{aligned}\tag{B.19}$$

This equation is similar to Fokker-Planck equation if $M_{\alpha'\alpha}$ is explicitly replaced by the summation $\left(\sum_{\alpha'}^{(i.i)}\right)$ over **i** the **2d** nearest neighbors of the cells α and the phenomenological fluctuation frequency $\mathscr{F}$ which follows

$$\mathscr{F}\equiv\nu^{\left(1+\frac{2}{d}\right)}\int\varepsilon^2\overline{\mathscr{T}}(\varepsilon)d\varepsilon\tag{B.20}$$

It leads to

$$\frac{\partial\rho}{\partial t} = \sum_{\alpha} \frac{\partial}{\partial X_\alpha}\left[\sum_{\beta}\frac{\mathscr{F}}{2\nu^{(1+\frac{2}{d})}}\left(2d\,\delta_{\alpha\beta} - \sum_{\alpha'}^{(i.i)}\delta_{\alpha'\beta}\right)\left(\frac{\partial F}{k_B T\partial x_\beta}\rho + \frac{\partial\rho}{\partial X_\beta}\right)\right] \tag{B.21}$$

Let multiply this equation by X_ω and then integrate over the configuration X, he first term becomes

$$\int X_\omega \frac{\partial\rho(X,t)}{\partial t}dX = \frac{\partial}{\partial t}\int X_\omega \rho(X,t)dX = \frac{\partial \overline{X}_\omega}{\partial t} \tag{B.22}$$

$\overline{X}_\omega$ is X_ω averaged over the fluctuation due to thermal reservoir. The right hand side becomes

$$\begin{aligned}
&\int X_\omega \sum_{\alpha}\frac{\partial}{\partial X_\alpha}\left[\sum_{\beta}\frac{\mathscr{F}}{2\nu^{(1+2/d)}}\left(2d\,\delta_{\alpha\beta} - \sum_{\alpha'}^{(i.i)}\delta_{\alpha'\beta}\right)\left(\frac{\partial F}{k_B T\partial X_\beta}\rho + \frac{\partial\rho}{\partial X_\beta}\right)\right]dX \\
&\approx -\int \sum_{\beta}\frac{\mathscr{F}}{2\nu^{(1+2/d)}}\left(2d\,\delta_{\omega\beta} - \sum_{\alpha'}^{(i.i)}\delta_{\alpha'\beta}\right)\left(\frac{\partial F}{k_B T\partial X_\beta}\rho + \frac{\rho}{\partial X_\beta}\right)dX_\omega \\
&\approx -\sum_{\beta}\frac{\mathscr{F}}{2\nu^{(1+2/d)}}\left(2d\,\delta_{\omega\beta} - \sum_{\alpha'}^{(i.i)}\delta_{\alpha'\beta}\right)\int \rho\frac{F}{k_B T\partial X_\beta}dX_\omega \\
&\approx -\sum_{\beta}\frac{\mathscr{F}}{2\nu^{(1+2/d)}}\left(2d\,\delta_{\omega\beta} - \sum_{\alpha'}^{(i.i)}\delta_{\alpha'\beta}\right)\left\langle\frac{\partial F}{k_B T\partial X_\beta}\right\rangle
\end{aligned} \tag{B.23}$$

Here, to make a transition to the continuum limit, the summations in equation above is replaced by their continuum analog, that is an integral. In $d-$dimensions, it is achieved by

$$\sum_{\alpha} \rightarrow \int \frac{1}{\nu a^d}dX \tag{B.24}$$

To encapsulate the volume that was previously contained within one cell, terms are divided by νa^d. Then

$$\left(2d\,\delta_{\omega\beta} - \sum_{\alpha'}^{(i.i)}\delta_{\alpha'\beta}\right) \rightarrow -(a^d\nu)(a^2\nu^{(2/d)})\nabla^2(X - X') \tag{B.25}$$

and

$$\frac{\partial}{\partial X_\alpha} \rightarrow \nu a^d \frac{\partial}{\partial X} \tag{B.26}$$

If we consider here $\overline{X}(r)$ and $\left\langle\frac{\partial F}{\partial X}\right\rangle$ which are values averaged over fluctuation due to the thermal reservoir, consequently, the term $\frac{\partial\rho}{\partial X}$ that corresponds to the fluctuation vanishes by this averaging. Then, equation B.21 becomes

$$\frac{\partial \overline{X}(r)}{\partial t} = \frac{\mathscr{F} a^{(2+d)}}{2k_B T} \nabla^2 \left\langle \frac{\partial F}{\partial X} \right\rangle \tag{B.27}$$

If the function $\rho(X)$ is sharply peaked at $X = \overline{X}$ so that the average of any quantity over ρ can be successfully approximated by its value at $\overline{X}$, then equation B.27 reduces to equation B.28 which is the famously known Cahn-Hilliard equation given in equation 4.6

$$\frac{\partial \overline{X}(x,t)}{\partial t} = \frac{\mathscr{F} a^{(2+d)}}{2k_B T} \nabla^2 \frac{\partial F\left(\overline{X}(x,t)\right)}{\partial \overline{X}(x,t)} \tag{B.28}$$

where x and t denote the spatial and temporal coordinates and $\overline{X}(c,t) = \phi(x,t)$.

Allen-Cahn equation

Let again consider a $d-$dimensional system in direct contact with thermal reservoir. The system has N degrees of freedom and is divided into $\frac{N}{\nu}$ cells. Let consider an order parameter ϕ_α in the cell . In a similar way as before

$$P(\phi, \phi') = \sum_\alpha \prod_{\beta \neq \alpha} \delta(\phi'_\beta - \phi_\beta) R(\phi, \phi') \tag{B.29}$$

The master equation B.9 becomes

$$\begin{aligned} \frac{\partial \rho(\phi,t)}{\partial t} = \sum_\alpha \int \overline{\mathscr{T}}(\varepsilon) \Big\{ & exp\left[\frac{F(\phi_\alpha + \varepsilon) - F(\phi_\alpha)}{2k_B T}\right] \rho(\phi_\alpha + \varepsilon) \\ & - exp\left[\frac{F(\phi_\alpha) - F(\phi_\alpha + \varepsilon)}{2k_B T}\right] \rho(\phi_\alpha \Big\} d\varepsilon \end{aligned} \tag{B.30}$$

Note that, from here, we followed procedure described in (Langer, 1971), therefore, we slightly change the mathematical expression of $\mathscr{T}$ because, the transition in the non conserved variable dynamics does not require the pair exchange mechanism to occur, therefore

$$\mathscr{F} \equiv \nu \int \varepsilon^2 \overline{\mathscr{T}}(\varepsilon) d\varepsilon \tag{B.31}$$

In a similar manner as before, we do the Taylor expansion on functions $\rho(\phi_\alpha + \varepsilon)$ and $F(\phi_\alpha + \varepsilon)$ and keeping up to the second order terms leads to

$$\frac{\partial \rho}{\partial t} = \sum_\alpha \varepsilon^2 \overline{\mathscr{T}} \frac{\partial}{\partial \phi_\alpha} \left(\frac{\partial F}{k_B T \partial \phi_\alpha} + \frac{\partial \rho}{\partial \phi_\alpha} \right) \tag{B.32}$$

If we multiply both side by ϕ_ω and do the integration as described in previous section

$$\frac{\partial\overline{\phi}_\omega}{\partial t} = -\frac{\mathscr{F}}{\nu}\int \frac{\partial F}{k_B T\partial\phi_\omega}\rho d\phi \tag{B.33}$$

The term corresponding to the fluctuation vanishes by averaging evolving quantity which leads to

$$\frac{\partial\overline{\phi}_\omega}{\partial t} = -\frac{\mathscr{F}}{\nu}\left\langle\frac{1}{k_B T}\frac{\partial F}{\partial\phi_\omega}\right\rangle \tag{B.34}$$

If we consider the continuum representation described in the previous section this equation leads to the Allen-Cahn equation

$$\frac{\partial\overline{\phi}}{\partial t} = -\frac{\mathscr{F}a^d}{k_B T}\frac{\partial F[\overline{\phi}(x,t)]}{\partial\overline{\phi}(x,t)} \tag{B.35}$$

B.2 Numerical solution of one dimensional KWC model

Numerical implementation of this model for one dimensional model requires providing the initial boundary conditions for the entire domain Ω_0 and use powerful numerical integration scheme to approximate the derivatives (numerical integration schemes are treated in section C.1.7). Initial boundary conditions are :

Table B.1: Values of parameters used in KWC model(Admal et al., 2018)

ε^2 $\times 10^{-10}$ $[Jm^{-1}]$	α^2 $\times 10^{-9}$ $[Jm^{-1}]$	s $[Jm^{-2}]$	e $\times 10^9$ $[Jm^{-3}]$	γ $\times 10^{-7}$ $[m]$	L $[nm]$	θ_0 [°]
2.133	5.3	1.7	2.1	5	20	30

$$\begin{aligned}
\phi &= \begin{cases} \phi(x,0) = 1 \\ \phi(L,t) = \phi(-L,t) = 1 \end{cases} \\
\theta &= \begin{cases} \theta(x,0) = -\dfrac{\theta_0}{2} + \dfrac{\theta_0}{1+\exp[-4(x-L/2)]} \\ \theta(L,t) = -\theta(-L,t) = \dfrac{\theta_0}{2} \end{cases}
\end{aligned} \tag{B.36}$$

Where θ_0 denotes the jump in the lattice orientation in grain boundary region. The functions $M_\phi^{\dot{\phi}}$ and $M_\theta^{\dot{\theta}}$ are assumed to be equal to $1\times 10^3 J.s.m^3$. In the numerical implementation, the values for the constants involved in the equations are summarised in the table B.1. Figure 117 compares the steady state analytical from numerical solution. For the derivation of analytical solution, see first the section B.3

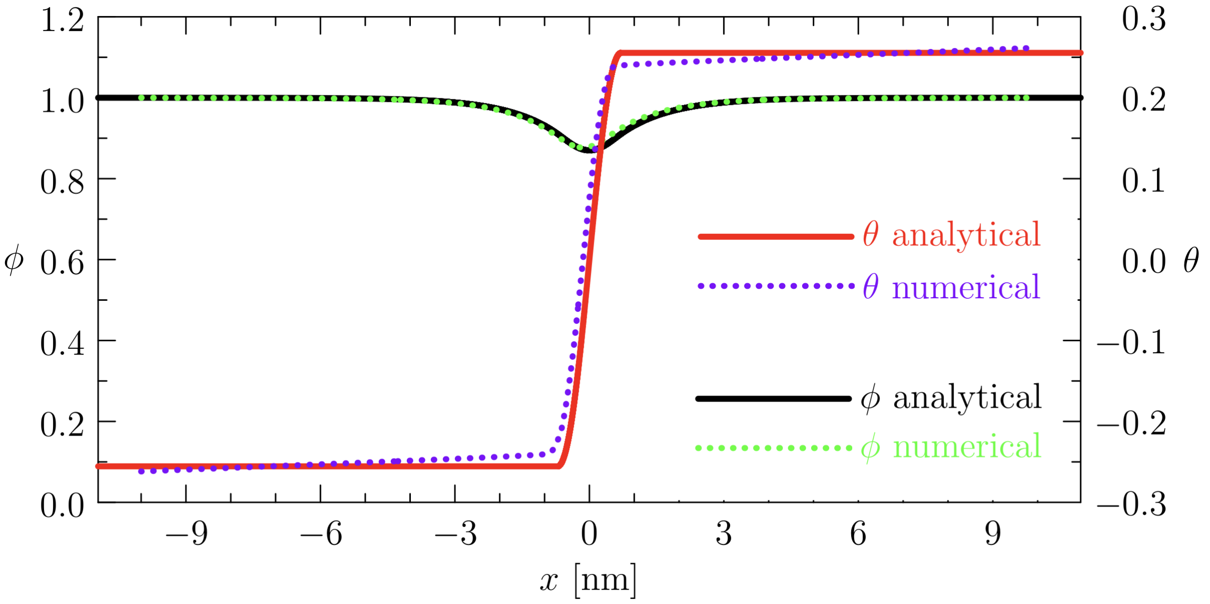

Figure 117: Comparison of the steady state analytical from steady state numerical solution for ϕ and θ(Admal et al., 2018)

B.3 Analytical solution of one dimensional KWC model

This section provides an analytical solution for a one dimension grain boundary by following the procedure devised by Lobkovsky and Warren (Lobkovsky and Warren, 2001). For a system Ω_0 extending from -L to +L and the grain boundary is located at center of the domain (at zero), the boundary condition of ϕ and θ are:

$$\begin{cases} \phi(\pm L) = 1 \\ \theta(\pm L) = \pm\theta_0 \end{cases}$$

The existence of a grain boundary creates a sub-domain $\Omega_0^{GB} \subset \Omega_0$ with distinct properties. Thus, $\nabla\theta \neq 0$ in Ω_0^{GB} and $\nabla\theta \equiv 0$ in Ω_0^{p} (for $\Omega_0^{p} = \Omega_0 \backslash \Omega_0^{GB}$). In Ω_0^{p}, ϕ meets the condition

$$\alpha^2 \frac{\partial^2\phi}{\partial x^2} - \frac{\partial f(\phi)}{\partial\phi} = 0$$

By multiplying both side of equation by $\frac{\partial\phi}{\partial x}$ leads to

$$\alpha^2 \left(\frac{\partial\phi}{\partial x}\frac{\partial^2\phi}{\partial x^2}\right) - \frac{\partial\phi}{\partial x}\frac{\partial f(\phi)}{\partial\phi} = 0$$

Knowing that

$$\frac{\partial\phi}{\partial x}\frac{\partial^2\phi}{\partial x^2}) = \frac{1}{2}\frac{\partial}{\partial x}(\frac{\partial\phi}{\partial x})^2$$

For $x \in \Omega_0^p$, integrating this resulting equation results in

$$\int \frac{\partial}{\partial x}\left[\alpha^2 \frac{1}{2}\left(\frac{\partial \phi}{\partial x}\right)^2 - f(\phi)\right] = \frac{\alpha^2}{2}\left(\frac{\partial \phi}{\partial x}\right)^2 - f(\phi) + c \tag{B.37}$$

Where c is integration constant. If we further integrate equation B.37, it returns the analytical solution of ϕ in Ω_0^p. Here, the solution is given in the inverted form

$$L - x = \int_\phi^1 \frac{\alpha}{\sqrt{2\,(f(\phi) + c)}} d\phi \tag{B.38}$$

In the grain boundary region Ω_0^{GB}, for $x \in \Omega_0^{GB}$,

$$\frac{\partial \theta}{\partial x} \neq 0, \frac{\frac{\partial \theta}{\partial x}}{|\frac{\partial \theta}{\partial x}|} \equiv 1$$

ϕ and θ must satisfy both conditions

$$\alpha^2 \frac{\partial^2 \phi}{\partial x^2} - \frac{\partial f(\phi)}{\partial \phi} - s\frac{\partial g(\phi)}{\partial \phi}\left|\frac{\partial \theta}{\partial x}\right| = 0 \tag{B.39}$$

and

$$\frac{\partial}{\partial x}\left(\varepsilon^2 \frac{\partial \theta}{\partial x} + sg(\phi)\right) = 0 \tag{B.40}$$

If we integrate equation B.40, it leads to

$$\frac{\partial \theta}{\partial x} = \frac{\left(d - sg(\phi)\right)}{\varepsilon^2} \tag{B.41}$$

Where $d \in \Omega_0^{GB}$ is integration constant which is equal to $sg(\phi_2)$ and $\phi_2 := \phi(\pm L)$. By substituting equation B.41 in equation B.39 and multiplying the resultant equation by $\frac{\partial \phi}{\partial x}$ lead to

$$\frac{\partial}{\partial x}\left(\frac{\alpha^2}{2}(\frac{\partial \phi}{\partial x})^2 - f(\phi) + \frac{s^2}{2\varepsilon^2}\big(g(\phi_2) - g(\phi)\big)^2\right) = 0$$

By integrating this equation leads to

$$\left(\frac{\alpha^2}{2}\frac{\partial \phi}{\partial x} - f(\phi) + \frac{S^2}{2\varepsilon^2}\left(g(\phi_2) - g(\phi)\right)^2\right) = 0 \tag{B.42}$$

An other integration of this equation returns the spatial evolution of $\phi(x) \in \Omega_0^{GB}$ in the inverted form.

$$x(\phi) = \int_{\phi_1}^{\phi_2} \frac{\alpha d\phi}{\sqrt{2(f(\phi) + c - (\frac{s}{\varepsilon})^2(g(\phi_2) - g(\phi))^2}})$$

Where $\phi_1 := \phi(0)$ and $\phi < \phi_2$ for the solution of $\theta \in \Omega_0^{GB}$ is obtained by integrating equation B.41 and substituting in the expression for $\frac{\partial \phi}{\partial x}$ from equation B.42 which leads to

$$\begin{aligned}\theta(\phi) &= \frac{1}{\varepsilon^2}\int_{\phi_1}^{\phi_2} \frac{s\Big(g(\phi_2) - g(\phi)\Big)}{\frac{\partial \phi}{\partial x}} d\phi \\ &= \frac{\alpha s}{\varepsilon^2}\int_{\phi_1}^{\phi_2} \frac{(g(\phi_2) - g(\phi))\, d\phi}{\sqrt{2\left(f(\phi) + c - \left(\frac{s}{\varepsilon}\right)^2 (g(\phi_2) - g(\phi))^2\right)}}\end{aligned} \tag{B.43}$$

Note that all derived solutions are expressed in terms of constant c, ϕ_1 and ϕ_2 which are obtained from the relations

$$\begin{aligned}\theta_0 &= \frac{\alpha s}{\varepsilon^2}\int_{\phi_1}^{\phi_2} \frac{g(\phi_2) - g(\phi)}{\sqrt{2\Big(f(\phi) + c - \left(\frac{s}{\varepsilon}\right)^2 [g(\phi_2) - g(\phi)]^2\Big)}} d\phi \\ c &= -f(\phi_1) + \frac{s^2}{2\varepsilon^2}\Big(g(\phi_2) - g(\phi_1)\Big)^2, \\ L &= \int_{\phi_1}^{\phi_2} \frac{\alpha}{\sqrt{2\,(f(\phi + c) - \left(\frac{s}{\varepsilon}\right)^2 (g(\phi_2) - g(\phi))^2}} d\phi + \int_{\phi_2}^{1} \frac{\alpha}{\sqrt{2\,(f(\phi) + c)}} d\phi\end{aligned} \tag{B.44}$$

From this one dimensional solution, one can easily note that as $\varepsilon \to 0$, $\phi_2 \to \phi_1$ consequently θ converges to a step-wise function with a discontinuity at $x = 0$.

Appendix C

C.1 More on the Phase field model of Admal and Marian

C.1.1 Weak convergence

The theory of weak convergence [8] (Admal et al., 2017) gives a physical interpretation of the decomposition in equation 5.32. A sequence of distributions ω^n converge weakly to a distribution ω if

$$\lim_{n\to\infty} \omega^n(\phi) = \omega\phi$$

for all ϕ in the space of functions with compact support C_c^∞ [9]. Then for a constant rotation field R, a sequence of plastic deformation gradient $(F^p)^n$ leaves the lattice with a constant a^n unchanged and $a^n \to 0$ as $n \to \infty$. If this is viewed on average sense then

$$\lim_{n\to\infty} (F^p)^n = R^T$$

as the lattice constant tends to zero. For example let us consider a square lattice, from which $(F^p)^n = \nabla\tilde{x}^n(X)$ for

$$\tilde{x}^n(X) = \left\lfloor \frac{R^T X}{a^n} \right\rfloor a^n \tag{C.3}$$

and this deformation ensures that lattice remains unchanged (where $\lfloor . \rfloor$ denotes the floor function). Since $(F^p)^n$ is a distribution supported by the grain boundary surface, conse-

---

[8] **Theory of weak convergence:** A sequence $\{x_n\}$ of vectors in a inner product space $\mathbb{M}$ is called weakly convergent to a vector in $\mathbb{M}$ if

$$\langle x_n, y\rangle \to \langle x, y\rangle \text{ as } n \to \infty \ , \ \forall y \in \mathbb{M}$$

[9] **Definition of a compact support**: Let $\mathscr{D}$ be an open set in $\mathbb{R}^n$ and let the function $f(x)$ defined such that $f(x) : D \to \mathbb{R}^n$ be a continuous function, the support of $f(x)$ is C^∞ such that $\mathscr{S} = \{x \in \mathscr{D} : f(x) \neq 0\}$. Then, one can say that $f(x)$ has compact support C_c^∞ if C^∞ is a closed bounded set located at a distance δ from the boundary $\mathscr{T}$ of $\mathscr{D}$, such that $\delta > 0$ and δ is sufficiently small.

quently;

$$\lim_{a^n \to 0} \tilde{x}^n(X) = R^T X \tag{C.4}$$

Interestingly, $(F^p)^n$ does not converge point-wise or uniformly to R^T but weakly to R^T. By using the divergence theorem along with $\varphi = 0$ on $\partial\Omega$ and the uniform convergence of $\tilde{x}^n$ to interchange the limit and integral signs in this equality (equation C.5).

$$\lim_{n \to 0} \int_\Omega (F^p)^n \phi dX = \lim_{n \to 0} \int_\Omega \tilde{x}^n \otimes \nabla \phi dX \tag{C.5}$$

leads to

$$\int_\Omega R^T X \otimes \nabla \phi dX = \int_\Omega R^T \phi dX$$

by using weak convergence theory explained above $(F^p)^n \to R^T$ weakly. For $F^e \to R$ and the sequence

$$F^n = F^e (F^p)^n \to R R^T \tag{C.6}$$

C.1.2 Virtual power formulation of the force balance

The purpose of applying this virtual power formulation is to arrive at the necessary macroscopic and microscopic force balance equations. In order to apply this virtual power formulation on an isolated system necessitates determining virtual powers of the system from the applied generalised force. Note that, in this context, generalised forces and generalised stresses denote all events or reactions contributing to the energy equation (Fried and Gurtin, 1994; Gurtin, 1996). It is imperative to note that, in this method, generalised stresses are not directly introduced but rather by the value of the virtual power they produce for a given order parameter. This section uses virtual power formulation following the framework described in papers (Gurtin, 2008; Gurtin et al., 2010; Admal et al., 2018) for kinematic variables introduced in previous sections.

The principle of virtual power is based on the power balance between external power $\mathscr{W}(\Omega)$ and internal power $\mathbf{I}(\Omega)$ expended within an arbitrary part of the body Ω (for $\Omega \subset \beta_t$) (Admal et al., 2018; Gurtin, 2008; Gurtin et al., 2010). Mathematically, it reads

$$\mathscr{W}(\Omega) = \mathbf{I}(\Omega) \tag{C.7}$$

It is assumed that internal power is expended by stresses summarised in table C.1

The internal power expended within Ω reads

$$\mathbf{I}(\Omega) = \int_\Omega \left(P.\dot{F} + \varrho.\nabla\dot{\phi} + \pi\dot{\phi}\right) dV + \sum_\alpha \int_\Omega \left(\Pi^\alpha v^\alpha + \xi^\alpha.\nabla v^\alpha\right) dV \tag{C.8}$$

On the other hand, external power $\mathscr{W}(\Omega)$ comes from the body forces and traction force

Table C.1: Internal power expended at point $\Omega \in \beta_t$ and their conjugate (Admal et al., 2018).

Internal power is expended by stress	Conjugate of
P	F
a stress vector ϱ	$\nabla\dot{\phi}$
a scalar internal microscopic force π	$\dot{\phi}$
for each slip system α, a scalar internal microscopic force Π^α	the slip v^α
a vector microscopic stress ξ^α	∇v^α

acting on $\partial\Omega$. The surface integral $\mathcal{L}(\Omega)$ resulting from the expression of internal power given in equation C.8 gives the structure of the work done by external traction forces

$$\begin{aligned}\mathcal{L}(\Omega) = &\int_{\partial\Omega}\left[PN.\dot{y} + \varrho.N\dot{\phi} + \sum_\alpha (\xi^\alpha.N)\, v^\alpha\right] dA \\ &+ \int_\Omega \left[\dot{\phi}\,(\pi - \mathrm{Div}\varrho) - \dot{y}.\mathrm{Div}P\right] dV + \sum_\alpha \int_\Omega (\Pi^\alpha - \mathrm{Div}\xi^\alpha)\, v^\alpha dV\end{aligned} \tag{C.9}$$

Equation C.9 contains a macroscopic surface traction which is conjugate to $\dot{y}$ and two types of microscopic traction which are conjugate to $\dot{\phi}$ and slip rates v^α. Therefore, based on equation C.9, the surface integral $\mathscr{W}(\Omega)$ has the form

$$\mathscr{W}(\Omega) = \int_{\partial\Omega}\left[t(N).\dot{y} + s(N)\dot{\phi} + \Xi^\alpha(N)v^\alpha\right] dA \tag{C.10}$$

Where t is the macroscopic traction conjugate to $\dot{y}$, s is microscopic traction conjugate to $\dot{\phi}$ and Ξ^α is microscopic traction conjugate to v^α.

C.1.3 Macroscopic and microscopic force balance

To arrive at the force balance equations requires taking independent variation of equation C.10 with respect to $\dot{y}$, $\dot{\phi}$ and $v^\alpha(\alpha = 1, ..., n)$. Here we list all macroscopic and microscopic force balance equations obtained:

1. Macroscopic force balance equations are

$$\begin{cases}\mathrm{Div}P = 0, & \text{in } \beta_t \\ t = PN, & \text{on } \partial\beta_t\end{cases} \tag{C.11}$$

2. Microscopic force balance for each slip system α reads

$$\begin{cases}\mathrm{Div}\xi^\alpha - \Pi^\alpha = 0, & \text{in } \beta_t \\ \Xi^\alpha = \xi^\alpha.N, & \text{on } \partial\beta_t\end{cases} \tag{C.12}$$

3. Microscopic force balance equations for ϕ reads

$$\begin{cases} \mathrm{Div}\varrho - \pi = 0, & \text{in } \beta_t \\ s = \varrho.N, & \text{on } \partial\beta_t \end{cases} \tag{C.13}$$

C.1.4 Energy balance

Here, we derive laws of energy balance in terms of the previously defined variables and then link the equation derived in sections C.1.2 and C.1.3 to the second law of thermodynamics expressed in the form of the Clausius–Duhem inequality. Energy balance for $\Omega \subset \beta_t$ reads

$$\dot{\overline{\int_\Omega \varepsilon dV}} = -\int_{\partial\Omega} (\mathbf{q}.\mathbf{n}) dA + \int_\Omega r dV + \mathscr{W}(\Omega) \tag{C.14}$$

Where ε is energy density, $\dot{\overline{\int_\Omega \varepsilon dV}} \equiv \frac{d}{dt}\left(\int_\Omega \varepsilon dV \right)$, $\mathbf{q}$ is heat flux vector and r is external heat source. If we substitute equation C.8 into equation C.14 gives the following differential equation

$$\dot{\varepsilon} = -\mathrm{div}\mathbf{q} + r + \left(P.\dot{F} + \varrho.\nabla\dot{\phi}\right) + \sum_\alpha \left(\Pi^\alpha v^\alpha + \xi^\alpha.\nabla v^\alpha\right) + \pi\dot{\phi} \tag{C.15}$$

Note from equation C.15 that configurational forces act in response to changes in the order parameter. The term $P.\dot{F}$ in equation C.15 that describes the power extended due to deformation can be expressed in terms of lattice Lagrangian strain E^e and the right Cauchy-Green tensor C^e as follows

$$\begin{aligned} P.\dot{F} &= S.\dot{E}^e + \sum_{\alpha=1}^{A} \left(sm^\alpha.C^e s^\alpha\right) v^\alpha \\ &= S.\dot{E}^e + \sum_{\alpha=1}^{A} \tau^\alpha v^\alpha \end{aligned} \tag{C.16}$$

The lattice stress tensor S in equation C.16 reads

$$S := F^{e-1} P F^{pT} \tag{C.17}$$

and the resolved shear stress τ on α slip plane reads

$$\tau := S m^\alpha.C^e s^\alpha \tag{C.18}$$

C.1.4.1 Clausius-Duhem inequality

As per the second law of thermodynamics, in a situation where thermal effects are suppressed, the rate of energy increase can never exceed the total amount of energy expended in a process. Next we present the use of the second law of thermodynamics expressed in the form of the Clausius-Duhem inequality at our arbitrary part $\Omega \subset \beta_t$. Clausius-Duhem inequality gathers most of the quantities which intervene when deriving constitutive laws. Thus, here we write the second law in the form of a dissipation inequality that has to be satisfied at all time t and $\forall X \in \Omega$.

$$\dot{\overline{\int_{\Omega} \eta dV}} \geq -\int_{\partial\Omega} \frac{q.n}{T} dA + \int_{\Omega} \frac{r}{T} dV \tag{C.19}$$

$\eta(X,t)$ is entropy density ($\eta(X,t) = \frac{\varepsilon}{T}$), $T(X,t)$ is temperature fields and r denotes a heat source. Then, equation C.19 becomes

$$\dot{\eta} \geq -\text{div}\left(\frac{q}{T}\right) + \frac{r}{T} \tag{C.20}$$

By multiplying equation C.20 by T leads to

$$T\dot{\eta} \geq -\text{div}q + \frac{q.\nabla T}{T} + r \tag{C.21}$$

If we replace div$q$ by expression derived from equation C.15 leads to

$$\dot{\varepsilon} - \left(S.\dot{E}^e + \varrho.\nabla\dot{\phi}\right) - \sum_{\alpha} \left(\Pi^\alpha v^\alpha + \tau^\alpha v^\alpha + \xi^\alpha.\nabla v^\alpha\right) - \pi\dot{\phi} + \frac{q.\nabla T}{T} \leq T\dot{\eta} \tag{C.22}$$

If we finally introduce the free energy density $\psi = \varepsilon - T\eta$ in our inequality C.22 leads to dissipation inequality which links the derived equations in sections C.1.2 and C.1.3 to the second law of thermodynamics in the form of the Clausius-Duhem inequality.

$$\dot{\psi} + \dot{T}\eta - \left(S.\dot{E}^e + \varrho.\nabla\dot{\phi}\right) - \sum_{\alpha} \left(\Pi^\alpha v^\alpha + \tau^\alpha v^\alpha + \xi^\alpha.\nabla v^\alpha\right) - \pi\dot{\phi} + \frac{q.\nabla T}{T} \leq 0 \tag{C.23}$$

C.1.5 Thermodynamically consistent Constitutive equations

In this section, we reproduce the thermodynamically consistent constitutive laws. The purpose is to emerge grain boundary energy and bulk elastic energy into the free energy density functional through its dependence. We use the Coleman-Noll procedure discussed in section C.1.5.1 to connect the kinematic variables derived in section 5.3.1 to the force laws derived in section C.1.2. But before using the Coleman–Noll procedure, important constitutive assumptions are made. Free energy density ψ is assumed to be

$$\psi = \hat{\psi}(s, v, \nabla v)$$

For

$$\begin{cases} s = (T, \nabla T, E^e, G, \phi, \dot{\phi}, \nabla\phi) \\ v = (v^1, v^2, ..., v^\alpha) \\ \nabla v = (\nabla v^1, \nabla v^2, ..., \nabla v^\alpha) \end{cases}$$

A second assumption is that the fields $\eta, q, \xi^\alpha, \pi, \Pi^\alpha$ and S are function of $s, v, \nabla v$ and F^p. The third assumption is that the free energy depends only on E^e and G. The lack of dependence of free energy on F^e, F^p and ∇F^p is attributed to the frame invariance of ψ described in (Berdichevsky, 2006).

C.1.5.1 The Coleman–Noll procedure

The central idea of the Coleman-Noll procedure is to ensure that the second law of thermodynamics described above in the form of Clausius-Duhem inequality is met for any admissible thermodynamic process (Coleman and Noll, 1974). An admissible thermodynamic process is defined as the process that is compatible with the constitutive assumptions given above and meets the principles of mechanics and the law of conservation of energy. (see references (Coleman and Noll, 1974) and (Hütter, 2016) for more details on admissible thermodynamic processes).
In this section, we only use the Coleman–Noll procedure to arrive at thermodynamically consistent constitutive law of the Admal and Marian model (Admal et al., 2018). It allows expressing all forces in the force balance equations 5.34, 5.35 and 5.36 and the governing equation C.22 in terms of temperature, temperature gradient and kinematic variables.

By emerging the functional form given in section C.1.5 in equation C.23 leads to [10]

$$\begin{aligned} &(\psi_{,T} + \eta)\,\dot{T} + \Psi_{,\nabla T}.\nabla\dot{T} + (\psi_{,E^e} - S)\,.\dot{E}^e + \left(\psi_{,\phi} - \pi\right)\dot{\phi} \\ &+ \left(\psi_{,\nabla\phi} - \varrho\right).\nabla\dot{\phi} - \sum_{\alpha=1}^{A}\left(\Pi^\alpha v^\alpha + \tau^\alpha v^\alpha + \xi^\alpha.\nabla v^\alpha\right) + \Psi_{,G}\dot{G} \\ &+ \psi_{,v}.\dot{v} + \Psi_{,\nabla v}.\nabla\dot{v} + \Psi_{,\dot{\phi}}\ddot{\phi} + \frac{q.\nabla T}{T} \le 0 \end{aligned} \tag{C.24}$$

This inequality must be satisfied $\forall X \in \beta_t$. However this inequality can be oversimplified by evaluating each term individually. For example, note that $\nabla\dot{T}$ appears in only one term and the coefficient of $\nabla\dot{T}$ in that term does not depend on $\nabla\dot{T}$. In addition, the coefficients of the terms $\dot{v}$, $\nabla\dot{v}$ and $\ddot{\phi}$ appearing in inequality have no dependence on these

---

[10] Note that $f_{,x}$ denotes the independent differentiation of the functional f with respect to the quantity x. Throughout this textbook $\wedge$ stands for a cross product.

terms. This implies that

$$\psi_{,\nabla T} \equiv \psi_{,\dot{\phi}} \equiv \psi_{,v} \equiv \psi_{,\nabla v} \equiv 0$$

, otherwise inequality C.24 is not met. Consequently, with this simplification, inequality C.24 becomes

$$\begin{aligned}&(\psi_{,T} + \eta)\,\dot{T} + (\psi_{,E^e} - S)\,.\dot{E}^e + \left(\psi_{,\phi} - \pi\right)\dot{\phi} + \left(\psi_{,\nabla\phi} - \varrho\right).\nabla\dot{\phi}\\ &-\sum_{\alpha=1}^{A}\left(\Pi^\alpha v^\alpha + \tau^\alpha v^\alpha + \xi^\alpha.\nabla v^\alpha\right) + \psi_{,G}\dot{G} + \frac{q.\nabla T}{T} \leq 0\end{aligned} \tag{C.25}$$

If we consider again that $\dot{T}$ appears in one term and the coefficient of that term does not depend on $\dot{T}$ and the same goes for $\dot{E}^e$ and $\nabla\dot{\phi}$ our inequality is verified if and only if

$$\begin{cases}\psi_{,T} = -\eta(T, E^e, G, \phi, \nabla\phi)\\ \psi_{,E^e} = S(T, E^e, G, \phi, \nabla\phi)\\ \psi_{,\nabla\phi} = \varrho(T, E^e, G, \phi, \nabla\phi)\end{cases} \tag{C.26}$$

Remark *: Restrictions above (equation C.26) on functional forms make associated functional form thermodynamically-consistent. One realises that* Ψ *has no dependence on* ∇T*,* $\dot{\phi}$*,*v*, and* ∇v*.*

The inequality becomes

$$\left(\psi_{,\phi} - \pi\right)\dot{\phi} - \sum_{\alpha=1}^{A}\left(\Pi^\alpha v^\alpha + \tau^\alpha v^\alpha + \xi^\alpha.\nabla v^\alpha\right) + \psi_{,G}\dot{G} + \frac{q.\nabla T}{T} \leq 0 \tag{C.27}$$

The term $\dot{G}$ can be expressed in terms of slip rate by using the plastic flow equation (Cermelli and Gurtin, 2002)

$$\dot{G} = L^p G + G\left(L^p\right)^T + J^p \sum_{\alpha=1}^{A}\left[\left(F^p\right)^{-T}\nabla v^\alpha \wedge m^\alpha\right] \otimes s^\alpha \tag{C.28}$$

The term $\Psi_{,G}.\dot{G}$ becomes

$$\psi_{,G}.\dot{G} = \sum_{\alpha=1}^{A}\left[\psi_{,G}.\left(\mathscr{V}G + G\mathscr{V}^T\right)v^\alpha + J^p\left(F^p\right)^{-1}\left(m^\alpha \wedge \Psi_{,G}s^\alpha\right).\nabla v^\alpha\right] \tag{C.29}$$

Where $\mathscr{V} := s^\alpha \otimes m^\alpha$ which is the Schmid tensor described in section 5.3.1.1. If we substitute equation C.28 and C.29 into our dissipation inequality in equation C.27 leads to

$$\begin{aligned}&\left(\psi_{,\phi}-\pi\right)\dot{\phi}+\sum_{\alpha=1}^{A}\Bigg\{\left(\psi_{,G}:\left(\mathscr{V}G+G\mathscr{V}^{T}\right)-\Pi^{\alpha}-\tau^{\alpha}\right)v^{\alpha}\\&+\Big[J^{p}(F^{p})^{-1}\left(m^{\alpha}\wedge\psi_{,G}s^{\alpha}\right)-\xi^{\alpha}\Big].\nabla v^{\alpha}\Bigg\}+\frac{q.\nabla T}{T}\leq 0\end{aligned} \tag{C.30}$$

The microscopic stress ξ^{α} is additively decomposed into an energetic ξ^{α}_{energy} part which does not depend on ∇v and dissipative part ξ^{α}_{diss} which depends on ∇v

$$\xi^{\alpha}=\xi^{\alpha}_{energy}+\xi^{\alpha}_{diss} \tag{C.31}$$

By substituting C.31 into our inequality leads to

$$\begin{aligned}&\left(\psi_{,\phi}-\pi\right)\dot{\phi}+\sum_{\alpha=1}^{A}\Bigg\{\left(\psi_{,G}:\left(\mathscr{V}G+G\mathscr{V}^{T}\right)-\Pi^{\alpha}-\tau^{\alpha}\right)v^{\alpha}\\&+\Big[J^{p}(F^{p})^{-1}\left(m^{\alpha}\wedge\psi_{,G}s^{\alpha}\right)-\xi^{\alpha}_{energy}-\xi^{\alpha}_{diss}\Big].\nabla v^{\alpha}\Bigg\}+\frac{q.\nabla T}{T}\leq 0\end{aligned} \tag{C.32}$$

Again $J^{p}(F^{p})^{-1}\left(m^{\alpha}\wedge\psi_{,G}s^{\alpha}\right)-\xi^{\alpha}_{energy}=0$, then our inequality is met if

$$\xi^{\alpha}_{energy}=J^{p}(F^{p})^{-1}\left(m^{\alpha}\wedge\psi_{,G}s^{\alpha}\right) \tag{C.33}$$

For $J^{p}=\det F^{p}$ and ξ^{α}_{energy} is regarded as the Peach-Koehler force [11] due to pile up of dislocations. The ξ^{α}_{diss} is the dissipative micro-stress conjugate to the gradient in slip rate. By substituting equations C.33 into C.32 leads

$$\left(\psi_{,\phi}-\pi\right)\dot{\phi}+\sum_{\alpha=1}^{A}\Bigg\{\left(\psi_{,G}:\left(\mathscr{V}G+G\mathscr{V}^{T}\right)-\Pi^{\alpha}-\tau^{\alpha}\right)v^{\alpha}-\xi^{\alpha}_{diss}.\nabla v^{\alpha}\Bigg\}+\frac{q.\nabla T}{T}\leq 0 \tag{C.34}$$

A solution to equation C.34 reads

$$\begin{cases}\Pi^{\alpha}=\psi_{,G}:\left(\mathscr{V}G+G\mathscr{V}^{T}\right)-\tau^{\alpha}+b^{\alpha}(s,v,\nabla v)v^{\alpha},\\ q=-K\left(s,v,\nabla v\right)\nabla T\\ \pi=\psi_{,\phi}+b^{\phi}\left(s,v,\nabla v\right)\dot{\phi}\\ \xi^{\alpha}_{diss}=B^{\alpha}\left(s,v,\nabla v\right)\nabla v^{\alpha}\end{cases} \tag{C.35}$$

K is the positive valued definite tensor of thermal conductivity, b^{α} is inverse mobility function associated with the slip rate v^{α}, B^{α} is inverse mobility function associated with ∇v and b^{ϕ} is inverse mobility function associated with $\dot{\phi}$.

---

[11] Peach-Koehler force is a configurational force due to equilibrium between a dislocation and the adjacent elastic medium. The dislocation pile up increases the magnitude of this configurational force so that it becomes capable of driving dislocation outside of equilibrium (Gurtin, 1999; Hirth et al., 1983).

C.1.5.2 Reliability of replacing gradient of lattice rotation by G

The aim of this section is to show that $\boldsymbol{G}$ can be expressed in terms of the gradient of lattice rotations, $\boldsymbol{U}^e$ and the gradient of $\boldsymbol{U}^e$. Let start by expressing $\boldsymbol{G}$ in terms of $\boldsymbol{F}^e$

$$G = J^e \left(F^e\right)^{-1} \operatorname{curl}\left(F^e\right)^{-1} \tag{C.36}$$

Note that $\boldsymbol{J}^e = \det \boldsymbol{F}^e$. The gradient of lattice rotation $\boldsymbol{R}^{eT}\left(\mathrm{curl}\boldsymbol{R}^{eT}\right)$ reads

$$\boldsymbol{R}^{eT}\left(\mathrm{curl}\boldsymbol{R}^{eT}\right) = \left(\boldsymbol{J}^e\right)^{-1}\left(\boldsymbol{U}^e\boldsymbol{G}\boldsymbol{U}^{eT} + \boldsymbol{U}^e\overline{\mathrm{curl}}\boldsymbol{U}^e\right) \tag{C.37}$$

curl denotes the curl operators with the derivative appearing with respect to the deformed configuration whereas $\overline{\mathrm{curl}}$ denotes the curl operators with the derivatives appearing with respect to the lattice configurations. By using polar decomposition in equation 5.24 to express $\boldsymbol{F}^e$ function of $\boldsymbol{U}^e$ and substitute the resulting equation into equation C.36 and denoting the resulting using tensor [12] notation gives

$$\begin{aligned} G_{\overline{ij}} &= J^e F^{e-1}_{ik}\left[\operatorname{curl}\left(F^{e-1}\right)\right]_{k\bar{j}} \\ &= J^e U^{e-1}_{i\bar{k}} R^{e-1}_{\bar{k}k}\varepsilon_{krs} F^{e-1}_{\bar{j}s,r} \\ &= J^e U^{e-1}_{i\bar{k}} R^{e-1}_{\bar{k}k}\varepsilon_{krs}\left[U^{e-1}_{\bar{j}\bar{l},r} R^{e-1}_{\bar{l}s} + U^{e-1}_{\bar{j}\bar{l}} R^{e-1}_{\bar{l}s,r}\right] \end{aligned} \tag{C.38}$$

The indices with over-line in the expressions above denote components corresponding to lattice configurations. Note that $U^{e-1}_{\bar{j}\bar{l},r}U^{e}_{\bar{l}\bar{t}} + U^{e-1}_{\bar{j}\bar{l}}U^{e}_{\bar{l}\bar{t},r} = 0$ because the $U^{e-1}_{\bar{j}\bar{l}}U^{e}_{\bar{l}\bar{t}} = \delta_{\bar{j}\bar{t}}$ and the gradient of $U^{e-1}_{\bar{j}\bar{l}}U^{e}_{\bar{l}\bar{t}}$ with respect to the spatial coordinate identically equals zero. Consequently,

$$U^{e-1}_{\bar{j}\bar{l},r} = -U^{e-1}_{\bar{j}\bar{p}}U^{e-1}_{\bar{t}\bar{l}}U^{L}_{\bar{p}\bar{t},r}$$

Now let express the gradient of the stretch tensor with respect to the coordinates of the lattice configuration.

$$\begin{aligned} U^{e-1}_{\bar{j}\bar{l},r} &= -U^{e-1}_{\bar{j}\bar{p}}U^{e-1}_{\bar{t}\bar{l}}U^{e}_{\bar{p}\bar{t},\bar{r}}F^{e-1}_{\bar{r},r} \\ &= -U^{e-1}_{\bar{j}\bar{p}}U^{e-1}_{\bar{t}\bar{l}}U^{e}_{\bar{p}\bar{t},\bar{r}}U^{e-1}_{\overline{rs}}R^{e-1}_{\bar{s}r} \end{aligned} \tag{C.39}$$

Now let substitute equation C.39 into equation C.38 leads to

$$G_{\overline{ij}} = J^e\left[-\varepsilon_{krs}R^{e}_{k\bar{k}}R^{e}_{r\bar{s}}R^{e}_{s\bar{l}}U^{e-1}_{\bar{i}\bar{k}}U^{e-1}_{\bar{j}\bar{p}}U^{e-1}_{\bar{t}\bar{l}}U^{e-1}_{\overline{rs}}U^{e}_{\bar{p}\bar{t},\bar{r}} + U^{e-1}_{\bar{i}\bar{k}}R^{e}_{k\bar{k}}\varepsilon_{krs}R^{e-1}_{\bar{l}s,r}U^{e-1}_{\bar{j}\bar{l}}\right]$$

By considering that $\varepsilon_{krs}R^{e}_{k\bar{k}}R^{e}_{r\bar{s}}R^{e}_{s\bar{l}} = \varepsilon_{\bar{k}\bar{s}\bar{l}}(\det R^e)$ and substituting in the equation

---

[12] An example of tensor notation: $[u \wedge v]_i = \varepsilon_{ijk}u_j v_k$ see more details on `https://www.continuummechanics.org/tensornotationbasic.html`

above leads to

$$G_{\bar{i}\bar{j}} = -J^{e}\varepsilon_{\bar{k}\bar{s}\bar{l}}U^{e-1}_{\bar{i}\bar{k}}U^{e-1}_{\bar{r}\bar{s}}U^{e-1}_{\bar{t}\bar{l}}U^{e-1}_{\bar{j}\bar{p}}U^{e}_{\bar{p}\bar{t},\bar{r}} + J^{e}\left[U^{e-1}R^{eT}\left(\mathrm{curl}R^{eT}\right)U^{e-T}\right]_{\bar{i}\bar{j}}$$

Again, by replacing $\varepsilon_{\bar{k}\bar{s}\bar{l}}U^{e-1}_{\bar{i}\bar{k}}U^{e-1}_{\bar{r}\bar{s}}U^{e-1}_{\bar{t}\bar{l}} = \varepsilon_{\bar{i}\bar{r}\bar{t}}\left(\det U^{e-T}\right)$ in the equation above leads to

$$G_{\bar{i}\bar{j}} = -\varepsilon_{\bar{i}\bar{r}\bar{t}}U^{e}_{\bar{p}\bar{t},\bar{r}}U^{e-1}_{\bar{j}\bar{p}} + J^{e}\left[U^{e-1}R^{eT}\left(\mathrm{curl}R^{eT}\right)U^{e-T}\right]_{\bar{i}\bar{j}}$$

By considering $\left[\overline{\mathrm{curl}}U^{e}\right]_{\bar{i}\bar{p}} := \varepsilon_{\bar{i}\bar{r}\bar{t}}U^{e}_{\bar{p}\bar{t},\bar{r}}$ and substituting in the equation leads to

$$G_{\bar{i}\bar{j}} = \left[-\left(\overline{\mathrm{curl}}U^{e}\right)U^{e-T} + J^{e}F^{e-1}\left(\mathrm{curl}R^{eT}\right)U^{e-T}\right]_{\bar{i}\bar{j}}$$

If this equation is expressed in non indicial notation leads to

$$G = -\left(\overline{\mathrm{curl}}U^{e}\right)U^{e-T} + J^{e}F^{e-1}\left(\mathrm{curl}R^{eT}\right)U^{e-T} \tag{C.40}$$

If equation 5.25 is substituted into equation C.37 and rearrange the resultant equation to obtain the expression of G leads to equation C.40. Therefore $|G|$ qualifies to replace $|\nabla\theta|$ and the resulting grain boundary energy ψ_{gb} reads

$$\psi_{gb}(T,\phi,\nabla\phi,G) = \frac{\alpha^{2}}{2}|\nabla\phi|^{2} + f(\phi) + g(\phi)s|G| + \frac{\varepsilon^{2}}{2}|G|^{2} \tag{C.41}$$

Where α, s and ε are constants that depend on temperature. Figure 118 shows the c contribution of the terms in equation C.41 to the total energy. It additions it compares their contribution from elastic energy $w^{el}(\mathbb{E}^{e})$. It is evident that large contribution to the total energy of the system comes from energy due to existence of a grain boundary. Note also that ψ_{gb} depends on the misorientation.

C.1.6 Mobility function of Admal &Marian's model

The Euler-Lagrange equations resulting from taking independent variations of ψ_{gb} with respect to ϕ and G are

$$\begin{aligned} M^{\dot{\phi}}_{\phi} &= \alpha^{2}\nabla^{2}\phi - f'_{\phi}(\phi) - g'(\phi)s|G| \\ M^{\dot{G}}_{G} &= g(\phi)s + \varepsilon^{2}|G| \end{aligned} \tag{C.42}$$

Similar to KWC model, $|G|$ in the functions above is approximated by $p(|G|)$ where the function p is given in equation 5.10. $M^{\dot{\phi}}_{\phi}$ and $M^{\dot{G}}_{G}$ are inverse mobility function with respect to ϕ and G.

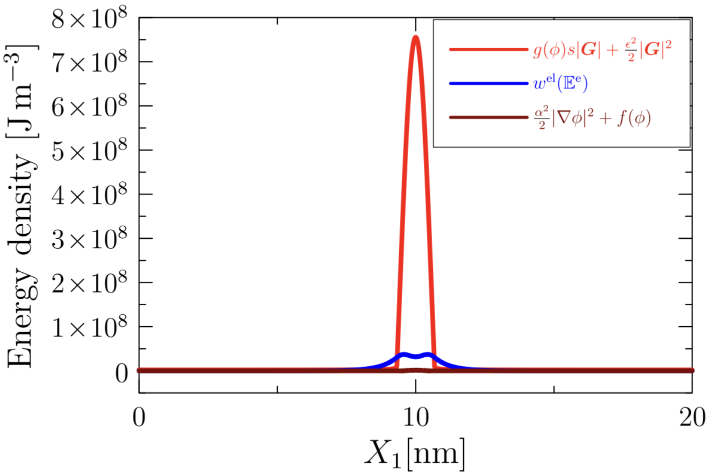

Figure 118: Comparison of energy contribution from different terms in equation C.41 which are shown in red and brown colour. The curve in blue colour shows elastic bulk energy described in section 5.3.5. They are obtained from a steady state simulation of flat symmetric tilt grain boundary of misorientation angle 30° with a misorientation axis [001] (Admal et al., 2018).

C.1.7 Algorithms to solve phase field equations

The quality of phase field simulations roots in both carefully choosing algorithm to solve partial differential equations appearing in phase field equations and on properly meshing the simulation domain. Therefore, it is important to compare available algorithms in order to make a proper choice on which one to use. This section reviews different algorithms used for discretisation and numerically solving phase field equations and related partial differential equations. Since in this project, we simulated only two dimensional phase field equations, in this section we limit ourselves to algorithms that are applicable to a two dimensional system. For that reason, this section discusses finite difference and finite element methods. In addition, it describes the implicit and explicit algorithms for time marching and compares their stability.

C.1.8 Finite difference algorithm

Finite difference algorithms provide a more direct approach for solving partial differential equations. The central idea of finite difference algorithms is to replace each derivative term by a difference quotient (Vetterling et al., 2002; Biner et al., 2017).

C.1.8.1 Spatial discretization

Let consider a continuous and smooth function $\phi(x,t)$ on a one dimensional grid such that dx is a distance between two adjacent grid points, the following algorithms are used to estimate the following terms:

1. The backward difference
$$(\nabla\phi)_i^- = \frac{\phi_i^n - \phi_{i-1}^n}{dx}$$
2. The forward difference
$$(\nabla\phi)_i^+ = \frac{\phi_{i+1}^n - \phi_i^n}{dx}$$
3. The central difference
$$(\nabla\phi)_i^\pm = \frac{\phi_{i+1}^n - \phi_{i-1}^n}{dx}$$
4. The central second difference
$$\left(\nabla^2\phi\right)_i = \frac{\phi_{i+1}^n - 2\phi_i^n + \phi_{i-1}^n}{dx^2}$$

In a two dimensional grid of grid spacing dx along x axis and dy along the y axis shown in figure 119, the Laplacian operator in the centered second difference above is approximated at each node using five points, therefore it is called a five stencil. Figure 119 shows arrangement of grid points which are used to formulate an equation C.43

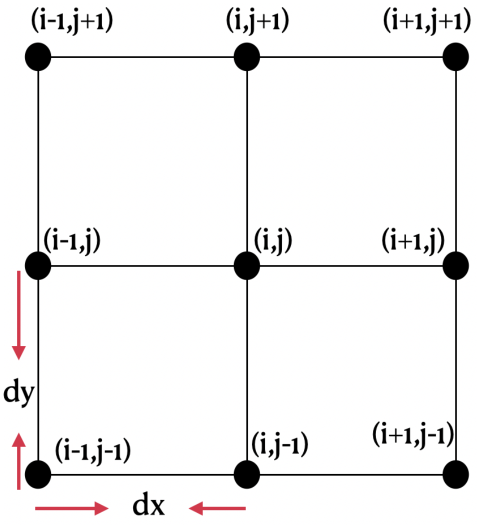

Figure 119: Schematic representation of the uniform rectangular grid showing node ordering representation for a two-dimensional grid

$$\begin{aligned}\left(\Delta^2\phi\right)_{i,j} &= \left(\nabla^2_{xx}\phi\right)^n_{i,j} + \left(\nabla^2_{yy}\phi\right)^n_{i,j} \\ &= \frac{\phi^n_{i+1,j} - 2\phi^n_{i,j} + \phi^n_{i-1,j}}{dx^2} + \frac{\phi^n_{i,j+1} - 2\phi^n_{i,j} + \phi^n_{i,j-1}}{dy^2}\end{aligned} \tag{C.43}$$

C.1.8.2 Temporal discretization

The temporal evolution of the quantity $\phi(x,t)$ on the grid shown in figure 119 is approximated using the simple forward differencing scheme as follows

$$\frac{\partial \phi}{\partial t} \approx \frac{\phi_{i,j}^{m+1} - \phi_{i,j}^{m}}{\Delta t} \tag{C.44}$$

Where $\Delta t = \left(t^{m+1} - t^{m}\right)$ is time increment between two consecutive time steps t^{m+1} and t^{m}. The value on n in equations above allows choosing the integration scheme to use whether explicit or implicit.

1. For $n = m$, we have an explicit scheme
2. For $n = m + 1$, we have an implicit scheme

The explicit scheme utilises information from the previous time (m) to propagate a field ϕ by Δt into the future $(m+1)$. However, implicit scheme uses information of ϕ from the future $(m+1)$ to propagate a field ϕ by Δt. The main advantages of the finite difference algorithms are that they easy to code, cost-effective to compute and easily adapted in a parallel computing environment. They have as well disadvantages in terms of accuracy. On the other hand, explicit scheme for time marching algorithm is conditionally stable compared from implicit scheme. For example for model type A (see section 4.3), it is only stable for

$$\Delta t < \frac{\Delta x^2}{4} \tag{C.45}$$

Whereas for model type B, explicit scheme is stable only when

$$\Delta t < \frac{\Delta x^4}{32} \tag{C.46}$$

Note the extra Δx^2 which is due to the extra Laplacian in the conservation law of model type B.

C.1.9 Finite element analysis

Finite element analysis FEA also called finite element method was first deployed in the simulation in 1960s (Biner et al., 2017). As of today, it is a very mature technique widely used in computational engineering and sciences to solve partial differential equations whose initial and boundary conditions are known. Similar to finite difference technique, finite element analysis is also local in nature. Contrary to finite difference method, finite element method has superior and unique characteristics because it has capability of describing complex geometries.

This section discusses fundamental aspect of finite element analysis. It starts by discussing the representation of the domain and then, it discusses strong and weak forms of finite element method formulation. Note that, Weak formulation serves for turning differential equation (strong form) into an integral equation (weak form) in order to lessen the burden on the numerical algorithm in evaluating derivatives.

C.1.9.1 Isoparametric representation of the domain

Isoparametric formulation consists of describing a simulation domain in terms of nodal coordinates and shape functions. Shape functions are very important because they are used to interpolate unknowns such as temperature, displacement etc... on a node within element of a mesh. On the other hand, shape functions are customary expressed in terms of a dimensionless localised coordinate system (ζ,η) and they are allowed to vary only from -1 to 1 over an element. Note that, the adaptation of this new local coordinate system is important for numerical integration required for forming a system of equations in the finite element analysis.

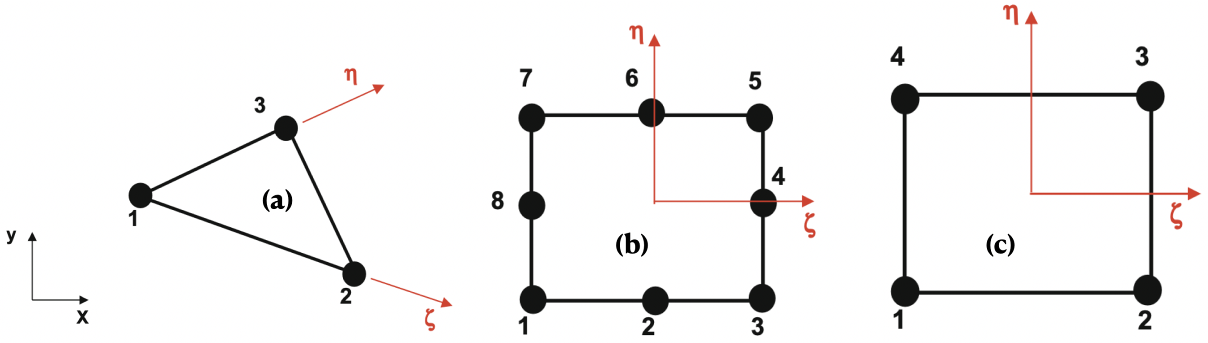

Figure 120: Examples of isoparametric elements shaped differently with their nodes numbered. The red coordinate system defines an element in a local coordinate system whereas the back coordinated system describes an element in a global coordinate system (Biner et al., 2017).

Figure 120 shows example of isoparametric element whose nodes are numbered. Figure 121 gives an example of a mesh made of twelve square elements and each element is made of four nodes. As figures 120 and 121 show, the transfer of global coordinates to local coordinates requires a transfer function or shape function. Any point within an element with x and y cartesian coordinates in a global system is presented in a local coordinate (ζ,η) as follows:

$$\begin{cases} x\left(\zeta,\eta\right) = \sum_{j}^{n} N_j^e x_j^e \\ y\left(\zeta,\eta\right) = \sum_{j}^{n} N_i^e y_j^e \end{cases} \tag{C.47}$$

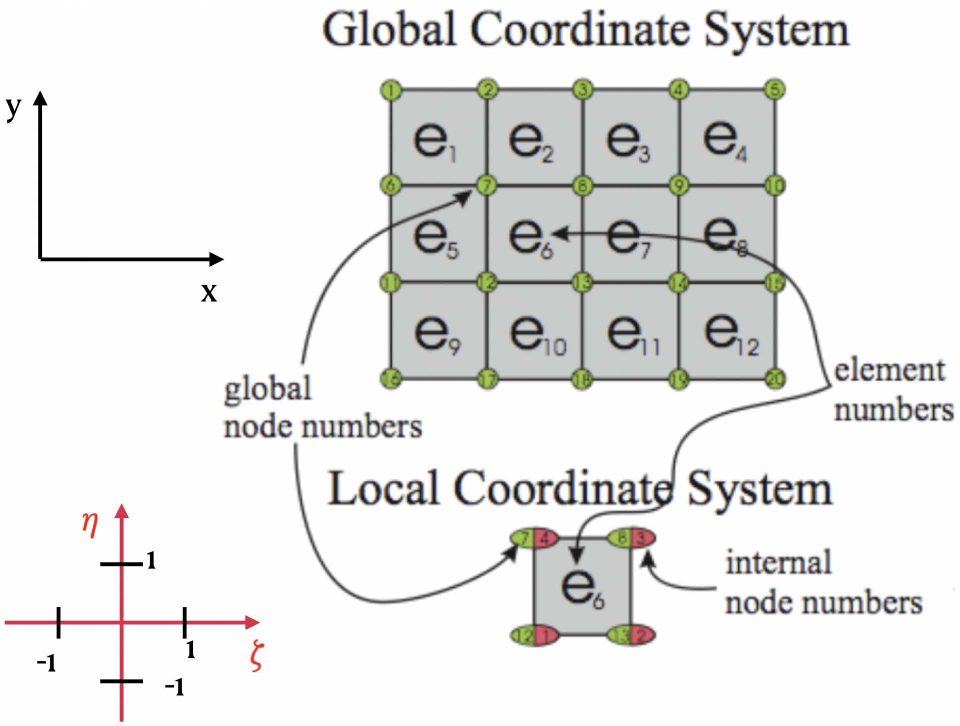

Figure 121: AN example of a mesh made of 12 squared elements and each elements is made of four nodes.

Where n denotes the number of nodes in the element (for example four nodes in figure 121), N_j^e denotes nodal values of shape functions, x_j^e and y_j^e are the nodal coordinate values in a Cartesian coordinate system. An element of four nodes as in figure 121 requires four shape functions. For example let consider element 6 (e_6) and use linear Lagrange interpolation to obtain the shape functions. There are two 1-dimensional linear interpolation function $\Upsilon_j(\zeta)$ along ζ which are

$$\begin{cases} \Upsilon_1^{e_6}(\zeta) = 1/2(1-\zeta) \\ \Upsilon_2^{e_6}(\zeta) = 1/2(1+\zeta) \end{cases} \tag{C.48}$$

and two linear $\Upsilon_j(\eta)$ along η axis which are

$$\begin{cases} \Upsilon_1^{e_6}(\eta) = 1/2(1-\eta) \\ \Upsilon_2^{e_6}(\eta) = 1/2(1+\eta) \end{cases} \tag{C.49}$$

If we take the product of these four functions (equation C.48 and C.49) to find the two dimensional shape functions for each nodes results in

$$\begin{cases} N_1^{e_6}(\zeta,\eta) = \dfrac{1}{4}(1-\zeta)(1-\eta) \\ N_2^{e_6}(\zeta,\eta) = \dfrac{1}{4}(1+\zeta)(1-\eta) \\ N_3^{e_6}(\zeta,\eta) = \dfrac{1}{4}(1+\zeta)(1+\eta) \\ N_4^{e_6}(\zeta,\eta) = \dfrac{1}{4}(1-\zeta)(1+\eta) \end{cases}$$

In isoparametric formulation, the transformation from local to global coordinate system for e_6 leads to a trial function $U(x,y)$

$$U(x,y) = \begin{cases} x = N_1^{e_6}(\zeta,\eta)x_1^{e_6} + N_2^{e_6}(\zeta,\eta)x_2^{e_6} + N_3^{e_6}(\zeta,\eta)x_3^{e_6} + N_4^{e_6}(\zeta,\eta)x_4^{e_6} \\ y = N_1^{e_6}(\zeta,\eta)y_1^{e_6} + N_2^{e_6}(\zeta,\eta)y_2^{e_6} + N_3^{e_6}(\zeta,\eta)y_3^{e_6} + N_4^{e_6}(\zeta,\eta)y_4^{e_6} \end{cases}$$

Where $x_j^{e_6}$ and $y_j^{e_6}$ (for $j = [1,2,3,4]$) are coordinates of four nodes of element e_6. The Finite element method is not limited to linear polynomial approximations, it is extensible to higher-degree polynomials. For instance, the quadratic Lagrange polynomial (Burden, 1993) in which an extra nodes are added at the mid points of each element. For example, our element e_6 of four nodes results in element of nine nodes as figure 122 shows. The three one dimensional interpolation functions $\Upsilon_j(\zeta)$ along the ζ axis are

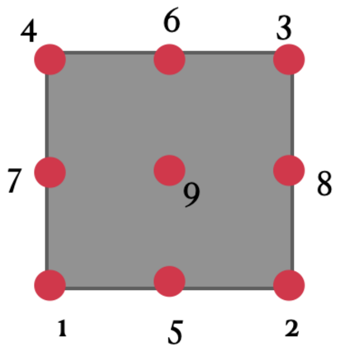

Figure 122: The quadratic Lagrange interpolation introduces extra nodes in element.

$$\begin{cases} \Upsilon_1^{e_6}(\zeta) = \zeta(\zeta-1)/2 \\ \Upsilon_2^{e_6}(\zeta) = 1-\zeta^2 \\ \Upsilon_3^{e_6}(\zeta) = \zeta(1+\zeta)/2 \end{cases} \tag{C.50}$$

The three one dimensional interpolation functions $\Upsilon_j(\zeta)$ along the η axis are

$$\begin{cases} \Upsilon_1^{e_6}(\eta) = \eta(\eta-1)/2 \\ \Upsilon_2^{e_6}(\eta) = 1-\eta^2 \\ \Upsilon_3^{e_6}(\eta) = \eta(1+\eta)/2 \end{cases} \tag{C.51}$$

In addition, shape function must satisfy continuity between adjacent elements over any elementary boundary that includes node i. Any function $f(x,y)$ defined in a global coordinate system is transformed into local coordinate system as follows. First a Jacobian matrix J_m is defined by following formulations above.

$$J_m = \begin{bmatrix} \frac{\partial x}{\partial \zeta} & \frac{\partial y}{\partial \zeta} \\ \\ \frac{\partial x}{\partial \eta} & \frac{\partial y}{\partial \eta} \end{bmatrix} = \begin{bmatrix} \sum_i^n \frac{\partial N_i^e}{\partial \zeta}.x_i^e & \sum_i^n \frac{\partial N_i^e}{\partial \zeta}.y_i^e \\ \\ \sum_i^n \frac{\partial N_i^e}{\partial \eta}.x_i^e & \sum_i^n \frac{\partial N_i^e}{\partial \eta}.y_i^e \end{bmatrix}$$

Second, a function $f(x,y)$ is transferred to local coordinate system as

$$\begin{aligned} \int_{\Omega^e}\int f(x,y)dxdy &= \int_{-1}^{+1} f(\zeta,\eta)\det J_m d\zeta d\eta \\ &= \int_{-1}^{+1}\int_{-1}^{+1} g(\zeta,\eta)d\zeta d\eta \end{aligned} \tag{C.52}$$

where Ω^e denotes the domain in this case element e. Note that $dxdy = \det J_m d\zeta d\eta$ is the area of the element. By using Gauss-Legendre rule [13] for a four node isoparametric element with n-integration, this integration is expressed as

$$\int_{-1}^{1}\int_{-1}^{1} g(\zeta,\eta)d\zeta d\eta = \sum_{i=1}^{n}\sum_{j}^{n} W_i W_j g(\overline{\zeta}_i,\overline{\eta}_i) \tag{C.54}$$

Where W_i and W_j are the weight coefficients and $g(\overline{\zeta}_i,\overline{\eta}_i)$ is the value evaluated at the sampling points.

C.1.9.2 Strong and Weak Forms of FEM Formulation

In general, phase field models contain high order derivative terms (often second order derivative). For example, the mobility function of ϕ in Admal and Marian phase field

---

[13] Gauss Legendre rule is used to approximate definite integrals. For example, the integral of a polynomial function $f(x)$is approximated as :

$$\int_{-1}^{1} f(x) \approx \sum_{i=1}^{n} w_i f(x_i) \tag{C.53}$$

where x_i is coordinate of the node i and W_i is weight function for $i = 1, ..., n$.

model described in section 5.3 contains the second derivative of ϕ.

$$\begin{aligned} \tau_\phi \frac{\partial \phi}{\partial t} &= \alpha^2 \mathrm{div} q - f_\phi^{'}(\phi) - g_\phi^{'}(\phi) s|G| \\ q &= \mathrm{grad}\phi \end{aligned} \tag{C.55}$$

The second derivative terms cause numerical issues in practical situations where the differentiability of the ϕ profile may be limited especially at domain's boundary. The first derivative of ϕ can be evaluated but the second derivative can not be evaluated numerically. The central idea of the weak formulation is to turn the differential equation into an integral equation. This permits to lessen the burden on numerical algorithms in evaluating higher order derivatives. The weak form of phase field equations to be solved with finite element method are obtain in following four main steps.

1. Multiplying the phase field equation with a test function η to reduce the equation to a scalar.
2. Integrating the resulting equation over the domain of consideration Ω.
3. Integrating by parts using Green's theorem in order to reduce the order of derivatives
4. The last step is to supplement the resulting equation with boundary conditions.

Let use equation C.55 for demonstration. Let start by multiplying C.55 by test function η

$$\eta \tau_\phi \frac{\partial \phi}{\partial t} - \eta \alpha^2 \mathrm{div} q + \eta f_\phi^{'}(\phi) + \eta g_\phi^{'}(\phi) s|G| = 0 \tag{C.56}$$

Let integrate this equation over the domain Ω

$$\int_\Omega \eta \tau_\phi \frac{\partial \phi}{\partial t} d\Omega - \int_\Omega \eta \alpha^2 \mathrm{div} q d\Omega + \int_\Omega \eta f_\phi^{'}(\phi) d\Omega + \int_\Omega \eta g_\phi^{'}(\phi) s|G| d\Omega = 0 \tag{C.57}$$

Now let integrate the term involving high order derivative using Green's theorem[14]

$$\int_\Omega \alpha^2 \eta \mathrm{div} q d\Omega = \alpha^2 \left[\int_A (\eta . q) . n dA - \int_\Omega (\mathrm{grad}\eta)\, q d\Omega \right] \tag{C.59}$$

To recall that $q(\pm L) = 0$ then the term $\int_A (\eta . q) . n dA = 0$. By substituting equation C.59 into C.57 leads

$$\int_\Omega \eta \tau_\phi \frac{\partial \phi}{\partial t} d\Omega + \int_\Omega \alpha^2 \nabla \eta \nabla \phi d\Omega + \int_\Omega \eta f_\phi^{'}(\phi) d\Omega + \int_\Omega \eta g_\phi^{'}(\phi) s|G| d\Omega = 0 \tag{C.60}$$

---

[14] Green's formula:

$$\int_\Omega u.v_{,i} d\Omega = \int_A (u.v).n_i dA - \int_\Omega u_{,i}.v d\Omega \tag{C.58}$$

Where A is surface around the domain Ω and n_i is the component of the outward vector normal to A.

Since solving equation C.60 requires only first order derivatives in comparison to equation C.55. Equation C.60 is a weak form.

C.1.9.3 Discretization of Weak Form

Now casting equation C.60 into FEM solution is achieved by using the isoparametric representation presented above. In order words, the test function η is replaced by the shape functions. But before going any further, note that integrals appearing in equation C.60 are at an element level and the cartesian derivative of function f is defined over an element by using shape functions as follows:

$$f(\zeta,\eta) = \sum_{i}^{n} N_i^e f_i^e \tag{C.61}$$

where f_i^e is the value of the function at the element nodal positions. By using the chain rule of differentiation, independent variation of f are :

$$\begin{cases} \dfrac{\partial f}{\partial x} = \dfrac{\partial f}{\partial \zeta}.\dfrac{\partial \zeta}{\partial x} + \dfrac{\partial f}{\partial \eta}.\dfrac{\partial \eta}{\partial x} \\ \dfrac{\partial f}{\partial y} = \dfrac{\partial f}{\partial \zeta}.\dfrac{\partial \zeta}{\partial y} + \dfrac{\partial f}{\partial \eta}.\dfrac{\partial \eta}{\partial y} \end{cases} \tag{C.62}$$

With

$$\begin{cases} \dfrac{\partial f}{\partial \zeta} = \displaystyle\sum_{i}^{n} \dfrac{\partial N_i^e}{\partial \zeta}.f_i^e \\ \dfrac{\partial f}{\partial \eta} = \displaystyle\sum_{i}^{n} \dfrac{\partial N_i^e}{\partial \eta}.f_i^e \end{cases} \tag{C.63}$$

Thus, in the similar way as in equation C.61, the function ϕ in equation C.60 is expressed as

$$\phi(\zeta,\eta) = \sum_{i}^{n} N_i^e \phi_i^e \tag{C.64}$$

and the gradient terms appearing in Equation C.60 can be expressed with shape functions as follows

$$\nabla\phi = \begin{bmatrix} \dfrac{\partial N_1^e}{\partial x} & \dfrac{\partial N_2^e}{\partial x} \cdots\cdots & \dfrac{\partial N_n^e}{\partial x} \\ & & \\ \dfrac{\partial N_1^e}{\partial y} & \dfrac{\partial N_2^e}{\partial y} \cdots\cdots & \dfrac{\partial N_n^e}{\partial y} \end{bmatrix} \phi_i^e = B^e \phi_1^e \tag{C.65}$$

It is evident that the components of B matrix are easily evaluated by forming the Jacobian matrix and taking advantage of the chain rule of differentiation as described above. Utilising equations C.47, C.61 and C.65, equation C.60 is expressed as

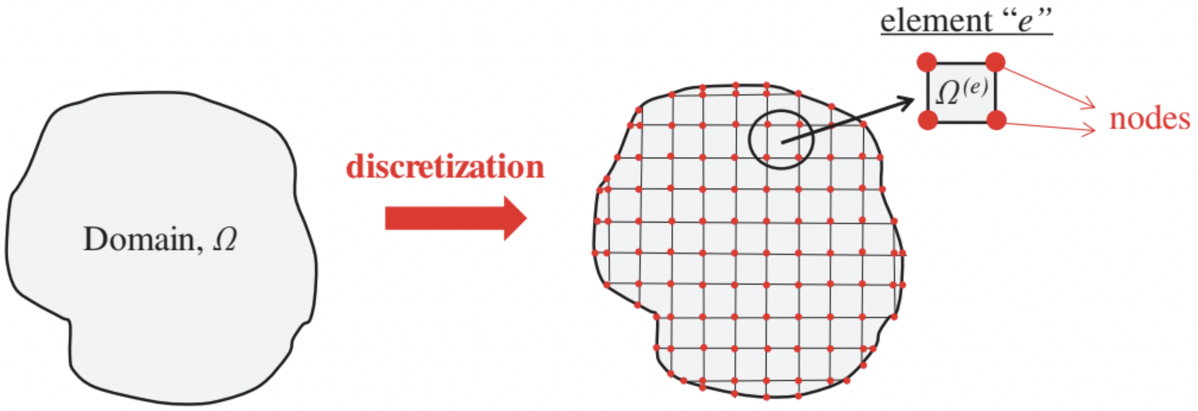

Figure 123: Spatial discretisation of a domain Ω into square noded elements.

$$\int_{\Omega} \underbrace{N \tau_{\phi} N}_{A} \frac{\partial \phi^e}{\partial t} d\Omega + \int_{\Omega} \underbrace{\alpha^2 [B.B]}_{M} \phi^e d\Omega + \int_{\Omega} \underbrace{2eN.N}_{F_1} (\phi^e - 1) d\Omega + \int_{\Omega} \underbrace{2sN.N|G|}_{F_2} \phi^e d\Omega$$

for $f_{\phi}^{'}(\phi) = 2e(\phi - 1)$ and $g_{\phi}^{'}(\phi) = 2\phi$ from equation 5.7. Our equation becomes

$$A \frac{\partial \phi^e}{\partial t} + M\phi^e + F_1\phi^e + F_2\phi^e = F_1 \tag{C.66}$$

Where A, M, F_1 and F_2 are matrices. Figure 123 gives an example of a discretisation in space of the domain.

C.1.9.4 Discretization in time

The discretization of equation C.66 follows the trapezoid method described in this textbook (Hughes, 2012) in which stability and accuracy of discretization algorithms are fully discussed. By following procedure described in (Hughes, 2012), the final equation reads

$$\left[\frac{A}{\Delta t} + \mathscr{J} \left(M + F_1 + F_2 \right) \right] (\phi^e)^{m+1} = \left[\frac{A}{\Delta t} - \left(1 - \mathscr{J} \right) \left(M + F_1 + F_2 \right) \right] (\phi^e)^m + F_1 \tag{C.67}$$

Where $\Delta t = \left(t^{m+1} - t^m \right)$ is time increment between two consecutive time steps t^{m+1} and t^m. The constant $\mathscr{J}$ controls the discretization method to use:

1. If $\mathscr{J}$=0 leads to forward Euler method (explicit method).
2. If $\mathscr{J}$=0.5 leads to Crank–Nicholson method.
3. $\mathscr{J}$=1 leads to backward Euler method ((implicit method).

Explicit scheme utilises information from the previous time (m) to propagate a field ϕ one time step into the future $(m + 1)$. However, Explicit scheme has also main advantage of requiring minimal overhead in terms of memory allocation. In addition, they are easy to program on a computer. However, the forward Euler method has limitations. The main disadvantage is that explicit scheme has a conditional stability. It is limited to small time step Δt. For larger time step Δt, numerical integration becomes highly inaccurate and ultimately fails to converge. Contrary to forward Euler method, both Crank–Nicholson and backward Euler methods are unconditionally stable. Comparatively, backward Euler method is usually preferred over Crank–Nicholson method. Even if the Crank–Nicholson method is second-order accurate, the solutions obtained with this method contains undesirable oscillations.

C.1.10 Boundary conditions

In numerical simulations, one intends to simulate a large system in order to statistically collect thermodynamic quantities over a large sample. It is therefore very important to properly define boundary conditions that allow to extend the simulation domain. One usually use **Periodic Boundary Conditions**, discussed in section 2.2.3, to achieve an infinite simulation domain. However, other boundary conditions can be imposed to reflect different flow conditions. They can be classified into two types. The first type contains boundary conditions that indicate the value of the solution on the boundary of the domain Ω.

Dirichlet boundary conditions

The Dirichlet boundary conditions state the value that the solution function $f(x, y)$ to the phase field equation must have in the boundary of the domain Ω (Dirichlet, 1852). For a two dimensional domain Ω that is described by x and y and it has a boundary $\partial\Omega$, its typical Dirichlet boundary condition would be

$$f(x, y) = g(x, y) \text{ for } (x, y) \in \partial\Omega$$

Where the function $g(x, y)$ may not only depend on x and y but also on other additional independent variable for instance time. In addition, $g(x, y)$ can also be a constant.

Neumann boundary conditions

The second type of boundary conditions state that the derivative of the solution function $f(x, y)$ to the phase field equation must have a given value on the boundary $\partial\Omega$ of the domain Ω. These boundary conditions are known as Neumann boundary conditions (Neumann, 1865). A typical Neumann boundary condition would be

$$\frac{\partial f(x,y}{\partial x} = g(x,y) \text{ for } (x,y) \in \partial\Omega$$

or

$$\frac{\partial f(x,y}{\partial y} = g(x,y) \text{ for } (x,y) \in \partial\Omega$$

Where the function $g(x,y)$ may not only depend on x and y, but also on other additional variables such as time. Recall that in section 2.2.3, we have stated that the top surface of a domain must have a shear stress equals zero and this boundary conditions was denoted Free surface. Free surface boundary conditions are regarded as the Neumann boundary condition since shear stress is calculated from the first derivative of velocity.

Appendix D

D.1 Analytical solution of Admal & Marian's phase field model

A one dimension bi-crystalline system

In this sections we give a solution of a one dimension Admal and Marian's boundary value problems by following the procedure devised by Lobkovsky et al.(Lobkovsky and Warren, 2001). We consider a domain $\Omega_0 = [-L, L]$ with boundary conditions $\phi(\pm L) = 1$ and $|G|(\pm L) = 0$.

Here, we have assumed that $\exists\ \Omega_0^{GB} \subset \Omega_0$ and $\Omega_0^{GB} = [-l, l]$ (in order words a grain boundary extends from $-l$ to l). It is important to note that in Ω_0^{GB} $\nabla\phi \not\equiv 0$ and $|G| \neq 0$. On contrary, in the region $\Omega_0^{p} = \Omega_0 \backslash \Omega_0^{GB}$, $\nabla\phi \equiv 0$ and $|G| = 0$.

Therefore in the region Ω_0^{p}, ϕ satisfies the equation

$$\alpha^2 \frac{\partial^2\phi}{\partial x^2} - \frac{\partial f(\phi)}{\partial\phi} = 0 \tag{D.1}$$

If we multiply D.1 with $\frac{\partial\phi}{\partial x}$ leads

$$\alpha^2 \frac{\partial^2\phi}{\partial x^2}\frac{\partial\phi}{\partial x} - \frac{\partial f(\phi)}{\partial\phi}\frac{\partial\phi}{\partial x} = 0$$

(D.2)

If $\frac{\partial^2\phi}{\partial x^2}\frac{\partial\phi}{\partial x} = \frac{1}{2}\frac{\partial}{\partial x}\left(\frac{\partial\phi}{\partial x}\right)^2$ is replaced in the equation above, it will lead

$$\frac{\alpha^2}{2}\frac{\partial}{\partial x}\left(\frac{\partial\phi}{\partial x}\right)^2 - \frac{\partial f(\phi)}{\partial x} = 0 \tag{D.3}$$

By integrating equation D.3 leads

$$\frac{\alpha^2}{2}\left(\frac{\partial\phi}{\partial x}\right)^2 - f(\phi) = c \tag{D.4}$$

Now the solution for ϕ in the region Ω_0^p in the inverted form reads

$$L - x = \int_\phi^1 \frac{\alpha}{\sqrt{2\Big(c + f(\phi)\Big)}} d\phi, \text{ for } x \in \Omega^p \text{ and } \phi < 1 \tag{D.5}$$

Where c is an integration constants.
At grain boundary (in the region Ω_0^{GB}), $|G| \neq 0$ and $\nabla\phi \not\equiv 0$, therefore ϕ and $|G|$ satisfy both conditions

$$\alpha^2 \frac{\partial^2 \phi}{\partial x^2} - \frac{\partial f(\phi)}{\partial \phi} - s\frac{\partial g(\phi)}{\partial \phi}|G| = 0 \tag{D.6}$$

and

$$\frac{\partial}{\partial x}\Big(\varepsilon^2 |G| + s g(\phi)\Big) = 0 \tag{D.7}$$

Integrating equation D.7 leads to

$$\varepsilon^2 |G| + s g(\phi) = d \tag{D.8}$$

For

$$\lim_{x\to\infty} \phi \simeq \phi_2$$
$$\lim_{x\to\infty} |G| \simeq 0$$

Then $d = sg(\phi_2)$. Equation D.8 becomes

$$|G| = \frac{s}{\varepsilon^2}\Big(g(\phi_2) - g(\phi)\Big) \text{ for } \phi \ll \phi_2 \tag{D.9}$$

Now let multiply equation D.6 by $\frac{\partial \phi}{\partial x}$

$$\alpha^2 \frac{\partial^2 \phi}{\partial x^2}\frac{\partial \phi}{\partial x} - \frac{\partial f(\phi)}{\partial \phi}\frac{\partial \phi}{\partial x} - s\frac{\partial \phi}{\partial x}\frac{\partial g(\phi)}{\partial \phi}|G| = 0 \tag{D.10}$$

By rearranging this equation and knowing that $\frac{\partial \phi}{\partial x}\frac{\partial g(\phi)}{\partial \phi}|G| = -\frac{s^2}{2\varepsilon^2}\frac{\partial}{\partial x}\Big(g(\phi_2) - g(\phi)\Big)^2$, it leads to

$$\alpha^2 \frac{\partial}{\partial x}\left(\frac{1}{2}\left[\frac{\partial \phi}{\partial x}\right]^2\right) - \frac{\partial f(\phi)}{\partial x} + \frac{s^2}{2\varepsilon^2}\frac{\partial}{\partial x}\Big(g(\phi_2) - g(\phi)\Big)^2 = 0 \tag{D.11}$$

Integrating this equation and integrate it lead to

$$\frac{\alpha^2}{2}\left(\frac{\partial \phi}{\partial x}\right)^2 - f(\phi) + \frac{s^2}{2\varepsilon^2}\Big(g(\phi_2) - g(\phi)\Big)^2 = c \tag{D.12}$$

Rearranging this equations leads to

$$x(\phi) = \int_{\phi_1}^{\phi} \frac{\alpha d\phi}{\sqrt{2\left\{f(\phi) + c - \frac{s^2}{\varepsilon^2}\left(g(\phi_2) - g(\phi)\right)^2\right\}}}, \text{ for } \phi < \phi_2,\ \phi_1 = \phi(0) \text{ and } x \in \Omega_0^{GB} \tag{D.13}$$

Then in the region Ω_0, the solution of ϕ in the inverted form reads

$$[-L, L] = \int_{\phi}^{1} \frac{\alpha}{\sqrt{2\left(c + f(\phi)\right)}} d\phi + \int_{\phi_1}^{\phi} \frac{\alpha d\phi}{\sqrt{2\left\{f(\phi) + c - \frac{s^2}{\varepsilon^2}\left(g(\phi_2) - g(\phi)\right)^2\right\}}} \tag{D.14}$$

The value of the integration constant c, ϕ_1 and ϕ_2 are obtained implicitly from equations D.4 and D.14.

D.2 Effect of slip systems on migration mechanism of a grain boundary

To investigate the influence of each slip system on migration mechanism of grain boundary, a shear rate of $\dot{\gamma} = 1.5 \times 10^{-4} m.s^{-1}$ was applied to the system at 100K and the system was allowed to evolve for $9 \times 10^5 s$. To investigate the influence of a given slip system, the others were kept inactive. Figures and 124 shows the evolution of normalised density of geometrically necessary dislocation of $\Sigma 25(7\bar{1}0)$ symmetric tilt grain boundary as a representative of other investigated grain boundaries.

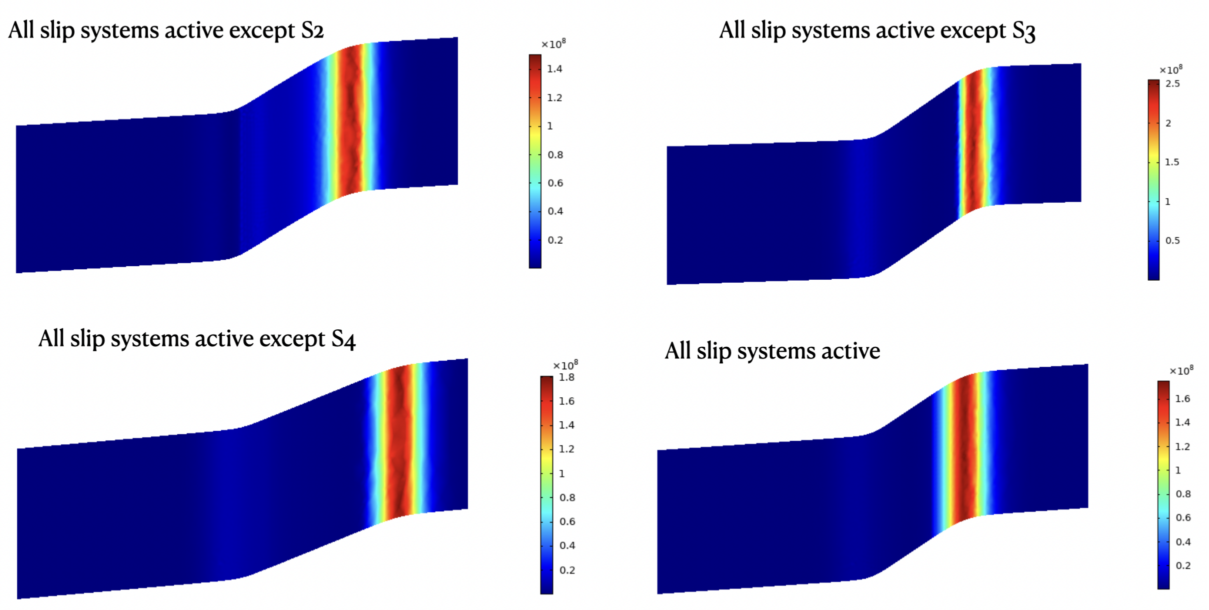

Figure 124: Effect of slip systems on migration mechanism of $\Sigma 25(7\bar{1}0)$ symmetric tilt grain boundary.

D.3 Sensitivity test

To investigate the role of different parameters in Phase Field equation on mobility of grain boundary, we have carried out several tests at each time varying the value of the parameter of interest for other parameters remaining fixed with the values reported in table 6.2. The system was allowed to evolve for $9 \times 10^5 s$ at 100K with a shear rate $\dot{\gamma} = 1.5 \times 10^{-4} m.s^{-1}$.

D.3.1 Dependence of grain boundary evolution on ε

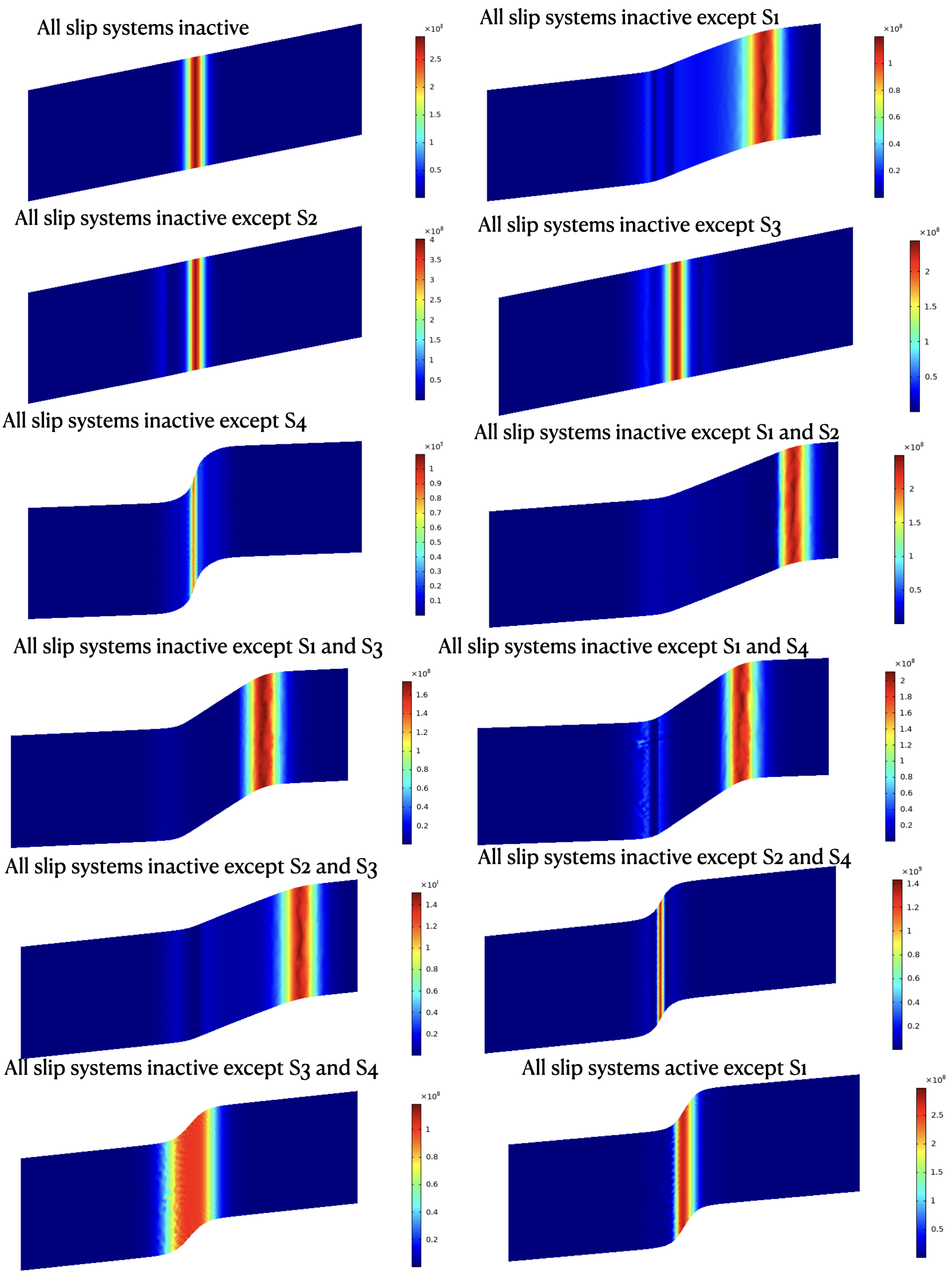

All slip systems inactive

All slip systems inactive except S1

All slip systems inactive except S2

All slip systems inactive except S3

All slip systems inactive except S4

All slip systems inactive except S1 and S2

All slip systems inactive except S1 and S3

All slip systems inactive except S1 and S4

All slip systems inactive except S2 and S3

All slip systems inactive except S2 and S4

All slip systems inactive except S3 and S4

All slip systems active except S1

Figure 125: Effect of slip system on migration mechanism of $\Sigma 25(7\bar{1}0)$ symmetric tilt grain boundary.

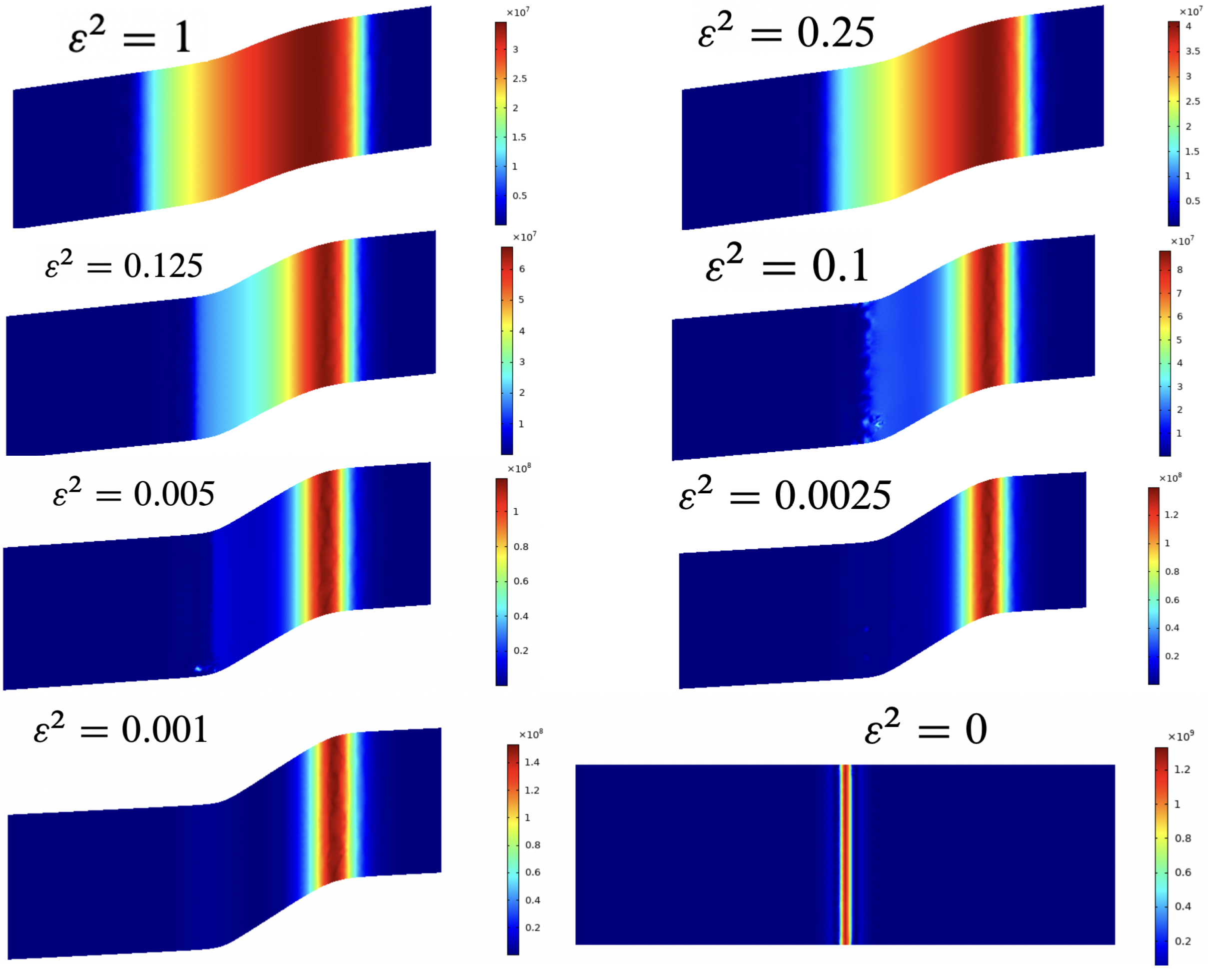

Figure 126: Effect of ε on the evolution of the norm of density of geometrically necessary dislocations in $\Sigma 25(7\bar{1}0)$ symmetric tilt grain boundary at 100K with a shear rate $\dot{\gamma} = 1.5 \times 10^{-4} m.s^{-1}$.

D.3.2 Dependence of grain boundary evolution on e

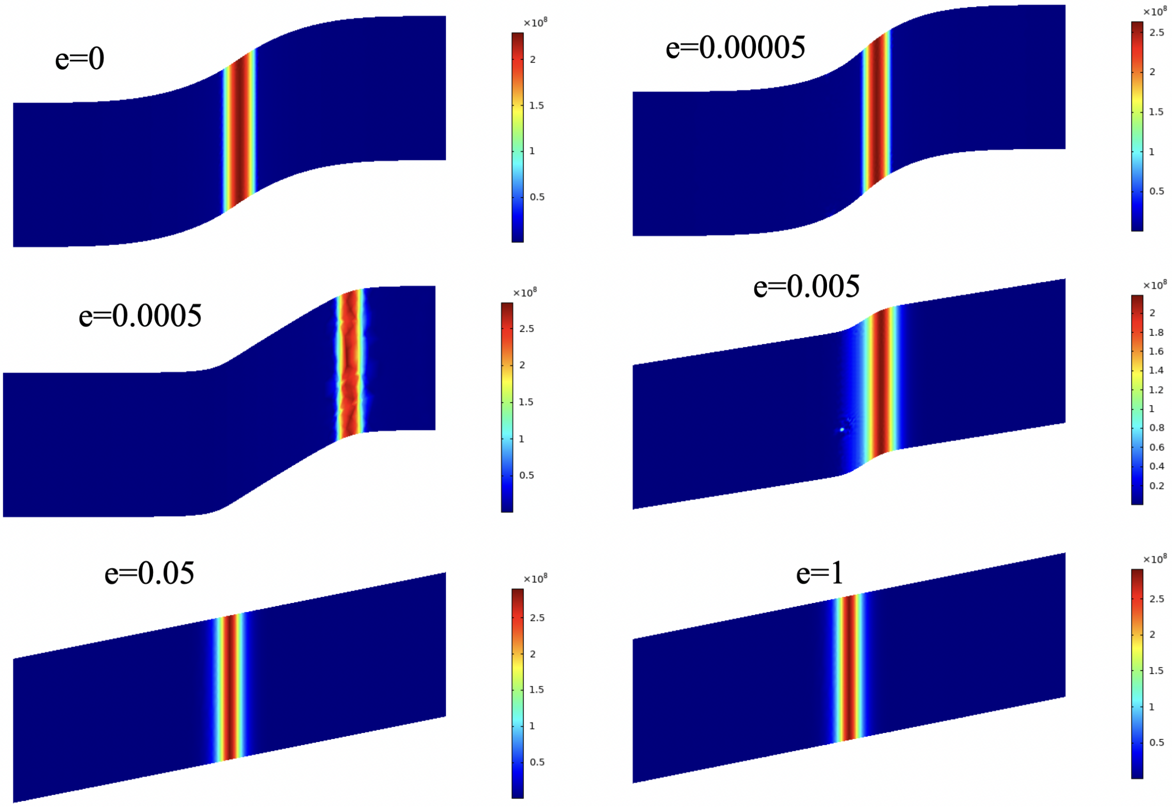

Figure 127: The effect of e on the evolution of the norm of density of geometrically necessary dislocation in $\Sigma 25(7\bar{1}0)$ symmetric tilt grain boundary at $100K$ with a shear rate of $\dot{\gamma} = 1.5 \times 10^{-4} m.s^{-1}$

D.4 Evolution of both elastic and plastic deformation gradient

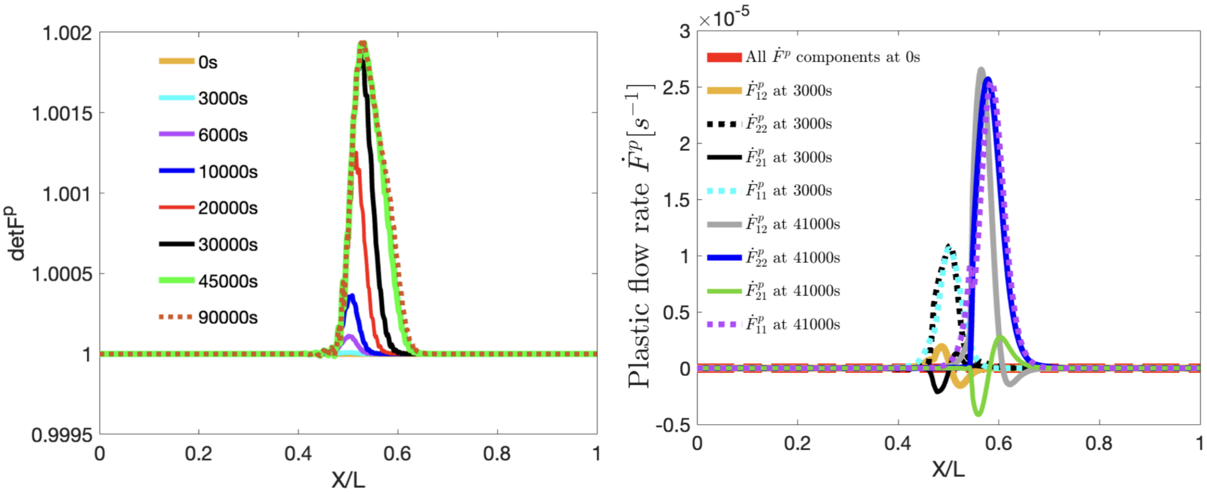

a) b)

Figure 128: a) Determinant of plastic deformation gradient $\boldsymbol{F}^p$ b) the evolution of plastic flow rate $\dot{\boldsymbol{F}}^p$ in $\Sigma 5(3\bar{1}0)$ symmetric tilt grain boundary at different time step and a shear rate $\dot{\gamma} = 2 \times 10^{-4} ms^{-1}$.

D.5 Evolution of plastic stretch tensor

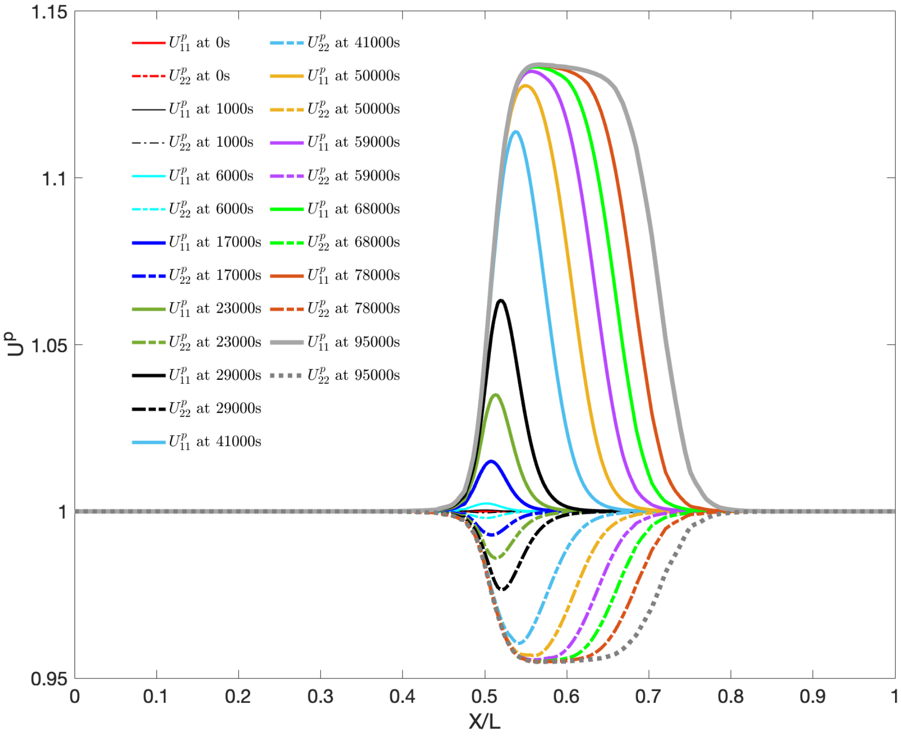

Figure 129: Evolution of components U^p_{11} and U^p_{22} of plastic stretch tensor in $\Sigma 25(7\bar{1}0)$ at 100K with a shear rate $\dot{\gamma} = 2 \times 10^{-4} m s^{-1}$.

D.6 Evolution of slip mobility

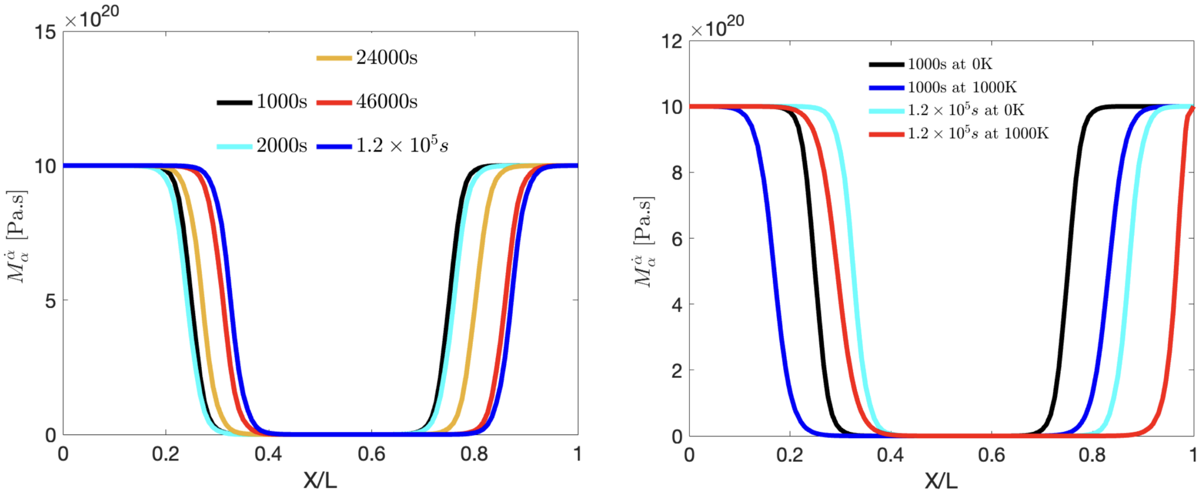

a) b)

Figure 130: Evolution of the inverse mobility $M^{\dot{\alpha}}_{\alpha}$ in $\Sigma 5(3\bar{1}0)$ grain boundary at a) 100K and b) comparison of evolution at 0K and 1000K with a shear rate $\dot{\gamma} = 2 \times 10^{-4} m s^{-1}$.

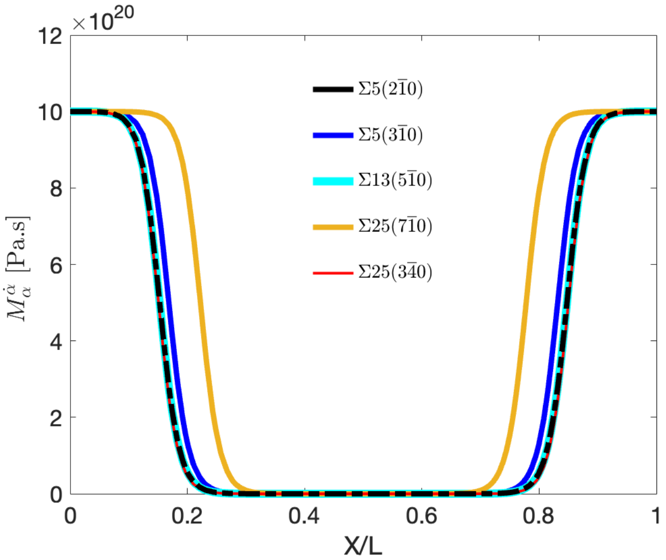

Figure 131: Comparison of inverse slip mobility of different grain boundaries from a list of investigated grain boundaries at 100K after 1000s with a shear rate $\dot{\gamma} = 2 \times 10^{-4} ms^{-1}$.

Bibliography

G. Abrivard, E. P. Busso, S. Forest, and B. Appolaire. Phase field modelling of grain boundary motion driven by curvature and stored energy gradients. part ii: application to recrystallisation. *Philosophical magazine*, 92(28-30):3643–3664, 2012a.

G. Abrivard, E. P. Busso, S. Forest, and B. Appolaire. Phase field modelling of grain boundary motion driven by curvature and stored energy gradients. part i: theory and numerical implementation. *Philosophical magazine*, 92(28-30):3618–3642, 2012b.

A. Acharya. A counterpoint to cermelli and gurtin's criteria for choosing the 'correct'geometric dislocation tensor in finite plasticity. In *IUTAM Symposium on theoretical, computational and modelling aspects of inelastic media*, pages 99–105. Springer, 2008.

T. Ackermann, C. Brooks III, M. Karplus, and B. Pettitt. Proteins: a theoretical perspective of dynamics, structure and thermodynamics, volume lxxi. *advances in chemical physics, John Wiley & Sons, New York*, pages 96–96, 1988.

N. C. Admal, G. Po, and J. Marian. Diffuse-interface polycrystal plasticity: expressing grain boundaries as geometrically necessary dislocations. *Materials Theory*, 1(1):1–16, 2017.

N. C. Admal, G. Po, and J. Marian. A unified framework for polycrystal plasticity with grain boundary evolution. *International Journal of Plasticity*, 106:1–30, 2018.

N. C. Admal, J. Segurado, and J. Marian. A three-dimensional misorientation axis-and inclination-dependent kobayashi–warren–carter grain boundary model. *Journal of the Mechanics and Physics of Solids*, 128:32–53, 2019.

M. Allen and D. Tildesley. Computer simulation of liquids, 1988.

M. P. Allen and D. J. Tildesley. *Computer simulation of liquids.* Oxford university press, 2017.

S. M. Allen and J. W. Cahn. A microscopic theory for antiphase boundary motion and its application to antiphase domain coarsening. *Acta metallurgica*, 27(6):1085–1095, 1979.

H. C. Andersen. Molecular dynamics simulations at constant pressure and/or temperature. *The Journal of chemical physics*, 72(4):2384–2393, 1980.

P. M. Anderson, J. P. Hirth, and J. Lothe. *Theory of dislocations*. Cambridge University Press, 2017.

A. J. Archer and M. Rauscher. Dynamical density functional theory for interacting brownian particles: stochastic or deterministic? *Journal of Physics A: Mathematical and General*, 37(40):9325, 2004.

M. Ashby, F. Spaepen, and S. Williams. The structure of grain boundaries described as a packing of polyhedra. *Acta Metallurgica*, 26(11):1647 – 1663, 1978. ISSN 0001-6160. doi: https://doi.org/10.1016/0001-6160(78)90075-5. URL `http://www.sciencedirect.com/science/article/pii/0001616078900755`.

A. Ask, S. Forest, B. Appolaire, K. Ammar, and O. U. Salman. A cosserat crystal plasticity and phase field theory for grain boundary migration. *Journal of the Mechanics and Physics of Solids*, 115:167–194, 2018.

K. T. Aust, U. Erb, and G. Palumbo. *Interfacial Structures and Properties*, pages 107–128. Springer Netherlands, Dordrecht, 1993. ISBN 978-94-011-1765-4. doi: 10.1007/978-94-011-1765-4_5. URL `https://doi.org/10.1007/978-94-011-1765-4_5`.

S. Babcock and R. Balluffi. Grain boundary kinetics—i. in situ observations of coupled grain boundary dislocation motion, crystal translation and boundary displacement. *Acta Metallurgica*, 37(9):2357–2365, 1989.

X.-M. Bai, Y. Zhang, and M. R. Tonks. Testing thermal gradient driving force for grain boundary migration using molecular dynamics simulations. *Acta Materialia*, 85:95–106, 2015.

D. W. Bainbridge, H. L. Choh, and E. H. Edwards. Recent observations on the motion of small angle dislocation boundaries. *Acta metallurgica*, 2(2):322–333, 1954.

R. Balluffi and P. Bristowe. On the structural unit/grain boundary dislocation model for grain boundary structure. *Surface Science*, 144(1):28 – 43, 1984. ISSN 0039-6028. doi: https://doi.org/10.1016/0039-6028(84)90701-5. URL `http://www.sciencedirect.com/science/article/pii/0039602884907015`.

R. W. Balluffi and G. B. Olson. On the hierarchy of interfacial dislocation structure. *Metallurgical Transactions A*, 16:529–541, 1985. ISSN 1543-1940. doi: 10.1007/BF02814227. URL `https://doi.org/10.1007/BF02814227`.

A. D. Banadaki and S. Patala. An efficient algorithm for computing the primitive bases of a general lattice plane. *Journal of Applied Crystallography*, 48(2):585–588, 2015.

A. D. Banadaki, M. A. Tschopp, and S. Patala. An efficient monte carlo algorithm for determining the minimum energy structures of metallic grain boundaries. *Computational Materials Science*, 155:466–475, 2018.

D. Banadaki and S. Patala. A three-dimensional polyhedral unit model for grain boundary structure in fcc metals. *npj Computational Materials*, 3(13), 2017. ISSN 2057-3960. doi: 10.1038/s41524-017-0016-0. URL `https://doi.org/10.1038/s41524-017-0016-0`.

J. J. Bean and K. P. McKenna. Origin of differences in the excess volume of copper and nickel grain boundaries. *Acta Materialia*, 110:246–257, 2016.

V. L. Berdichevsky. Continuum theory of dislocations revisited. *Continuum Mechanics and Thermodynamics*, 18(3):195–222, 2006.

S. Bergmann, K. Albe, E. Flegel, D. Barragan-Yani, and B. Wagner. Anisotropic solid–liquid interface kinetics in silicon: an atomistically informed phase-field model. *Modelling and Simulation in Materials Science and Engineering*, 25(6):065015, 2017.

M. Bernacki, R. E. Logé, and T. Coupez. Level set framework for the finite-element modelling of recrystallization and grain growth in polycrystalline materials. *Scripta Materialia*, 64(6):525–528, 2011.

B. Beucia, S. Queyreau, C. Kahloun, D. Chaubet, P. Franciosi, and B. Bacroix. Plastic strain-induced grain boundary migration (sibm) in pure aluminum: Sem in-situ and afm examinations. *International Journal of Plasticity*, 115:29–55, 2019.

B. Bilby. Types of dislocation source. in: Bristol conference report on defects in crystalline solids. *The Physical Society, London*, 124, 1955.

K. Binder. Theory of first-order phase transitions. *Reports on progress in physics*, 50(7): 783, 1987.

S. B. Biner et al. *Programming phase-field modeling.* Springer, 2017.

G. H. Bishop and B. A. Chalmers. coincidence-ledge-dislocation description of grain boundaries. *Scr. Metal.*, 2(13):133–139, 1968. ISSN 2057-3960. doi: 10.1038/s41524-017-0016-0. URL `https://doi.org/10.1038/s41524-017-0016-0`.

W. Bollman. Crystal defects and crystalline interfaces. berlin, heidelberg, and new york (springer-verlag), 1970. xi 254 pp., 158 figs. together with a set of moiré models. *Mineralogical Magazine*, 38(297):645–646, 1972. doi: 10.1180/minmag.1972.038.297.25.

W. Bollmann. On the geometry of grain and phase boundaries: Ii. applications of general theory. *Philosophical Magazine*, 16(140):383–399, 1967.

W. Bollmann. The basic concepts of the 0-lattice theory. *Surface Science*, 31:1 – 11, 1972. ISSN 0039-6028. doi: https://doi.org/10.1016/0039-6028(72)90250-6. URL `http://www.sciencedirect.com/science/article/pii/0039602872902506`.

J. Bragard, A. Karma, Y. H. Lee, and M. Plapp. Linking phase-field and atomistic simulations to model dendritic solidification in highly undercooled melts. *Interface Science*, 10(2):121–136, 2002.

J. Broughton, W. Krakow, and S. Pantelides. Computer-based microscopic description of the structure and properties of materials. 1986.

V. Bulatov and W. Cai. *Computer Simulations of Dislocations (Oxford Series on Materials Modelling)*. Oxford University Press, Inc., USA, 2006. ISBN 0198526148.

V. V. Bulatov, B. W. Reed, and M. Kumar. Grain boundary energy function for fcc metals. *Acta Materialia*, 65:161–175, 2014.

R. Burden. Jd faires numerical analysis. *PWS, Boston*, 1993.

J. Cahn and D. Hoffman. A vector thermodlnamics for anisotropic surfaces—ii. curved and faceted surfaces. *Acta Metallurgica*, 22(10):1205–1214, 1974.

J. W. Cahn. On spinodal decomposition. *Acta metallurgica*, 9(9):795–801, 1961.

J. W. Cahn and J. E. Taylor. A unified approach to motion of grain boundaries, relative tangential translation along grain boundaries, and grain rotation. *Acta Materialia*, 52 (16):4887–4898, 2004.

J. W. Cahn, Y. Mishin, and A. Suzuki. Coupling grain boundary motion to shear deformation. *Acta materialia*, 54(19):4953–4975, 2006.

D. Caillard, F. Mompiou, and M. Legros. Grain-boundary shear-migration coupling. ii. geometrical model for general boundaries. *Acta Materialia*, 57(8):2390–2402, 2009.

P. R. Cantwell, E. A. Holm, M. P. Harmer, and M. J. Hoffmann. Anti-thermal behavior of materials. *Scripta Materialia*, 103:1–5, 2015.

P. Cermelli and M. E. Gurtin. On the characterization of geometrically necessary dislocations in finite plasticity. *Journal of the Mechanics and Physics of Solids*, 49(7): 1539–1568, 2001.

P. Cermelli and M. E. Gurtin. Geometrically necessary dislocations in viscoplastic single crystals and bicrystals undergoing small deformations. *International Journal of Solids and Structures*, 39(26):6281–6309, 2002.

N. Chandra and P. Dang. Atomistic simulation of grain boundary sliding and migration. *Journal of Materials Science*, 34(4):655–666, Feb 1999. ISSN 1573-4803. doi: 10.1023/A:1004531706998. URL `https://doi.org/10.1023/A:1004531706998`.

L.-Q. Chen. A novel computer simulation for modeling grain growth. *Scripta Metallurgica et Materialia;(United States)*, 32(1), 1995.

L.-Q. Chen and W. Yang. Computer simulation of the domain dynamics of a quenched system with a large number of nonconserved order parameters: The grain-growth kinetics. *Physical Review B*, 50(21):15752, 1994.

T. Chookajorn, H. A. Murdoch, and C. A. Schuh. Design of stable nanocrystalline alloys. *Science*, 337(6097):951–954, 2012.

P. G. Ciarlet, C. PG, et al. Sur les lois de comportement en élasticité non linéaire compressible. 1982.

B. D. Coleman and W. Noll. The thermodynamics of elastic materials with heat conduction and viscosity. In *The foundations of mechanics and thermodynamics*, pages 145–156. Springer, 1974.

S. P. Coleman, D. E. Spearot, and S. M. Foiles. The effect of synthetic driving force on the atomic mechanisms associated with grain boundary motion below the interface roughening temperature. *Computational materials science*, 86:38–42, 2014.

N. Combe, F. Mompiou, and M. Legros. Heterogeneous disconnection nucleation mechanisms during grain boundary migration. *Physical Review Materials*, 3(6):060601, 2019.

G. Costantini and F. Marchesoni. Threshold diffusion in a tilted washboard potential. *EPL (Europhysics Letters)*, 48(5):491, 1999.

A. H. Cottrell and B. A. Bilby. Dislocation theory of yielding and strain ageing of iron. *Proceedings of the Physical Society. Section A*, 62(1):49–62, jan 1949. doi: 10.1088/0370-1298/62/1/308. URL `https://doi.org/10.1088%2F0370-1298%2F62%2F1%2F308`.

M. S. Daw and M. I. Baskes. Embedded-atom method: Derivation and application to impurities, surfaces, and other defects in metals. *Physical Review B*, 29(12):6443, 1984.

M. S. Daw, S. M. Foiles, and M. I. Baskes. The embedded-atom method: a review of theory and applications. *Materials Science Reports*, 9(7-8):251–310, 1993.

M. De Koning, R. J. Kurtz, V. Bulatov, C. H. Henager, R. G. Hoagland, W. Cai, and M. Nomura. Modeling of dislocation–grain boundary interactions in fcc metals. *Journal of Nuclear Materials*, 323(2-3):281–289, 2003.

C. Deng and C. A. Schuh. Atomistic simulation of slow grain boundary motion. *Physical Review Letters*, 106(4):045503, 2011a.

C. Deng and C. A. Schuh. Diffusive-to-ballistic transition in grain boundary motion studied by atomistic simulations. *Physical Review B*, 84(21):214102, 2011b.

Y. Deng and C. Deng. Size and rate dependent grain boundary motion mediated by disconnection nucleation. *Acta Materialia*, 131:400–409, 2017.

C. Denoual, A. M. Caucci, L. Soulard, and Y.-P. Pellegrini. Phase-field reaction-pathway kinetics of martensitic transformations in a model fe 3 ni alloy. *Physical review letters*, 105(3):035703, 2010.

O. Dimitrov. Migration des joints de grains. la migration des joints intergranulaires. *Le Journal de Physique Colloques*, 36(C4):C4–319, 1975.

D. Dingley and R. Pond. On the interaction of crystal dislocations with grain boundaries. *Acta Metallurgica*, 27(4):667–682, 1979.

P. G. L. Dirichlet. *Über einen neuen Ausdruck zur Bestimmung der Dichtigkeit einer unendlich dünnen Kugelschale, wenn der Werth des Potentials derselben in jedem Punkte ihrer Oberfläche gegeben ist.* Dümmler in Komm., 1852.

D. Du, H. Zhang, and D. J. Srolovitz. Properties and determination of the interface stiffness. *Acta materialia*, 55(2):467–471, 2007.

O. H. Duparc and M. Torrent. A new type of periodie boundary condition useful for high-temperature atomistic simulations of grain boundaries: Applications in semiconductors. *Interface Science*, 2(1):7–16, 1994.

O. H. Duparc, S. Poulat, J. Thibault, and L. Larere, A.and Priester. *Phil. Mag.*, A 80: 853, 2000.

J. Eiken, B. Böttger, and I. Steinbach. Multiphase-field approach for multicomponent alloys with extrapolation scheme for numerical application. *Physical review E*, 73(6): 066122, 2006.

K. Elder and M. Grant. Modeling elastic and plastic deformations in nonequilibrium processing using phase field crystals. *Physical Review E*, 70(5):051605, 2004.

K. Elder, M. Katakowski, M. Haataja, and M. Grant. Modeling elasticity in crystal growth. *Physical review letters*, 88(24):245701, 2002.

F. Ercolessi and J. B. Adams. Interatomic potentials from first-principles calculations: the force-matching method. *EPL (Europhysics Letters)*, 26(8):583, 1994.

J. Eshelby, F. Frank, and F. Nabarro. Xli. the equilibrium of linear arrays of dislocations. *The London, Edinburgh, and Dublin Philosophical Magazine and Journal of Science*, 42(327):351–364, 1951. doi: 10.1080/14786445108561060. URL `https://doi.org/10.1080/14786445108561060`.

D. J. Evans and S. Sarman. Equivalence of thermostatted nonlinear responses. *Physical Review E*, 48(1):65, 1993.

T.-T. Fang. Part ii. defects of crystalline materials. In T.-T. Fang, editor, *Elements of Structures and Defects of Crystalline Materials*, page 81. Elsevier, 2018. ISBN 978-0-12-814268-4. doi: https://doi.org/10.1016/B978-0-12-814268-4.00024-2. URL `http://www.sciencedirect.com/science/article/pii/B9780128142684000242`.

M. Finnis and J. Sinclair. A simple empirical n-body potential for transition metals. *Philosophical Magazine A*, 50(1):45–55, 1984.

G. Fix. Phase field models for free boundary prolems. *Free boundary problems*, 2, 1983.

S. Foiles. Calculation of the surface segregation of ni-cu alloys with the use of the embedded-atom method. *Physical Review B*, 32(12):7685, 1985.

S. Foiles, M. Baskes, and M. S. Daw. Embedded-atom-method functions for the fcc metals cu, ag, au, ni, pd, pt, and their alloys. *Physical review B*, 33(12):7983, 1986.

S. M. Foiles and J. Hoyt. Computation of grain boundary stiffness and mobility from boundary fluctuations. *Acta Materialia*, 54(12):3351–3357, 2006.

F. Frank. The resultant content of dislocations in an arbitrary intercrystalline boundary. in: Symposium on the plastic deformation of crystalline solids, mellon institute, pittsburgh,(navexos-p-834), vol.150. 1950a.

F. Frank. Procedings of the symposium on the plastic deformation of crystalline solids. *Pittsburgh, PA, Carnegie Institute of Technology*, page 89, 1950b.

F. Frank. Capillary equilibria of dislocated crystals. *Acta Crystallographica*, 4(6):497–501, 1951.

D. Frenkel and B. Smit. *Understanding molecular simulation: from algorithms to applications*, volume 1. Elsevier, 2001.

E. Fried and M. E. Gurtin. Dynamic solid-solid transitions with phase characterized by an order parameter. *Physica D: Nonlinear Phenomena*, 72(4):287–308, 1994.

T. Frolov, M. Asta, and Y. Mishin. Phase transformations at interfaces: observations from atomistic modeling. *Current Opinion in Solid State and Materials Science*, 20(5):308–315, 2016.

M. Furtkamp, G. Gottstein, D. Molodov, V. Semenov, and L. Shvindlerman. Grain boundary migration in fe–3.5boundaries. *Acta Materialia*, 46(12):4103 – 4110, 1998. ISSN 1359-6454. doi: https://doi.org/10.1016/S1359-6454(98)00105-0. URL `http://www.sciencedirect.com/science/article/pii/S1359645498001050`.

R. Gautier, A. Rajabzadeh, M. Larranaga, N. Combe, F. Mompiou, and M. Legros. Shear-coupled migration of grain boundaries: the key missing link in the mechanical behavior of small-grained metals? *Comptes Rendus. Physique*, 22(S3):19–34, 2021. doi: 10.5802/crphys.52.

M. Gilbert, S. Queyreau, and J. Marian. Stress and temperature dependence of screw dislocation mobility in α-fe by molecular dynamics. *Physical Review B*, 84(17):174103, 2011.

J. J. Gilman. Micromechanics of shear banding. *Mechanics of Materials*, 17(2):83 – 96, 1994. ISSN 0167-6636. doi: https://doi.org/10.1016/0167-6636(94)90051-5. URL `http://www.sciencedirect.com/science/article/pii/0167663694900515`.

N. Gjostein and F. Rhines. Absolute interfacial energies of [001] tilt and twist grain boundaries in copper. *Acta Metallurgica*, 7(5):319 – 330, 1959. ISSN 0001-6160. doi: https://doi.org/10.1016/0001-6160(59)90198-1. URL `http://www.sciencedirect.com/science/article/pii/0001616059901981`.

H. Gleiter. Chapter 9 - microstructure. In R. W. CAHN and P. HAASEN†, editors, *Physical Metallurgy (Fourth Edition)*, pages 843 – 942. North-Holland, Oxford, fourth edition edition, 1996. ISBN 978-0-444-89875-3. doi: https://doi.org/10.1016/B978-044489875-3/50014-4. URL `http://www.sciencedirect.com/science/article/pii/B9780444898753500144`.

T. Gorkaya, D. A. Molodov, and G. Gottstein. Stress-driven migration of symmetrical< 1 0 0> tilt grain boundaries in al bicrystals. *Acta Materialia*, 57(18):5396–5405, 2009.

G. Gottstein and L. S. Shvindlerman. *Grain boundary migration in metals: thermodynamics, kinetics, applications.* CRC press, 2009a.

G. Gottstein and L. S. Shvindlerman. *Grain boundary migration in metals: thermodynamics, kinetics, applications.* CRC press, 2009b.

G. Gottstein, D. A. Molodov, and L. S. Shvindlerman. Grain boundary migration in metals: Recent developments. *Interface Science*, 6(1):7–22, 1998.

L. Gránásy, T. Pusztai, and J. A. Warren. Modelling polycrystalline solidification using phase field theory. *Journal of Physics: Condensed Matter*, 16(41):R1205, 2004.

L. Gránásy, T. Pusztai, G. Tegze, J. A. Warren, and J. F. Douglas. Growth and form of spherulites. *Physical Review E*, 72(1):011605, 2005.

H. Grimmer. Coincidence-site lattices. *Acta Crystallographica Section A*, 32(5):783–785, Sep 1976. doi: 10.1107/S056773947601231X. URL `https://doi.org/10.1107/S056773947601231X`.

P. Gu, M. Dao, and S. Suresh. Analysis of size-dependent slip transfer and inter-twin flow stress in a nanotwinned fcc metal. *Acta Materialia*, 67:409 – 417, 2014. ISSN 1359-6454. doi: https://doi.org/10.1016/j.actamat.2013.12.028. URL `http://www.sciencedirect.com/science/article/pii/S1359645413009634`.

J. Gunton and M. San Miguel. Ps sahni in phase transitions and critical phenomena, c. domb and jl lebowitz, eds, 1983.

M. E. Gurtin. Generalized ginzburg-landau and cahn-hilliard equations based on a microforce balance. *Physica D: Nonlinear Phenomena*, 92(3-4):178–192, 1996.

M. E. Gurtin. *Configurational forces as basic concepts of continuum physics*, volume 137. Springer Science & Business Media, 1999.

M. E. Gurtin. On the plasticity of single crystals: free energy, microforces, plastic-strain gradients. *Journal of the Mechanics and Physics of Solids*, 48(5):989–1036, 2000.

M. E. Gurtin. A finite-deformation, gradient theory of single-crystal plasticity with free energy dependent on densities of geometrically necessary dislocations. *International Journal of Plasticity*, 24(4):702–725, 2008.

M. E. Gurtin, E. Fried, and L. Anand. *The mechanics and thermodynamics of continua*. Cambridge University Press, 2010.

R. Hadian, B. Grabowski, M. W. Finnis, and J. Neugebauer. Migration mechanisms of a faceted grain boundary. *Physical Review Materials*, 2(4):043601, 2018.

J. Haile. Molecular dynamics simulation: elementary methods. Technical report, 1992.

J. Haile. Molecular dynamics simulation: Elementary methods, j. wiley&sons. 1997.

E. O. Hall. The deformation and ageing of mild steel: II characteristics of the l ders deformation. *Proceedings of the Physical Society. Section B*, 64(9):742–747, sep 1951. doi: 10.1088/0370-1301/64/9/302. URL `https://doi.org/10.1088%2F0370-1301%2F64%2F9%2F302`.

J. Han, V. Vitek, and D. J. Srolovitz. The grain-boundary structural unit model redux. *Acta Materialia*, 133:186 – 199, 2017a. ISSN 1359-6454. doi: https://doi.org/10.1016/j.

actamat.2017.05.002. URL `http://www.sciencedirect.com/science/article/pii/S1359645417303798`.

J. Han, V. Vitek, and D. J. Srolovitz. The grain-boundary structural unit model redux. *Acta Materialia*, 133:186–199, 2017b.

J. Han, S. L. Thomas, and D. J. Srolovitz. Grain-boundary kinetics: A unified approach. *Progress in Materials Science*, 98:386–476, 2018.

R. Hanus, A. Garg, and G. J. Snyder. Phonon diffraction and dimensionality crossover in phonon-interface scattering. *Communications Physics*, 1(1):1–11, 2018.

P. E. Hart, N. J. Nilsson, and B. Raphael. A formal basis for the heuristic determination of minimum cost paths. *IEEE transactions on Systems Science and Cybernetics*, 4(2): 100–107, 1968.

G. Henkelman, B. P. Uberuaga, and H. Jónsson. A climbing image nudged elastic band method for finding saddle points and minimum energy paths. *The Journal of chemical physics*, 113(22):9901–9904, 2000.

J. Hirth, R. Pond, and J. Lothe. Disconnections in tilt walls. *Acta Materialia*, 54(16): 4237–4245, 2006.

J. Hirth, R. Pond, and J. Lothe. Spacing defects and disconnections in grain boundaries. *Acta materialia*, 55(16):5428–5437, 2007.

J. P. Hirth and J. Lothe. *Theory of Dislocations.* Krieger Publishing Company, 1992. ISBN 0894646176. URL `http://www.amazon.com/Theory-Dislocations-John-Price-Hirth/dp/0894646176/ref=sr_1_1?s=books&ie=UTF8&qid=1293986464&sr=1-1`.

J. P. Hirth, J. Lothe, and T. Mura. Theory of dislocations. *Journal of Applied Mechanics*, 50(2):476, 1983.

D. W. Hoffman and J. W. Cahn. A vector thermodynamics for anisotropic surfaces: I. fundamentals and application to plane surface junctions. *Surface Science*, 31:368–388, 1972.

E. Homer. Investigating the mechanisms for grain boundary migration during recrystallization using molecular dynamics. In *IOP Conf. Series: Mater. Sci. Eng*, volume 89, page 012006, 2015.

E. R. Homer, S. M. Foiles, E. A. Holm, and D. L. Olmsted. Phenomenology of shear-coupled grain boundary motion in symmetric tilt and general grain boundaries. *Acta Materialia*, 61(4):1048–1060, 2013.

E. R. Homer, E. A. Holm, S. M. Foiles, and D. L. Olmsted. Trends in grain boundary mobility: Survey of motion mechanisms. *JOM*, 66(1):114–120, Jan 2014a. ISSN 1543-1851. doi: 10.1007/s11837-013-0801-2. URL `https://doi.org/10.1007/s11837-013-0801-2`.

E. R. Homer, E. A. Holm, S. M. Foiles, and D. L. Olmsted. Trends in grain boundary mobility: Survey of motion mechanisms. *Jom*, 66(1):114–120, 2014b.

E. R. Homer, S. Patala, and J. L. Priedeman. Grain boundary plane orientation fundamental zones and structure-property relationships. *Scientific reports*, 5:15476, 2015.

J. D. Honeycutt and H. C. Andersen. Molecular dynamics study of melting and freezing of small lennard-jones clusters. *Journal of Physical Chemistry*, 91(19):4950–4963, 1987.

W. G. Hoover and B. L. Holian. Kinetic moments method for the canonical ensemble distribution. *Physics Letters A*, 211(5):253–257, 1996.

J. Hoyt, M. Asta, and A. Karma. Method for computing the anisotropy of the solid-liquid interfacial free energy. *Physical review letters*, 86(24):5530, 2001.

K. Huang. Statistical mechanics. *Statistical Mechanics*, page 512, 1987.

T. J. Hughes. *The finite element method: linear static and dynamic finite element analysis.* Courier Corporation, 2012.

D. Hull and D. J. Bacon. *Introduction to dislocations.* Butterworth-Heinemann, 2001.

J. D. Humberson. The Motion Mechanism and Thermal Behavior of Sigma 3 Grain Boundaries. 9 2016. doi: 10.1184/R1/6723725.v1. URL `https://kilthub.cmu.edu/articles/thesis/The_Motion_Mechanism_and_Thermal_Behavior_of_Sigma_3_Grain_Boundaries/6723725`.

G. Hütter. An extended coleman–noll procedure for generalized continuum theories. *Continuum Mechanics and Thermodynamics*, 28(6):1935–1941, 2016.

V. Ivanov and Y. Mishin. Dynamics of grain boundary motion coupled to shear deformation: An analytical model and its verification by molecular dynamics. *Physical Review B*, 78(6):064106, 2008.

K. G. Janssens, D. Olmsted, E. A. Holm, S. M. Foiles, S. J. Plimpton, and P. M. Derlet. Computing the mobility of grain boundaries. *Nature materials*, 5(2):124–127, 2006.

R.-J. Jhan and P. Bristowe. A molecular dynamics study of grain boundary migration without the participation of secondary grain boundary dislocations. *Scripta Metallurgica et Materialia*, 24(7):1313–1318, 1990.

Y. Jin, B. Lin, M. Bernacki, G. S. Rohrer, A. Rollett, and N. Bozzolo. Annealing twin development during recrystallization and grain growth in pure nickel. *Materials Science and Engineering: A*, 597:295–303, 2014.

W. G. Johnston and J. J. Gilman. Dislocation velocities, dislocation densities, and plastic flow in lithium fluoride crystals. *Journal of Applied Physics*, 30(2):129–144, 1959. doi: 10.1063/1.1735121. URL `https://doi.org/10.1063/1.1735121`.

J. Jones. On the determination of molecular fields. iii.—from crystal measurements and kinetic theory data. *Proceedings of the Royal Society of London. Series A, Containing Papers of a Mathematical and Physical Character*, 106(740):709–718, 1924.

S.-H. Jung, D. Y. Yoon, and S.-J. L. Kang. Mechanism of abnormal grain growth in ultrafine-grained nickel. *Acta materialia*, 61(15):5685–5693, 2013.

J. Kacher, B. Eftink, B. Cui, and I. Robertson. Dislocation interactions with grain boundaries. *Current Opinion in Solid State and Materials Science*, 18(4):227 – 243, 2014. ISSN 1359-0286. doi: https://doi.org/10.1016/j.cossms.2014.05.004. URL `http://www.sciencedirect.com/science/article/pii/S1359028614000217`. Slip Localization and Transfer in Deformation and Fatigue of Polycrystals.

C. L. Kelchner, S. Plimpton, and J. Hamilton. Dislocation nucleation and defect structure during surface indentation. *Physical review B*, 58(17):11085, 1998.

A. Kelly and K. M. Knowles. *Crystallography and crystal defects.* John Wiley & Sons, 2020.

H.-K. Kim, W.-S. Ko, H.-J. Lee, S. G. Kim, and B.-J. Lee. An identification scheme of grain boundaries and construction of a grain boundary energy database. *Scripta Materialia*, 64(12):1152–1155, 2011.

R. Kobayashi and Y. Giga. Equations with singular diffusivity. *Journal of statistical physics*, 95(5):1187–1220, 1999.

R. Kobayashi and J. A. Warren. Modeling the formation and dynamics of polycrystals in 3d. *Physica A: Statistical Mechanics and its Applications*, 356(1):127–132, 2005.

R. Kobayashi, J. A. Warren, and W. C. Carter. Vector-valued phase field model for crystallization and grain boundary formation. *Physica D: Nonlinear Phenomena*, 119 (3-4):415–423, 1998.

R. Kobayashi, J. A. Warren, and W. C. Carter. A continuum model of grain boundaries. *Physica D: Nonlinear Phenomena*, 140(1-2):141–150, 2000.

U. F. Kocks, A. AS, and A. MF. Thermodynamics and kinetics of slip. 1975.

C. Krill Iii and L.-Q. Chen. Computer simulation of 3-d grain growth using a phase-field model. *Acta materialia*, 50(12):3059–3075, 2002.

M. Kronberg and F. Wilson. *Met. Trans*, 185:501, 1949.

E. Kröner. Allgemeine kontinuumstheorie der versetzungen und eigenspannungen. *Archive for Rational Mechanics and Analysis*, 4(1):273–334, 1959.

A. Lacasta, J. Sancho, A. Romero, and K. Lindenberg. Sorting on periodic surfaces. *Physical review letters*, 94(16):160601, 2005.

L. Landau. Em lifshitz statistical physics, part i pergamon, 1980.

J. Langer. Models of pattern formation in first-order phase transitions. In *Directions in condensed matter physics: memorial volume in honor of Shang-Keng Ma*, pages 165–186. World Scientific, 1986.

J. S. Langer. Statistical theory of the decay of metastable states. *Annals of Physics*, 54 (2):258–275, 1969.

J. S. Langer. Theory of spinodal decomposition in alloys. *Annals of Physics*, 65(1):53–86, 1971.

J. Lebowitz, J. Percus, and L. Verlet. Ensemble dependence of fluctuations with application to machine computations. *Physical Review*, 153(1):250, 1967.

B.-J. Lee and S.-H. Choi. Computation of grain boundary energies. *Modelling and Simulation in Materials Science and Engineering*, 12(4):621, 2004.

B.-J. Lee, J.-H. Shim, and M. Baskes. Semiempirical atomic potentials for the fcc metals cu, ag, au, ni, pd, pt, al, and pb based on first and second nearest-neighbor modified embedded atom method. *Physical Review B*, 68(14):144112, 2003.

E. H. Lee. Elastic-plastic deformation at finite strains. 1969.

H. Li, X. Sun, and H. Yang. A three-dimensional cellular automata-crystal plasticity finite element model for predicting the multiscale interaction among heterogeneous deformation, drx microstructural evolution and mechanical responses in titanium alloys. *International Journal of Plasticity*, 87:154–180, 2016.

J. Li. Disclination model of high angle grain boundaries. *Surface Science*, 31:12 – 26, 1972. ISSN 0039-6028. doi: https://doi.org/10.1016/0039-6028(72)90251-8. URL `http://www.sciencedirect.com/science/article/pii/0039602872902518`.

A. Lim, D. Srolovitz, and M. Haataja. Low-angle grain boundary migration in the presence of extrinsic dislocations. *Acta materialia*, 57(17):5013–5022, 2009.

A. Lobkovsky, A. Karma, M. Mendelev, M. Haataja, and D. Srolovitz. Grain shape, grain boundary mobility and the herring relation. *Acta materialia*, 52(2):285–292, 2004.

A. E. Lobkovsky and J. A. Warren. Sharp interface limit of a phase-field model of crystal grains. *Physical Review E*, 63(5):051605, 2001.

E. A. LORD. Coincidence sites for rational lattices. *Zeitschrift für Kristallographie*, 2006. ISSN 0044-2968.

M. T. Lusk. A phase–field paradigm for grain growth and recrystallization. *Proceedings of the Royal Society of London. Series A: Mathematical, Physical and Engineering Sciences*, 455(1982):677–700, 1999.

J. Lutsko, D. Wolf, S. Yip, S. Phillpot, and T. Nguyen. Molecular-dynamics method for the simulation of bulk-solid interfaces at high temperatures. *Physical Review B*, 38(16): 11572, 1988.

G. J. Martyna, D. J. Tobias, and M. L. Klein. Constant pressure molecular dynamics algorithms. *The Journal of chemical physics*, 101(5):4177–4189, 1994.

M. Masteller and C. Bauer. Migration of special< 110> tilt boundaries in aluminum bicrystals. *Acta Metallurgica*, 27(3):483–488, 1979.

M. Mendelev, C. Deng, C. Schuh, and D. Srolovitz. Comparison of molecular dynamics simulation methods for the study of grain boundary migration. *Modelling and Simulation in Materials Science and Engineering*, 21(4):045017, 2013.

K. Merkle, L. Thompson, and F. Phillipp. In-situ hrem studies of grain boundary migration. *Interface Science*, 12(2):277–292, 2004.

K. L. Merkle, R. Csencsits, K. L. Rynes, J. P. Withrow, and P. A. Stadelmann. The effect of three-fold astigmatism on measurements of grain boundary volume expansion by high-resolution transmission electron microscopy. *Journal of Microscopy*, 190(1-2):204–213, 1998. doi: 10.1046/j.1365-2818.1998.2890841.x. URL `https://onlinelibrary.wiley.com/doi/abs/10.1046/j.1365-2818.1998.2890841.x`.

N. Metropolis, A. W. Rosenbluth, M. N. Rosenbluth, A. H. Teller, and E. Teller. Equation of state calculations by fast computing machines. *The journal of chemical physics*, 21 (6):1087–1092, 1953.

Y. Mishin, D. Farkas, M. Mehl, and D. Papaconstantopoulos. Interatomic potentials for monoatomic metals from experimental data and ab initio calculations. *Physical Review B*, 59(5):3393, 1999.

Y. Mishin, M. Mehl, D. Papaconstantopoulos, A. Voter, and J. Kress. Structural stability and lattice defects in copper: Ab initio, tight-binding, and embedded-atom calculations. *Physical Review B*, 63(22):224106, 2001.

Y. Mishin, M. Asta, and J. Li. Atomistic modeling of interfaces and their impact on microstructure and properties. *Acta Materialia*, 58(4):1117–1151, 2010.

N. Moelans, B. Blanpain, and P. Wollants. An introduction to phase-field modeling of microstructure evolution. *Calphad*, 32(2):268–294, 2008.

D. Molodov, G. Gottstein, F. Heringhaus, and L. Shvindlerman. Motion of planar grain boundaries in bismuth bicrystals driven by a magnetic field. *Scripta materialia*, 37(8): 1207–1213, 1997.

D. Molodov, U. Czubayko, G. Gottstein, and L. Shvindlerman. On the effect of purity and orientation on grain boundary motion. *Acta materialia*, 46(2):553–564, 1998a.

D. Molodov, G. Gottstein, F. Heringhaus, and L. Shvindlerman. True absolute grain boundary mobility: motion of specific planar boundaries inbi-bicrystals under magnetic driving forces. *Acta materialia*, 46(16):5627–5632, 1998b.

D. Molodov, V. Ivanov, and G. Gottstein. Low angle tilt boundary migration coupled to shear deformation. *Acta Materialia*, 55(5):1843–1848, 2007.

F. Mompiou, D. Caillard, and M. Legros. Grain boundary shear–migration coupling—i. in situ tem straining experiments in al polycrystals. *Acta Materialia*, 57(7):2198–2209, 2009.

B. Morin, K. R. Elder, M. Sutton, and M. Grant. Model of the kinetics of polymorphous crystallization. *Physical review letters*, 75(11):2156, 1995.

S. Naamane, G. Monnet, and B. Devincre. Low temperature deformation in iron studied with dislocation dynamics simulations. *International Journal of Plasticity*, 26(1):84–92, 2010.

B. Nestler and A. A. Wheeler. Phase-field modeling of multi-phase solidification. *Computer Physics Communications*, 147(1-2):230–233, 2002.

B. Nestler, H. Garcke, and B. Stinner. Multicomponent alloy solidification: phase-field modeling and simulations. *Physical Review E*, 71(4):041609, 2005.

C. Neumann. *Das Dirischlet'sche princip in seiner anwendung auf die Reimann'schen flächen.* BG Teubner, 1865.

E. Ngenzi, Z. El Omari, B. Bacroix, and S. Queyreau. Mobility functions for [001] csl grain boundaries in ni from molecular dynamics. 2021.

C. F. Nigro. *Phase-field modeling of stress-induced precipitation and kinetics in engineering metals*. Chalmers Tekniska Hogskola (Sweden), 2020.

S. Nosé. A unified formulation of the constant temperature molecular dynamics methods. *The Journal of chemical physics*, 81(1):511–519, 1984.

J. F. Nye. Some geometrical relations in dislocated crystals. *Acta metallurgica*, 1(2): 153–162, 1953.

D. L. Olmsted, S. M. Foiles, and E. A. Holm. Grain boundary interface roughening transition and its effect on grain boundary mobility for non-faceting boundaries. *Scripta Materialia*, 57(12):1161–1164, 2007.

D. L. Olmsted, S. M. Foiles, and E. A. Holm. Survey of computed grain boundary properties in face-centered cubic metals: I. grain boundary energy. *Acta Materialia*, 57 (13):3694–3703, 2009a.

D. L. Olmsted, S. M. Foiles, and E. A. Holm. Survey of computed grain boundary properties in face-centered cubic metals: I. grain boundary energy. *Acta Materialia*, 57 (13):3694–3703, 2009b.

D. L. Olmsted, E. A. Holm, and S. M. Foiles. Survey of computed grain boundary properties in face-centered cubic metals—ii: Grain boundary mobility. *Acta materialia*, 57(13):3704–3713, 2009c.

Z. E. OMAR. *Etude de la migration des joints de grain mixtes flexion-torsion dans le Ni par dynamique moléculaire*. PhD thesis, 2019.

E. Orowan. Zur kristallplastizität. i. *Zeitschrift für Physik*, 89(9):605–613, 1934.

A. Otsuki and M. Mizuno. Grain boundary energy and liquid metal embrittlement of aluminium. *Transactions of the Japan Institute of Metals (Supplement)*, 27:789–796, 1986.

C. O'Brien and S. Foiles. Exploration of the mechanisms of temperature-dependent grain boundary mobility: search for the common origin of ultrafast grain boundary motion. *Journal of Materials Science*, 51(14):6607–6623, 2016.

S. Patala and C. A. Schuh. Symmetries in the representation of grain boundary-plane distributions. *Philosophical Magazine*, 93(5):524–573, 2013.

R. Pathria and P. Beale. Statistical mechanics butterworth, 1996.

W. B. Paul. Molecular dynamics simulation, elementary methods. by jm haile, wiley, chichester 1992, 489 pp., hardcover,£ 47.50, isbn 0-471-81966-2, 1993.

N. Petch. The cleavage strength of polycrystals. *Journal of the Iron and Steel Institute*, 174:25–28, 1953.

K. Piękoś, J. Tarasiuk, K. Wierzbanowski, and B. Bacroix. Generalized vertex model-study of recrystallization in copper. In *Materials Science Forum*, volume 558, pages 1157–1162. Trans Tech Publ, 2007.

S. Plimpton. Fast parallel algorithms for short-range molecular dynamics. *Journal of computational physics*, 117(1):1–19, 1995.

E. Popova, Y. Staraselski, A. Brahme, R. Mishra, and K. Inal. Coupled crystal plasticity–probabilistic cellular automata approach to model dynamic recrystallization in magnesium alloys. *International Journal of Plasticity*, 66:85–102, 2015.

D. Porter and K. Easterling. Phase transformations in metals and alloys, 1992.

L. Priester. *Grain boundaries: from theory to engineering*, volume 172. Springer Science & Business Media, 2012.

N. Provatas and K. Elder. *Phase-field methods in materials science and engineering.* John Wiley & Sons, 2011.

T. Pusztai, G. Bortel, and L. Gránásy. Phase field modeling of polycrystalline freezing. *Materials Science and Engineering: A*, 413:412–417, 2005a.

T. Pusztai, G. Bortel, and L. Gránásy. Phase field theory of polycrystalline solidification in three dimensions. *EPL (Europhysics Letters)*, 71(1):131, 2005b.

S. Queyreau, J. Marian, M. Gilbert, and B. Wirth. Edge dislocation mobilities in bcc fe obtained by molecular dynamics. *Physical Review B*, 84(6):064106, 2011.

D. Raabe. Cellular automata in materials science with particular reference to recrystallization simulation. *Annual review of materials research*, 32(1):53–76, 2002.

D. Raabe and R. C. Becker. Coupling of a crystal plasticity finite-element model with a probabilistic cellular automaton for simulating primary static recrystallization in aluminium. *Modelling and Simulation in Materials Science and Engineering*, 8(4):445, 2000.

C. Race, J. von Pezold, and J. Neugebauer. Role of the mesoscale in migration kinetics of flat grain boundaries. *Physical Review B*, 89(21):214110, 2014.

A. Rajabzadeh, F. Mompiou, M. Legros, and N. Combe. Elementary mechanisms of shear-coupled grain boundary migration. *Physical review letters*, 110(26):265507, 2013.

V. Randle. *The Role Of The Coincidence Site Lattice In Grain Boundary Engineering.* Maney Publishing, Department of Materials Engineering University of Wales, Swansea, 1996. ISBN 1861250061.

S. Ranganathan. On the geometry of coincidence-site lattices. *Acta Crystallographica*, 21(2):197–199, Aug 1966. doi: 10.1107/S0365110X66002615. URL `https://doi.org/10.1107/S0365110X66002615`.

S. Ratanaphan, D. L. Olmsted, V. V. Bulatov, E. A. Holm, A. D. Rollett, and G. S. Rohrer. Grain boundary energies in body-centered cubic metals. *Acta Materialia*, 88: 346–354, 2015.

W. Read. Dislocations in crystals mcgraw-hill. *New York, London, Toronto*, 1953.

W. T. Read and W. Shockley. Dislocation models of crystal grain boundaries. *Phys. Rev.*, 78:275–289, May 1950. doi: 10.1103/PhysRev.78.275. URL `https://link.aps.org/doi/10.1103/PhysRev.78.275`.

C. Reina and S. Conti. Kinematic description of crystal plasticity in the finite kinematic framework: A micromechanical understanding of f= fefp. *Journal of the Mechanics and Physics of Solids*, 67:40–61, 2014.

C. Reina, L. Sandoval, and J. Marian. Mesoscale computational study of the nanocrystallization of amorphous ge via a self-consistent atomistic phase-field model. *Acta materialia*, 77:335–351, 2014.

S. E. Restrepo, S. T. Giraldo, and B. J. Thijsse. Using artificial neural networks to predict grain boundary energies. *Computational materials science*, 86:170–173, 2014.

D. Rodney. Molecular dynamics simulation of screw dislocations interacting with interstitial frank loops in a model fcc crystal. *Acta Materialia*, 52(3):607 – 614, 2004. ISSN 1359-6454. doi: https://doi.org/10.1016/j.actamat.2003.09.044. URL `http://www.sciencedirect.com/science/article/pii/S1359645403006128`.

D. Rodney and L. Proville. Stress-dependent peierls potential: Influence on kink-pair activation. *Physical Review B*, 79(9):094108, 2009.

G. S. Rohrer, D. M. Saylor, B. El Dasher, B. L. Adams, A. D. Rollett, and P. Wynblatt. The distribution of internal interfaces in polycrystals. *International Journal of Materials Research*, 95(4):197–214, 2004.

S. Rokkam, A. El-Azab, P. Millett, and D. Wolf. Phase field modeling of void nucleation and growth in irradiated metals. *Modelling and simulation in materials science and engineering*, 17(6):064002, 2009.

J. H. Rose, J. R. Smith, F. Guinea, and J. Ferrante. Universal features of the equation of state of metals. *Physical Review B*, 29(6):2963, 1984.

W. Rudin. *Functional Analysis*. International series in pure and applied mathematics. McGraw-Hill, 1991. ISBN 9780070542365. URL `https://books.google.fr/books?id=Sh\_vAAAAMAAJ`.

G. Saada. Elastic field of dislocation networks and grain boundaries. *Acta Metallurgica*, 27(6):921–931, 1979.

M. D. Sangid, H. Sehitoglu, H. J. Maier, and T. Niendorf. Grain boundary characterization and energetics of superalloys. *Materials Science and Engineering: A*, 527(26):7115–7125, 2010.

A. Satoh. *Introduction to practice of molecular simulation: molecular dynamics, Monte Carlo, Brownian dynamics, Lattice Boltzmann and dissipative particle dynamics*. Elsevier, 2010.

B. Schönfelder. *Atomistic simulations of grain boundary migration in face-centered cubic metals*. PhD thesis, 2003.

B. Schönfelder, G. Gottstein, and L. Shvindlerman. Comparative study of grain-boundary migration and grain-boundary self-diffusion of [0 0 1] twist-grain boundaries in copper by atomistic simulations. *Acta Materialia*, 53(6):1597–1609, 2005.

B. Schönfelder, G. Gottstein, and L. S. Shvindlerman. Atomistic simulations of grain boundary migration in copper. *Metallurgical and Materials Transactions A*, 37(6): 1757–1771, June 2006. doi: 10.1007/s11661-006-0118-7.

A. Sheikh-Ali, D. Molodov, and H. Garmestani. Boundary migration in zn bicrystal induced by a high magnetic field. *Applied physics letters*, 82(18):3005–3007, 2003a.

A. Sheikh-Ali, D. Molodov, and H. Garmestani. Migration and reorientation of grain boundaries in zn bicrystals during annealing in a high magnetic field. *Scripta materialia*, 48(5):483–488, 2003b.

T. Shen, J. Zhang, and Y. Zhao. What is the theoretical density of a nanocrystalline material? *Acta Materialia*, 56(14):3663 – 3671, 2008. ISSN 1359-6454. doi: https://doi.org/10.1016/j.actamat.2008.04.003. URL `http://www.sciencedirect.com/science/article/pii/S1359645408002541`.

Z. Shen, R. Wagoner, and W. Clark. Dislocation and grain boundary interactions in metals. *Acta metallurgica*, 36(12):3231–3242, 1988.

L. S. Shvindlerman, G. Gottstein, V. A. Ivanov, D. A. Molodov, D. Kolesnikov, and W. Łojkowski. Grain boundary excess free volume—direct thermodynamic measurement. *Journal of Materials Science*, 41(23):7725–7729, Dec 2006. ISSN 1573-4803. doi: 10.1007/s10853-006-0563-0. URL `https://doi.org/10.1007/s10853-006-0563-0`.

W. Spitzig and A. Keh. Orientation dependence of the strain-rate sensitivity and thermally activated flow in iron single crystals. *Acta metallurgica*, 18(9):1021–1033, 1970.

I. Steinbach and F. Pezzolla. A generalized field method for multiphase transformations using interface fields. *Physica D: Nonlinear Phenomena*, 134(4):385–393, 1999.

I. Steinbach, F. Pezzolla, B. Nestler, M. Seeßelberg, R. Prieler, G. J. Schmitz, and J. L. Rezende. A phase field concept for multiphase systems. *Physica D: Nonlinear Phenomena*, 94(3):135–147, 1996.

A. Stukowski. Visualization and analysis of atomistic simulation data with ovito–the open visualization tool. *Modelling and Simulation in Materials Science and Engineering*, 18 (1):015012, 2009.

A. Stukowski. Structure identification methods for atomistic simulations of crystalline materials. *Modelling and Simulation in Materials Science and Engineering*, 20(4):045021, 2012.

A. Stukowski and K. Albe. Extracting dislocations and non-dislocation crystal defects from atomistic simulation data. *Modelling and Simulation in Materials Science and Engineering*, 18(8):085001, 2010.

A. Stukowski, V. V. Bulatov, and A. Arsenlis. Automated identification and indexing of dislocations in crystal interfaces. *Modelling and Simulation in Materials Science and Engineering*, 20(8):085007, 2012.

R. Sun and C. Bauer. Measurement of grain boundary mobilities through magnification of capillary forces. *Acta Metallurgica*, 18(6):635–638, 1970.

X.-Y. Sun, V. Taupin, C. Fressengeas, and P. Cordier. Continuous description of the atomic structure of grain boundaries using dislocation and generalized-disclination density fields. *International Journal of Plasticity*, 77:75–89, 2016.

A. Sutton. Rw balluffi interfaces in crystalline materials, 1996.

A. Sutton and R. Balluffi. Overview no. 61 on geometric criteria for low interfacial energy. *Acta Metallurgica*, 35(9):2177 – 2201, 1987. ISSN 0001-6160. doi: https://doi.org/10.1016/0001-6160(87)90067-8. URL `http://www.sciencedirect.com/science/article/pii/0001616087900678`.

A. Sutton and V. Vitek. On the structure of tilt grain boundaries in cubic metals i. symmetrical tilt boundaries. *Philos. Trans. R. Soc. Lond. A Math. Phys. Sci.*, 309(13): 1–36, 1983a.

A. Sutton and V. Vitek. On the structure of tilt grain boundaries in cubic metals ii. asymmetrical tilt boundaries. *Philos. Trans. R. Soc. Lond. A Math. Phys. Sci.*, 309 (13):37–54, 1983b.

A. P. Sutton. Interfaces in crystalline materials. *Monographs on the Physice and Chemistry of Materials*, pages 349–352, 1995.

T. Takaki, T. Hirouchi, Y. Hisakuni, A. Yamanaka, and Y. Tomita. Multi-phase-field model to simulate microstructure evolutions during dynamic recrystallization. *Materials transactions*, 49(11):2559–2565, 2008.

M. Talaei, N. Nouri, and S. Ziaei-Rad. An optimized approach for computing coincidence-site-lattice grain boundary energy. *Computational Condensed Matter*, 19:e00363, 2019a.

M. S. Talaei, N. Nouri, and S. Ziaei-Rad. An optimized approach for computing coincidence-site-lattice grain boundary energy. *Computational Condensed Matter*, 19, 2019b.

M. Tang, L. Kubin, and G. Canova. Dislocation mobility and the mechanical response of bcc single crystals: a mesoscopic approach. *Acta Materialia*, 46(9):3221–3235, 1998.

V. Taupin, L. Capolungo, C. Fressengeas, M. Upadhyay, and B. Beausir. A mesoscopic theory of dislocation and disclination fields for grain boundary-mediated crystal plasticity. *International Journal of Solids and Structures*, 71:277–290, 2015.

G. I. Taylor. The mechanism of plastic deformation of crystals. part i. theoretical. *Proceedings of the Royal Society of London. Series A, Containing Papers of a Mathematical and Physical Character*, 145(855):362–387, 1934. ISSN 09501207. URL `http://www.jstor.org/stable/2935509`.

S. L. Thomas, K. Chen, J. Han, P. K. Purohit, and D. J. Srolovitz. Reconciling grain growth and shear-coupled grain boundary migration. *Nature communications*, 8(1): 1–12, 2017.

B. J. Torby. Advanced dynamics for engineers, 1984.

M. Tschopp and D. McDowell. Structures and energies of σ 3 asymmetric tilt grain boundaries in copper and aluminium. *Philosophical Magazine*, 87(22):3147–3173, 2007.

M. A. Tschopp, S. P. Coleman, and D. L. McDowell. Symmetric and asymmetric tilt grain boundary structure and energy in cu and al (and transferability to other fcc metals). *Integrating Materials and Manufacturing Innovation*, 4(1):11, 2015.

G. J. Tucker and D. L. McDowell. Non-equilibrium grain boundary structure and inelastic deformation using atomistic simulations. *International Journal of Plasticity*, 27(6):841 – 857, 2011. ISSN 0749-6419. doi: https://doi.org/10.1016/j.ijplas.2010.09.011. URL `http://www.sciencedirect.com/science/article/pii/S0749641910001439`.

G. J. Tucker, M. A. Tschopp, and D. L. McDowell. Evolution of structure and free volume in symmetric tilt grain boundaries during dislocation nucleation. *Acta Materialia*, 58(19):6464 – 6473, 2010. ISSN 1359-6454. doi: https://doi.org/10.1016/j.actamat.2010.08.008. URL `http://www.sciencedirect.com/science/article/pii/S1359645410005124`.

T. Uesugi and K. Higashi. First-principles calculation of grain boundary energy and grain boundary excess free volume in aluminum: role of grain boundary elastic energy. *Journal of Materials Science*, 46(12):4199–4205, Jun 2011. ISSN 1573-4803. doi: 10.1007/s10853-011-5305-2. URL `https://doi.org/10.1007/s10853-011-5305-2`.

F. Ulomek and V. Mohles. Molecular dynamics simulations of grain boundary mobility in al, cu and γ-fe using a symmetrical driving force. *Modelling and Simulation in Materials Science and Engineering*, 22(5):055011, 2014.

A. Vattré and M. Demkowicz. Determining the burgers vectors and elastic strain energies of interface dislocation arrays using anisotropic elasticity theory. *Acta Materialia*, 61 (14):5172–5187, 2013.

W. T. Vetterling, W. H. Press, S. A. Teukolsky, and B. P. Flannery. *Numerical recipes example book (c++): The art of scientific computing.* Cambridge University Press, 2002.

A. Voter and S. Chen. Mrs symp. *Proc. 82*, pages 175–180, 1987.

A. F. VOTER. Accurate interatomic potentials for ni, al and ni3ai arthur f. voter and shao ping chen.

G. Z. Voyiadjis and M. Yaghoobi. Chapter 1 - introduction: Size effects in materials. In G. Z. Voyiadjis and M. Yaghoobi, editors, *Size Effects in Plasticity*, pages 1 – 79. Academic Press, 2019. ISBN 978-0-12-812236-5. doi: https://doi.org/10.

1016/B978-0-12-812236-5.00001-3. URL `http://www.sciencedirect.com/science/article/pii/B9780128122365000013`.

R. S. Wagner and B. Chalmers. Grain boundaries in germanium. *Journal of Applied Physics*, 31(581):581, 1960. ISSN 10.1063/1.1735632. doi: https://doi.org/10.1063/1.1735632. URL `https://aip.scitation.org/doi/10.1063/1.1735632`.

J. Wang and A. Misra. An overview of interface-dominated deformation mechanisms in metallic multilayers. *Current Opinion in Solid State Materials Science*, 15(1):20–28, 2011. doi: 10.1016/j.cossms.2010.09.002.

R. Wang and Q. Fang. Core structure and mobility of an edge dislocation in aluminum. *Journal of Alloys and Compounds*, 310(1):80 – 84, 2000. ISSN 0925-8388. doi: https://doi.org/10.1016/S0925-8388(00)00991-9. URL `http://www.sciencedirect.com/science/article/pii/S0925838800009919`. Intern. Conf. Internal Friction and Ultrasonic Attentuation in Solids (ICIFUAS-12).

J. A. Warren, W. C. Carter, and R. Kobayashi. A phase field model of the impingement of solidifying particles. *Physica A: Statistical Mechanics and its Applications*, 261(1-2): 159–166, 1998.

J. A. Warren, R. Kobayashi, A. E. Lobkovsky, and W. C. Carter. Extending phase field models of solidification to polycrystalline materials. *Acta materialia*, 51(20):6035–6058, 2003.

D. Warrington and W. Bollmann. Dislocation networks in high-angle grain boundaries. *Philosophical Magazine*, 25(5):1195–1199, 1972.

C. Wei, S. L. Thomas, J. Han, D. J. Srolovitz, and Y. Xiang. A continuum multi-disconnection-mode model for grain boundary migration. *Journal of the Mechanics and Physics of Solids*, 133:103731, 2019.

M. J. Weins. Structure and energy of grain boundaries. *Surface Science*, 31:138 – 160, 1972. ISSN 0039-6028. doi: https://doi.org/10.1016/0039-6028(72)90257-9. URL `http://www.sciencedirect.com/science/article/pii/0039602872902579`.

M. Winning, G. Gottstein, and L. Shvindlerman. On the mechanisms of grain boundary migration. *Acta Materialia*, 50(2):353–363, 2002.

D. Wolf. A read-shockley model for high-angle grain boundaries. *Scripta Metallurgica*, 23(10):1713 – 1718, 1989a. ISSN 0036-9748. doi: https://doi.org/10.1016/0036-9748(89)90348-7. URL `http://www.sciencedirect.com/science/article/pii/0036974889903487`.

D. Wolf. Correlation between energy and volume expansion for grain boundaries in fcc metals. *Scripta Metallurgica*, 23(11):1913 – 1918, 1989b. ISSN 0036-9748. doi: https://doi.org/10.1016/0036-9748(89)90482-1. URL `http://www.sciencedirect.com/science/article/pii/0036974889904821`.

X. Yan and H. Zhang. On the atomistic mechanisms of grain boundary migration in [0 0 1] twist boundaries: Molecular dynamics simulations. *Computational materials science*, 48(4):773–782, 2010.

L. Yang and S. Li. A modified synthetic driving force method for molecular dynamics simulation of grain boundary migration. *Acta Materialia*, 100:107–117, 2015.

S. Yip and . Wolf, Dieter. *Materials interfaces : atomic-level structure and properties*. London ; New York : Chapman Hall, 1st ed edition, 1992. ISBN 0412412705. URL `http://www.loc.gov/catdir/enhancements/fy0823/92021645-t.html`.

H. Zhang and D. J. Srolovitz. Simulation and analysis of the migration mechanism of sigma 5 tilt grain boundaries in an fcc metal. *Acta Materialia*, 54(3):623 – 633, 2006. ISSN 1359-6454. doi: https://doi.org/10.1016/j.actamat.2005.10.001. URL `http://www.sciencedirect.com/science/article/pii/S1359645405005719`.

H. Zhang, M. Mendelev, and D. Srolovitz. Computer simulation of the elastically driven migration of a flat grain boundary. *Acta materialia*, 52(9):2569–2576, 2004a.

H. Zhang, M. Mendelev, and D. Srolovitz. Computer simulation of the elastically driven migration of a flat grain boundary. *Acta materialia*, 52(9):2569–2576, 2004b.

H. Zhang, M. Upmanyu, and D. Srolovitz. Curvature driven grain boundary migration in aluminum: molecular dynamics simulations. *Acta materialia*, 53(1):79–86, 2005.

H. Zhang, D. Du, D. J. Srolovitz, and M. I. Mendelev. Determination of grain boundary stiffness from molecular dynamics simulation. *Applied physics letters*, 88(12):121927, 2006a.

H. Zhang, D. J. Srolovitz, J. F. Douglas, and J. A. Warren. Characterization of atomic motion governing grain boundary migration. *Physical Review B*, 74(11):115404, 2006b.

H. Zhang, D. J. Srolovitz, J. F. Douglas, and J. A. Warren. Atomic motion during the migration of general [0 0 1] tilt grain boundaries in ni. *Acta materialia*, 55(13):4527–4533, 2007.

P. Zhao, T. S. E. Low, Y. Wang, and S. R. Niezgoda. An integrated full-field model of concurrent plastic deformation and microstructure evolution: Application to 3d simulation of dynamic recrystallization in polycrystalline copper. *International Journal of Plasticity*, 80:38–55, 2016.

G. Zhou, Z. Li, D. Li, Y. Peng, H. S. Zurob, and P. Wu. A polycrystal plasticity based discontinuous dynamic recrystallization simulation method and its application to copper. *International Journal of Plasticity*, 91:48–76, 2017.

J. Zhou and V. Mohles. Towards realistic molecular dynamics simulations of grain boundary mobility. *Acta materialia*, 59(15):5997–6006, 2011.

T. Zhu and H. Gao. Plastic deformation mechanism in nanotwinned metals: An insight from molecular dynamics and mechanistic modeling. *Scripta Materialia*, 66(11):843 – 848, 2012. ISSN 1359-6462. doi: https://doi.org/10.1016/j.scriptamat.2012.01.031. URL `http://www.sciencedirect.com/science/article/pii/S1359646212000486`. Viewpoint set no. 49: Strengthening effect of nano-scale twins.

Y. Zhu, X. Wu, X. Liao, J. Narayan, L. Kecskés, and S. Mathaudhu. Dislocation–twin interactions in nanocrystalline fcc metals. *Acta Materialia*, 59(2):812 – 821, 2011. ISSN 1359-6454. doi: https://doi.org/10.1016/j.actamat.2010.10.028. URL `http://www.sciencedirect.com/science/article/pii/S1359645410006907`.